Magneto-Optical Studies of Semiconductor Heterostructures

Chin-chi Chang

A thesis submitted for the degree of Doctor of Philosophy

Wolfson College, Oxford

Michaelmas Term, 1998

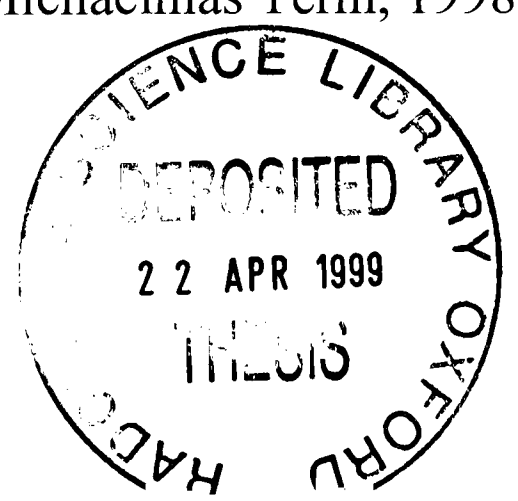

Magneto-Optical Studies of Semiconductor Heterostructures

Chin-chi Chang

A thesis submitted for the degree of Doctor of Philosophy
Wolfson College, Oxford
Michaelmas Term, 1998

Abstract

This thesis is primarily concerned with far infrared effects in semiconductor heterostructures. These properties have been studied as a function of magnetic fields at low temperature using various optical detection techniques. Cyclotron resonance has been studied in CdTe quantum wells. The results are compared with calculations using the memory function approach, which demonstrate that there is a large reduction in the resonant coupling due to level occupancy effects. Semimetallic GaSb/InAs superlattices have been studied by cyclotron resonance experiments. In samples with low InAs/GaSb ratios (~1), a pinning between the heavy hole subbands is predicted by theory which results in a suppression of heavy hole resonance at high magnetic fields. Photoluminescence measurements on a series of ultra-high mobility GaAs/AlGaAs heterojunctions have been performed. It has been found that the modulation caused by far infrared beam is entirely dependent on the filling factors, which is understood as the Landau level coupling effects between the subbands of 2DES. A GaAs/AlGaAs coupled quantum well photodiode has been studied by photoluminescence and photocurrent under the influence of far infrared beam. An enhancement of the photocurrent in the device is observed when the infrared photons are resonant with the intersubband transition between the anti-crossing electronic subbands of the coupled quantum wells, which makes the structure a potential tuneable far infrared detector. Most of the experimental works have been modelled with a ***k.p*** theory using momentum matrix approach. The self-consistency incorporated in this model proves to be useful while dealing with semimetallic or non-intrinsic systems. These calculations offer invaluable clues to the semiconductor heterostructures investigated.

Acknowledgements

I would like to thank all those whose help have made this thesis possible, in particular:

Prof. P.G.H. Sandars, Prof. R.A. Cowley and Prof. J.M. Baker for allowing me the use of the facilities of the Clarendon Laboratory.

My supervisor, Prof. Robin Nicholas, for constant enthusiasm and advice throughout my research and the "Tis' true that I know much, but I should like to know all" attitude towards physics. Dr. Mark Fox for many invaluable discussion in Chapter 7.

My research colleagues: Glen Summers for introducing me to the world of infrared, M'hamed Lakrimi for advice on everything, Andrew Poulter for all those brain-damaging "quizzes" during my thesis writing, Phil Shields for his tolerance with my English, Sungwon Khym and the smoking barrels, Javed Rehman and his "Moral tutor", Andy Tomlinson - the rising Michelin three-starred chef, Andrew Priest for demonstrating Scottish manhood, Tom Vaughan for the ingenious ***k.p*** programmes, Maarten van der Burgt for much help with the pulsed magnet, Edouard Alphandery for illustrating "eccentricity", Dave Kinder for the elaborate use of English, Joe Michels for his threatening presence, and also Dave Symons, Matt Daly, Henry Cheng, Karen Dalton, John Dykema, Rob Stone, Kei Takashina, Vicky Hales, Cattleya Petchsingh and all the others in the Nicholas Group.

HJ35 and HJ36 for sacrificing their lives for my research.

The technical staff at the Clarendon, especially Keith Belcher, Simon Moulder, Graham Read, Tony Hickman and George Matthews.

Wolfson college and Taipei Representative Office for financial support.

Special thanks and love go to Ya-lan and my brother, Yuan-chi.

Finally, I would like to dedicate this thesis to my parents for their unceasing love, support and encouragement throughout my education.

Table of Contents

1. Introduction

1.1 Overview

The study of semiconductor materials dates right back to the early nineteenth century [1]. However only since the creation of the first bipolar transistor in 1948 [2] has the area begun to take central stage of the modern technology revolution. In the next two decades, researches were mainly focused on fabrication and characterisation of pure semiconductor crystals. The limitation set by the availability of certain materials posted a serious problem. The solution to this was the superlattice, first suggested by Esaki and Tsu [3]. Since then, the research is carried out along two fronts – finding new materials and engineering superlattices (heterostructures) for wider applications. Today various structures are used in all sorts of devices, from supercomputers and communication networks to CD players and sensors.

This thesis describes researches conducted on the optical properties of semiconductor heterostructures in high magnetic field and low temperature. The electron-phonon interaction in CdTe quantum wells is investigated in Chapter 4. GaSb/InAs superlattices, famous for the intrinsic carrier transfer due to the crossed band gaps, are studied using cyclotron resonance in Chapter 5. Chapter 6 is concerned with the optical properties of the two dimensional electron gas in modulation doped GaAs/$Al_xGa_{1-x}As$ heterojunctions. The infrared modulated luminescence shows a striking behaviour depending on the filling factors and the carrier densities. At last, the photoconductivity and luminescence are measured on a GaAs/$Al_xGa_{1-x}As$ asymmetric coupled quantum well which has conceivable potential for tuneable infrared detectors. Most of the experimental works done in the thesis are modelled using the ***k.p*** theory described in Chapter 3.

1.2 Crystal Structure and Energy Bands

Most III-V semiconductors crystallise in a crystal with the zinc-blend structure that consists of two interpenetrating face centred cubic (fcc) lattices, displaced from one another by one quarter of the main cube diagonals so that the lattice can be described as two inter-penetrating cubes, one cube being offset from the other by one quarter of a cube diagonal [4-6]. Consequently, the corresponding reciprocal lattice is body-centred cubic (bcc) whose first Brillouin zone is truncated octahedron as shown in Figure 1-1. The high symmetry points are labelled Γ (zone centre), *X* (intersection of <100> and the first Brillouin zone boundary) or *L* (intersection of <111> with the first Brillouin zone boundary).

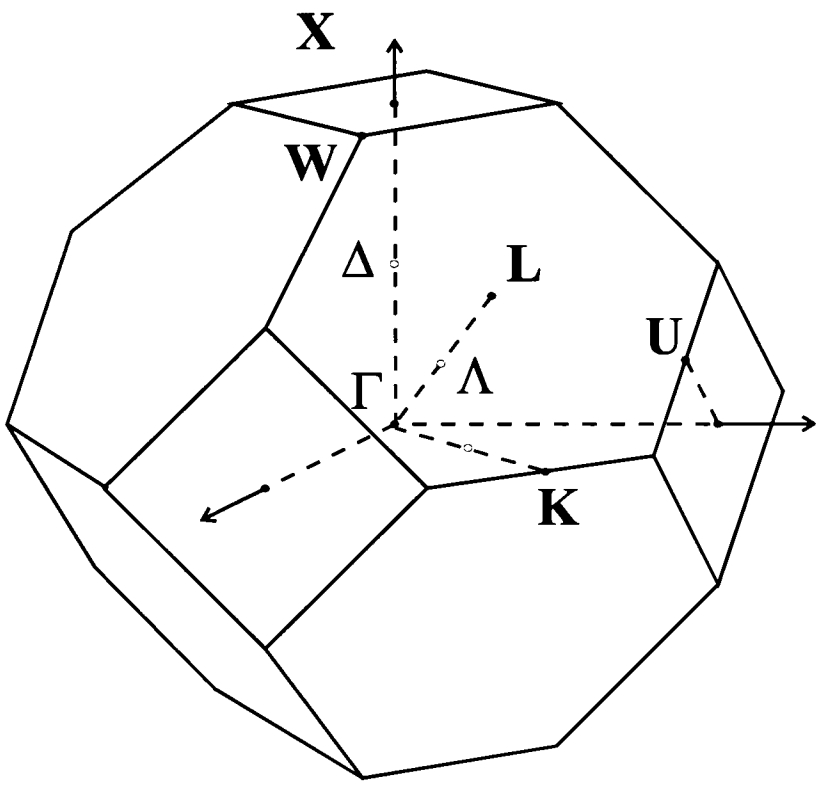

Figure 1-1: The first Brillouin Zone of a III-V semiconductor.

In each unit cell there are eight valence electrons from s- and p-orbitals that participate in the chemical bonding. As shown in Figure 1-2 (A), the eight electrons would fill the bonding s- and p-orbitals and leave the anti-bonding ones empty. The bonding p-orbitals constitute the valence levels and the anti-bonding s-orbital forms the conduction level. The energy difference between is called the energy gap. When a lot of atoms join in as in the real materials, the coupling with atoms at farther sites would contribute to fine splitting and finally create the continuous "band" (Figure 1-2 (B)). In

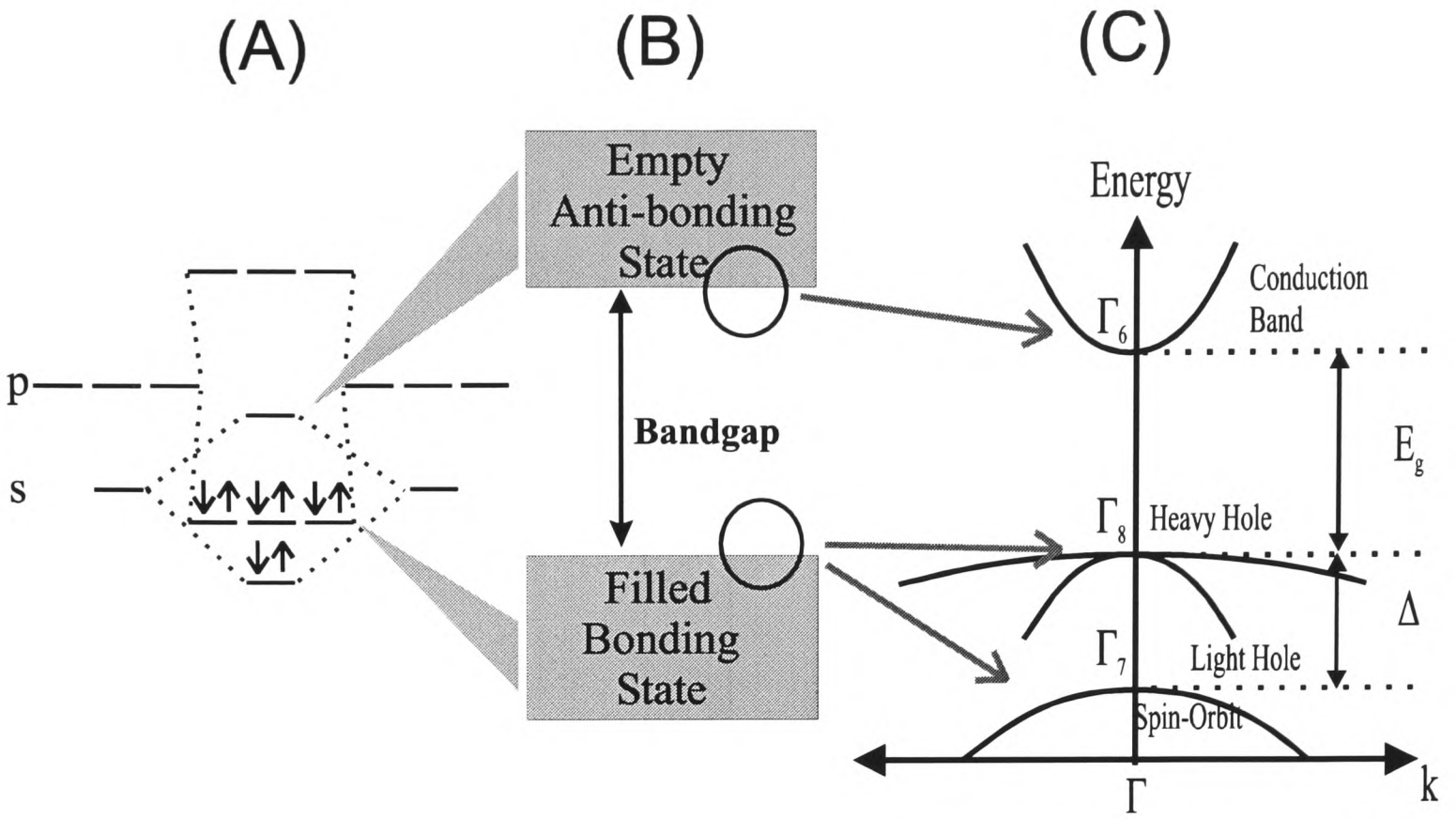

Figure 1-2 Schematic diagrams to show (A) two atoms close to each other to form the bonding – anti-bonding pairs, (B) the formation of "bands" and (C) direct-gap band structure near the Γ-point.

practice the only relevant bands are those close in energy to the Fermi level (which separates the filled from the unfilled states). Figure 1-2 (C) shows such a band structure in k-space near the band extrema. The valence band splits into heavy and light hole bands with four-fold degeneracy at the zone centre angular momentum **J** =3/2 and the spin-orbit band with **J** =1/2. In this region the bands are approximately parabolic, so that they can be described by effective mass m^*, defined as

$$\frac{1}{m^*} = \frac{1}{\hbar^2}\frac{d^2E(\vec{k})}{d^2\vec{k}}$$

where $\vec{k}$ is the wavevector and E the energy of the band as a function of $\vec{k}$. For a purely parabolic band m^* is a constant.

The actual bulk band structure of semiconductors is much more complicated than the one shown in Figure 1-2 (C). Figure 1-3 shows the band structure of InAs calculated using pseudo-potential techniques [5,6]. However, one can always reach reasonable accuracy by considering non-parabolicity (changing mass along the k-space) in the effective mass approximation since we are only usually interested in the band extreme points.

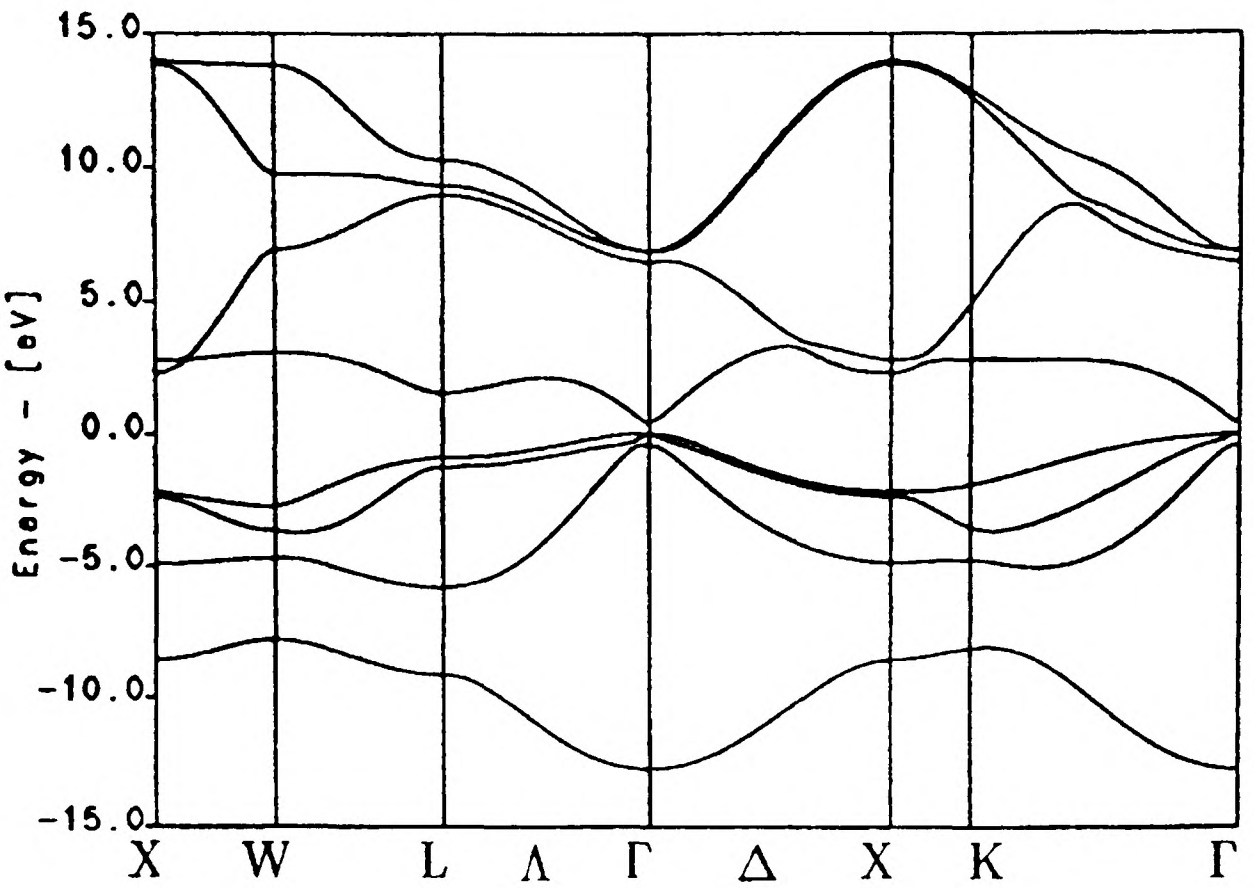

Figure 1-3 Calculated band structure for InAs, a narrow direct band gap material; thus even near Γ non-parabolicity of the conduction band must be included.

1.3 Semiconductor Heterostructures

When two materials with different band gaps are grown together the resulting energy levels for the electrons in the composite material will depend on the size of the band gaps and the way the bands line up, the band offset. Figure 1-4 illustrates the band offsets of several materials relative to gold. Using the band edge alignment as the criterion, we can categorise the hetero-structures to two types. In Type I systems (e.g.

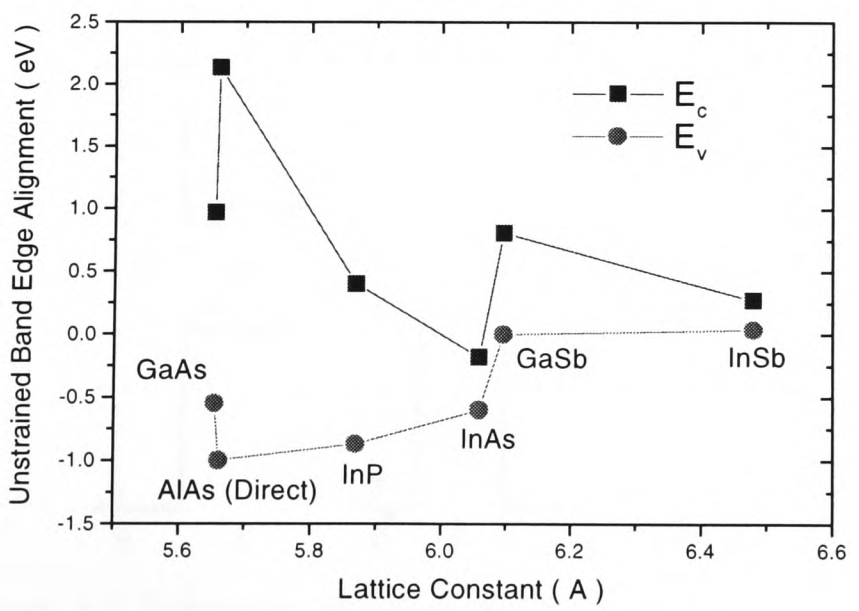

Figure 1-4 Band edge alignment of some semiconductor materials with E_c and E_v standing for the conduction and valence band edge, respectively.

$GaAs/Al_xGa_{1-x}As$) one material acts as a well for both electrons and holes. Type II systems (e.g. GaP/AlP) have one material as a well for electrons and a barrier for holes and vice versa. If the conduction band edge of one material is lower than the valence band edge of another, a net charge transfer between the layers is expected (e.g. InAs/GaSb). Figure 1-5 (A) outlines these different types of heterostructure [7]. The simplest type of heterostructure is a heterojunction (HET) between two materials. By growing two such heterojunctions in close proximity a quantum well (QW) is created. Growing a series of non-interacting wells constitutes a multi quantum well (MQW). Finally by growing a series of periodic quantum wells such that there is significant overlap between the carrier wavefunctions in adjacent wells a superlattice (SL) is formed. Figure 1-5 (B) summarises the various heterostructures.

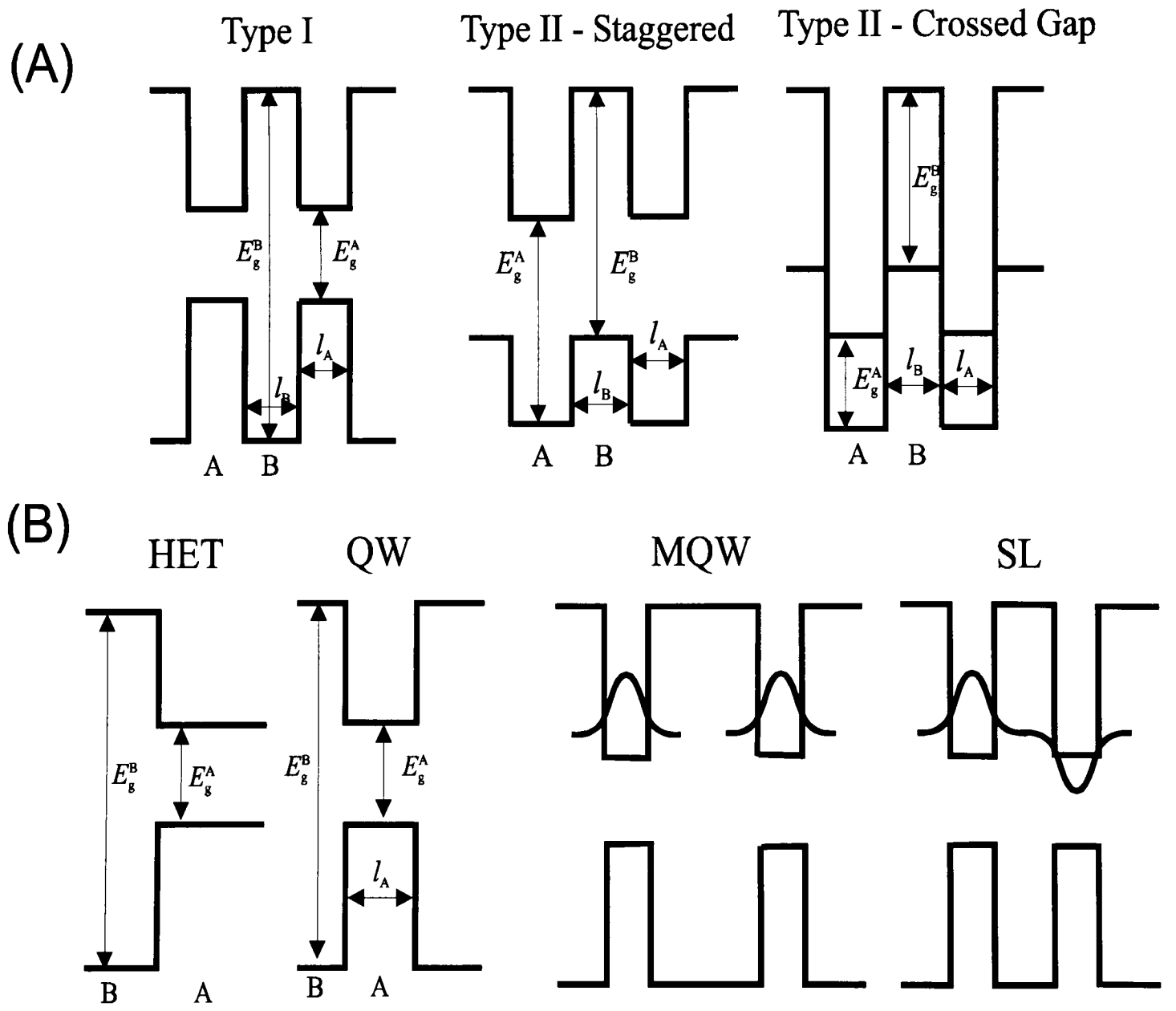

Figure 1-5 Schematic diagrams for (A) different band offset systems and (B) various types of heterostructures.

It is worth explaining the naming of z-axis in heterostructures, as we shall refer to it extensively later. The heterostructure growth direction offers an alternative definition of the z-axis while the chemical bonds in crystals provide another. In the case of samples grown along the [001] direction, these definitions coincide. Fortunately most of the samples studied were grown along or near [001] which saves us from the trouble of confusion.

1.3.1 Growth Techniques

Heterostructures are grown by "epitaxy", that is, the controlled growth of the structure, laying down one atomic layer at a time. To ensure the growth accuracy to atomic level, a high-quality substrate to start with is essential. GaAs wafers are used extensively in most of the III-V heterostructure growth due to their unfailing high quality and availability (people have been growing GaAs wafers for more than ten years). Though there is a lattice mismatch of 8%, the GaSb/InAs superlattices investigated in Chapter 5 are still grown on GaAs substrates with a thick layer of GaSb to buffer the strain.

There are currently two major deposition methods used to grow heterostructures: MOVPE (Metal Organic Vapour Phase Epitaxy) and MBE (Molecular Beam Epitaxy). As the name suggests in MBE, beams of atoms or molecules are directed at a heated single crystal substrate under ultra-high vacuum condition [8]. The atoms adhere to the substrate, continuing the crystal structure. Selecting the right substrate temperature encourages the atoms to migrate over the surface, helping to fill the vacant sites in one layer before another begins to form. Growth rates are typically 0.3 ~ 30 $Å s^{-1}$. Mechanical shutters are placed over the cells, allowing different materials to be grown. The shutters are controlled by computers and have a switching time that is shorter than the time required growing one monolayer. Reflection high energy electron diffraction (RHEED) allows each monolayer to be monitored as it is grown which is a significant advantage of this technique. A drawback is materials with high vapour pressure, such as phosphorous, are difficult to handle in the vacuum chamber. The ultra high vacuum and pure atom sources requirement means the running cost of MBE is rather high.

In contrast to MBE, MOVPE operates at atmospheric pressure [9]. The group III elements enter the reactor as an organo-metallic complex and the group V as hydrides [10]. The compounds react and are deposited on the heated substrate. The method is cheaper than MBE and there is no significant problem with the phosphorous compounds. However, interfaces of MOVPE-grown materials tend to be less sharp than those of MBE samples [11]. The continual gas flow through the chamber makes RHEED measurements impossible and a new technique has been developed in the Clarendon that uses absorption of ultra-violet light to monitor the growth process [12].

1.4 Magnetic Fields and Cyclotron Resonance

When a magnetic field is applied to an electron gas it reorganises the electron states into the celebrated Landau levels due to the Lorentz force and orbit quantisation. Assumptions made in the following analysis include constant effective masses (no non-parabolicity) and isotropic conduction bands.

Ignoring spin, the influence of a magnetic field on a single electron is represented by the following Hamiltonian

$$H = \frac{1}{2m^*}(\vec{p} - e\vec{A})^2 \tag{1.1}$$

where $\vec{p}$ is the electron momentum operator and $\vec{A}$ is the magnetic vector potential. For a magnetic field **B** oriented along the z-axis the vector potential in the Landau gauge is $\vec{A} = (0, xB, 0)$ and the Hamiltonian becomes

$$H = \frac{1}{2m^*}\left[p_x^2 + (p_y - exB)^2 + p_z^2\right] \tag{1.2}$$

The quantum equations of motion give

$$i\dot{p}_y = \left[p_y, H\right] = 0 \qquad i\dot{p}_z = \left[p_z, H\right] = 0 \tag{1.3}$$

As p_y and p_z both commute with the Hamiltonian they are constants of the motion and the substitutions $p_y = \hbar k_y$ and $p_z = \hbar k_z$ can be made. If we use the additional substitution

$$x' = x - x_0 = x - \frac{\hbar k_y}{m^* \omega_c} \tag{1.4}$$

where the cyclotron frequency is $\omega_c = \frac{e\mathbf{B}}{m^*}$, the Hamiltonian becomes

$$H = \frac{1}{2m^*}\left[p_x^2 + m^{*2}\omega_c^2 x'^2\right] + \frac{\hbar^2 k_z^2}{2m^*} \tag{1.5}$$

The first term is simply the Hamiltonian for a simple harmonic oscillator with the transition frequency ω_c, which gives rise to a set of discrete energy levels known as Landau levels with energy spacing $\hbar\omega_c$. The second term accounts for the free motion of the electrons in the z-direction.

To move to the two dimensional case, we need simply to add the confining potential to the Hamiltonian in Eq. (1.5). The resulting Hamiltonian can be written as

$$H = \frac{1}{2m^*}\left[p_x^2 + m^{*2}\omega_c^2 x'^2\right] + \frac{\hbar^2 k_z^2}{2m^*} + eV(z) \tag{1.6}$$

The last two terms involve only z. The eigenvalues of these are the subband energies E_i. The first term again gives rise to a ladder of Landau levels. The energy eigenvalues are thus

$$E(N,i) = E_i + (N + \tfrac{1}{2})\hbar\omega_c \tag{1.7}$$

where N is the Landau index. If the effects of spin are included, each of these states will be split into two levels with the energy of each spin state given by $\pm\frac{1}{2}g^*\mu_B B$, where g^* is the effective Landè g-factor and μ_B is the Bohr magneton. Adding all the different contributions to the energy together, the total energy of the Landau levels is then

$$E(N,i) = E_i + (N + \tfrac{1}{2})\hbar\omega_c \pm \tfrac{1}{2}g^*\mu_B B \tag{1.8}$$

Since the $E(N,I)$ is independent of momentum, the Landau levels are highly degenerate. To further determine the occupancy of the sample, one needs to know the density of states.

A sample with dimensions l_x, l_y gives allowed values of $(2\pi/\ l_x)I$ in k-space where I is an integer. There are $l_x/2\pi$ allowed values of k_x per unit length. An additional constraint is that the centre of the cyclotron orbit must be located within the sample extent which is expressed as

$$0 < y < l_y \text{ and } \quad 0 < l_0^2 k_x < l_y \tag{1.9}$$

Each layer therefore contains $l_x l_y / 2\pi l_0^2$ allowed states per k_x. Since the quantisation is complete, the levels are discrete and the density of states which is the number of states per Landau level per unit area is

$$D(E) = \frac{l_x l_y}{2\pi l_0^2} = \frac{eB}{h} \tag{1.10}$$

The density of states consists of a series of singularities at the Landau level energies and any phenomenon that depends on the density of states at the Fermi energy will show strong oscillatory behaviour when sweeping the magnetic field. If the carrier concentration is N_s per unit area, the number of filled Landau levels ν is then

$$\nu = \frac{N_s}{D(E)} = \frac{N_s h}{eB} \tag{1.11}$$

where ν is called the filling factor.

1.4.1 Cyclotron Resonance

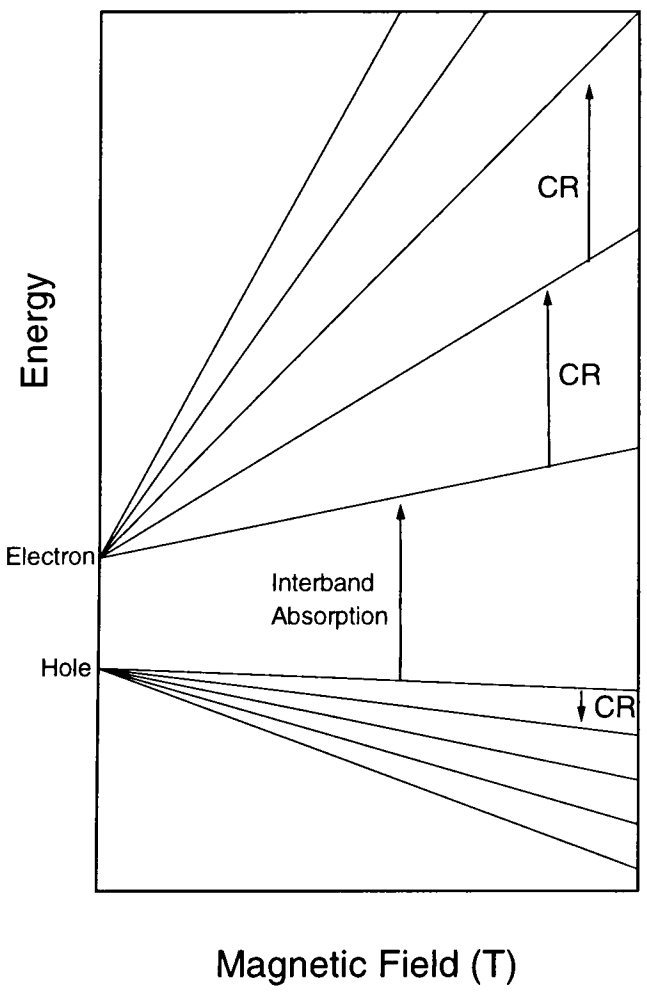

Figure 1-6 A diagram illustrates the cyclotron resonance (CR) and interband optical absorption.

Cyclotron resonance is one of the oldest and most widely used experimental techniques of semiconductor physics [13,14]. It was one of the first optical experiments to be performed on bulk materials due to the straightforward set-up involved, and it continues to be used for two reasons: the analysis is very elegant, and it is a powerful tool in the investigation of both heterostructures and bulk materials.

Cyclotron resonance corresponds to the intra-band excitation of an electron or hole from one Landau level to another. The selection rule is usually given as an

index change of 1 ($\Delta N = \pm 1$) and spin conservation due to the angular momentum conservation. This is however inaccurate and a more detailed model is shown in Chapter 3. The technique is principally used to determine the carrier effective mass by using $m^* = \frac{e\mathrm{B}}{\omega_c}$. Nonetheless, other information such as intersubband absorption can be collected as well. A cyclotron resonance can only be observed if the initial level is occupied and the final partially occupied. As recently discovered, the electron-electron interaction and disorder potential can influence the resonance and hence make it an ideal tool to study many body effects [15,16].

1.5 Resonance in Field - Plasma Background

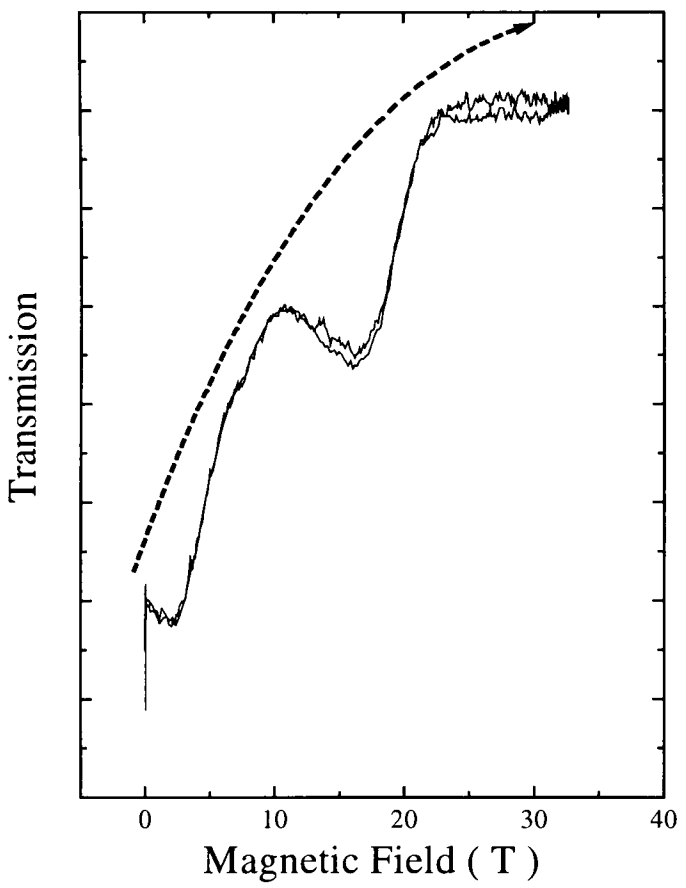

Figure 1-7 A conventional cyclotron resonance trace using a pulsed magnetic field and a wavelength of 163.08 μm.

Figure 1-7 shows a conventional cyclotron resonance trace. It is taken using fixed incident beam wavelength and sweeping magnetic field, a pulsed magnet in this case. Two clear absorptions can be seen – the one at 18 Tesla is the hole resonance and the other one around 3 Tesla is the electron resonance.

In addition to these two clear features, it is significant that the sample is four times more transparent at high field (~32 Tesla) than at zero field. This kind of background change is observed in nearly all the spectra taken. Highly dependent on wavelength and sample carrier density, the field dependant transparency in infrared range is understood as the magneto-optical effect of the collective plasma [17,18].

1.5.1 Free-Carrier Magneto-optical Effects

We consider the electromagnetic properties of a medium containing N particles of effective mass m^* and charge e to be the sum of individual particle properties. This is the plasma mode because all particles move together. The classical equations of motion of a particle subjected to external field $\mathbf{E}e^{i\omega t}$ (incident beam) and $\mathbf{B}$ (steady field), and viscously damped with frequency f, are

$$m^* \frac{d\vec{v}}{dt} + m^* f\vec{v} = e(\mathrm{E}e^{i\omega t} + \vec{v} \times \mathrm{B}) \tag{1.12}$$

For $\vec{v} \sim e^{i\omega t}$, taking coordinates along the principal axes of the effective mass tensor, and recalling that $\mathbf{J} = Ne\vec{v} = \sigma \cdot \mathbf{E}$, we obtain [19]

$$\sigma = Ne^2 \begin{bmatrix} (i\omega + f)m_x^* & -e\mathrm{B}_z & e\mathrm{B}_y \\ e\mathrm{B}_z & (i\omega + f)m_y^* & -e\mathrm{B}_x \\ -e\mathrm{B}_y & e\mathrm{B}_x & (i\omega + f)m_z^* \end{bmatrix}^{-1} \tag{1.13}$$

The algebra for even this simple model becomes tedious, but explicit results have been worked out, and further simplification results for a model with isotropic mass m^* and $\mathbf{B}$ along z axis. Then [20]

$$\sigma = \omega_p^2 \varepsilon_0 \kappa \begin{bmatrix} \dfrac{-i(\omega - if)}{(\omega - if)^2 - \omega_c^2} & \dfrac{-\omega_c}{(\omega - if)^2 - \omega_c^2} & 0 \\ \dfrac{\omega_c}{(\omega - if)^2 - \omega_c^2} & \dfrac{-i(\omega - if)}{(\omega - if)^2 - \omega_c^2} & 0 \\ 0 & 0 & \dfrac{-i}{(\omega - if)} \end{bmatrix} \tag{1.14}$$

where $\omega_p = \dfrac{Ne^2}{m^* \varepsilon_0 \kappa}$ and $\omega_c = \dfrac{e\mathrm{B}}{m^*}$ are the plasma and cyclotron frequency, respectively.

For the configuration in which most experiments are done, where the incident beam is parallel to magnetic field, the complex refractive index reads as

$$(n - ik)_{\pm}^2 = \kappa \left[1 - \frac{\omega_p^2}{\omega(\omega \mp \omega_c - if)} \right] \tag{1.15}$$

where $(n - ik)_{\pm}$ stands for right or left circularly polarised light. The damping frequency f can be measured by saturated cyclotron resonance experiments using a high power laser [21]. Taking the model a step further, we can include the effect of phonon interactions [22,23] and the refractive index turns to be

$$(n-ik)_{\pm}^2 = \kappa\left[1-\frac{\omega_p^2}{\omega(\omega\mp\omega_c-if)}+\frac{\omega_L^2-\omega_T^2}{\omega_T^2-\omega^2-i\Gamma\omega}\right] \tag{1.16}$$

where ω_L and ω_T represent the LO and TO phonon frequencies, respectively, and Γ is the phonon scattering angular frequency.

1.5.2 Multilayer Calculation by Transfer Matrix Approach

Following Eq. (1.16), the complex refractive index can be calculated and hence the corresponding reflectance and transmission coefficients. Nevertheless, this is true for systems with only one interface. For samples consisting of more than one layer, actually ALL the samples, multiple-reflection between the layers is expected. To model such a system, a transfer matrix approach based on boundary conditions is introduced [24-26].

Consider a semiconductor multilayer structure composed of N-2 layers. An incident plane wave has associated electric and magnetic field amplitudes E_k and $B_k = \frac{n_k}{c}E_k$, respectively. The corresponding reflected wave amplitudes are E_k' and B_k'. Applying the boundary conditions for the electric and magnetic fields at the interface between the m^{th} and $(m+1)^{\text{th}}$ layer we get

$$E_m e^{(ikz_{m,m+1}n_m)} + E_m' e^{(-ikz_{m,m+1}n_m)} = E_{m+1}e^{(ikz_{m,m+1}n_m)} + E_{m+1}' e^{(-ikz_{m,m+1}n_m)}$$

$$E_m n_m e^{(ikz_{m,m+1}n_m)} - E_m' n_m e^{(-ikz_{m,m+1}n_m)} = E_{m+1}n_{m+1}e^{(ikz_{m,m+1}n_m)} - E_{m+1}' n_{m+1} e^{(-ikz_{m,m+1}n_m)} \tag{1.17}$$

n_m, k and $z_{m,m+1}$ are the layer refractive index, light propagation vector in vacuum and the position of the interface between m^{th} and $(m+1)^{\text{th}}$ layer. Solving Eq. (1.17) we find

$$\begin{bmatrix} E_m \\ E_m' \end{bmatrix} = M_{m,m+1}\begin{bmatrix} E_{m+1} \\ E_{m+1}' \end{bmatrix}$$

where the transfer matrix $M_{m,m+1}$ is given by

$$M_{m,m+1} = \begin{bmatrix} (\frac{n_m+n_{m+1}}{2n_m})e^{ikz_{m,m+1}(n_m-n_{m+1})} & (\frac{n_m-n_{m+1}}{2n_m})e^{-ikz_{m,m+1}(n_m+n_{m+1})} \\ (\frac{n_m-n_{m+1}}{2n_m})e^{ikz_{m,m+1}(n_m+n_{m+1})} & (\frac{n_m+n_{m+1}}{2n_m})e^{-ikz_{m,m+1}(n_m-n_{m+1})} \end{bmatrix} \tag{1.18}$$

By calculating the matrices for all interfaces of the microstructure, one obtains an equation that connects the incident and reflected electric field amplitudes E_1 and E_1' with the transmitted amplitude E_N

$$\begin{bmatrix} E_1 \\ E_1' \end{bmatrix} = M \begin{bmatrix} E_N \\ 0 \end{bmatrix} \qquad \text{where } M = M_{1,2} M_{2,3} \ldots\ldots\ldots M_{N-1,N} \quad (1.19)$$

The reflectance and transmission coefficients R and T can be expressed as functions of the matrix elements of M.

$$R = \left|\frac{E_1'}{E_1}\right|^2 = \left|\frac{M_{21}}{M_{11}}\right|^2$$

$$T = \left|\frac{E_N}{E_1}\right|^2 = \left|\frac{1}{M_{11}}\right|^2 \qquad (1.20)$$

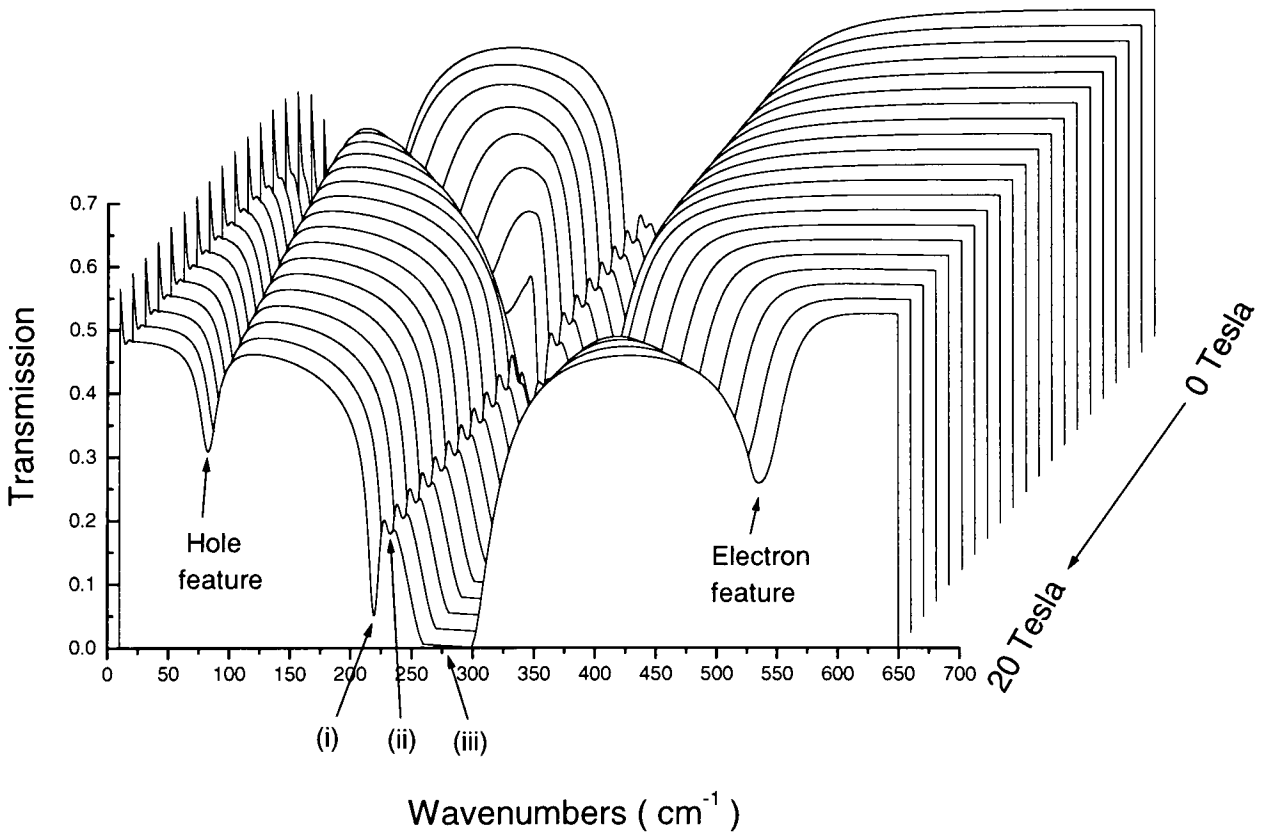

Figure 1-8 The calculated transmission spectrum of sample 2058 (see Chapter 5 for sample details) using the multi-layered plasma model. The field-independent absorption at (i), (ii) and (iii) are the TO phonon frequencies of InAs, GaSb and GaAs substrates, respectively.

With the help of Eq. (1.16) and Eq. (1.20), we can simulate a real semiconductor heterostructure and calculate the plasma response of it. One thing worth mentioning is that the spectra usually look like the spiky back of dinosaurs due to interference if the

boundary between substrate and air is included. This is, however, rather easy to remove by averaging neighbouring data points. Figure 1-8 shows such a calculation done on GaSb/InAs superlattice with GaAs substrates. Three TO phonon absorption peaks can be seen clearly which correlate with their respective thicknesses. Besides the three, two other resonances move with the magnetic field which agree with the electron and hole effective masses. Plotting the spectra with constant beam wavelength against magnetic field in Figure 1-9, the background changing observed in experiments is easily spotted. At long wavelength, the transmission coefficient goes up dramatically with field. This tendency is alleviated with decreasing wavelength (towards the plasma frequency, actually).

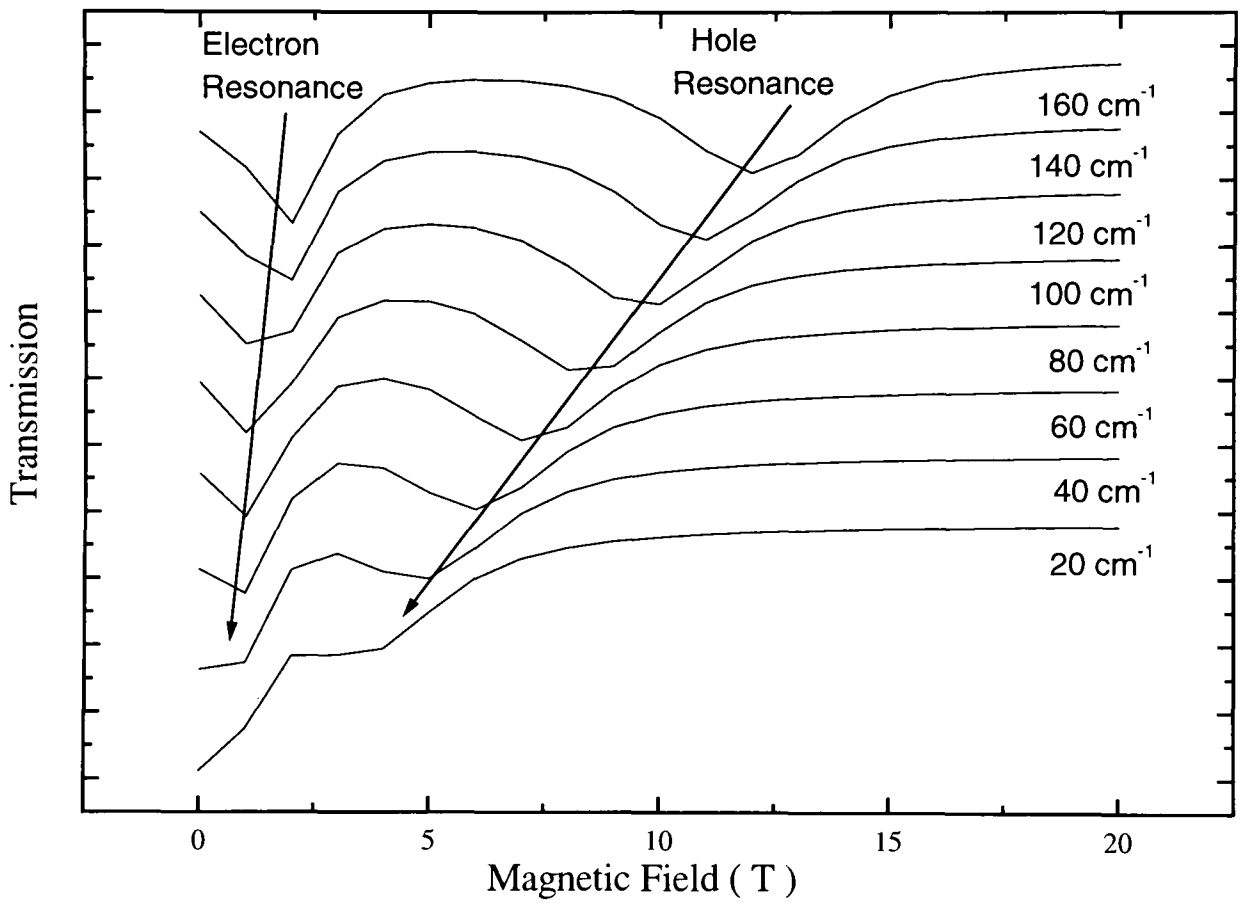

Figure 1-9 The same calculation as Figure 1-8 but presented at fixed energy and swept field, in which configuration the experiments are done.

Irrelevant as it may look like, the modelling can be very valuable to help with picking the exact resonance position when the plasma background dwarfs the actual feature. Chapter 4 describes such an example, in which case the resonance energy is within the reststrahlen.

References

[1] R. A. Smith, *Semiconductors*, 2nd edition, Cambridge University Press, London (1979).

[2] J. Bardeen, W.H. Brattain, *Phys. Rev.* **74**, 230 (1948).

[3] L. Esaki and R. Tsu, *IBM J. Res. Dev.* **14,** 61 (1970).

[4] C. Kittel, *Introduction to Solid State Physics*, 6th edition, John Wiley & Sons, New York (1989).

[5] E.O. Kane, *Semiconductors and Semimetals (Physics of III-V Compounds)*, edited by R.K. Willardson and A.C. Beer Vol. 1, Academic Press (1966).

[6] C. Kittel, *Quantum Theory of Solids*, 2nd edition, John Wiley & Sons, New York (1987).

[7] *Molecular Beam Epitaxy and Heterostructures,* edited by L. L. Chang and K. Ploog, Martinus Nijhoff (1985).

[8] B. A. Joyce, *Rep. Prog. Phys.* **48**, 1637 (1985).

[9] N. J. Mason, *Atomic Layer Epitaxy*, edited by T. Suntola and M. Simpson, Blakie (1990).

[10] N. J. Mason and P. J. Walker, *J. Cryst. Growth* **107**, 181 (1991).

[11] S. G. Lyapin, P. C. Klipstein, N. J. Mason and P. J. Walker, *Superlattices and Microstuctures* **15**, 1177 (1994).

[12] N. J. Mason and P. J. Walker, *private communication.*

[13] G. Dresselhaus, A. F. Kip and C. Kittel, *Phys. Rev.* **92**, 827 (1953).

[14] G. Dresselhaus, A. F. Kip and C. Kittel, *Phys. Rev.* **98**, 368 (1955).

[15] G. M. Summers, R. J. Warberton, J. G. Michels, R. J. Nicholas, J. J. Harris and C. T. Foxon, *Phys. Rev. Lett.* **70**, 2150 (1993).

[16] N. R. Cooper and J. T. Chalker, *Phys. Rev. Lett* **72,** 2057 (1994).

[17] E. D. Palik and G. B. Wright, *Semiconductors and Semimetals,* edited by R. K. Willardson and A. C. Beer, Vol. 3, Academic Press, New York (1970).

[18] R. L. Aggarwal, *Semiconductors and Semimetals,* edited by R. K. Willardson and A. C. Beer, Vol. 9, Academic Press, New York (1972).

[19] B. Lax and L. M. Roth, *Phys. Rev.* **98**, 544 (1955).

[20] B. Lax, H. J. Zeiger and R. N. Dexter, *Physica* **20**, 818 (1954).

[21] T. A. Vaughan, *D.Phil thesis*, Oxford (1995).

[22] E. D. Palik and J. K. Furdyna, *Rep. Prog. Phys* **33**, 1193 (1970).

[23] B. B. Varga, *Phys. Rev.* **137**, A1896 (1965).

[24] L. Schultheis and R. Ploog, *Phys. Rev. B* **30**, 1090 (1984).

[25] M. Born and E. Wolf, *Principles of Optics*, 6th edition, Pergamon, Oxford (1980).

[26] A. F. Terzis, X. C. Liu, A. Petrou and B. D. McCombe, submitted to *J. Appl. Phys.*

2. Experimental Details

2.1 Introduction

The experiments conducted in this thesis require a comprehensive variety of set-ups. Nevertheless, a far-infrared laser and magnetic fields are used in all of them. I am going to describe these pieces of apparatus in the following sections and leave the details of those arrangements to the corresponding chapters.

2.2 Far Infrared Laser

The laser used to produce the far infrared radiation actually consists of two separate lasers which are coupled together: a carbon dioxide laser with output wavelengths between 9~11 μm and a molecular gas laser whose cavity is usually filled with a low pressure gas of methanol or its derivatives [1].

The CO_2 laser is an industrial standard laser manufactured by Edinburgh Instruments with a maximum continuous output power of 50 W. The active medium in the laser is a mixture of carbon dioxide, nitrogen, and helium. Each gas has a distinct role. The nitrogen molecules absorb the energy from the electrons of the high voltage discharge and transfer it to the carbon dioxide molecules, thereby raising them to the upper energy level. Carbon dioxide is the light emitter. The molecules are first excited with the transferred energy so that they vibrate

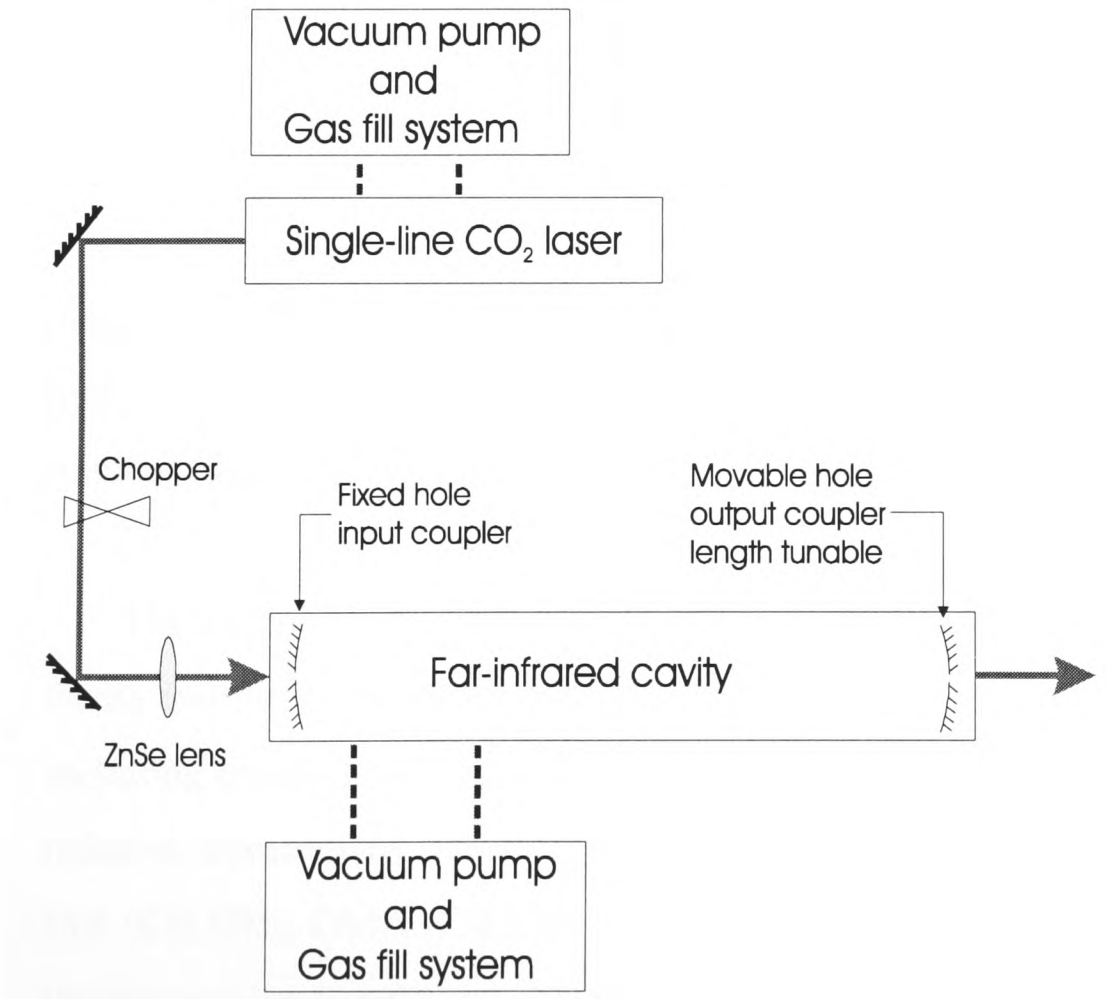

Figure 2-1 Typical arrangement for pumping a far-infrared laser optically.

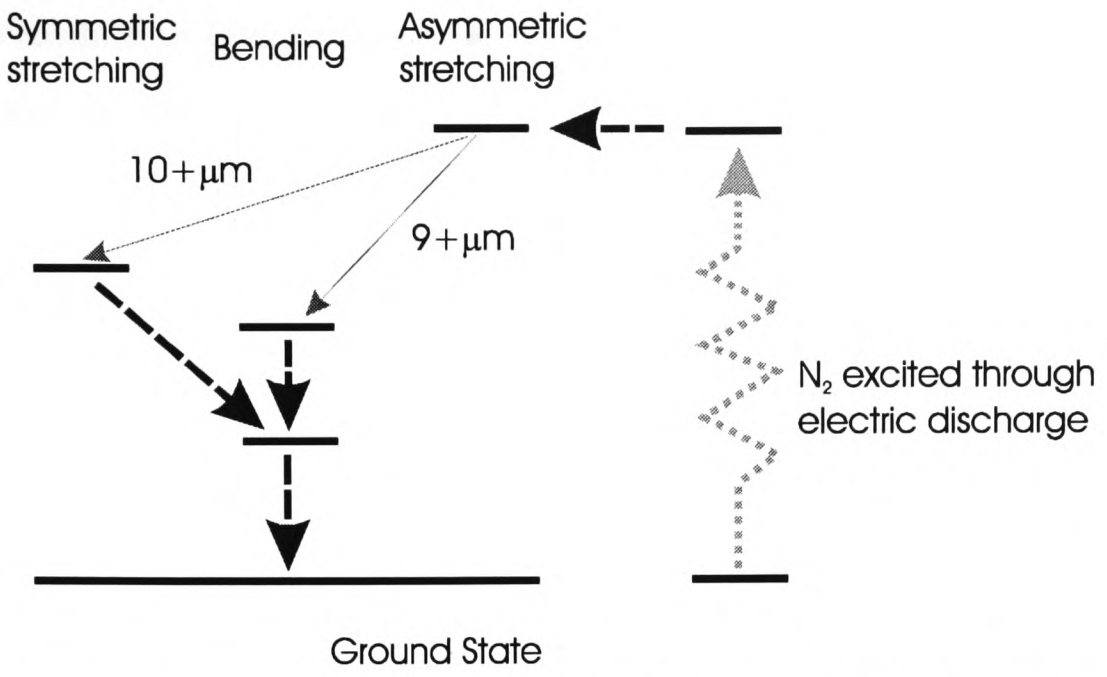

Figure 2-2 Energy-level structure in the CO_2 laser, showing the relevant vibrational modes of the CO_2 molecule.

in an asymmetrical stretching mode. The molecules then lose part of the excitation energy by dropping to one of two other lower-energy vibrational states shown in Figure 2-2. These two decay paths are the two principal laser transitions: a shift to a symmetrical stretching mode accompanied by emission of a 10.6 μm photon, or a shift to a bending mode accompanied by emission of a 9.6 μm photon. Superposition of changes in the molecules' rotational states on the vibrational transitions yields large families of laser lines surrounding these two major transitions. Once the molecules have emitted their laser photons, they continue to drop down the energy ladder until they reach the ground state. The crucial role of helium is to depopulate these lower energy levels, thus maintaining the population inversion needed for laser operation, which is often referred to simply as "cooling". The gas mixture is pumped through the laser cavity continuously during the operation due to the fact that the electrical discharge breaks down carbon dioxide molecules. If it were sealed in the cavity, the laser would stop working in a matter of minutes [1].

The output of the CO_2 laser is then fed into the far-infrared laser consisting of the cavity and the gas flowing system which delivers the active medium. A variety of media, including exotic gases like $C_2H_2F_2$ and CH_3F [2], can be used to produce different far-infrared wavelengths. Only four different molecules are employed in my experiments - MA (CH_3OH), DMA (CH_3OD), MAD (CD_3OH) and FA (Formic acid) - mainly because they are easy to handle and cover the range I am interested in quite nicely.

The procedure to find the laser line wanted is as follows. Initially, the grating on the CO_2 laser and the pressure of gas are set to what they are supposed to be. Then one tries to find the line by adjusting the piezo of the CO_2 laser and the cavity length of the far infrared. Finally, all four parameters - the piezo, the grating of CO_2 laser and the cavity length, gas pressure of the far-infrared laser - are finely tuned to get the maximum output, which usually happens to be the most stable. Differentiation between long and short wavelengths on the same setting is achieved by observing the attenuation of signal caused by a single sheet of standard graph paper. 57 μm is attenuated by a factor of ten, with longer wavelengths reduced proportionally less. When this measure fails, a Michelson interferometer comes to the rescue. The output of laser is then guided through evacuated brass pipes to the samples and detectors, as the water vapour in the air attenuates infrared strongly.

One problem, however, does persist in the configuration presented in Figure 2-1. Albeit attenuated by the active media in the far-infrared cavity, it is inevitable to have the 10 μm based CO_2 line as part of the output. This residue is usually so powerful that it would gradually melt the plastic windows in its way, which are crucial to keep the vacuum of the light pipes tight. To block this vicious beam, a quartz window is used at the output end of the cavity. Quartz blocks the 10 μm radiation effectively by cutting off any wavelength shorter than 40 μm, which affects some lines close to the threshold as well. To work around the problem, a special apparatus is mounted at the input end of the cavity. The apparatus uses the Brewster angle to eliminate the reflected 10 μm beam, so we can take the far infrared beam from the input end (Infrared comes from both ends of the cavity). The disadvantage of this configuration is it does not work as well with longer wavelengths (>100 μm).

Table 2-1 lists the details of all the laser lines used in this thesis.

Wavelength μm	CO_2 laser grating reading	CO_2 laser pump line	Gas	Cavity Pressure (torr)
405	3996	9R18	FA	0.3
393.63	3996	9R18	FA	0.3
305.73	4026	9R08	DMA	0.06~0.09
294.81	4026	9R08	DMA	0.06~0.09
251.14	4393	10R38	MA	0.08~0.09
250.78	4404	10R34	MA	0.1
215.37	4012	9R14	DMA	0.12
186.04	3996	9R18	MA	0.15
163.03	4393	10R38	MA	0.1
134.0	4084	9P10	DMA	0.07
129.55	4404	10R34	MA	0.1
118.88	4188	9P36	MA	0.15
117.23	4147	9P26	DMA	0.15
103.13	4164	9P30	DMA	0.15
96.52	4018	9R10	MA	0.15+
80.0	4170	9P32	DMA	0.15
70.51	4180	9P34	MA	0.1
61.61	4000	9R18	MA	0.1
57.2	4026	9R08	DMA	0.15
53.91	4399	10R36	MA	0.15
47.7	4026	9R08	DMA	0.15
43.69	4465	10R18	MAD	0.1

Table 2-1 Far-infrared laser lines used for experiments in this thesis. MA: CH_3OH, DMA: CH_3OD, MAD: CD_3OH and FA: Formic acid.

2.3 Superconducting Magnet and ^{3}He System

Some measurements at temperature between 330 mK and 2K have been carried out using an Oxford Instrument ^{3}He System as shown in Figure 2-3 [3,4]. This system fits inside the ^{4}He bath of an old superconducting magnet capable of 14.5 T. The internal components of the system are surrounded by the inner vacuum chamber (IVC), providing thermal isolation from the main bath.

The ^{3}He is condensed in the sample space and then pumped using a sorption pump containing activated charcoal. The pumping power of the sorb depends on its temperature and reaches a maximum when the temperature is below 8 K. When condensing the ^{3}He into the cryostat tail the temperature of the sorb is raised to 45 K using a heater and the majority of the ^{3}He gas leaves the charcoal. The 1 K pot is filled with ^{4}He sucked from the main bath and then pumped by an external vacuum pump which reduces its temperature to 1.2 K. The ^{3}He in thermal contact with the 1 K pot is then liquefied and collected in the tail where the sample is. The sorb is then cooled to 4 K by drawing liquid ^{4}He through the heat exchanger from the main bath using another external vacuum pump. When the temperature of the sorb is below 8 K it should be possible to evacuate the system to 10^{-5} mbar, giving a base temperature of 270 mK. However, the actual temperature achievable is around 300 mK due to the finite heat load both from stainless steel insert and the radiation (infrared and, sometimes, visible light). The sample temperature is measured using calibrated ruthenium oxide resister mounted close to the sample.

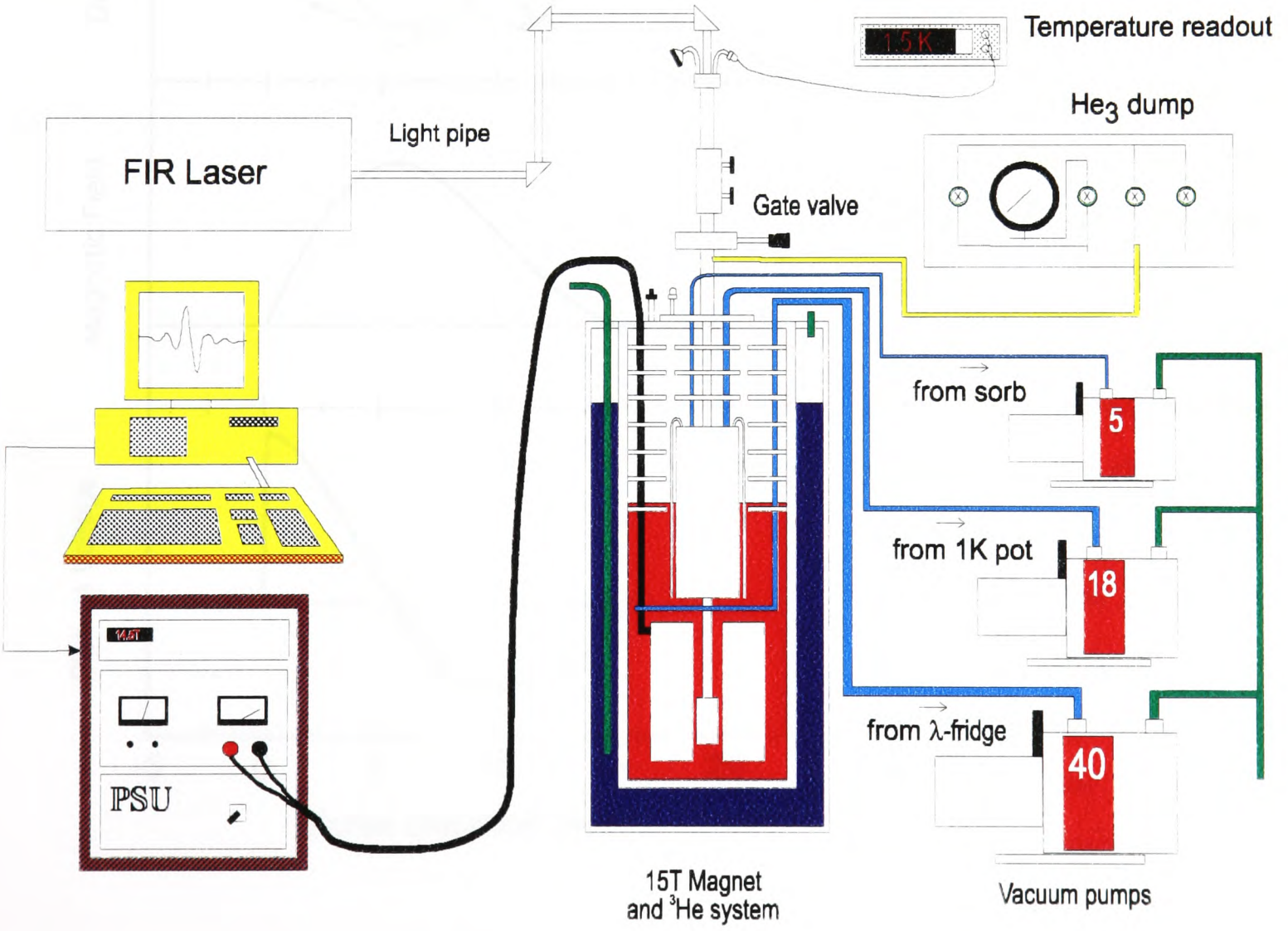

Figure 2-3 Schematic diagram of experimental set-up, including a superconducting magnet, far-infrared laser and the ^{3}He system.

Sample changing is very quick with this system due to its top loading design. The sample probe is fitted with a sliding seal which connects to the main body of the system through a gate valve. When the sample is removed, the sorb is cooled down to 4 K so all the ^{3}He gas is taken by the charcoal to minimise any gas loss. After the sample is changed, the sliding seal is evacuated before the gate valve is opened which prevents air from introducing into the system. When we finish the experiments, the ^{3}He gas is transferred back to the storage vessel using an external sorb which also contains activated charcoal.

2.4 Pulsed Magnetic Field

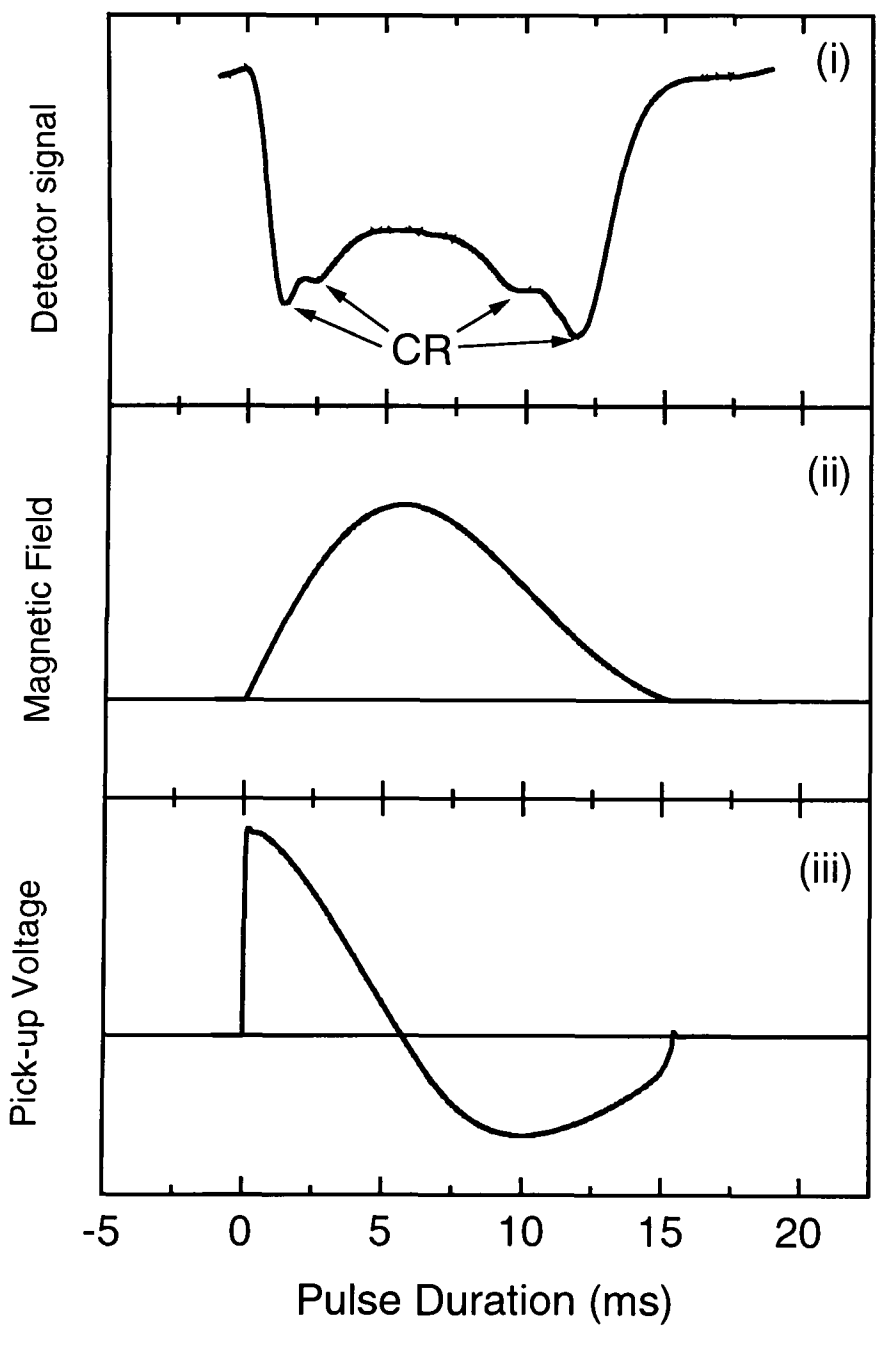

Figure 2-4 Profiles of (i) transmission signal (ii) magnetic field (iii) pick-up voltage as a function of time in a conventional cyclotron resonance set-up using the pulse magnet.

The maximum magnetic field attainable by superconducting magnets is around 18 Tesla. For experiments requiring fields higher than this, a non-explosive pulsed magnet is used. The basic design of the system includes capacitor bank and a solenoid coil [5]. To fire a pulse, the capacitor bank, consisting of four 8mF capacitors, is charged to suitable voltage which depends on the peak field intended. Then the bank discharges all the energy through the coil. To monitor the field change during the shot, the pick-up voltage is collected from a simple coil

wired at the bottom of the insert and then integrated to yield the profile shown in Figure 2-4.

The coils with a typical bore size of 20mm are solenoids wound from 2x3 mm Cu / Stainless steel composite wires [6]. Multiple layers of epoxy resin are used to strengthen the coils due to the high stress applied to them (up to 1.2 GPa during the pulse with a maximum field 0f 50 T). The whole coil is immersed in liquid nitrogen while operating for low impedance. Though "non-explosive" as the name suggested, these coils do have a limited lifetime around 3000 shots. When they explode, a magnificent display of refrigerant spilling should always be expected.

To do the cyclotron resonance experiments in pulsed field (actually all the cyclotron resonance measurements in the thesis have been done exclusively in this way), conventional signal detecting techniques using bolometer are no longer applicable because of the slow response. A time constant shorter than micro-second is necessary to make the sharpest resonance perceptible and this severe condition simply rules out any detector relying on bolometric effect. We therefore turn our eyes to photodetectors. The photodetectors utilized in this study are no more than slightly doped pieces of

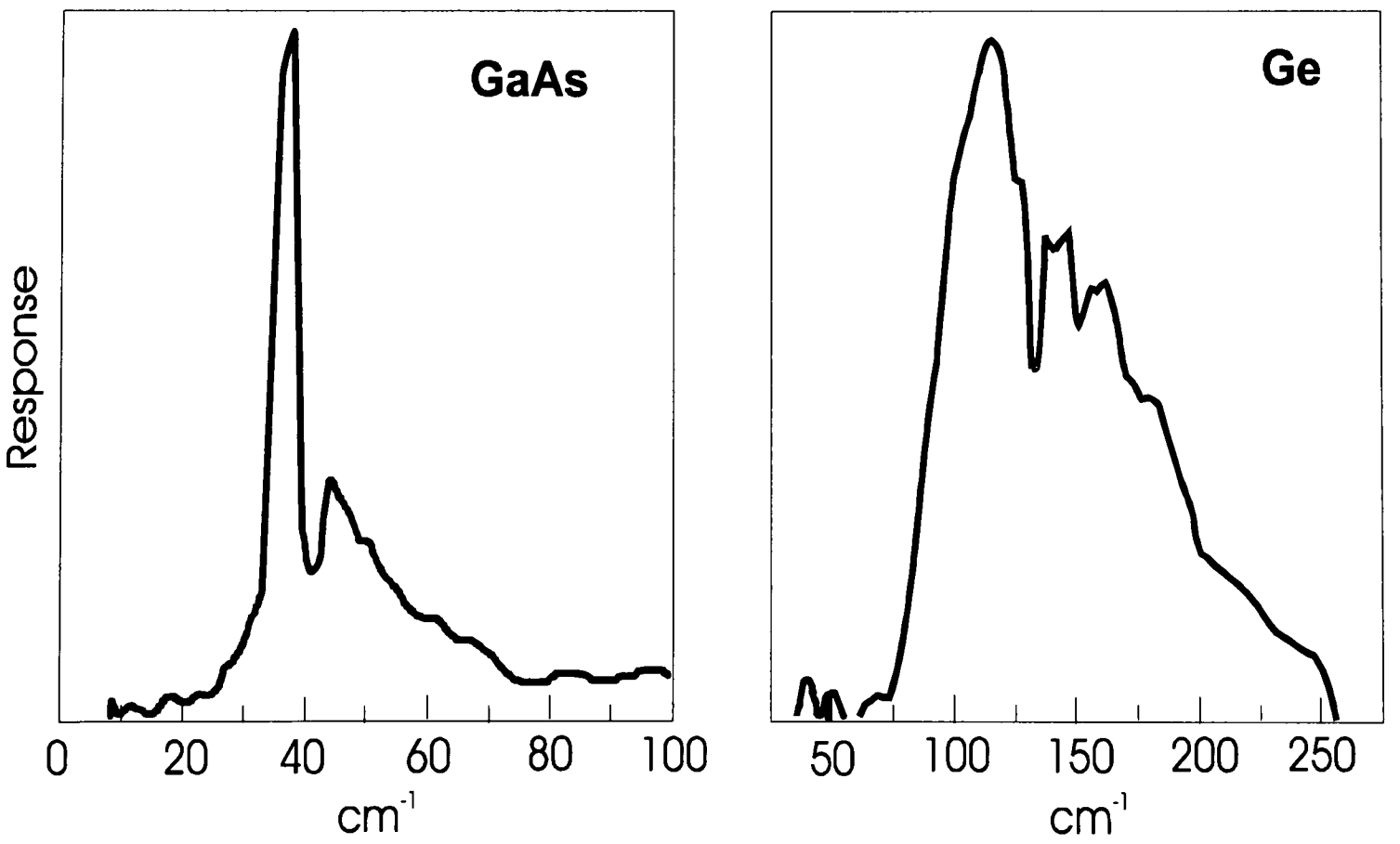

Figure 2-5 The response spectra of (i) GaAs (ii) Ge photodetectors used in the pulsed field cyclotron resonance experiments.

semiconductors. The donor centres offer a hydrogen-like potential for the electrons, and photons can be absorbed through the 1s-2p transition of all the impurity levels [7-10]. The photo-excitation is echoed by a dramatic change in conductivity. Giving a bandwidth of GHz, these photodetectors are ideal for pulsed field measurements.

Considering the fact that impurity transitions are determined by the materials, it is natural to have various detectors covering different wavelengths. In my experiments, Ge is used to work between 40 μm and 130 μm and GaAs up to 400 μm. Their response spectra are shown in Figure 2-5. The only drawback of these detectors is that their properties are highly dependent on magnetic fields [11]. A simple design to mount them close to the samples at the bottom of the insert is not appropriate and the transmitted beam must be guided out of the insert and sent to the detectors far away from the field centre. Since they can only work under low temperature, an extra cryostat is needed besides the one which accommodates samples and the magnet.

References

[1] J. Hecht, *The Laser Guidebook*, McGraw-Hill (1986).

[2] D. J. E. Knight, *National Physical Laboratory Report* **Qu45** (1980).

[3] G. M. Summers, *D.Phil thesis*, Oxford (1993).

[4] D. M. Symons, *D.Phil thesis*, Oxford (1994).

[5] W. J. Siertsema and H. Jones, *IEEE Trans* **30**, 1809 (1994).

[6] M. van Cleemput, H. Jones, M. van der Burgt, J. R. Barrau, J. A. Lee, Y. Eyssa and H. J. Schneider-Muntau, *Physica B* **216**, 226 (1996).

[7] A. von Klarenbosch, T. O. Klassen, W. T. Wenckebach and C. T. Foxon, *J. Appl. Phys.* **67,** 6323 (1990).

[8] H. P. Wagner and W. Prettl, *Solid State Communications* **66**, 367 (1988).

[9] R. T. Grimes, M. B. Stanaway, J. M. Chamberlain, M. Henini and O. H. Hughes, *Semiconductor Science and Technology* **4**, 548 (1989).

[10] J. Simola and J. Virtamo, *J. Phys. B* **11,** 3309 (1978).

[11] J.G. Michels, *D.Phil thesis*, Oxford (1994).

3. Selfconsistent algorithm of *k.p* theory

3.1 Introduction

For a quantitative understanding of the experimental results presented in this thesis, detailed bandstructures including the Landau levels and selection rules are needed. This has been done extensively by ***k.p*** calculations. Due to the fact that the majority of our samples are either doped or semimetallic, the "momentum matrix approach" [1] was used to deal with a non-flat bandedge potential. A selfconsistent algorithm has been developed to cope with the charge transfer of the semimetallic samples investigated.

Developed around 1955 to explain cyclotron resonance in bulk materials [2-4], ***k.p*** theory has become the most powerful tool to model semiconductor band structures. Following the development of the envelope function approximation, several theoretical approaches [5] were proposed to tackle heterostructures. In this chapter, I shall briefly review the framework of the ***k.p*** approximation and quickly move to the selfconsistent momentum matrix approach which constitutes the kernel of the model.

3.2 Bulk Lattices : *k.p* approximation

3.2.1 Framework of the *k.p* Approximation

To describe an electron travelling in a semiconductor crystal, the Schrödinger equation is given as [6]

$$H|\psi\rangle \equiv \left[\frac{\vec{p}^{\,2}}{2m_0} + V(\vec{r}) + \frac{\hbar}{4m_0^2c^2}(\sigma \times \nabla V(\vec{r}))\cdot\vec{p}\right]|\psi\rangle = E|\psi\rangle \qquad (3.1)$$

where $\frac{\hbar}{4m_0^2c^2}(\sigma \times \nabla V(\vec{r}))\cdot\vec{p}$ is the spin-orbit coupling term. The potential $V(\vec{r})$ has the periodicity of crystal lattice, such that,

$$V(\vec{r}) = V(\vec{r} + \sum_i n_i \vec{a}_i) \qquad \vec{a}_i : \text{Crystal basis vector, } n_i : \text{integer}$$

To solve a function of such complexity, one can not expect to tackle it directly through the evaluation of Coulomb potentials. Instead, symmetric and experimental

properties are exploited to extract solutions from Eq. (3.1). In a periodic potential, the Bloch theorem tells us that the wavefunction $|\psi\rangle$ can be rewritten as

$$|\psi\rangle = e^{i\vec{k}\cdot\vec{r}}|Bloch\rangle \tag{3.2}$$

where $\vec{k}$ represents the momentum wave vector and the "Bloch" function [6,7] has the periodicity of the lattice ($|Bloch(\vec{r})\rangle = |Bloch(\vec{r}+\vec{a}_i)\rangle$). By substituting Eq. (3.2) into Eq. (3.1), the Schrödinger equation reads as:

$$\left[\frac{\hbar^2\vec{k}^2}{2m_0}+\frac{\vec{p}^2}{2m_0}+\frac{\hbar}{m_0}\vec{k}\cdot\vec{p}+V(\vec{r})+\frac{\hbar}{4m_0^2c^2}(\sigma\times\nabla V(\vec{r}))\cdot(\hbar\vec{k}+\vec{p})\right]|Bloch\rangle = E|Bloch\rangle \tag{3.3}$$

Since both the Bloch function and the potential have the same periodicity, Eq. (3.3) can be solved numerically once the potential is assumed and $\vec{k}$ is designated [8]. The eigenenergy and eigenstates are therefore functions of the momentum vector $\vec{k}$ as illustrated in Figure 1-3.

Apparently, the pseudo-potential technique is tedious to calculate and it is difficult to find the right potential for calculation. To simplify the formulation, one picks up a limited number of basis states which are independent of $\vec{k}$ and span the Bloch function with them. The Bloch function can thus be represented as

$$|Bloch\rangle = \sum_m f_m(\vec{r})|Basis_m\rangle \tag{3.4}$$

where $f_m(\vec{r})$ is usually referred to as the envelope function.

Two important facts enlighten the path to choosing the right set of basis. First, the outer *s* and *p* orbits of the atoms offer the couplings which give birth to the electronic structures of semiconductors as shown in Chapter 1. Second, the Bloch function must be spanned at the most interesting point in momentum space where the majority of things happen - the band extrema. For direct band-gapped III-V crystals, this directs to the Γ point which is best described by the two conduction states $|s\updownarrow\rangle$ and the six valence states $|x\updownarrow\rangle$, $|y\updownarrow\rangle$ and $|z\updownarrow\rangle$ [9], where $\updownarrow$ represents the spin state.

3.2.2 Construct a Bulk Hamiltonian

Following Kane, Table 3-1 lists the eight basis states used in the [001] direction, which are linear superpositions of the atomic states [9,10].

Band	$\left\|J,m_J\right\rangle$	$\left\|Basis_m\right\rangle$	E_Γ
Conduction	$\left\|\frac{1}{2},+\frac{1}{2}\right\rangle$	$\left\|S\uparrow\right\rangle$	E_g
Heavy Hole	$\left\|\frac{3}{2},+\frac{3}{2}\right\rangle$	$\frac{-i}{\sqrt{2}}(\left\|X\uparrow\right\rangle + i\left\|Y\uparrow\right\rangle)$	0
Light Hole	$\left\|\frac{3}{2},-\frac{1}{2}\right\rangle$	$\frac{i}{\sqrt{6}}(\left\|X\uparrow\right\rangle - i\left\|Y\uparrow\right\rangle + 2\left\|Z\downarrow\right\rangle)$	0
Spin-Orbit	$\left\|\frac{1}{2},-\frac{1}{2}\right\rangle$	$-\frac{i}{\sqrt{3}}(\left\|X\uparrow\right\rangle - i\left\|Y\uparrow\right\rangle - \left\|Z\downarrow\right\rangle)$	-Δ
Conduction	$\left\|\frac{1}{2},-\frac{1}{2}\right\rangle$	$\left\|S\downarrow\right\rangle$	E_g
Light Hole	$\left\|\frac{3}{2},+\frac{1}{2}\right\rangle$	$-\frac{i}{\sqrt{6}}(\left\|X\downarrow\right\rangle + i\left\|Y\downarrow\right\rangle - 2\left\|Z\uparrow\right\rangle)$	0
Heavy Hole	$\left\|\frac{3}{2},-\frac{3}{2}\right\rangle$	$\frac{i}{\sqrt{2}}(\left\|X\downarrow\right\rangle - i\left\|Y\downarrow\right\rangle)$	0
Spin-Orbit	$\left\|\frac{1}{2},+\frac{1}{2}\right\rangle$	$\frac{-i}{\sqrt{3}}(\left\|X\downarrow\right\rangle + i\left\|Y\downarrow\right\rangle + \left\|Z\uparrow\right\rangle)$	-Δ

Table 3-1: Basis wavefunctions $\left|Basis_m\right\rangle$ and energies E_Γ. The zero of energy is defined as the top of the valence band.

With the Kane basis in hand, it seems reasonable to establish a Hamiltonian matrix which "absorbs" the expectation value of the basis states to simplify further theoretical treatment. The matrix is hence defined as

$$H_{ij} = \left\langle \Gamma_i \middle| H \middle| \Gamma_j \right\rangle \tag{3.5}$$

$\left|\Gamma_i\right\rangle$ stands for the i^{th} state of the Kane basis spanned at Γ point. A detailed treatment can be found in Luttinger [3]. Appendix I gives the bulk 8x8 ***k.p*** Hamiltonian for the [001] orientation following the notation by Weiler [11]. It must be mentioned that the ***k.p*** Hamiltonians presented in the Appendices are much more complicated than the one in Kane's original paper [12] which considers only interactions between the electronic bands of immediate interest. The extra parameters - modified Luttinger parameters F, γ_1, γ_2 and γ_3 - represent interactions with far bands that endow the valence band with non-parabolicity.

3.2.3 Parameters in the Hamiltonian

The ***k.p*** approximation is derived directly from the Schrödinger equation itself. It is natural that people would think that the parameters in the Hamiltonian can be theoretically obtained with only the atomic numbers and, perhaps, the lattice constants. This was done through pseudopotential approximation [6] in the past. However, this approach has been proved to be tedious and inaccurate due to the non-analytical nature of the problem. A more common method is to fit the experimental data with the ***k.p*** formulation over a small range to get the parameters and use them over a wider range. This by no means undermines the power of the ***k.p*** approximation. Various experimental results have been "predicted" by this formulation with parameters obtained from a handful of basic measurements. It certainly justifies the approach.

Of all the parameters, E_g and Δ (energy gap and spin-orbit splitting) can be measured optically. The rest of them are found though the effective mass approximation. Taking the bulk Hamiltonian in Appendix I for example, we can get the following relations by diagonalizing the Hamiltonian at small $\boldsymbol{k}$

$$\frac{1}{m_{hh}^{001}} = \gamma_1 - 2\gamma_2$$

$$\frac{1}{m_{lh}^{001}} = \gamma_1 + 2\gamma_2 + \frac{4P^2}{3E_g}$$

$$\frac{1}{m_{so}^{001}} = \gamma_1 + \frac{1}{2}\left(\frac{4P^2}{3E_g}\right)\frac{E_g}{E_g + \Delta}$$

$$\frac{1}{m_c^{001}} = 2\left(F + \frac{1}{2}\right) + \frac{4P^2}{3E_g}\left(1 + \frac{1}{2}\frac{E_g}{E_g + \Delta}\right)$$

$$\frac{1}{m_{hh}^{111}} = \gamma_1 - 2\gamma_3 \tag{3.6}$$

The $m_\Gamma^{Direction}$ corresponds to the effective mass of the Γ band along a certain direction, which can be measured in cyclotron resonance experiments. The other two parameters $\bar{\gamma}$ and μ are given by:

$$\mu = \frac{1}{2}(\gamma_2 - \gamma_3)$$

$$\bar{\gamma} = \frac{1}{2}(\gamma_2 + \gamma_3) \text{ [001] or } \bar{\gamma} = \frac{1}{2}(\gamma_2 + 2\gamma_3) \text{ [111]} \tag{3.7}$$

Finally, the spin-splitting parameter κ of the hole band can be determined by the magneto-optical measurements.

3.3 Envelope Function Approximation

The envelope function approximation [13] is the most common method used to calculate electronic states in a heterostructure using the bulk Hamiltonian formulation. The approximation is based on three assumptions.

1) It is assumed that the ***k.p*** formulation applies for the materials used in the heterostructures. In other words, the total wavefunctions can be represented as the basis functions multiplied by envelope functions.

$$|\psi\rangle = \sum_{m}^{Basis} Envelope(x, y, z)|Basis_m\rangle$$

2) The different materials used in the heterostructures share the same set of basis states. This is a good approximation for certain compounds such as InAs/GaSb, where both the band extrema are at the Γ-point. For materials such as Si/Ge, however, a complete description within the Brillouin zone is needed [14].

3) The periodicity of the envelope function is significantly larger than that of the Bloch functions. In other words, the "superlattice" period is longer than the crystal periods. This is the key to making the envelope function and Bloch function "separable". In this picture, a quasi-particle is described by the envelope function alone. All the operators in the ***k.p*** Hamiltonian will only apply to the envelope function but not to the Bloch functions. The total wavefunction $|\psi\rangle$ is no longer in real space with 3 axes but in a hyper space with many more dimensions.

Take a two material superlattice spanning at the Γ-point and growing along the z-axis for example. The wavefunction is

$$|\psi\rangle = e^{iqz} \sum_{m}^{\Gamma} \phi_m(z)\chi_m(x, y)|\Gamma\rangle \tag{3.8}$$

where ϕ_m and χ_m represent the z-direction and in-plane (x-y) envelope functions which are assume to be separable, and $|\Gamma\rangle$ stands for the set of basis functions spanned at Γ-point. The Schrödinger equation in material A or B can be written as

$$\left(H^{A,B}+V^{A,B}\right)\left|\psi^{A,B}\right\rangle=\varepsilon\left|\psi^{A,B}\right\rangle \qquad \text{where}\left|\psi^{A,B}\right\rangle=\left|\psi(z\in AorB)\right\rangle$$

The Bloch theorem comes into the envelope function again in the form of e^{iqz} as a result of the superlattice periodic potential [13] and $V^{A,B}$ describes the band offsets between the materials. The Hamiltonian only acts on the envelope function as mentioned previously. Therefore, the equation can be written as:

$$\left(H^{A,B}+V^{A,B}\right)e^{iqz}\phi_m^{A,B}(z)\chi_m^{A,B}(x,y)=Ee^{iqz}\phi_m^{A,B}(z)\chi_m^{A,B}(x,y) \qquad (3.9)$$

As in all quantum systems, two boundary conditions must be met for the envelope function. Assuming the discontinuities of the potential functions are finite, we have

$$\phi_m(z) \quad , \left(H_2k_z+\tfrac{i}{2}H_1\right)\phi_m(z) \quad \text{continuous.}$$

H_1 and H_2 are the k_z and k_z^2 dependent terms, respectively. $(H(k_z)=H_0+\tfrac{1}{2}(H_1k_z+k_zH_1)+k_zH_2k_z)$

3.3.1 Transfer Matrix Approach

The transfer matrix approach [15-19] is the most popular treatment developed under the framework of the envelope function approximation. Different formulations have been developed to match the boundary conditions and I am going to illustrate briefly one formulation by Ram-Mohan [20] to show how this approach works.

A vector of twice the dimension of the Hamiltonian is defined by

$$\Phi=\begin{pmatrix}\phi(z)\\ \left(H_2k_z+\tfrac{i}{2}H_1\right)\phi(z)\end{pmatrix} \qquad (3.10)$$

With the definition, the two boundary conditions reduce to Φ being continuous everywhere. The Schrödinger equation can thus be written as

$$\frac{d}{dz}\Phi(z)=\begin{pmatrix}-\tfrac{i}{2}H_1H_2^{-1} & H_2^{-1}\\ (H_0+V-E)-\tfrac{1}{4}H_1H_2^{-1}H_1 & -\tfrac{i}{2}H_2^{-1}H_1\end{pmatrix}\Phi(z)\equiv\Lambda\Phi(z) \qquad (3.11)$$

The solution at z is hence given by

$$\Phi(z) = e^{\Lambda z}\Phi(0) \tag{3.12}$$

which is valid only when Λ is not a function of z. In other words, the potential must be constant within a layer.

The Bloch periodicity of the envelope functions over the period that requires the function Φ satisfy the condition

$$\Phi(d_A + d_B) = e^{iq(d_A+d_B)}\Phi(0) \tag{3.13}$$

d_A and d_B stand for the thicknesses of layers A and B, respectively. At the same time, we can get an eigenvalue equation using the relation obtained above

$$e^{(\Lambda_A d_A + \Lambda_B d_B)}\Phi(0) = e^{iq(d_A+d_B)}\Phi(0) \tag{3.14}$$

The allowed values of eigenenergy are obtained by scanning in energy and performing a diagonalization of the transfer matrix to see if any eigenvalue is equal to $e^{iq(d_A+d_B)}$. For each eigenenergy, a corresponding $\Phi(0)$ can be solved. The envelope function $\phi(z)$ is then calculated using Eq. (3.12).

The major disadvantage of the approach is its incapability of handling the non-flat bandedge potential - confining the formulation to intrinsic systems. It has been proposed to evade this problem by breaking the layers into small sections. Practically, the mesh technique works poorly due to the spurious solutions which occur in wide layer structures [15,16].

3.3.2 Applied Magnetic Field and the Hamiltonian

As stated previously, the operators in a ***k.p*** Hamiltonian only apply to the envelope function which describes a particle (electron or hole) moving through the lattices. With no applied field, the in-plane functions are the plane waves $e^{ik_{//}\cdot\bar{r}}$, so that the in-plane momentum operators (k_x and k_y) convert themselves to parameters while the Hamiltonian applies to the envelope functions.

For a magnetic field being applied along the z-axis, a parabolic potential is introduced in the plane of layers. This can be treated as the well-known simple harmonic oscillator [7]. The raising and lowering operators are obtained accordingly

$$a_- = \sqrt{\frac{\hbar}{2eB}}\left[k_x - ik_y\right]$$

$$a_+ = \sqrt{\frac{\hbar}{2eB}}\left[k_x + ik_y\right] \tag{3.15}$$

with the property

$$a_-\left|\chi_n(x,y)\right\rangle = \sqrt{n}\left|\chi_{n-1}(x,y)\right\rangle$$

$$a_+\left|\chi_n(x,y)\right\rangle = \sqrt{n+1}\left|\chi_{n+1}(x,y)\right\rangle \tag{3.16}$$

The $\left|\chi_n(x,y)\right\rangle$ take the form of Hermite polynomials [21]. The in-plane momentum operators $k_\pm$ in the bulk Hamiltonian hence turn out to be the raising and lowering operators!

Bearing the idea of simplifying the non-magnetic Hamiltonian in mind, the raising and lowering operators $k_\pm$ quantize the in-plane motion and transform themselves to functions of B (magnetic field) and n (Landau level index). Taking the non-diagonal term between $\left|c\uparrow\right\rangle$ and $\left|hh\uparrow\right\rangle$ from Appendix I; the matrix reads like

$$\begin{pmatrix} (F + \tfrac{1}{2})k^2 + E_G & \cdots\cdots \\ \sqrt{\tfrac{1}{2}}Pk_- & \cdots\cdots \end{pmatrix}\begin{pmatrix} \chi_n \\ \chi_m \end{pmatrix}$$

hence $\sqrt{\tfrac{1}{2}}Pk_-\chi_n = C\chi_m$, where C stands for a certain coefficient. Also $\sqrt{\tfrac{1}{2}}Pk_-\chi_n = P\sqrt{nB}\chi_{n-1}$ (here we assume Planck's constant to be unity). Combining these

two equations, it is evident that $m = n - 1$. This is comprehensible because $|c\uparrow\rangle$ carries less spin angular momentum than $|hh\uparrow\rangle$. To keep the total angular momentum identical, the in-plane envelope function must carry more momentum. The in-plane angular momentum index of individual bands can be found in Appendix II. At the same time, we can express $k_x^2 + k_y^2$ as $\frac{1}{2}(k_+k_- + k_-k_+)$. The magnetic Hamiltonian therefore is written as

$$\begin{pmatrix} (F+\frac{1}{2})k_z^2 + E_G + \frac{1}{2}B & \\ +2(F+\frac{1}{2})(n+\frac{1}{2})B & ..... \\ & \\ P\sqrt{nB} & ..... \end{pmatrix}$$

Following this routine, we can generate the magnetic Hamiltonian from the non-magnetic one [4]. The [001] magnetic Hamiltonian in the form $H(k_z) = H_0 + H_1 k_z + H_2 k_z^2$ is given in Appendix II. Table 3-2 summarises different roles the operators played in different cases.

	Magnetic Field		Non-magnetic Field	
	Bulk	Hetero-structure	Bulk	Hetero-structure
Parameters	k_z, B, n	B, n	k_x, k_y, k_z	k_x, k_y
Operators		k_z		k_z

Table 3-2 A summary of parameters and operators in both magnetic and non-magnetic Hamiltonians.

Various papers have been constantly referring to the ***g***-factors (gyro-magnetic) of the materials to find out the spin splitting of a particular band. These numbers are quite different from the free electron ***g***-factor derived from quantum electrodynamics (~2). The reason is that the total angular momentum in the ***k.p*** approximation is broken down into three parts – the electron spin, the atomic orbital (Kane basis) and the envelope function. The superposition of the first two gives the "spin" used in semiconductor physics. As a matter of fact, the ***g***-factor of holes in GaAs even changes sign with increasing magnetic field.

3.3.3 Strain Effects

While growing a layer of semiconductor on top of another material, mismatch between the lattice constants is always expected. The electronic band structure change due to crystal structure deformation is the so-called strain effect. Since the energy shift due to the presence of strain (usually <100meV) is small compared to the energy gap of most semiconductors, it is sensible to treat the strain as a perturbation [22].

For a semiconductor layer of lattice constant a, grown on a substrate with lattice constant a_0, the in-plane strain $\varepsilon_{//}$ is defined as

$$\varepsilon_{//} = \frac{a_0}{a} - 1$$

The out-of-plane stain $\varepsilon_{\perp}$, which is orientation dependent, can be defined as

$$\varepsilon_{\perp}[001] = -2\frac{C_{12}}{C_{11}}\varepsilon_{//}$$

where the C_{ij} terms are the elastic constants for the semiconductor. The volume of the lattice unit cell change due to the strain is therefore

$$\frac{\Delta\Omega}{\Omega} = 2\varepsilon_{//} + \varepsilon_{\perp}$$

The strain enters the Hamiltonian as hydrostatic terms, which are responsible for the above change in the volume of the unit cells, and a uniaxial term, which mixes the light and heavy hole states [23]. The leads to the following contribution to the spin degenerate 4x4 Hamiltonian

$$H_{strain}[001] = \begin{matrix} c \\ hh \\ lh \\ so \end{matrix}\begin{bmatrix} C & 0 & 0 & 0 \\ 0 & K_1 + K_2 & 0 & 0 \\ 0 & 0 & K_1 - K_2 & \sqrt{2}K_2 \\ 0 & 0 & \sqrt{2}K_2 & K_1 \end{bmatrix}$$

$$C = a_c\frac{\Delta\Omega}{\Omega},\ K_1 = a_v\frac{\Delta\Omega}{\Omega},\ K_2 = 2b(\varepsilon_{//} - \varepsilon_{\perp})$$

where a_c and a_v are the conduction and valence band hydrostatic deformation potentials and b the tetragonal deformation potential. The strain component shifts the energies of the conduction and valence bands at zone centre and splits the light and heavy hole bands as well. This leads to a strongly anisotropic valence band structure as shown in Figure 3-1.

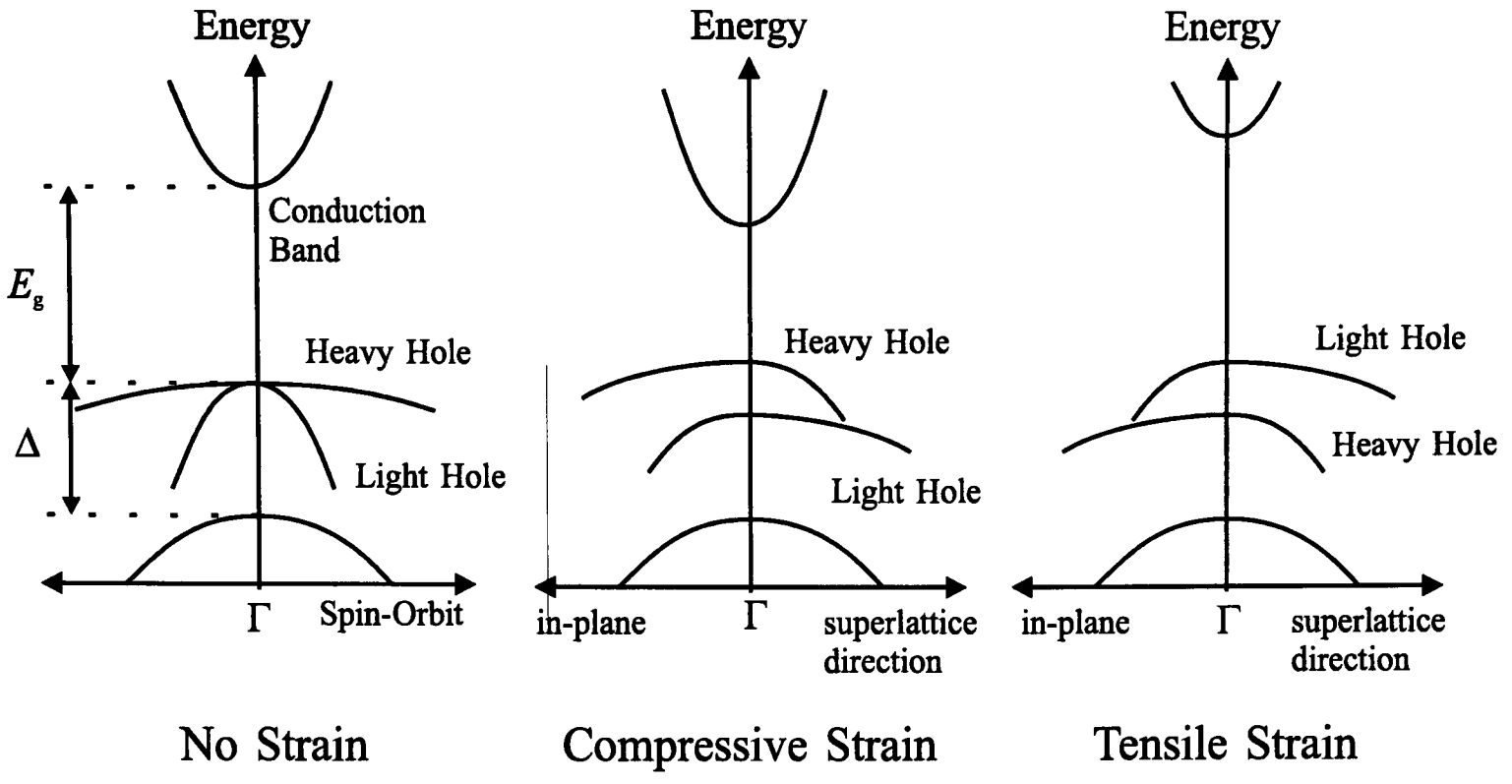

Figure 3-1 The effect of strain on band-edge energy. Note the degeneracy between heavy and light holes has been lifted.

3.4 Momentum Matrix Approach

The momentum matrix approach [1,24], as the name suggests, solves the z-direction envelope function in $\vec{k}$ space. Combining the benefits of arbitrary potentials with a spurious solution free treatment, the momentum matrix approach offers advantages which few other models can match.

Assuming that all the layers in the superlattice have the same band extrema point, we can span the electron wavefunctions with the same set of basis states. The Hamiltonian, potential and envelope function can then be written as functions of the Fourier components of $e^{i(2\pi n/d)}$:

$$H(z) = H_0(z) + \tfrac{1}{2}(H_1(z)k_z + k_z H_1(z)) + k_z H_2(z) k_z \qquad H_j = \sum_{n=0}^{FF} H_j^n e^{i(2\pi n/d)z}$$

$$\text{and} \qquad k_z = -i\frac{\partial}{\partial z}$$

$$V(z) = \sum_{n=0}^{FF} V^n e^{i(2\pi n/d)z}$$

$$\phi(z) = e^{iqz} \sum_{n=0}^{FF} \phi^n e^{i(2\pi n/d)z} \tag{3.17}$$

FF is the number of Fourier term used and d is the superlattice period. Assigning every term according to its Fourier components, the Schrödinger equation reads

$$\sum_m \left((q+2\pi n/d)(q+2\pi m/d)H_2^{n-m}+(q+\pi(n+m)/d)H_1^{n-m}+H_0^{n-m}+V^{n-m}\right)\phi^m = E\phi^n$$

Formulate the function in the matrix form at q=0, and it would look like:

$$\begin{bmatrix} H_0^0+V^0 & 0 & 0 \\ (\frac{\pi}{d})H_1^1+H_0^1+V^1 & (\frac{2\pi}{d})^2 H_2^0+(\frac{2\pi}{d})H_1^0+H_0^0+V^0 & 0 \\ \cdots\cdots & \cdots\cdots & \cdots\cdots \end{bmatrix}\begin{bmatrix}\phi^0\\ \phi^1\\ \phi^2\end{bmatrix} = E\begin{bmatrix}\phi^0\\ \phi^1\\ \phi^2\end{bmatrix}$$

The next step is to diagonalize the matrix to retrieve the eigenenergy and corresponding eigenstates. Note that ϕ^n is a vector with the same dimension as the Hamiltonian itself. The total electron wavefunction can then be written

$$|\psi\rangle = e^{iqz}\sum_n^{\Gamma}\sum_{m=0}^{FF}\phi_n^m e^{i(2\pi m/d)z}\chi^n(x,y)|\Gamma_n\rangle \tag{3.18}$$

where ϕ_n^m stands for the m^{th} Fourier term of the n^{th} Kane state.

To solve a structure in zero magnetic field, the z-propagation wavevector q is selected first. Then a series of $k_{//}$ are fed into the Hamiltonian which is diagonalized to give the eigenenergy and eigenstates. Since different $k_{//}$ would result in different coupling strength, the corresponding z envelope function would be different, albeit the actual variance might be small near the band edge. Therefore, talking about "the envelope function of subband E_0" is theoretically inaccurate but numerically acceptable. It is also apparent from the above formulation that the idea of a "subband" is not an accurate quantum number as in the Kronig-Penney model [25] but merely a collection of states (both $k_{//}$ and q dependant) sharing similar wavefunctions.

To solve the structure in magnetic fields, one diagonalizes the Hamiltonian with magnetic field B and Landau level index n as input parameters. Since index n is actually the superposition of the spin and the in-plane angular momentum, not all the basis states necessarily contribute to the eigenstates due to the different spin the basis carries. To get the possible combination, the corresponding in-plane angular momentum index of each basis states in Appendix II offers the clue. For each basis state, the corresponding in-plane angular momentum must not be negative. Following this rule, the $|hh\downarrow\rangle$ starts from n=-2 and up, $|c\downarrow\rangle$, $|lh\uparrow\rangle$ and $|so\uparrow\rangle$ start from n=-1 ...etc. Therefore, the dimension of the Hamiltonian is exactly the number of basis states allowed at particular n. Take n=-1 for example, a 4x4 matrix is used instead of the full 8x8.

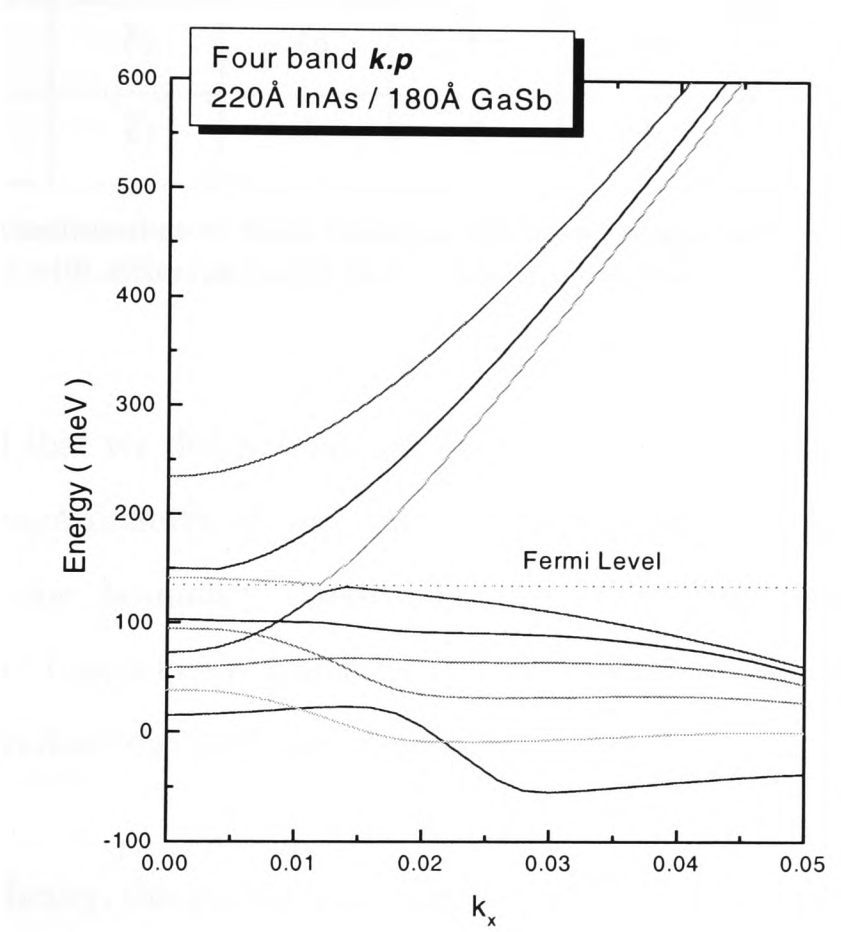

Figure 3-2 k-dispersion relation calculated using the momentum matrix approach.

Table 3-3 illustrates the possible combination of Kane states with Landau level indices from -2 to 1. In a symmetric structure, the z-direction envelope wavefunctions must be either even or odd, and the operator k_z in the Hamiltonian changes the parity. We can therefore separate the eight Kane states to two categories. The states hold the

same parity within their own category but different parity relative to the other. For the ground state in conduction band, this can be represented as $f_c\chi_0\left|c\downarrow\right\rangle + f_{hh}\chi_1\left|hh\downarrow\right\rangle + g_{lh}\chi_0\left|lh\uparrow\right\rangle + g_{so}\chi_0\left|so\uparrow\right\rangle$ where f_c, f_{hh} are even and g_{lh}, g_{so} are odd. Table 3-3 is particularly important to evaluate the transition probability as I shall indicate later.

	Category A				Category B			
	$\left\|c\downarrow\right\rangle$	$\left\|hh\downarrow\right\rangle$	$\left\|lh\uparrow\right\rangle$	$\left\|so\uparrow\right\rangle$	$\left\|c\uparrow\right\rangle$	$\left\|hh\uparrow\right\rangle$	$\left\|lh\downarrow\right\rangle$	$\left\|so\downarrow\right\rangle$
n = -2		χ_0						
n = -1	χ_0	χ_1					χ_0	χ_0
n = 0	χ_1	χ_2	χ_0	χ_0	χ_0		χ_1	χ_1
n = 1	χ_2	χ_3	χ_1	χ_1	χ_1	χ_0	χ_2	χ_2

Table 3-3 Possible combination of Kane states at different Landau level index. Category A and B have *z* envelope functions with different parity in a symmetric structure.

It is apparent that we did not say anything about the boundary conditions that affect the formulation significantly in the transfer matrix approach as previously illustrated. This is because the boundary conditions have been automatically met within this formulation. Any function spanned by limited numbers of Fourier terms must be continuous, and so does the corresponding quantum flux.

Just like any theory, the momentum matrix approach is not fault-free. One weak point is the need to diagonalize a big matrix. As stated above, the size of the matrix is proportional to the number of Fourier terms used, which is as large as 640x640. While dealing with an intrinsic Type-I structure, it may significantly lag behind a calculation based on the transfer matrix approach without any benefit at all. Despite the need for longer computer time, the momentum matrix approach offers undeniable advantages over other algorithms.

1) An automatic satisfaction of the boundary conditions, which not only clarifies the theoretical formulation but also embeds the cross coupling between layers more naturally than the transfer matrix approach.

2) Automatically cutting off the spurious solutions which haunt any other formulation. This is done because the Fourier terms are truncated well before the Brillouin zone [1].
3) Most importantly, the momentum matrix approach can deal with any potential. Nearly all the studies done in this thesis have been on either doped or semimetallic samples. The ability to incorporate literally any kind of potential is the key to obtaining a convincing comparison between experiments and theoretical predictions.

Figure 3-3 illustrates a calculation based on a barrier-doped superlattice to simulate the remote doping techniques employed extensively to enhance the sample mobility. This particular calculation took a well-equipped PC only 10 minutes to do, and would be unimaginable using conventional transfer matrix techniques.

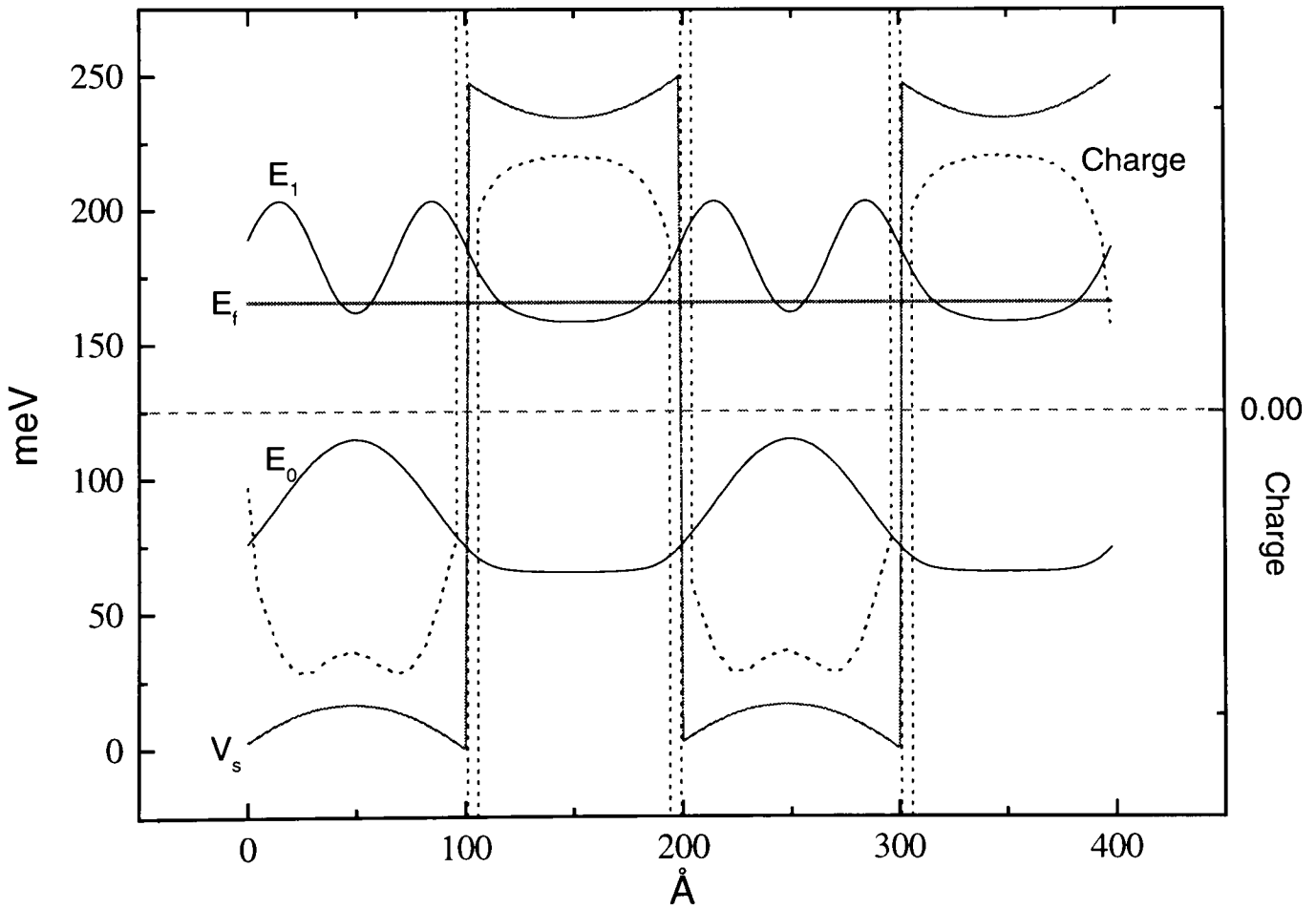

Figure 3-3 The conduction band profile of a GaAs/AlGaAs (100Å/100Å) superlattice with n-type donors in the barriers. The charge distribution, denoted by dash lines, is actually derived by double differentiating the potential. The postive charge in the barriers is due to the ionized donors. Notice the negative charge ditribution in the wells corroborates well with a superposition of the populated E_0 and the half-populated E_1.

3.5 Selfconsistent Algorithm

We have developed a procedure to acquire the band profiles of superlattices. All the coefficients needed in the calculations have been given except one – the bandedge potential.

In previous treatments, the band offset was fetched from measurements and the potentials are presumed to be flat within each layer. This is simply untrue. Take an n-type sample for example, electrons would escape from the donors which left the sites with positive charges, and the escaping electrons then filled the empty states. The induced electrostatic force must therefore be counted accordingly to give a full picture [26].

Figure 3-4 illustrates the flow chart of the selfconsistent algorithm. To start with, a flat band potential is used accounting for nothing but the band offsets between layers. The eigenfunctions are then calculated using the ***k.p*** Hamiltonian.

The second step is to find out the Fermi energy. Different approaches have been taken to evaluate the Fermi levels in zero and non-zero magnetic fields. In the zero field case, a special routine which simulates the effective mass approximation (hence a parabolic dispersion along

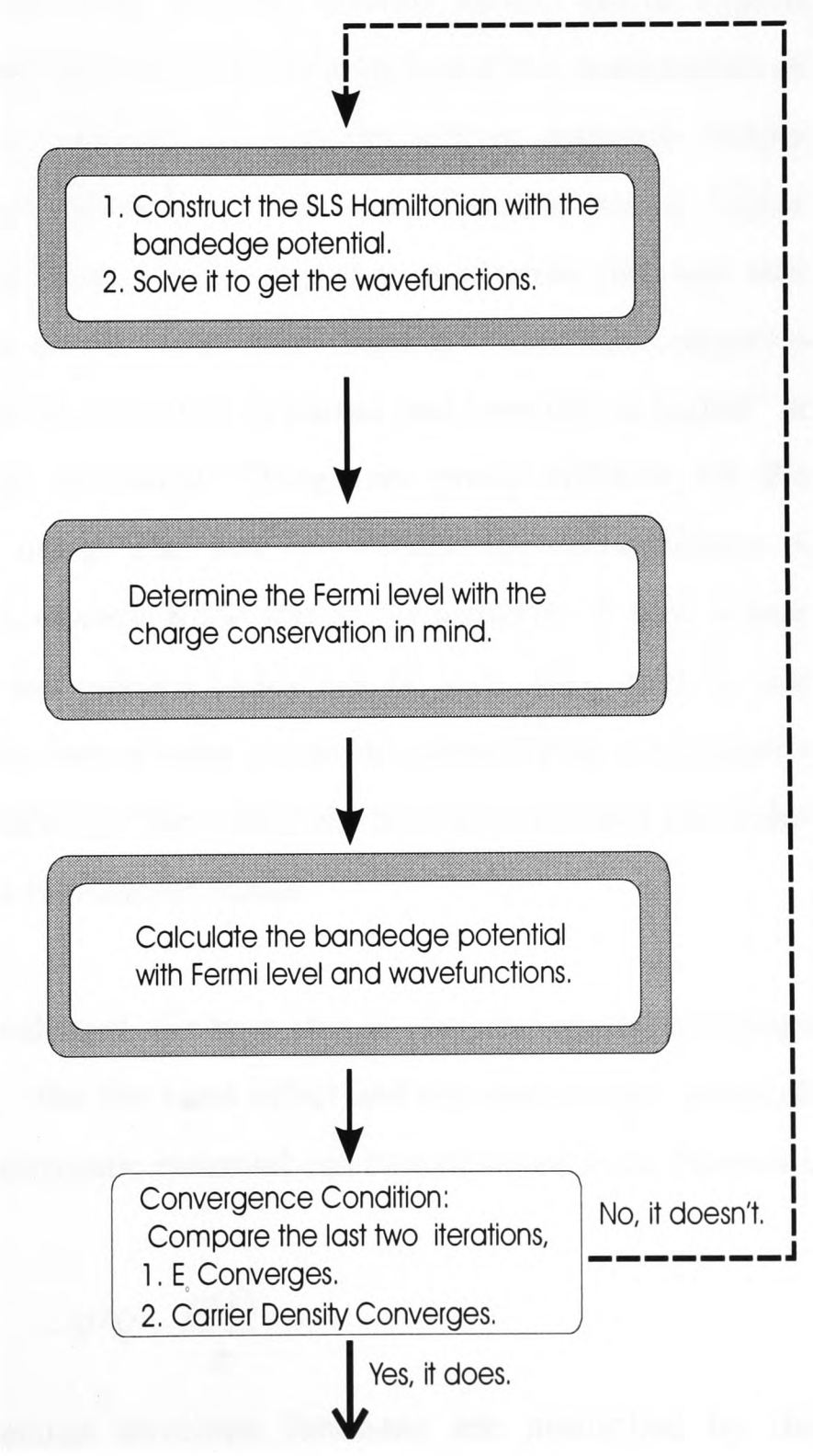

Figure 3-4 Block diagram for a selfconsistent algorithm.

$k_{//}$) has been employed to acquire the $k_{//}$ dispersion for each band. A Fermi level is assumed and the two dimensional density of states can be easily calculated giving the total number of populated states which is exactly the area of populated states in $k_{//}$ space divided by $(2\pi)^2$. The same procedure is repeated until charge conservation is achieved.

Magnetic fields quantize the in-plane motion and give a degenerate density of states $\frac{eB}{h}$ per Landau level. For every single Landau level, a judgement must be made to determine the electron or hole occupancy of this particular level. For Type-I wide gap materials, this is straightforward due to the weak coupling between conduction and valence bands. However, it is not trivial if the structure is either narrow gap or Type-II crossed gap. The strong coupling between bands makes the eigenstates a combination of all Kane basis states. To tackle this problem, the transfer matrix approach simply evaluates the z-propagation envelope function. If the wavefunction has a higher proportion in the wells, this particular state will be regarded as electron-like and vice versa. It is rather convenient because all the states have been put into four categories "electron-like in well, hole-like in well, electron-like in barrier and hole-like in barrier" at the stage when the states have been calculated. Things are pretty different for the momentum matrix approach we are using. The way to evaluate the characteristics is through counting the contributions from each Kane states. As a matter of fact, a near 50:50 contribution from conduction and valence bands can be seen quite often in our GaSb/InAs semimetallic structures. For such a state, it will be counted both as electron's and hole's to avoid the numerical instability. The ambiguity between electrons and holes gently reminds us of the poverty of the two-carrier model.

After the Fermi level has been evaluated, the next step is constructing the bandedge potential, which comprises two parts - the flat band offset and the electrostatic potential contributed from the charges. The electrostatic potential can be calculated from Poisson's equation [27]

$$-\nabla^2 V = \frac{\rho(z)}{\varepsilon}$$

For zero magnetic field, the z-direction envelope functions are multiplied by the corresponding density of states at each $k_{//}$ value. The sum from $k_{//} = 0$ (zone centre) to

Fermi surface is then used to represent the whole populated states and hence the charge distribution. For finite magnetic field, the envelope functions of each Landau levels are employed instead.

The complete band profiles are calculated thus far. The next thing is to determine the convergence which can easily be done by comparing the eigenenergy change in the last two iterations with the tolerance we designate. Table 3-4 lists the calculation results of one particular sample using both non-selfconsistent and selfconsistent algorithms. The bandgap (C_0- V_0) is significant smaller with selfconsistency, because the transferred charges pull the bandedges close to each other. At the time when the selfconsistent calculation was not available, people simply played with the band offset between layers to match the carrier density and eigenenergies [28]. This is, of course, hard to justify and ignorant of the possible charge density variation that results in the effective mass oscillations observed in numerous two carrier systems [29,30].

	Non-selfconsistent	Selfconsistent
C_2	119.044 meV	152.751 meV
C_1	94.625 meV	106.148 meV
C_0	20.273 meV	63.475 meV
V_0	159.926 meV	149.09 meV
V_1	132.198 meV	124.645 meV
V_2	86.05 meV	78.818 meV

Table 3-4 Calculated conduction and valence bands of Sls GaSb/InAs (110/330 Å)

3.6 Selection Rules

In the previous sections, a step-by-step procedure has been established to find the eigenstates and energies of semiconductor superlattices. However, since the scope of this thesis focuses on the optical detectable phenomena such as cyclotron resonance, a detailed optical selection rule is needed to understand the spectra taken. Practically, there are quit a few factors which can affect the selection rules. I am going to present these

rules based on the configuration most experiments were done. This involves a steady zero or non-zero magnetic field along the z-axis (the growth direction) and a normal incidence of light.

Fermi's Golden Rule tells us how to calculate the transition probability of an electron from the initial state $|i\rangle$ to the final state $|f\rangle$, under the interaction Hamiltonian H_I [7]. For incident radiation with energy $\hbar\omega$ and wavevector $\vec{q}$, the transition probability is:

$$P_{if} = \frac{2\pi}{\hbar}\left|\langle f|H_I|i\rangle\right|^2 \delta\left[E_f - E_i - \hbar\omega\right] \tag{3.19}$$

where $$H_I = \frac{ieA}{4m_0\omega}\left[\vec{\varepsilon}\cdot\vec{p}e^{-i\vec{q}\cdot\vec{r}} + e^{-i\vec{q}\cdot\vec{r}}\vec{\varepsilon}\cdot\vec{p}\right]$$

Under the electric dipole approximation, we can reduce it to

$$H_I = \frac{ieA}{2m_0\omega}\vec{\varepsilon}\cdot\vec{p} \tag{3.20}$$

where A, $\vec{\varepsilon}$ and $\vec{p}$ correspond to the intensity of the beam, polarisation and the momentum, respectively. With the help of the transition probability, one can put down the absorption coefficient as

$$\alpha(\omega) = \frac{\pi e^2 A^2}{2m_0{}^2\omega}\left|\langle f|\vec{\varepsilon}\cdot\vec{p}|i\rangle\right|^2 \delta\left[E_f - E_i - \hbar\omega\right]\left[f(E_i) - f(E_f)\right] \tag{3.21}$$

$f(E)$ stands for the Fermi filling factor of an energy state. It is intuitive that the absorption must happen between an occupied and an unoccupied state and the total energy must be conserved. Therefore, the selection rule falls mainly on the evaluation of the dipole term $\left|\langle f|\vec{\varepsilon}\cdot\vec{p}|i\rangle\right|^2$.

Since we can always categorise photons to either right-circularly or left-circularly polarisation, $\vec{\varepsilon}\cdot\vec{p}$ can be put as $p_x + ip_y(p_+)$ or $p_x - ip_y(p_-)$. Expressing the initial and final states in Kane basis:

$$|i\rangle = \sum_j^{\Gamma} e^{iq_i z}\phi_j^i(z)\chi_j^i(x,y)\left|\Gamma_j\right\rangle$$

and $$|f\rangle = \sum_j^{\Gamma} e^{iq_f z}\phi_j^f(z)\chi_j^f(x,y)\left|\Gamma_j\right\rangle$$

$$\left|\left\langle f\left|\vec{\varepsilon}\cdot\vec{p}\right|i\right\rangle\right| \propto \sum_{m,n}^{\Gamma}\left\langle \Gamma_m\left|e^{iq_f z}\phi_m^f(z)\chi_m^f(x,y)p_{\pm}e^{iq_i z}\phi_n^i(z)\chi_n^i(x,y)\right|\Gamma_n\right\rangle \qquad (3.22)$$

It is important to note that no attempt should be made to express the Kane states $\left|\Gamma_n\right\rangle$ as functions of *x, y, z*. The wavefunctions are represented not only by the three axes but also by the Kane states, which makes them to be functions of 11 parameters in a spin non-degenerate case. In other words, the envelope functions and the Kane states are separable. This is based on the assumption that the envelope functions change little within a unit cell.

$$\left|\left\langle f\left|\vec{\varepsilon}\cdot\vec{p}\right|i\right\rangle\right| \propto \sum_{m,n}^{\Gamma}\left(\int_{-\infty}^{\infty} e^{i(q_i-q_f)z}\phi_m^{f^*}\phi_n^i\cdot dz\right)$$
$$\bullet\left(\int \chi_m^{f^*}p_{\pm}\chi_n^i\cdot dxdy\left\langle\Gamma_m\middle|\Gamma_n\right\rangle+\int\chi_m^{f^*}\chi_n^i\cdot dxdy\left\langle\Gamma_m\middle|p_{\pm}\middle|\Gamma_n\right\rangle\right) \qquad (3.23)$$

For the first term, it requires the overlapping between *z*-direction envelope functions and the condition $q_i = q_f$, which can also be seen as momentum conservation along the *z*-axis. The first half of the second term stands for intraband transition. In the case of zero magnetic field, χ_n^i is a free travelling wave and this term is zero. The second half can be regarded as the $p_{\pm}$ (hence $k_{\pm}$) dependant coupling terms in $\left\langle\Gamma_m\middle|H\middle|\Gamma_n\right\rangle$, which includes $\left|c\uparrow\right\rangle-\left|hh\uparrow\right\rangle$, $\left|c\uparrow\right\rangle-\left|lh\downarrow\right\rangle$, $\left|c\uparrow\right\rangle-\left|so\downarrow\right\rangle$ and $\left|c\downarrow\right\rangle-\left|hh\downarrow\right\rangle$, $\left|c\downarrow\right\rangle-\left|lh\uparrow\right\rangle$, $\left|c\downarrow\right\rangle-\left|so\uparrow\right\rangle$. The coupling strength can be estimated from the squares of the coefficients which gives a ratio of 1/2:1/6:1/3 between *hh, lh* and *so* transitions. These are usually referred to as interband transitions.

3.6.1 Applied Magnetic Field

When a magnetic field is applied along the z-direction, the in-plane envelope functions would be quantized to form the Landau levels. The selection rules hence turn out to be:

$$\left|\left\langle f\left|\vec{\varepsilon}\cdot\vec{p}\right|i\right\rangle\right| \propto \sum_{m,n}^{\Gamma}\left(\int_{-\infty}^{\infty} e^{i(q_i-q_f)z}\phi_m^{f^*}\phi_n^i\cdot dz\right) \bullet\left(\left\langle LL_m\left|LL_n\right\rangle\right\langle\Gamma_m\left|p_{\pm}\right|\Gamma_n\right\rangle+\sqrt{2\hbar\omega}\left\langle LL_m\left|LL_n+1\right\rangle\right\langle\Gamma_m\left|\Gamma_n\right\rangle\right) \quad (3.24)$$

The interband terms are allowed only between states with the same Landau level indices. At the same time, the intraband was activated between the adjacent Landau levels which was forbidden without the magnetic field.

Hierarchy of Selection Rules			
$q_i = q_f$			
$\int_{-\infty}^{\infty}\phi^{f^*}\phi^i.dz \neq 0$			
Interband		**Intraband**	
$B=0$	$B\neq 0$	$B=0$	$B\neq 0$
$k_i^{//} = k_f^{//}$	$LL_i = LL_f$	Forbidden	$LL_i = LL_f \pm 1$

Table 3-5 Hierarchy of selection rules for Kane states with in-plane electromagnetic fields.

Table 3-5 summarises the selection rules for normal incidence with or without magnetic fields along the z-direction. The first condition is momentum conservation along the growth direction - $q_i = q_f$. The second condition asks for an overlap between the initial and final z-propagating envelope functions. For a structure with a symmetric potential, the envelope functions are either even or odd. This condition rules out any possible transition between the adjacent subbands. It can also be deduced easily that the interband transition is weak in a type-II structure due to the spatial separation between the envelope functions.

It must be emphasised that the selection rules listed in Table 3-5 are for the pure Kane states only. Practically speaking, all eigenstates of are more or less mixtures of the full Kane base. To understand the possibility of transitions qualitatively in a spin non-degenerate system, the following steps can be taken:

1) Following Table 3-3, put down the initial and final eigenstates in a complete form, for n= 0

$$|\psi\rangle = \hat{f}\left(\chi_2\left|hh\downarrow\right\rangle + \chi_1\left|c\downarrow\right\rangle + \chi_0\left|lh\uparrow\right\rangle + \chi_0\left|so\uparrow\right\rangle\right) + \hat{g}\left(\chi_0\left|c\uparrow\right\rangle + \chi_1\left|lh\downarrow\right\rangle + \chi_1\left|so\downarrow\right\rangle\right)$$

where $\hat{f}$ and $\hat{g}$ have different parity.

2) Use common sense to name the parity and the major term of the eigenstates. For E_0 band, the main term must be either $\left|c\downarrow\right\rangle$ or $\left|c\uparrow\right\rangle$ with the corresponding $\phi(z)$ being even.

3) With the help of selection rules, determine the transition should be major (transition allowable between the major terms), minor (transition allowable between the coupling terms) or forbidden.

To get a quantitative understanding, of course, the full Hamiltonian must be calculated. This is particularly vital for heterojunctions as a result of the parity breakdown due to the non-symmetric potential.

From the selection rules listed above, it is apparent that no transition between two subbands within one band is allowed in a symmetric structure. These forbidden channels are activated either by applying an in-plane magnetic field or perturbing the system with time-varying electric field along the growth direction. These two methods actually take different routes to achieve the results. Tilted steady magnetic fields break down the form of the "eigenstate Hamiltonian", the part which gives the eigenstates and energies as those in the Appendices. In this case, the good quantum numbers discussed in previous sections, such as Landau level indices, cease to be "good". Transitions are allowed even between states with the same Landau level indices which is forbidden for the sake of angular momentum conservation. However, this is by no means the meltdown of basic principles. It must be remembered all the terms, such as Landau level, subband index.. etc, should be dropped since they cannot describe the system properly any more. We keep on using them just because of the incapability to find a set of good quantum numbers for this complicated system. Besides, it seems the eigenenergies change little with the extra

in-plane magnetic fields [31]. Hence it is safe to keep the old terms and only claim the in-plane magnetic fields change the selection rules.

The second approach can be achieved by either applying narrow metal stripes [32] on top of the samples or sending the incident beams through in a wave-guide configuration. Both methods introduce an electric field component along the z-axis to the very interaction Hamiltonian which originates the selection rules. This extra term gives some extra transitions between the subbands. At the same time, no polarisation dependant experiment can be done since this extra term does not carry any polarisation dependant information. Care must be taken since not all the transitions in the name of "intersubband coupling" are allowed. Some of them are strictly forbidden even though they "look like" that may be possible. I shall discuss this matter further in Chapter 7.

3.7 Conclusion

We have illustrated a selfconsistent algorithm based on the matrix momentum approach of the ***k.p*** theory. The proposed framework successfully tackles the spurious solution problem appearing through the incompleteness of the Hamiltonian. It also shows decisive advantage over any other non-selfconsistent algorithms in a Type-II crossed gap systems. A computer program based on this algorithm is extensively used in this thesis to calculate the band structures of the samples.

References

[1] T. A. Vaughan, *D.Phil thesis*, Oxford (1995).

[2] L. M. Luttinger and W. Kohn, *Phys. Rev.* **97**, 869 (1955).

[3] L. M. Luttinger, *Phys. Rev.* **102**, 1030 (1956).

[4] C. R. Pidgeon and R. N. Brown, *Phys. Rev.* **146**, 575 (1966).

[5] M. Altarelli, *Heterojunctions and SemiconductorSuperlattices*, edited by G. Allan, G. Bastard, N. Boccora and M. Voos, Springer-Verlag, Berlin (1986).

[6] C. Kittel, *Quantum Theory of Solids*, 2nd edition, John Wiley & Sons (1987).

[7] G. Bastard, *Wave Mechanics Applied to Semiconductor Heterostructures*, Halsted Press, John Wiley & Sons, New York (1988).

[8] M. L. Cohen and T. K. Bergstresser, *Phys. Rev.* **141**, 789 (1966).

[9] E. O. Kane, *J. Phys. Chem. Solids* **1**, 852 (1957).

[10] E. O. Kane, *J. Phys. Chem. Solids* **1**, 83 (1956).

[11] M. H. Weiler, *Semiconductors and Semimetals*, edited by R.K. Willardson and A.C. Beer Vol. 16, Academic Press (1981).

[12] E.O. Kane, *Semiconductors and Semimetals (Physics of III-V Compounds)*, edited by R.K. Willardson and A.C. Beer Vol. 1, Academic Press (1966).

[13] R. J. Warberton, *D.Phil thesis*, Oxford (1991).

[14] M. G. Burt, *J. Phys. Cond. Matt.* **4**, 6651 (1992).

[15] D. L. Smith and C. Mailhiot, *Phys. Rev. B* **33**, 8345 (1986).

[16] D. L. Smith and C. Mailhiot, *Rev. Mod. Phys.* **62**, 173 (1990).

[17] F. Szmulowicz and G. J. Brown, *Phys. Rev. B* **51**, 13203 (1995).

[18] F. Szmulowicz, *Superlattices and Microstructures* **22**, 295 (1997).

[19] F. Szmulowicz and G. J. Brown, *Appl. Phys. Lett.* **66**, 1659 (1995).

[20] L. R. Ram-Mohan, K. H. Yoo and R. L. Aggarwal, *Phys. Rev. B* **38**, 6151 (1988).

[21] M. L. Boas, *Mathematical Methods in the Physical Sciences,* 2nd edition, John Wiley & Sons, New York (1983).

[22] G. E. Bir and G. E. Pikus, *Symmetry and Strain-Induced Effects in Semiconductors*, John Wiley & Sons, New York (1974).

[23] C. G. van de Walle, *Phys. Rev. B* **39**, 1871 (1989).

[24] R. Winkler and U. Rossler, *Phys. Rev. B* **48**, 8918 (1993).

[25] R. de L. Kronig and W. G. Penney, *Proc. Roy. Soc.* **A130**, 499 (1931).

[26] F. Stern, *Phys. Rev. B* **5**, 4891 (1972).

[27] P. Lorrain and D. R. Corson, *Electromagnetic Fields and Waves,* 2nd edition, W. H. Freeman & Co., San Francisco (1972).

[28] G. M. Sundarem, R. J. Warberton, R. J. Nicholas, G. M. Summers, N. J. Mason and P. J. Walker, *Semi. Sci. Tech.* **7**, 985 (1992).

[29] D. Heitmann, M. Ziesmann and L. L. Chang, *Phys. Rev. B* **34**, 7463 (1986).

[30] J. Kono, B. D. McCombe, J. P. Cheng, I. Lo, W. C. Mitchel and C. E. Stutz, *Phys. Rev. B* **55**, 1617 (1997).

[31] F. Stern and W. E. Howard, *Phys. Rev.* **163**, 816 (1967).

[32] Lian Zheng, W. L. Schaich and A. H. MacDonanld, *Phys. Rev. B* **41**, 8493 (1990)

4. The Resonant Polaron Coupling in $CdTe/Cd_{1-x}Mg_xTe$ Quantum Wells

4.1 Introduction

A polaron is the combination of an electron and its associated strain field in a polar crystal. The electron polarises its surroundings and the resulting lattice distortion is equivalent to a cloud of longitudinal optic (LO) phonons [1-3]. In a cyclotron resonance experiment, the polaron effect manifests itself by modifying the Landau level structure and hence the observed effective masses.

4.1.1 Electron-Phonon Coupling Effects

This long-range Coulomb interaction induced coupling was first introduced by Fröhlich [2]. The Hamiltonian is given by:

$$H = H_0 + \hbar\omega_{LO}\sum_q a_q^+ a_q + H_I \tag{4.1}$$

where $$H_I = \sum_q (V_q a_q e^{iq\cdot r} + V_q^* a_q^+ e^{-iq\cdot r})$$

Here, ω_{LO} represents the LO phonon frequency, and a_q^+ and a_q are the creation and annihilation operators respectively for an LO phonon of wavevectors q. H_I is the interacting term, within which the V_q is the interaction coefficient. In a three dimensional case, it is

$$|V_q|^2 = \frac{1}{q^2}\frac{2\sqrt{2}\pi\alpha}{V} \tag{4.2}$$

V is the volume of the crystal and α is the so-called Fröhlich constant given by

$$\alpha = \frac{e^2}{4\pi\varepsilon_0\hbar}\left[\frac{m^*}{2\hbar\omega_{LO}}\right]^{1/2}\left[\frac{1}{\varepsilon(\infty)} - \frac{1}{\varepsilon(0)}\right] \tag{4.3}$$

$\varepsilon(\infty)$ and $\varepsilon(0)$ are the high frequency and static dielectric constants respectively. For most semiconductors, α is smaller than 1. The Fröhlich constant actually determines the strength of the polaron coupling. In the limit of small q, the Hamiltonian can be solved by perturbation theory to the second order, which leads to the following well-known result for the energy of a polaron

$$E_{pol} = \frac{\hbar^2 k^2}{2m_{pol}^*} - \alpha\hbar\omega_{LO} \tag{4.4}$$

where m^*_{pol} is the polaron effective mass, given by

$$m^*_{pol} = \frac{m^*}{(1-\alpha/6)} \tag{4.5}$$

Thus the effect of the electron-LO phonon interaction is to reduce the energy by an amount $\Delta E = \alpha\hbar\omega_{LO}$ (the self-energy correction) and to increase the effective mass by a factor $(1-\alpha/6)^{-1}$ (mass renormalization).

When dealing with the two-dimensional case, the crudest way is to remove the z-dependant component from the Hamiltonian; the interaction coefficient is thus

$$\left|V_q\right|^2 = \frac{1}{q}\frac{\sqrt{2}\pi\alpha}{A} \tag{4.6}$$

where A represents the area of the sample. This is the ideal two-dimensional model. Further investigations show that the corresponding mass renormalization in 2D is more significant than in the 3D case [4]. In addition, this ideal approximation overestimates the polaron effects relative to a finite-width infinite-barrier approximation [5,6].

A real system is certainly much more complicated than the ideal 2D case. This over-simplified model deals only with the 3D phonon modes of the materials of the quantum wells. Heterostructures always consist of two different materials with a finite bandedge potential instead of the same material with infinite barriers. In addition, the difference between the dielectric constants of the wells and barriers generate polar fields which contribute to the interface optical (IO) phonon mode. Both the interface (IO) and slab-bulk (BO) phonon modes have been studied extensively in the case of zero magnetic field [7,8].

4.1.2 Polaron effects in Magnetic Field

At sufficiently high magnetic field, the cyclotron energy is equal to the LO phonon energy $\hbar\omega_{LO}$ and, in the absence of the electron-phonon coupling, an electron in the n^{th} Landau level is degenerate with an electron in the $n\text{-}1^{th}$ Landau level and a LO phonon. When we include the coupling term in Eq. (4.1), the degeneracy will be lifted to give hybridised states and anti-crossing behaviour as shown in Figure 4-1. When the cyclotron

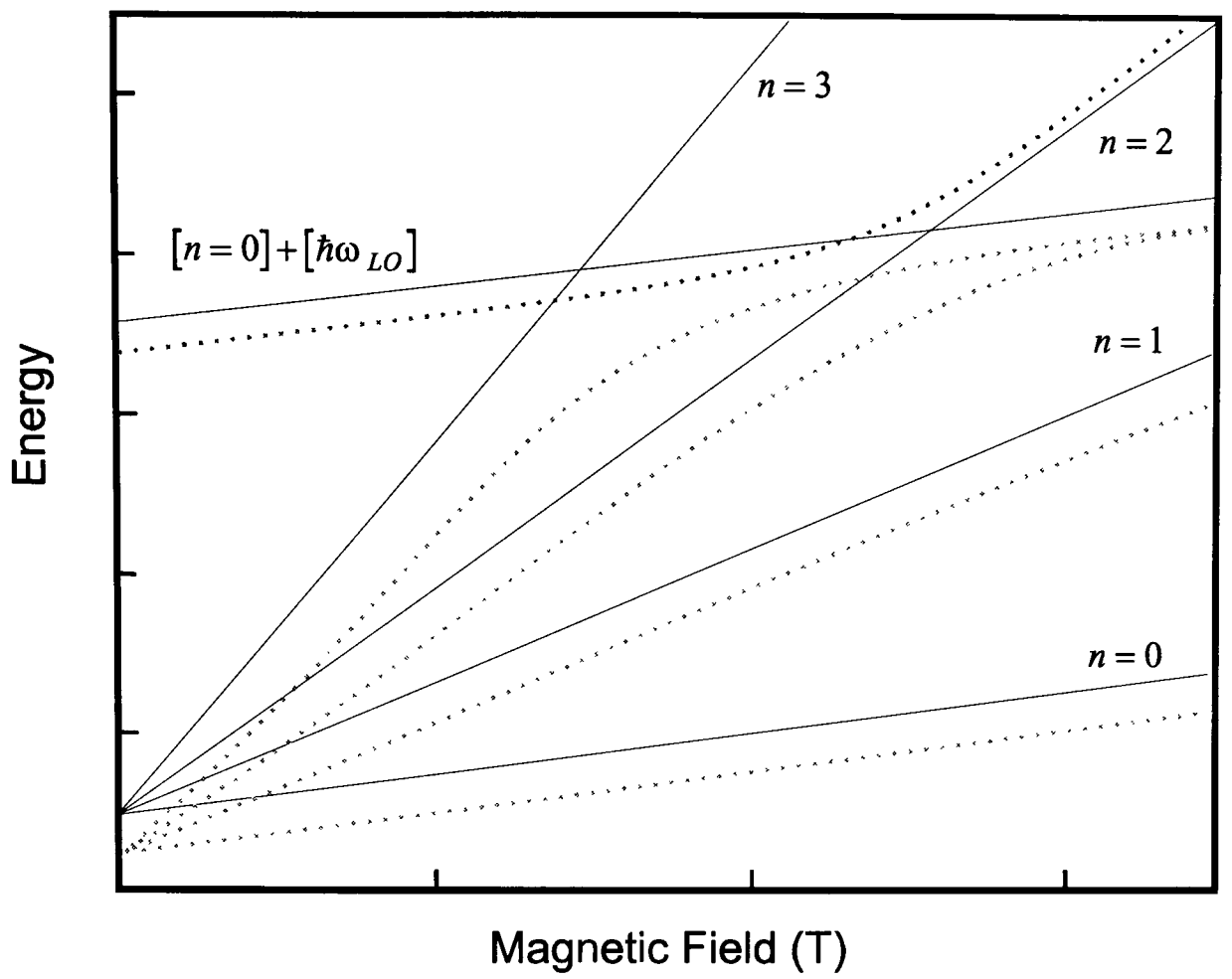

Figure 4-1 Schematic diagram of the spin degenerate Landau levels as a function of magnetic field, reproduced from Ref. [9]. The corresponding Landau level indices (*n*) are indicated. The solid and dashed lines are the unperturbed and perturbed levels, respectively.

energy exceeds the LO phonon energy, the "Landau level pinning" can be seen as the lower branch of the eigenenergies follows the phonon energy. The smooth line marks the transition from an electron dominated state to an LO phonon dominated state. Meanwhile, both the mass renormalization and polaron self energy shift are added on to it. This is the so-called "resonant polaron coupling", which was first observed in InSb [3].

4.1.3 Samples

CdTe has been recognised for several years as one of the best materials for testing experimentally the predictions of the polaron effect [10]. With a Fröhlich constant of 0.3 relative to the 0.065 of GaAs, CdTe offers more significant coupling effects than most other III-V materials. At the same time, the light effective mass of the material means the possibility of experiments at an achievable magnetic field. In addition, the MBE growth makes it possible to achieve mobility high enough to permit the measurement of sharp narrow transitions.

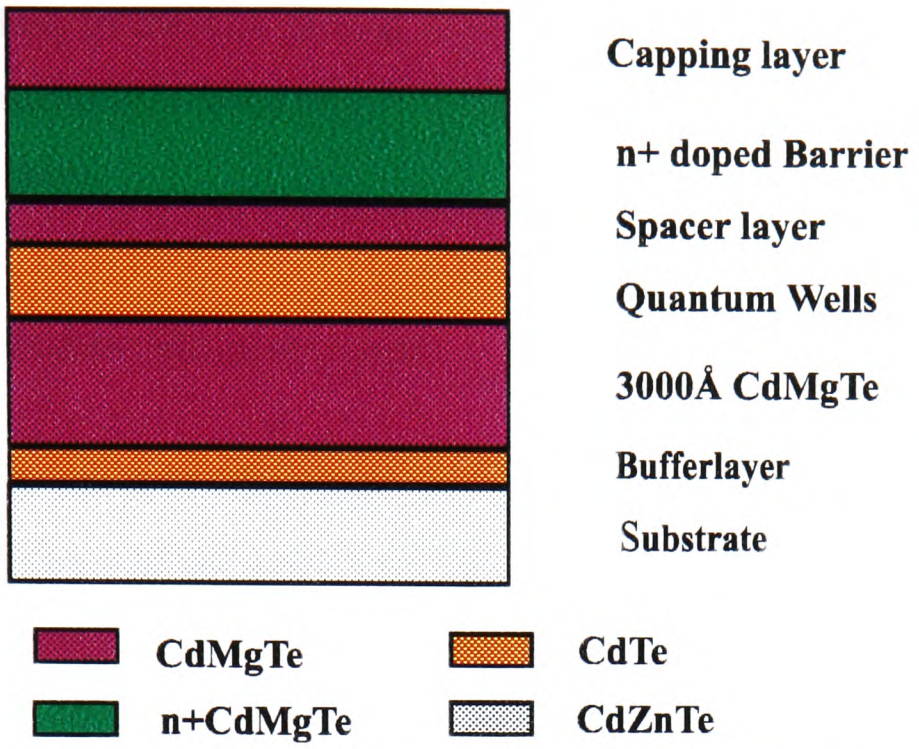

Figure 4-2 A schematic diagram of the samples investigated.

Three n-type based CdTe samples were studied, which were grown by MBE at Würzburg on undoped CdZnTe substrates with a 100Å undoped CdTe buffer layer followed by 3000Å of $Cd_{1-x}Mg_xTe$. The quantum wells were typical by 100Å wide and modulation doped in $Cd_{1-x}Mg_xTe$ barriers, using a spacer layer. The Mg concentration in the $Cd_{1-x}Mg_xTe$ is around 30%. The resulting two-dimensional carrier densities were in the range 7~8.5 x 10^{11} cm^{-2} (Table 4-1). A schematic diagram is shown in Figure 4-2.

Table 4-1 Sample details of the CdTe single quantum wells.

Sample	Barrier Materials	Carrier density (10^{11} cm^{-2})	Mg Content (%)	Mn Content (%)
CT1047	$Cd_{1-x}Mg_xTe$	8.0	30	0
CT1089	$Cd_{1-x}Mg_xTe$	8.6	30	0
CT1091	$Cd_{1-x}Mn_yMg_xTe$	7.0	30	0.5

4.2 Experimental Setup

Conventional cyclotron resonance transmission measurements have been done using various far-infrared wavelengths except those close to the optical phonon frequencies due to the strong absorption of incident beam within the reststrahlen band of the substrate. Despite the bi-polar properties of CdZnTe wafer, the optical phonon frequencies are very close to those of the CdTe quantum wells. This means it is hopeless to investigate the

polaron effect close to the LO phonon frequency of the CdTe by the traditional way. Reflectivity measurements were hence developed to overcome the strong absorption within the reststrahlen.

4.2.1 Transmission Measurement

The far infrared laser described in Chapter 2 is used as the source in this investigation together with the pulsed magnet owing to the fact that a magnetic field of up to 35 Tesla is necessary to reach the resonant coupling region. Because of the limited space available in the pulsed field room, the infrared laser is positioned on the floor above. The beam travels in an evacuated brass pipe through a hole in the ceiling due to the strong attenuation by the air.

The insert was built around two 5mm stainless steel tubes - one guides the beam down and the second one collects the signals out. The pickup coil is positioned close to

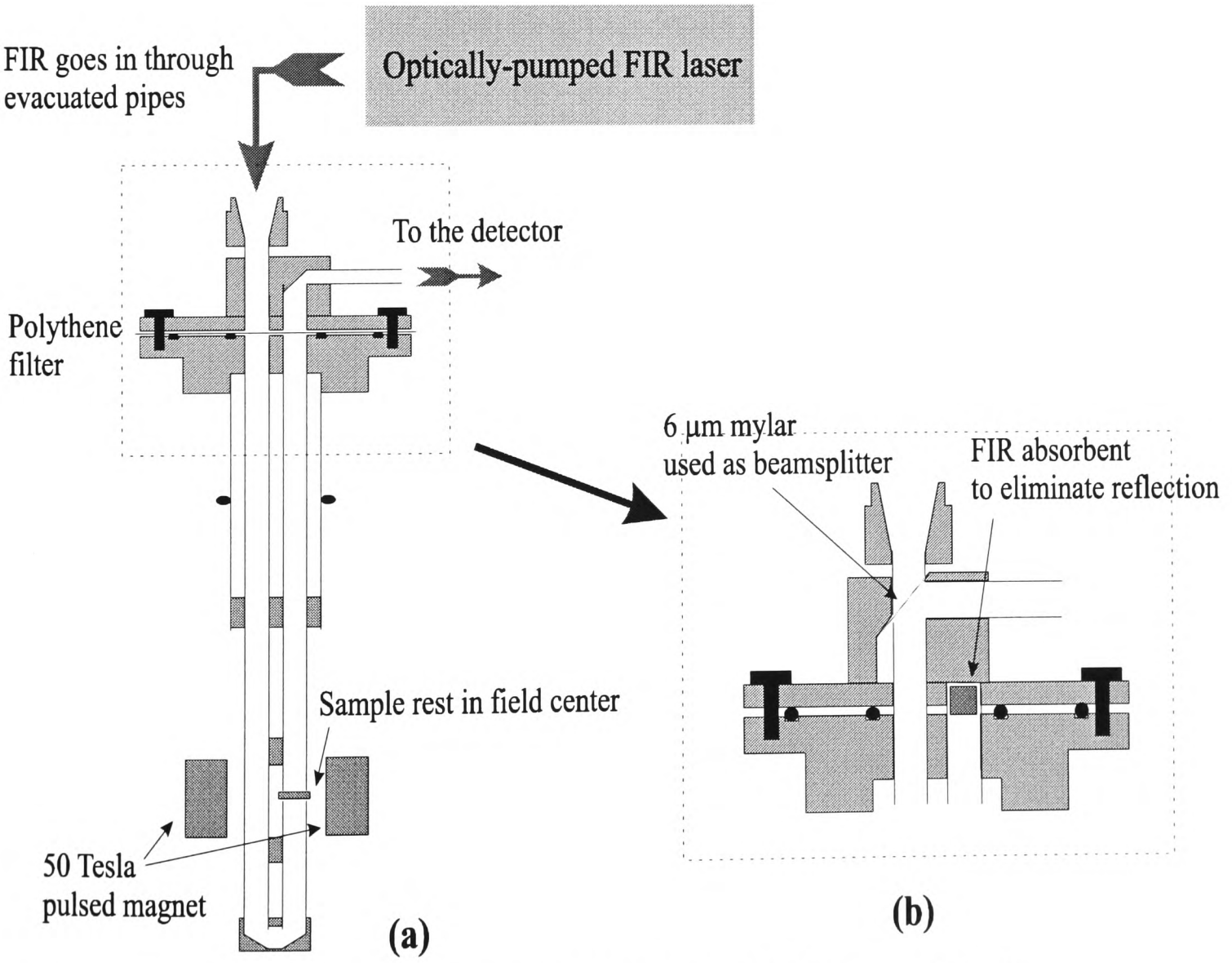

Figure 4-3 Insert used to conduct (a) transmission and (b) reflectivity experiments.

the sample holder to give accurate readouts of the fields. In addition, several sample holders were built at different angles to conduct tilted field experiments when needed. Two pieces of fine polished brass were plated with gold and carefully placed at the bottom of the tubes to reflect the transmitted beam back to top of the insert. Owing to the tremendous amount of force applied on the brass mirrors during the field sweep, they were ripped ruthlessly off their position from time to time. Some reinforcements were applied to keep them in position.

Signal is fed into photodetectors at liquid ^{4}He temperature as described in Section 2.4. A constant current source and a broad bandwidth preamplifier are used to monitor the minute changes of conductivity. The amplified signal is then sent to the recorder that is automated with a computer. Precautions have been taken to arrange the wires connecting these instruments because of the strong induced pickup voltage through a closed area which usually results in distortion of the signal.

Both the magnet and the recorder are triggered at the same time. The recorder then takes the pickup voltage and photodetector signals synchronously over the next 20ms. The pickup voltage is then integrated to give the magnetic field at each moment. Photoconductivity traces for both the rising and lowering fields are recorded. Figure 4-3 illustrates a detailed diagram of the arrangement. This conventional cyclotron resonance experimental arrangement is extensively used through the whole thesis.

4.2.2 Reflectivity Measurement

The same insert described above is employed in this study, but a new top plate was designed instead. A piece of 10μm Mylar is stretched on a 45 degree frame as the beamsplitter (Figure 4-3). Mylar is nearly transparent to far infrared radiation. However, different thicknesses always result in different frequency response due to the interference of light. 10μm is the optimised thickness considering the far infrared wavelengths we used. The collecting light pipe is blocked with black tissues to absorb any possible reflection from inside. The original delivering light pipe is employed to send the beam down and collect the reflected light from the samples.

4.3 Results and Discussion

The experiments were carried at 4.2 K. More than 10 different wavelengths from the infrared laser were used in the experiment. Clear resonances were seen in transmission both above and below the Reststrahlen band. Within the Reststrahlen band of the CdZnTe wafer (between 77 μm and 50 μm), reflectivity measurements were done instead. Two usable wavelengths of the laser are in this region. One wavelength (70.51 μm), which sits right on the TO phonon frequency of CdTe, gives only an unclear signal in reflectivity and none in transmission as we expected. Another one (57.2 μm) gives an ambiguous broad peak around 23 T, which should be taken as having considerable errors. The traces for several different wavelengths are illustrated in Figure 4-4.

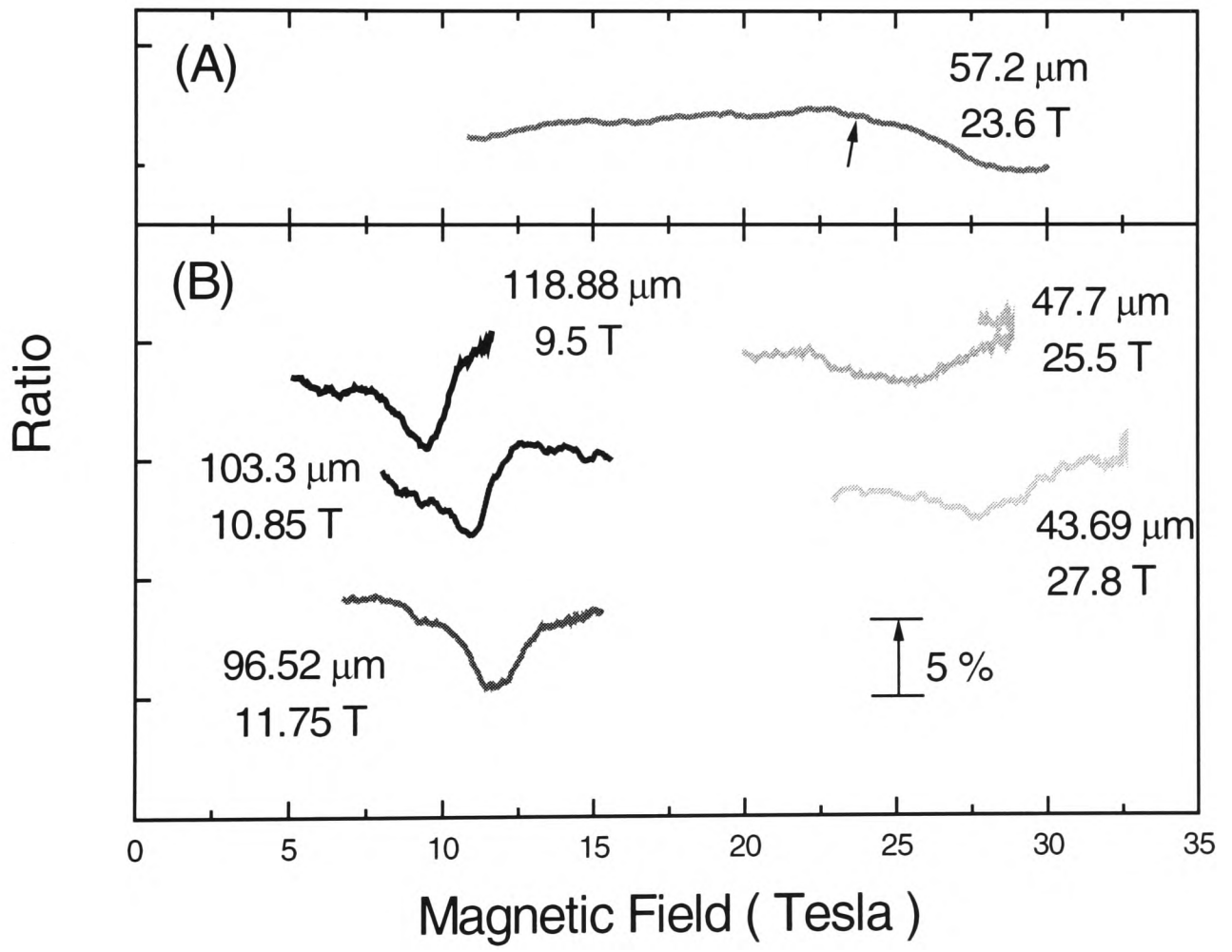

Figure 4-4 Normalised resonance traces in magnetic fields at different cyclotron energies measured by (A) reflectivity and (B) transmission.

4.3.1 Plasma Background Extraction

As shown in Section 1.5, the changing dielectric constants in magnetic fields always give strong effects on the spectra. Besides that, the carrier densities, hence the plasma frequency, can cause a similar amount of change to the spectra as having been shown in previous studies [11].

Here we are more interested in the effect due to the phonon frequencies. Since the third term in Eq. (1.16) is imaginary if the radiation wavelength is equal to the TO phonon's, a strong modulation to the dielectric constants is expected. Figure 4-5 illustrates the calculated reflectivity for several wavelengths within the Reststrahlen of CdTe. Outside the Reststrahlen (50 μm), the spectrum is a peak with 8% increase around the resonance position. As the resonance energy moves close to the LO phonon, the spectrum begins to look like a differential. After the wavelength passes through the LO phonon and heads for the TO phonon, the resonance feature becomes weaker and weaker, although the total reflection from the sample can reach as high as 60% of the incident

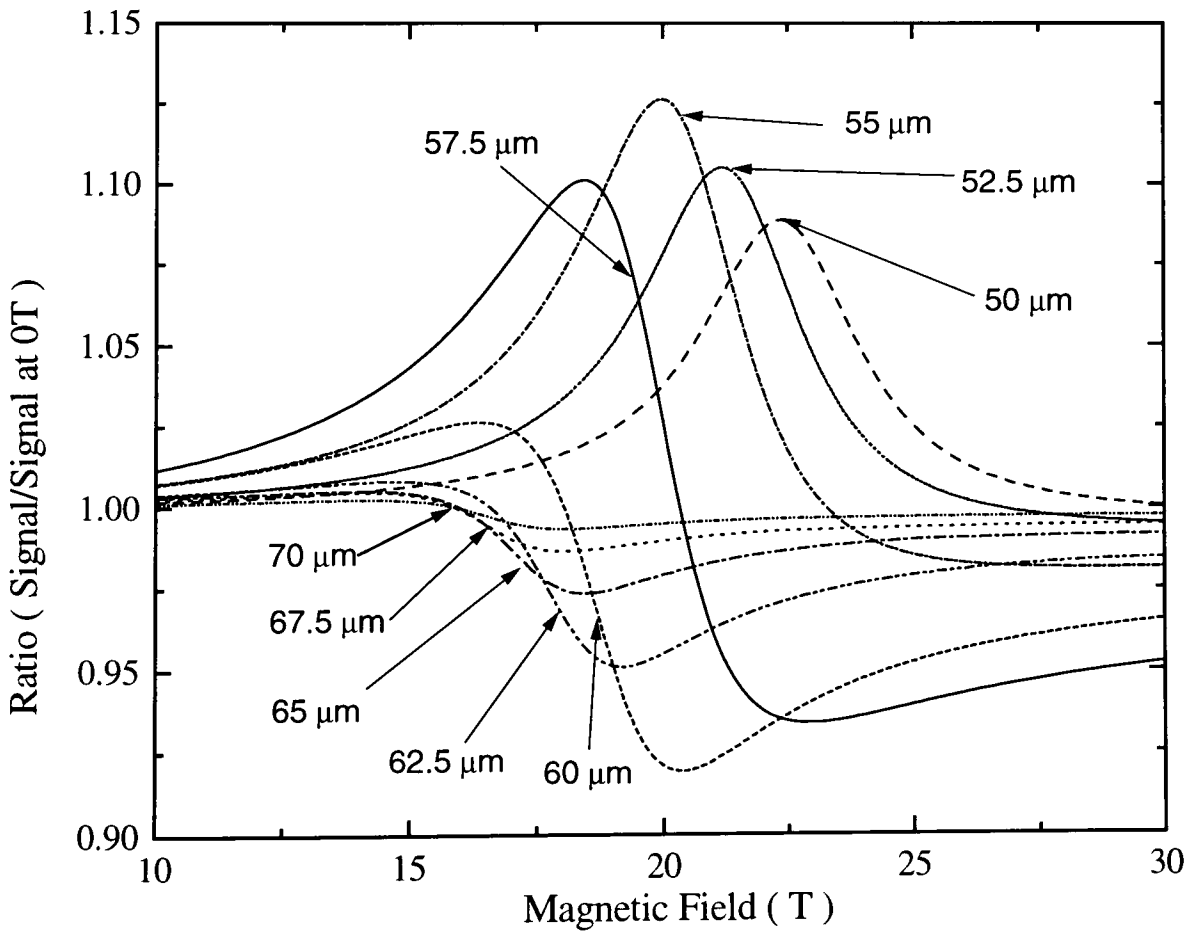

Figure 4-5 Theoretical calculated reflectivity traces of different resonance energies within the Reststrahlen using the model introduced in Section 1.5. The arrows point at the corresponding resonance fields.

beam intensity. This phenomenon agrees with our measurement at 70.51 μm, at which point, a clear reflection spectrum is recorded with virtually no feature at all.

The conventional way of picking the resonance positions is using the Lorentzian function to fit the spectra with a background offset on top of it [12]. However, this method cannot be applied to the spectra taken within the Reststrahlen as stated above. Further studies reveal a more interesting relation between the resonance positions and the "features" on the spectra. Figure 4-6 illustrates the result of a theoretical treatment assuming a fixed effective mass of 0.105 m_e. At 57.2 μm, the corresponding resonance field is 19.55 T. Although the peak of the transmission corresponds nicely to that value, the reflection spectrum does not. This indicates the necessity to fit each spectrum individually to deduce the polaron masses. The resonance traces in Figure 4-4 are treated with this model to yield the effective masses accordingly.

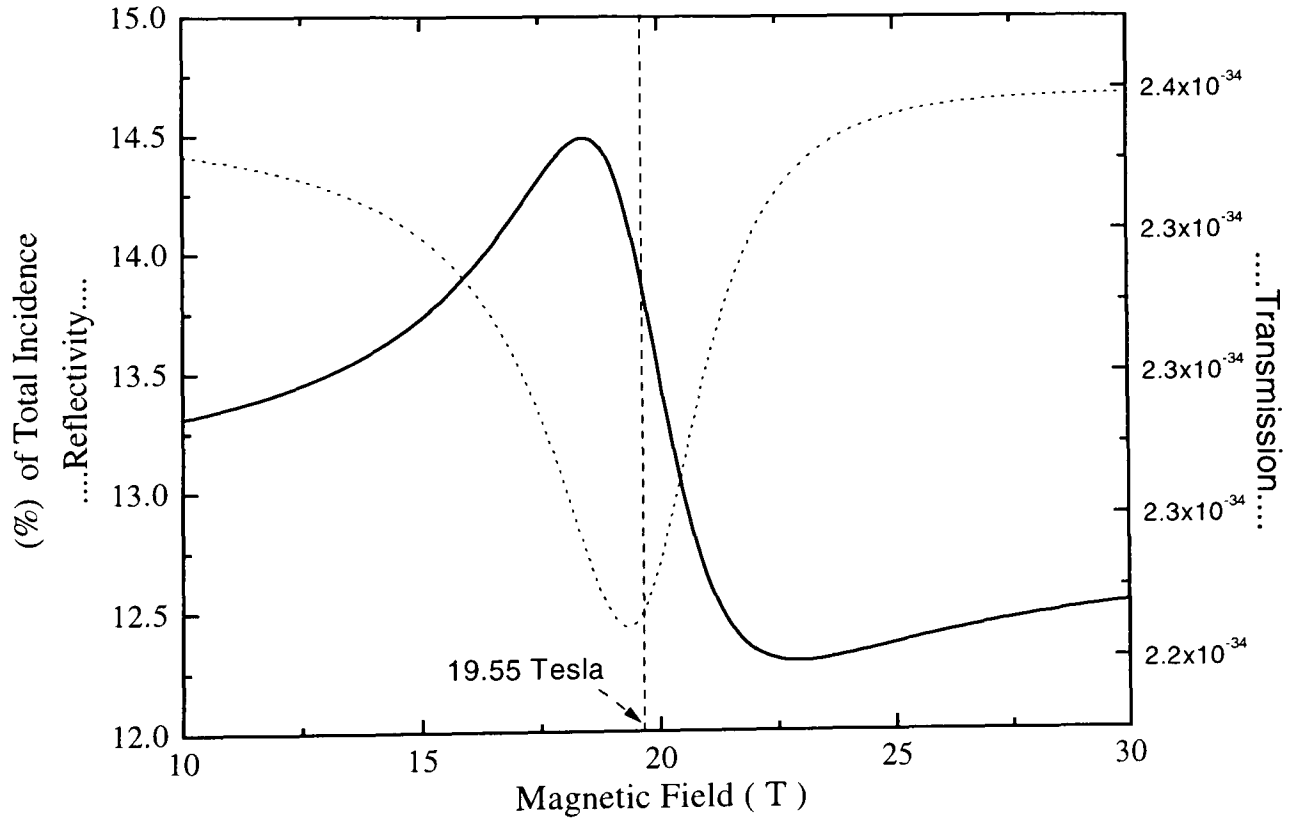

Figure 4-6 Theoretical prediction of the reflectivity and transmission spectra at 57.2 mm. Solid and dotted lines represent the reflectivity and transmission, respectively.

4.3.2 Theoretical Modelling

Figure 4-7 illustrates effective masses extracted from resonance traces using the plasma model together with the theoretical predictions. Since the theoretical model does not include the contribution from the quantum well confinement, it is worth mentioning that the result presented here has been shifted by 6% which is predicted by the ***k.p*** model and confirmed by the experimental data. The quantum well effective masses show a gentle background increase as a function of magnetic field, due to both the band non-parabolicity and the resonant polaron contribution. At around 20 Tesla, where the LO phonon energy passes through the first Landau level, a small discontinuity of around 5% in the mass is observed. A small overall increase relative to the bulk value (0.096 m_0) is also observed resulting from the confinement potential of quantum wells. The experimental data is in excellent agreement with the high carrier density ($7x10^{11}$ cm^{-2}) calculation, indicating a strong suppression of the coupling strength. However, the suppression observed in experiments is slightly stronger.

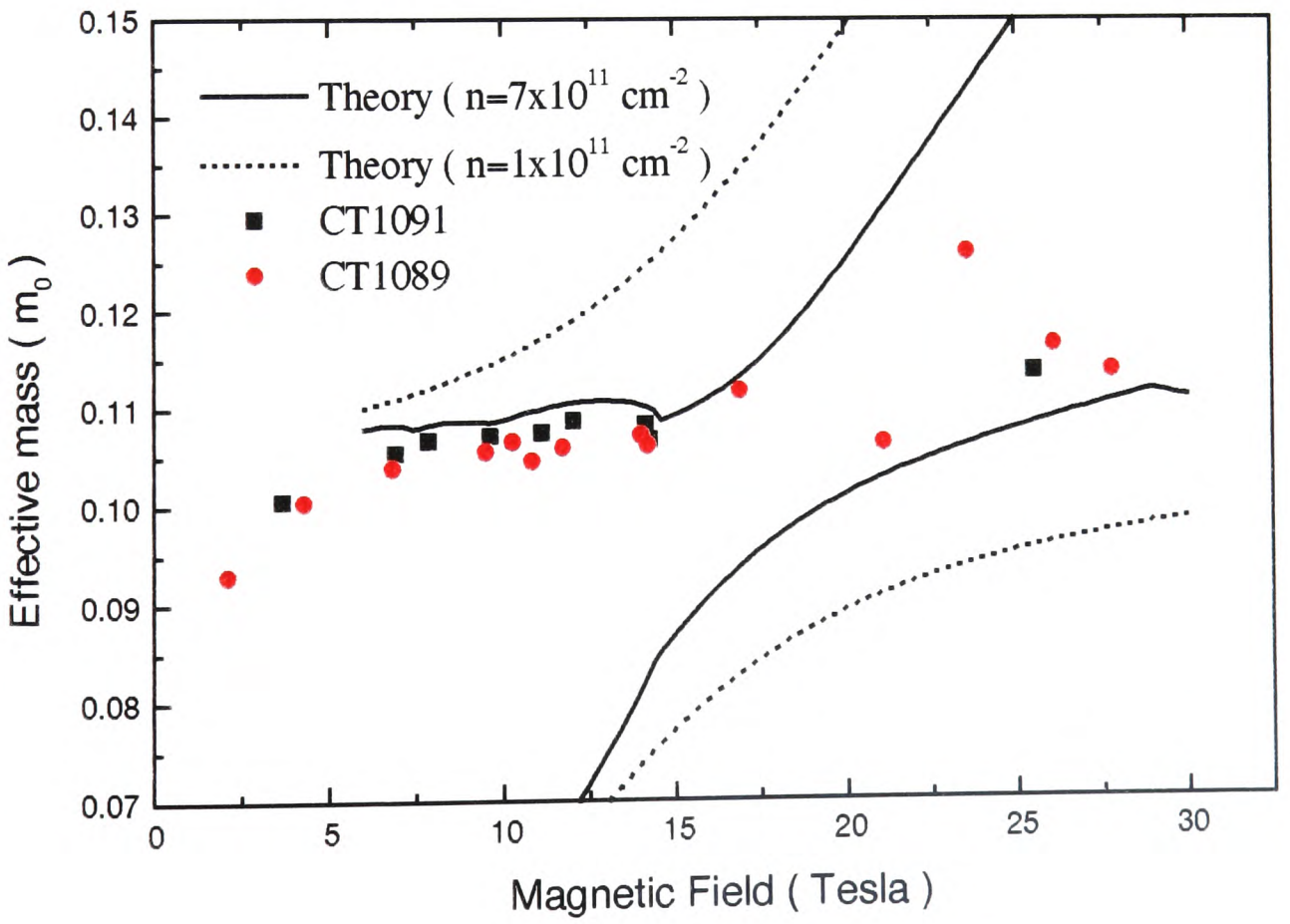

Figure 4-7 Effective masses of samples and the theoretical predictions.

Figure 4-7 also shows the results of the theoretical calculations at two different carrier densities. For the lower density (1 x 10^{11} cm^{-2}) there is a large resonant polaron coupling which leads to a very large divergence in the effective mass similar to what would be expected from a single polaron model. For the higher density (7 x 10^{11} cm^{-2}), a strong suppression on the coupling strength is obvious with a small oscillatory term in mass that corresponds to the Landau level filling factors. This is understood as the level occupancy effect [13]. If the lowest Landau level (n=0) is almost filled, the resonant part of the polaron effects will be suppressed as the Pauli exclusion principle will reduce the number of final states for this virtual transition. In addition, the inclusion of static screening causes a further, but smaller reduction [14]. Nevertheless, the theory presented here only incorporates the 3D phonon modes within infinite barriers [15]. It will therefore be interesting to compare our results with a more thorough treatment to test the validity of applying 3D model in this study.

Due to the complexity of including the IO and BO in the Hamiltonian, an analytical solution in magnetic fields is not available as far as we know. However, numerous works [8,9] have been done in zero field. Both the ground Landau level energy shifts and effective masses have been calculated in practical systems with finite barrier heights and both phonon modes. Figure 4-8 shows the result of different theoretical models based on such systems. With narrow wells, the wavefunctions of electrons will diffuse into the barriers and couple with the phonons there. At the extreme condition (W~0), a polaron effective mass close to that of the 3D barrier polarons is expected. On the other hand, when the width of the well approaches infinity the effective mass should be exactly the value of the 3D well polarons. This is clearly shown in Figure 4-8.

The conventional thickness of our samples is around 100Å, at which point, the difference of effective masses between the models is minimal. Although the system illustrated (GaAs quantum wells) is different from what we have here, a similar pattern is still expected due to the similar magnitude of the Fröhlich constants of the barrier and well. We are thus quite confident in the idealised theory applied in this study.

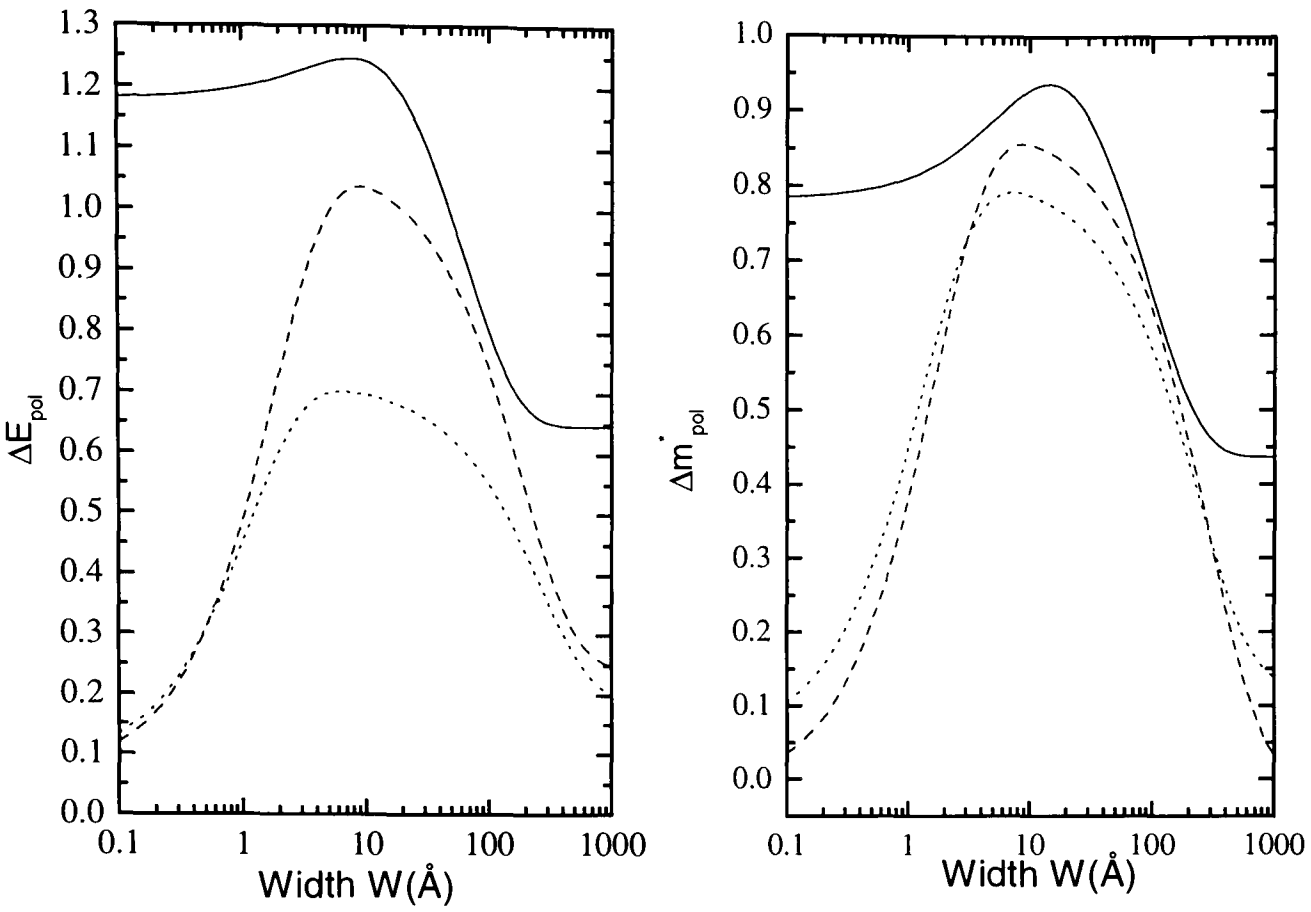

Figure 4-8 Reproduced from Ref. [16], showing polaron binding energy and effective mass in a GaAs quantum well as a function of the well width. Solid curves correspond to the finite barrier with IO and BO phonons. Dashed and dotted curves correspond to the leading term approximation results with IO and slab modes and 3D phonon modes, respectively.

4.4 Conclusion

In summary, the polaron effects of a series of CdTe/$Cd_{1-x}Mg_xTe$ single quantum wells have been studied by cyclotron resonance. This is the first time such work been done in II-VI quantum wells. Both the transmission and reflectivity were measured to collect as much information as possible near and within the reststrahlen band. The spectra were then fitted with a plasma background model to deduce the effective masses.

None of the samples show significant discontinuities in the effective masses near the LO phonon frequency, which is a sign of strong coupling. A polaron model in magnetic field, which includes a treatment of only the bulk phonon modes but not interface optical phonon and confined slab LO phonon modes, fits reasonably well with the data. The lack of strong coupling is explained as the level occupancy effect due to the high carrier

densities. Such behaviour was first observed in GaAs/$Ga_{1-x}Al_xAs$ heterojunctions [11], following the predictions of Wu [17], although only the lower polaron branch was seen in this less polar material. A comparison between the different models justifies the adequacy of using the idealised 3D theory in this case. Our conclusion from the comparison of the fits to the experimental data is that if anything the resonant polaron coupling has been suppressed even more than predicted by theory.

References

[1] C. Kittel, *Quantum Theory of Solids* 2nd Edition, Chap. 7 (1983).

[2] H. Fröhlich, *Advances in Physics* **3**, 325 (1954).

[3] D. H. Dickey, E. J. Johnson and D. M. Larson, *Phys. Rev. Lett.* **18**, 599 (1967).

[4] R. J. Nicholas, *Handbook on Semiconductors*, edited by T. S. Moss, Elsevier Science, Berlin (1994).

[5] Das Sarma, *Phys. Rev. B* **27**, 2590 (1983).

[6] Das Sarma and M. Stopa, *Phys. Rev. B* **36**, 9595 (1987).

[7] Tianquan Lu and Yisong Zheng, *Phys. Rev. B* **53**, 1438 (1996).

[8] J. J. Licari and R. Evrard, *Phys. Rev. B* **15**, 2254 (1977).

[9] G. Lindemann, R. Lassnig, W. Seidenbusch and E. Gornik, *Phys. Rev. B* **28**, 4693 (1983).

[10] J. Waldman, D. M. Larson, P. E. Tannenwald, C. C. Bradley, D. R. Cohn and B. Lax, *Phys. Rev. Lett.* **23**, 1033 (1969).

[11] C. J. G. M. Langerak, J. Singleton, P. J. Van der Wel, J. A. A. J. Perenboom, D. J. Barnes, R. J. Nicholas, M. A. Hopkins and C. T. B. Foxon, *Phys. Rev. B* **38**, 13133 (1988).

[12] G. M. Summers, *D.Phil Thesis*, Oxford (1993).

[13] Wu Xiaoguang, F. M. Peeters and J. T. Devreese, *Proceedings of 18th International Conference on the Physics of Semiconductors*, edited by O. Engström, World Scientific, Singapore (1987).

[14] F. M. Peeters, Wu Xiaoguang and J. T. Devreese, *Surf. Sci.* **196**, 437 (1988).

[15] F. M. Peeters and J. T. Devreese, *Phys. Rev. B* **31**, 3689 (1985).

[16] Guo-qiang Hai, F. M. Peeters and J. T. Devreese, *Phys. Rev. B* **42**, 11063 (1990).

[17] Wu Xiaoguang, F. M. Peeters and J. T. Devreese, *Phys. Rev. B* **34**, 8800 (1986).

5. Cyclotron Resonance Study of Holes in Semimetallic GaSb/InAs Superlattices

5.1 Introduction

The GaSb/InAs system is a unique Type-II system [1,2]. The feature which sets it aside from other systems is that the valence band of GaSb lies above the conduction band of InAs. This cross-gap feature leads to a region of energy where both electron and hole states reside in the structure at the same time. For narrow wells, confinement pushes the electron and hole levels far apart, causing a system with a positive band gap, which we call the semiconducting regime. Wide layer widths, however, result in the electron and hole levels settling further down into their respective energy wells, thus crossing each other. Electrons spill out from the atomic sites into the lower lying electron levels, leading to intrinsic carriers at low temperature without any doping. In the semiconducting regime, the effective band gap is tuneable for anything less than 150 meV simply by growing structures with different layer width. Comparing this property to other narrow gap III-V semiconductors, which need to use dopants to change the band gap, GaSb/InAs has the advantage of no extra scattering mechanism coming with the doping materials, which usually deteriorate the optical and transport properties. In the semimetallic regime, carrier densities are determined only by the width of the layers without the risk of low mobility caused by doping.

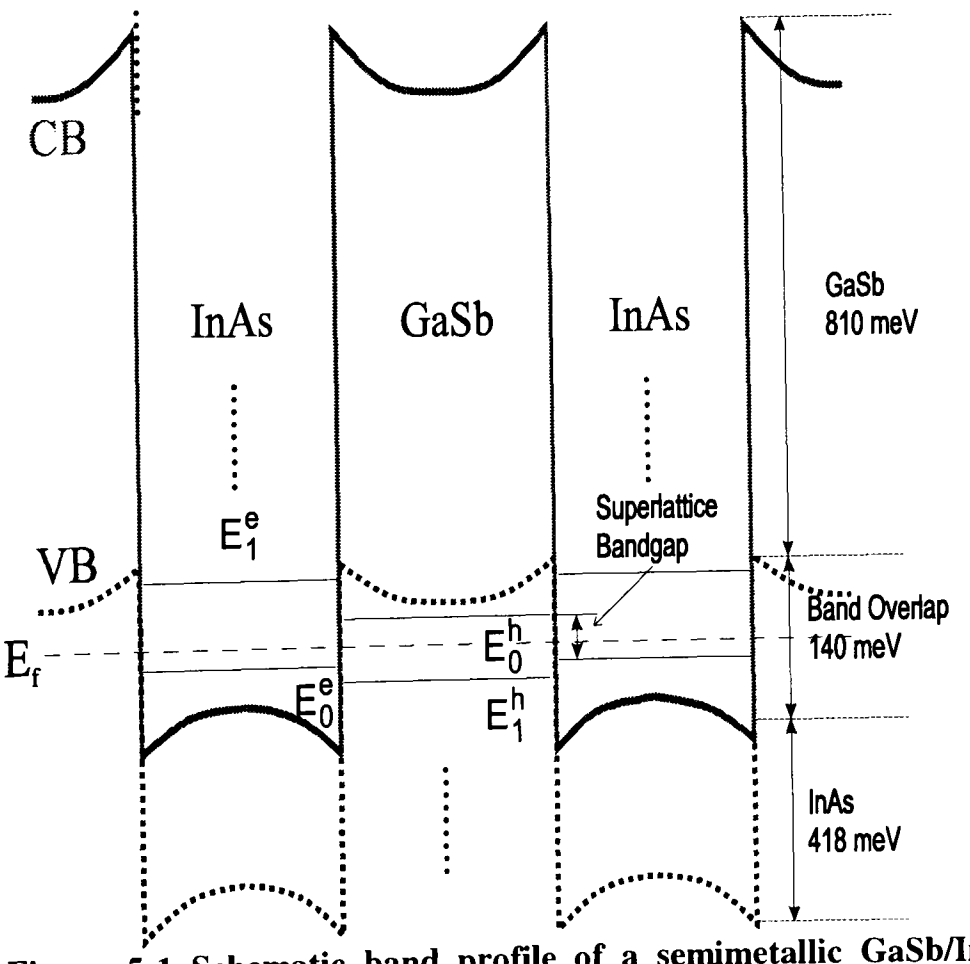

Figure 5-1 Schematic band profile of a semimetallic GaSb/InAs superlattice.

The narrow layer width system deserves study for its potential of near-zero band gap. This allows one to tailor devices for operation in the infrared regions, while avoiding problems common to other small band gap systems such as $Hg_{1-x}Cd_xTe$, for notable light effective mass which gives rise to large tunnelling currents. The wider layer width systems, with large two-carrier populations, exhibit interesting properties in transport, particularly compensated Hall plateaux [3]. Optically, one can observe transitions involving both carrier types simultaneously which are strongly coupled to each other [4]. Conduction band cyclotron resonance studies have been done in InAs/GaSb systems extensively [5]. Due to the low mobility and high magnetic fields needed in the studying of valence bands, this work has been put off relative to the electrons. The purpose of our work mainly focused on the complicated behaviour of holes and some conduction band results that were observed at the same time are included as well.

5.1.1 Growth Techniques

The samples studied are grown at the Clarendon by metal-organic vapour-phase epitaxy (MOVPE), a process by which metal-organic molecules of the group III elements are mixed with hybrids (organic compounds) of the group V elements, and passed over a heated substrate. Due to the gas flow in the growth chamber, RHEED cannot be used to monitor the process, but a new method of monitoring the UV absorption line of particular alkyls has been used which gives a measurement of the concentration of precursors entering the growth chamber [6]. With due care, the GaSb/InAs samples grown at Clarendon can reach a perfect balance between the electron and hole concentrations.

5.1.2 Samples

The samples included in this study are a series of superlattices with periods of 20 to 80 layers. The thicknesses of each layer are between 80 Å and 400 Å with a total period width (combined thickness of InAs and GaSb layers) more than 150 Å. This is because anything less than 150 Å will make the sample semiconducting due to the high confinement energy. Cyclotron resonance measurements, therefore, will give nothing for the lack of carriers in the system. As I shall show later in this chapter, different combinations of

layer width will dramatically change the energy states of the system, especially those of the holes.

The linewidth of the cyclotron resonance ($\Delta B_{1/2}$) can be written as [7]

$$\Delta B_{1/2} \propto \frac{1}{\mu} \tag{5.1}$$

where μ represents the mobility. To make the resonance distinguishable, the mobility must be high enough. This can easily be achieved for the electrons but more laborious for the holes due to the higher effective masses, which shrinks the number of applicable samples further down. Table 5-1 lists all the samples that have been investigated in this chapter with carrier densities and mobilities determined by two carrier fits to the Hall resistivity [8].

Sample	GaSb/InAs Thickness (Å)	Indium Content (%)	Carrier density Electron/Hole (10^{11} cm^{-2})	e-Mobility (cm^2 V^{-1} s^{-1})	h-Mobility (cm^2 V^{-1} s^{-1})
1690	111 / 330	0	5.0 / 4.5	36000	6000
1691	108 / 303	0	5.5 / 4.0	38000	6000
1692	87 / 274	0	6.0 / 3.2	11000	3100
2058	180 / 220	0	6.7 / 6.7	54700	9500
2064	287 / 276	0	7.3 / 7.2	115000	8100
2035	90 / 110	0	3 / ?	8600	
1546	108 / 465	0	7.2 / 4.6		
1296	84 / 403	4	7.5 / 3.4	47200	2800
1269	74 / 254	10	7.5 / 7.4	72400	8800
2029	100 / 110	0	1.1 / 1.3	11000	900
1135	244 / 140	0	9 / 5.9	25500	2000
2028	180 / 220	0	5.5 / 4.3	47500	6500

Table 5-1 Structural and electrical properties of GaAs/InAs samples.

5.1.3 Experimental Setup

The setup similar to that described in Section 4.2 is used for this study. The GaAs and Ge photodetectors are employed to cover wavelengths from 40 μm to 300 μm. In addition, a nitrogen cooled $Hg_xCd_{1-x}Te$ detector, manufactured by Graseby Infrared, is used with the 10 μm based CO_2 laser output. While conducting experiments using the 10 μm

beam, extra care is taken to avoid the possible heating due to the tremendous power. The optics is disarranged slightly to cut down the power and all the optical windows between the laser and the insert are removed as well.

5.2 Semimetallic Semiconducting Transition

Due to the cross gap properties of the GaSb/InAs system, a charge transfer between the layers is expected if the confinement potential is not high enough to push the lowest subbands of electrons and holes across each other. Such a semimetallic sample is then put in a magnetic field perpendicular to the growth direction and the in-plane motions are consequently quantized to form degenerate Landau levels. The electron Landau levels

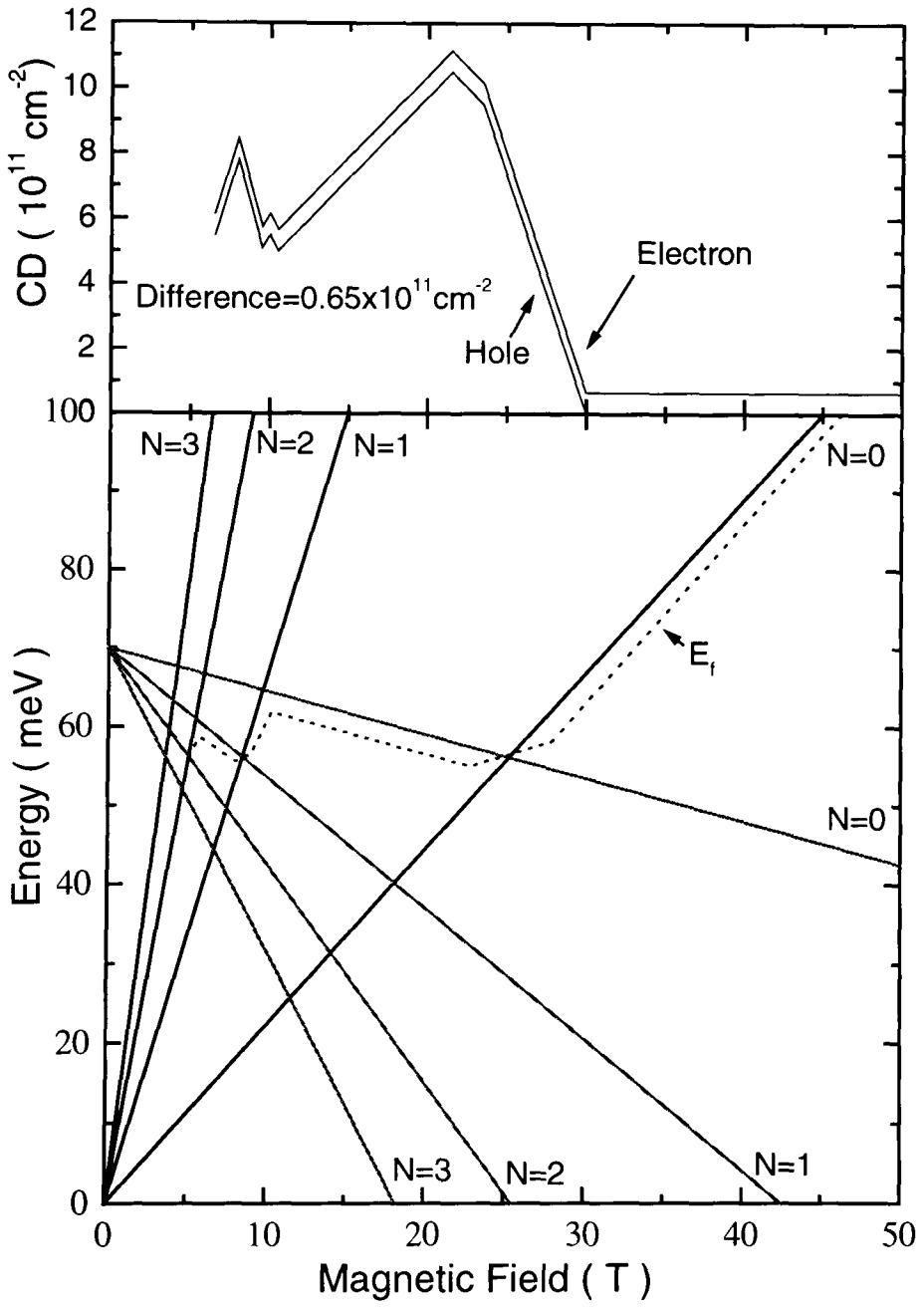

Figure 5-2 Schematic Landau fans of a semimetallic structure in magnetic fields. The upper half illustrates the corresponding carrier densities.

shift to higher energies and the hole levels move towards lower energies while the magnetic field increases. At high enough field, the electron ground state will go across the hole ground state and consequently depopulate the carriers in the system to make the sample semiconducting. This is the so-called magnetic-field-induced semimetallic-semiconducting transition [9,10].

Figure 5-2 illustrates the Landau levels of a simplified 4-band model – consisting of both spins of electron and heavy hole. A small imbalance between the electron and hole carrier densities is assumed, which is common in most of the samples grown by either MBE or MOCVD due to the interface potential between the superlattices and the substrate [6]. The spin splitting is omitted to make the diagram less complicated. Still, the contribution towards the carrier densities is included shown in the form of the little wiggles. The carrier density oscillates drastically with every electron-hole level crossing. At around 27 Tesla, where the electron ground state passes across the hole ground state, the carrier density plunges down to zero quickly leaving only the residual electron density in the system.

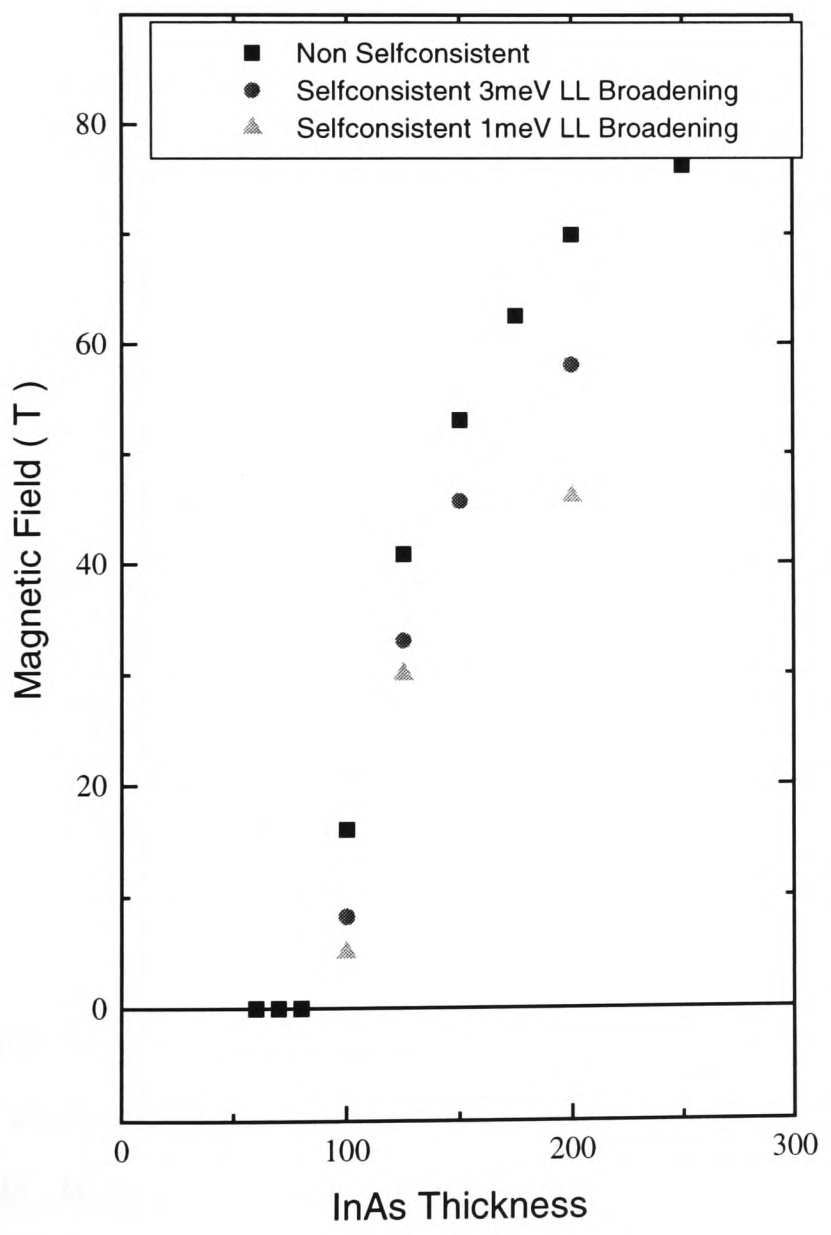

Figure 5-3 Theoretical prediction of the magnetic field induced semimetallic semiconducting transition. The thickness of the GaSb is equal to that of the InAs.

Figure 5-3 illustrates the theoretical prediction of the magnetic fields at which the transition happens. In contrast to the previous work [9], where the calculation is done non-selfconsistently, a full 8x8 ***k.p*** selfconsistent model described in Chapter 3 is employed. This gives me the benefit of assuming

one band overlap (~150meV) for all layer widths instead of guessing different values for each structure. The result presented in Figure 5-3 is based on superlattices with identical InAs and GaSb thicknesses. With period widths less than 150 Å, the superlattice would be semiconducting at zero field. Once the width passes that limit, the transition fields increase quickly with the layer thickness and the corresponding carrier densities increase accordingly. This trend, however, does not carry on indefinitely. For the longest period superlattice possible - a heterojunction, a charge transfer at zero field is expected but these carriers will push the band edge potential higher than the Fermi energy leaving only a finite region filled with charges. There is thus a maximum carrier density set for charge transfers between two layers and also a maximum semimetallic semiconducting transition field. Further investigation reveals that the "threshold" field - the maximum magnetic field to observe the semimetallic semiconducting transition in InAs/GaSb - is around 110~120 Tesla.

Figure 5-3 also shows a comparison between different theoretical calculations. The non-selfconsistent model, which excludes the contribution to electrostatic potential from the transferred charges, gives the highest transition field. This is expected since the flat bands imply more carriers are drawn into the wells. On the other hand, using the selfconsistent algorithm is not trouble free either. As indicated in Chapter 3, a slight energy difference in either the Fermi level or a Landau level will result in the population or depopulation of an entire Landau state. This can have a great influence on carrier densities under high magnetic fields. To evade this problem, a broadening of Landau levels has been introduced. This parameter smoothes out the abrupt change of the carrier density and improves the numerical stability in our calculations. Calculations with smaller broadening give lower carrier densities that oscillate more dramatically in magnetic fields. With larger broadening, carrier densities would increase but still smaller than the values given by the non-selfconsistent model. At the same time, the semimetallic semiconducting transition becomes more gradual. The non-selfconsistent model, without broadening, predicts an avalanche type of transition, which means the carrier density plunges down steeply in field. With a sensible broadening employed in the selfconsistent model, the process of transition is much smoother. This is understandable since the effect of the charges works in two ways. The electrostatic force contributed by the transferred charges is actually pushing the conduction and valence bands away from each other. As a result, the charge

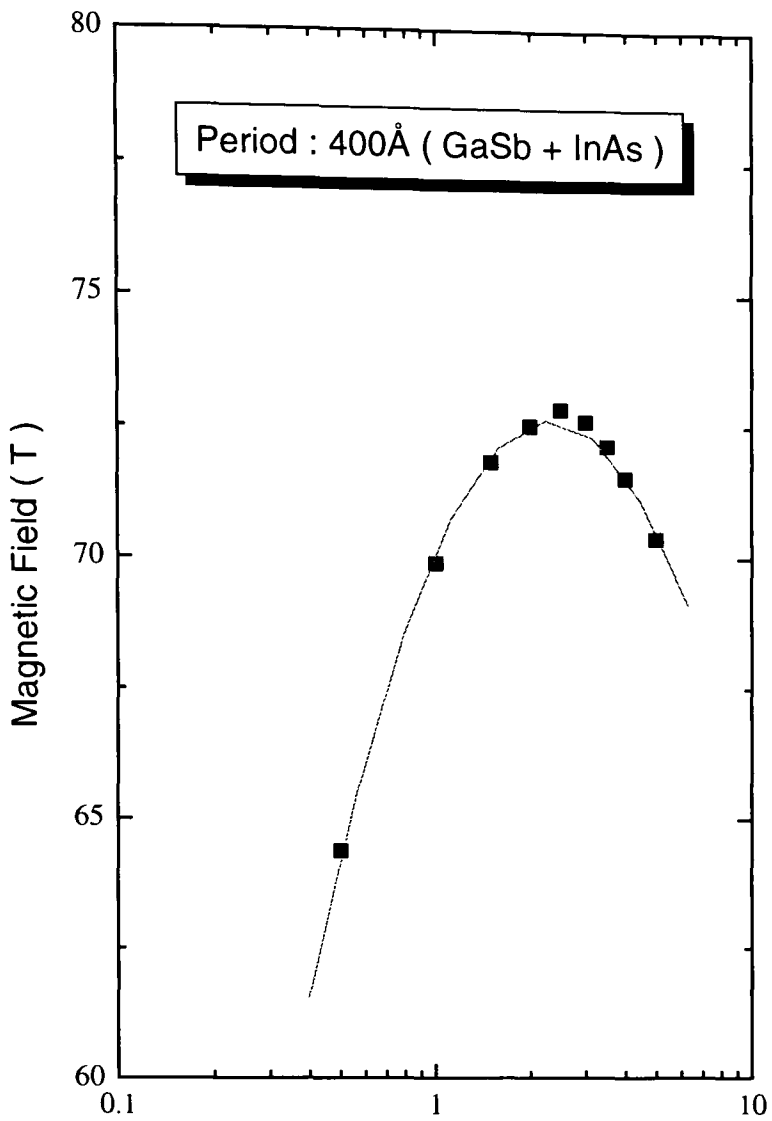

Figure 5-4 The semimetallic-semiconducting transition field with different InAs:GaSb ratio.

density drops down and the separation between bands increases again. Eventually the electron and hole ground states are pinned to each other for a certain field range instead of a clean crossing predicted by a non-selfconsistent algorithm.

Figure 5-4 shows the transition field of superlattices with a fixed period width but different ratio between InAs and GaSb. According to previous studies [11], a ratio of 2.5 gives the maximum band overlap, which is also reflected in the transition magnetic field. A parabola fits the curve nicely when the ratio is on the log scale.

Due to the high magnetic field required to investigate this phenomenon, the direct output from the CO_2 laser was used exclusively. Considering both the wavelengths it can

Sample	GaSb / InAs (Å)	Low Field CD (10^{11} cm^{-2})	90% Field (Tesla)	50% Field (Tesla)	Transition (Tesla)
2035	90 / 110	~3.5	~20.0	27.5	30.0
2029	100 / 110	~3.5	~20.0	28.0	30.5
1135	244 / 140	~5.7	~35.0	41.8	~55.0
2058	180 / 220	~7.0	42.0	~54.0	61.0

Table 5-2 Theoretical calculations of the seminmetallic semiconducting trasition fields.

give (9.2 μm to 10.8 μm) and the effective masses of the electrons, the resonance will be around 34 to 42 Tesla. Table 5-2 shows the theoretical prediction of carrier densities of the samples studied together with the transition fields. A Landau level broadening of 3meV is employed in the theoretical calculations which is later justified by experimental results. The low field carrier densities, 90 percent density fields, 50 percent density fields and the transition fields are shown in the table which offer certain information about the process of the transition.

From the table above, it is obvious that both samples 2035 and 2029 would not give any resonance in this study, which had been confirmed later by experiments. At the same time, sample 2058 is not suitable due to the high energy and fields needed. The only interesting sample will be 1135. Unlike 2058, which has short period superlattices grown on top of the substrate to block the possible interface effect, 1135 has a rather large imbalance of carrier density between electrons and holes (Table 5-1). With an electron density 50% higher than the holes', a "mutual-annihilation" type of transition is not expected. Instead, a declining strength of the cyclotron resonance is more likely.

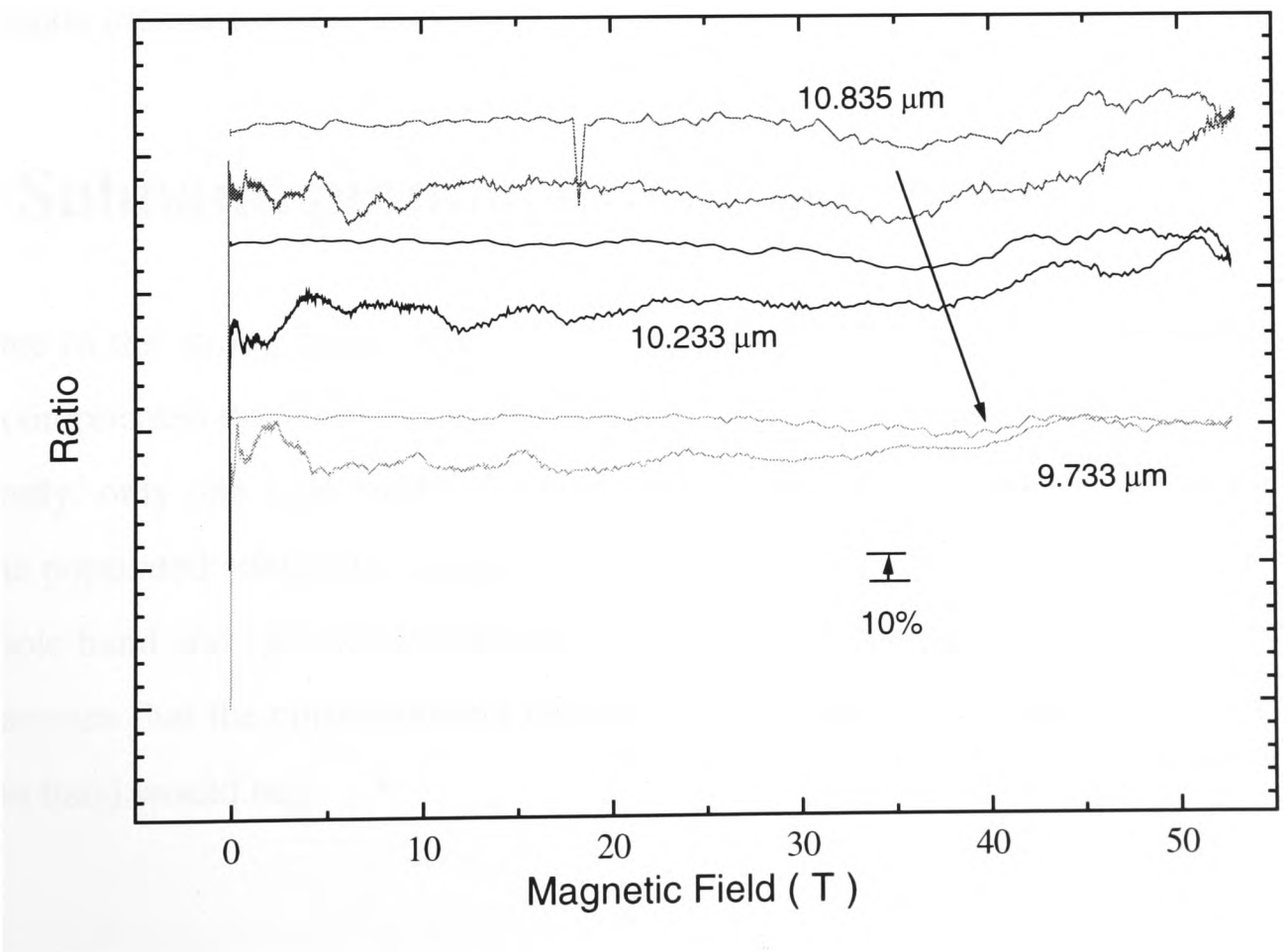

Figure 5-5 Cyclotron resonance traces of sample 1135 at high magnetic fields.

Figure 5-5 shows the cyclotron resonance traces of sample 1135. With 10.835 μm, the longest wavelength achievable with the CO_2 laser, the sample gives a resonance of 10% at 36 Tesla which corresponds to an effective mass around 0.037 m_0 - higher than the low field mass (0.034 m_0) due to the non-parabolicity. When the incident wavelength decreases to 9.733 μm, the resonance strength drops down to less than 5% and the feature is also more ambiguous. For any wavelength shorter, the resonance positions are so much weaker that they can not be identified. It must be noted that features weaker than 2~3% will not be detected due to the laser noise. In this particular sample, 3% of absorption is quite a significant figure compared to a bare 10% absorption at low field though.

Considering the imbalance between electron and hole densities, the transition observed is more abrupt than predicted by the ***k.p*** theory. However, the theoretical prediction of the transition process is highly dependant on the Landau level broadening. The broadening is determined by not only the sample temperature but also the mobility and effective mass, which means different values for electrons and holes. Due to the complicated conduction and valence band coupling in a semimetallic structure, a single parameter is used instead of two. This, of course, should be counted as one of the factors causing the deviation. Despite all, the selfconsistent algorithm does reveal its strength by giving an accurate estimate of the transition fields.

5.3 Subband pinning in Valence band

Due to the strong band mixing in the valence band, the experimental results are far more complicated than those of the conduction band. For most of the samples involved in this study, only one hole subband is populated. Magneto-transport measurements show that the populated subbands are always the lowest of the heavy hole bands since both the light hole band and spin-orbit band have a much lower energy [12]. Nevertheless, this is no guarantee that the corresponding band structure would be as simple as that of the conduction band would be.

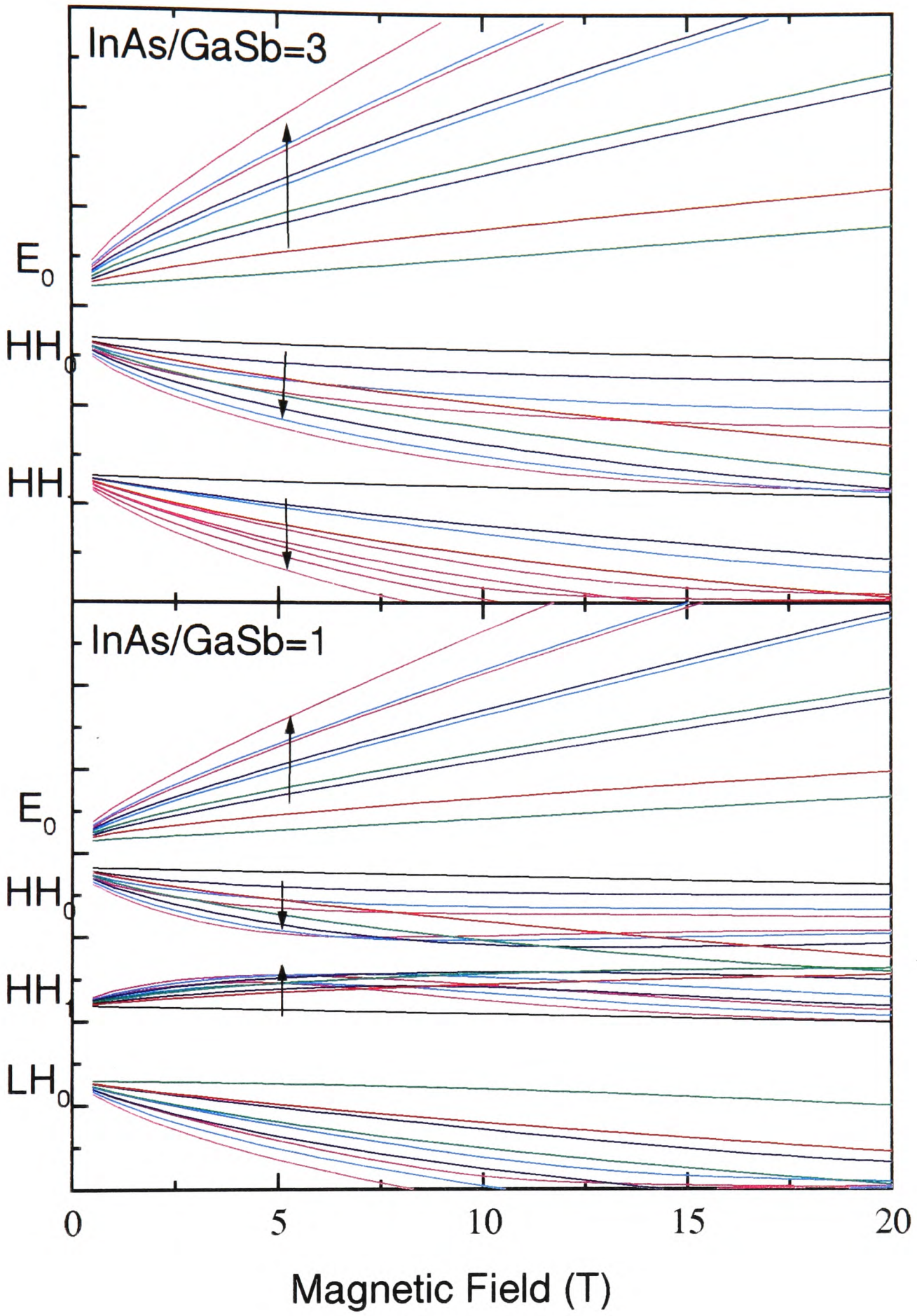

Figure 5-6 Landau fans of two structures with similar periods (120Å) but different InAs/GaSb ratio.

Figure 5-6 shows the band structures of two semiconducting superlattices with similar period width but different layer thickness ratios. I particularly choose these two ratios, InAs/GaSb=1 or 3, mainly because the samples in this study belong to either of them and also they outline the coupling effect between heavy hole subbands which I am going to

explain next. Since electron and hole carry opposite charges, one should expect the eigenenergies move up with Landau level index in the conduction band and down in the valence band. This is true for the InAs/GaSb=3 structure shown in the upper half of the figure. For the InAs/GaSb=1 structure, the first subband (HH_1) actually behaves like an electron level. The Landau levels from the two subbands even anti-cross each other at certain fields. It is believed that the strong coupling with the nearby light hole band is responsible for this phenomenon. The strength of this coupling is highly dependant on the confinement energy in heterostructures and hence the layer ratios. For a superlattice with wider InAs and narrower GaSb layers (InAs/GaSb=3), the confinement potential pushes the light hole states further away. Therefore, the heavy hole states are more likely to be composed of one single basis with conventional hole behaviour. The counter shifting of Landau levels in InAs/GaSb=1 has also been seen in GaAs/Al_xGa_{1-x}As quantum wells in the past [13]. However, due to the relatively weak valence band coupling, the "inverse behaviour" of heavy hole band only happens at higher subbands which are usually not populated and hence insignificant in experiments.

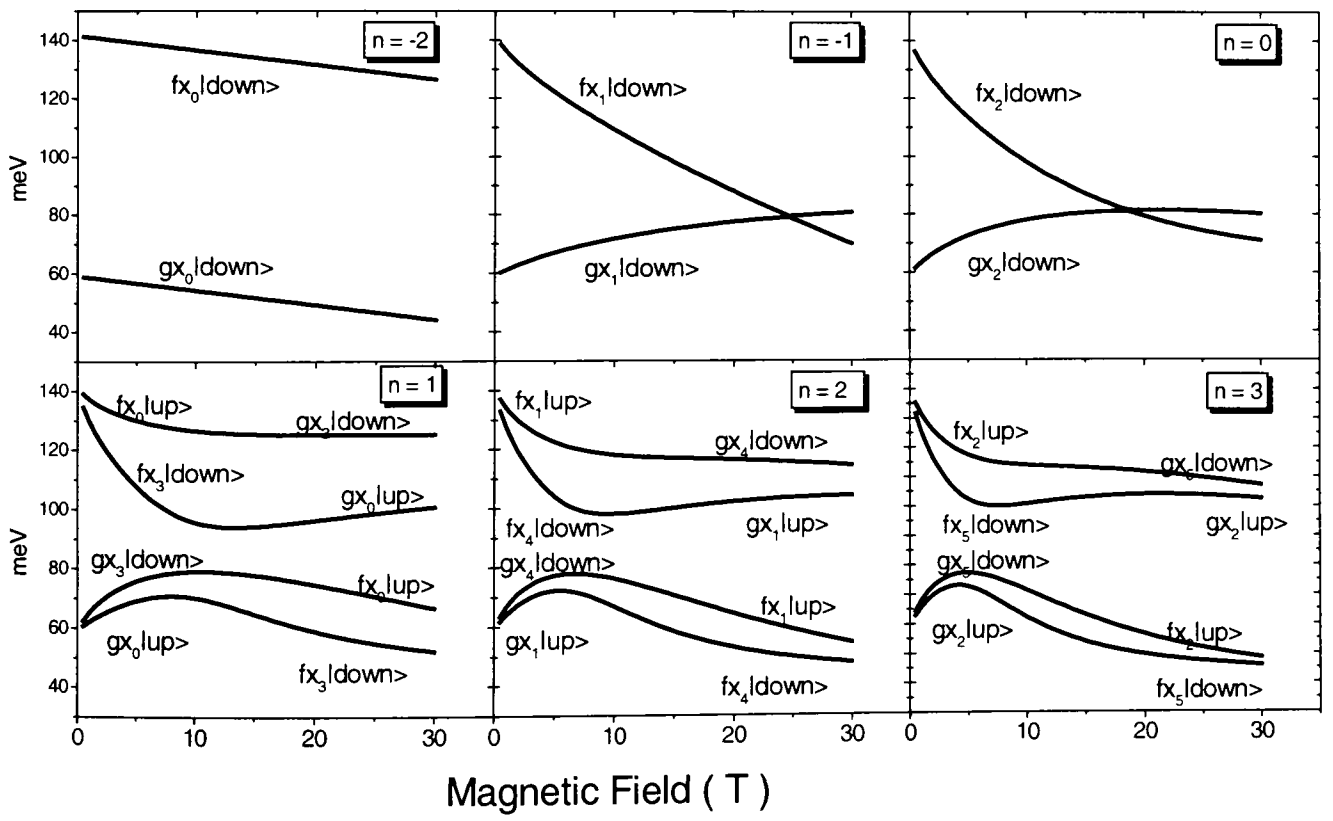

Figure 5-7 Landau fans of the top two heavy hole states ($HH_1$and HH_0), shown according to the level index with the main basis on top.

Figure 5-7 shows the Landau fans of the structure used in the lower half of Figure 5-6 with Landau level indices between -2 and 3. With an index between -2 and 0, the Landau levels from the neighbouring subbands simply go straight through each other. For all other indices, a classical anticrossing between the Landau levels can be seen. To understand this phenomenon, I propose a possible explanation based on the ***k.p*** formulation and the insight gained from the Kronig-Penney model.

From Table 3-3, the wavefunctions for n=1 can be written as

$$\left|\psi; HH_0\right\rangle^{up} = g\chi_3\left|hh\downarrow\right\rangle + g\chi_1\left|lh\uparrow\right\rangle + \underline{f\chi_0\left|hh\uparrow\right\rangle} + f\chi_2\left|lh\downarrow\right\rangle \quad \text{for } HH_0\text{, spin-up}$$

$$\left|\psi; HH_0\right\rangle^{down} = \underline{f\chi_3\left|hh\downarrow\right\rangle} + f\chi_1\left|lh\uparrow\right\rangle + g\chi_0\left|hh\uparrow\right\rangle + g\chi_2\left|lh\downarrow\right\rangle \quad \text{for } HH_0\text{, spin-down}$$

$$\left|\psi; HH_1\right\rangle^{up} = f\chi_3\left|hh\downarrow\right\rangle + f\chi_1\left|lh\uparrow\right\rangle + \underline{g\chi_0\left|hh\uparrow\right\rangle} + g\chi_2\left|lh\downarrow\right\rangle \quad \text{for } HH_1\text{, spin-up}$$

$$\left|\psi; HH_1\right\rangle^{down} = \underline{g\chi_3\left|hh\downarrow\right\rangle} + g\chi_1\left|lh\uparrow\right\rangle + f\chi_0\left|hh\uparrow\right\rangle + f\chi_2\left|lh\downarrow\right\rangle \quad \text{for } HH_1\text{, spin-down}$$

Here I only list the heavy hole and light hole bands to simplify the representation. f and g are used to label the parity of the z envelope functions: f for even and g for odd. The basis states underlined are the main contributors to each eigenstate. A closer investigation can tell us that $\left|\psi; HH_1\right\rangle^{down}$ and $\left|\psi; HH_0\right\rangle^{up}$ share the same parity for each individual component and the only difference is the relative intensity of them as $\left|\psi; HH_1\right\rangle^{up}$ and $\left|\psi; HH_0\right\rangle^{down}$. This, of course, leads to anticrossing if they ever get close enough. At the same time, one can imagine the eigenstates will swap around in energy once they are beyond the crossing magnetic field. The main basis states are marked in Figure 5-7 beside the Landau fans to show how they change.

Three conclusions can be drawn from the above statement. First, the anticrossing would only happen at $n > 0$ since it originates from the coupling between the spin-up and spin-down heavy hole states. For $n \leq 0$, the coupling is not happening because the spin-up state does not exist. This explains the crossings between two subbands in Figure 5-7. Second, one must use the language "only the lowest heavy hole subband is populated" more carefully. As I just showed, parity - a traditional signature of subband index - is highly dependent on the magnetic field. At high enough field, HH_1 can be populated

leaving HH_0 empty! Third, the critical field where the level parity changes over is not constant, but inversely proportional to the Landau level index. It offers excellent ground for the suppression of any optical transition within the field range, as I shall show in the next section.

Another question waiting to be settled is the actual condition under which the subband anticrossing may happen. It is found in a number of my calculations that the InAs/GaSb ratio alone determines whether the pinning between HH_0 and HH_1 will happen or not if the period width is between 120 Å and 500 Å. This is sensible because the confinement potential scales up equally for both heavy hole and light hole bands with fixed ratio, and, as a result, the relation between them does not change much. Previous studies [11] also indicate the similarity in band structures between different samples with the same ratio. It is therefore convincing to classify the valence band structures according to this magic number but not the period.

5.3.1 InAs/GaSb=1

Of all five samples measured with clear hole resonances, two have a similar InAs/GaSb ratio around 1 - samples 2064 and 2058. Figure 5-8 illustrates the experimental results on sample 2058. The left half shows a selection of all wavelengths measured on this sample. The longest wavelength - 300 μm - has the most dramatic change in its plasma background, agreeing with the theory presented in Section 1.5. This behaviour goes away as the incident beam moves to shorter wavelength.

A clear electron resonance is seen with a corresponding effective mass ($m^* \equiv eB/\omega_c$), introduced in Section 1.4) of 0.028 m_0 all the way to the shortest wavelength reachable by the FIR laser. Two hole resonances are observed: one with a mass of 0.15 m_0, and one with a mass of 0.25 m_0. These two resonance did not last for long: The lighter one went up to only 11 Tesla and the heavier one to 25 Tesla. Since the light hole band is too far away to be populated, the lighter hole mass cannot be due to the light holes. First observed in GaAs/$Al_xGa_{1-x}As$ system [14], the dual heavy hole resonances are attributed to

the different masses of the different spin states. The lifting of the degeneracy is believed to be a result of the inversion asymmetry.

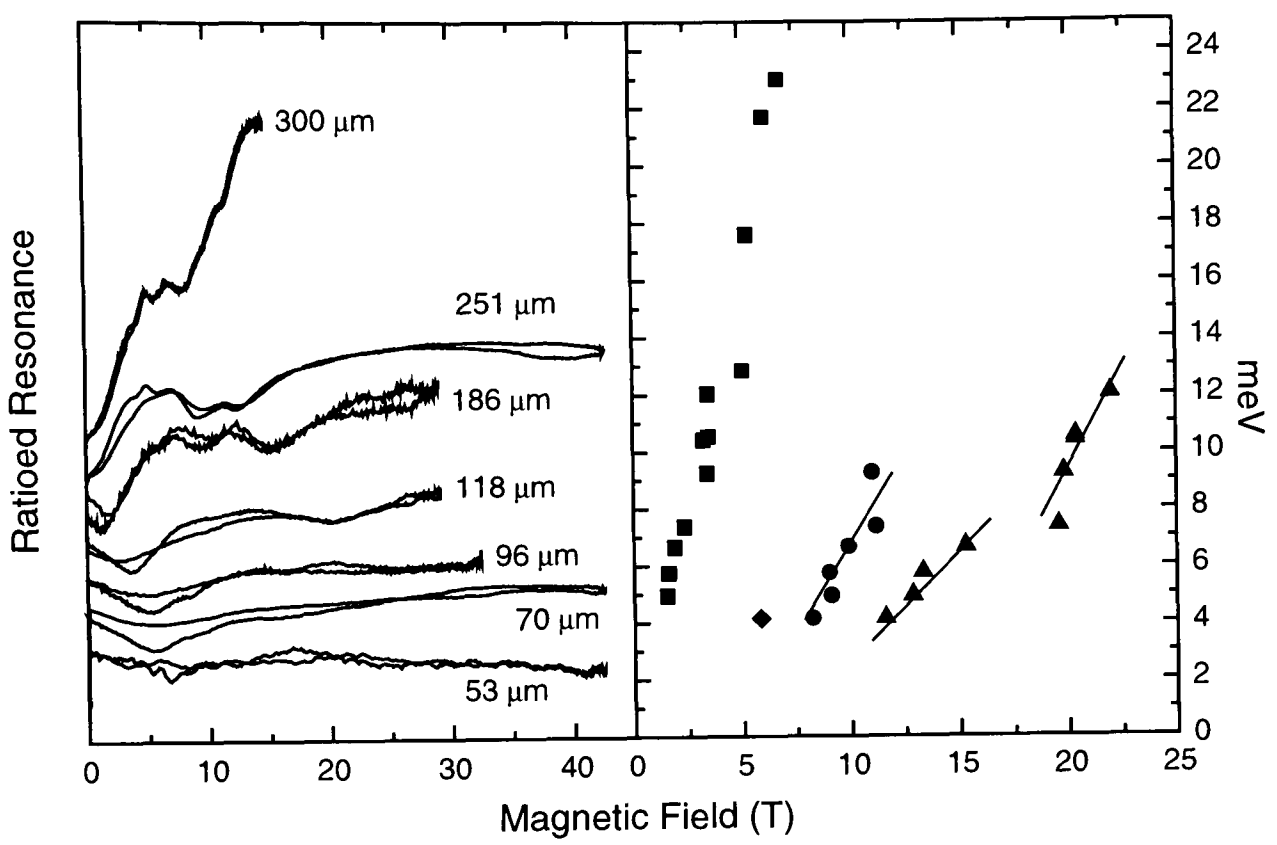

Figure 5-8 The cyclotron resonance traces of a few wavelengths measured on sample 2058 with the resonance energies vs. magnetic fields plot on the right half.

The 8 band ***k.p*** calculation of this sample is shown in Figure 5-9. Since the carrier density is sensitive to the population or depopulation of Landau levels, the calculated densities using the selfconsistent algorithm always oscillate vigorously in magnetic field and so do the eigenenergies. To show the movement of the Landau levels more clearly and to allow us to deduce the observable transitions, the levels relative to the Fermi energy are plotted in Figure 5-10, which includes only the ones that may contribute to the cyclotron resonance - a filled initial state and an empty final state. In Figure 5-10 (A), the spin-down heavy hole state (n=-2) is partly populated below 13 Tesla (assuming the Landau level broadening to be 3 meV), which means we should expect the light heavy hole resonance until then instead of the 11 Tesla from the experiments. Nevertheless, the only final state allowed (n=-1) anti-crosses with the conduction band of the same index at 12 Tesla. In other words, the eigenstates close to this field must consist of less $|hh\downarrow\rangle$, sup-

pressing any possible optical transition. The energy splitting between the initial and final states is around 10 meV at 8 Tesla, agreeing reasonably well with the lighter hole resonance measured in experiments.

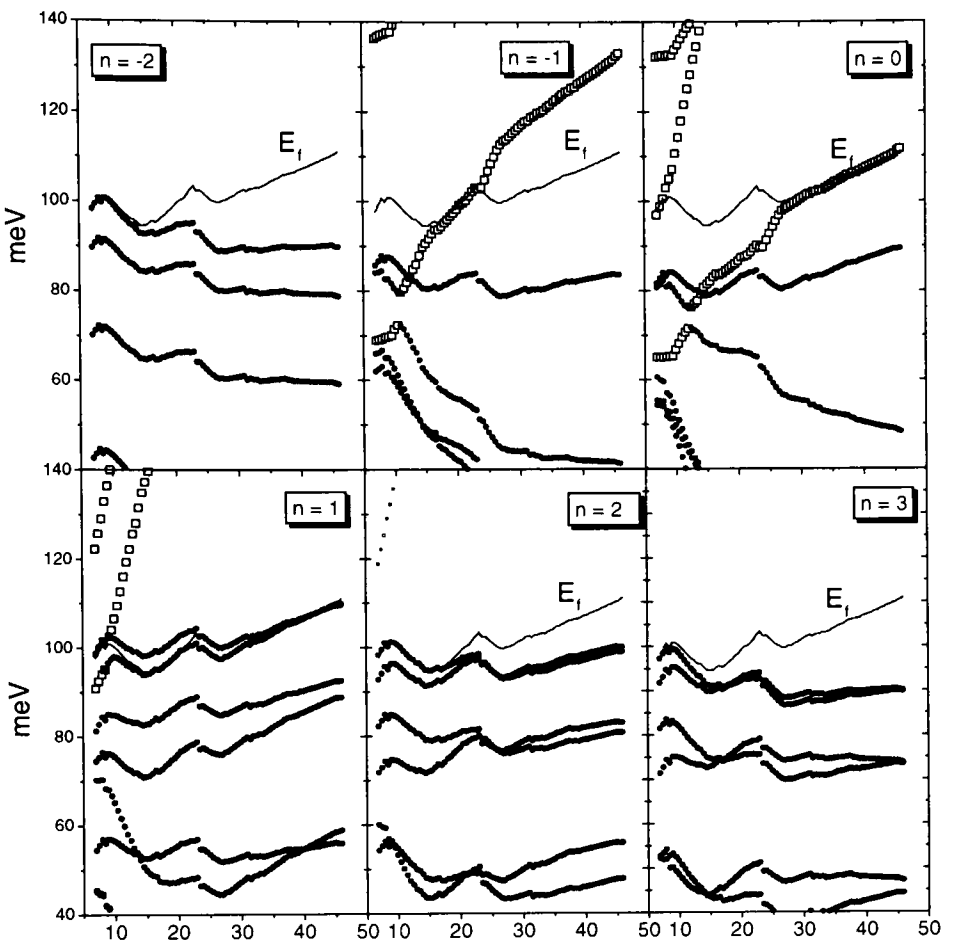

Figure 5-9 Landau fans of sample 2058 are illustared according to Landau level index. Electron and Hole states are shown by open and solid scatters, respectively, and Fermi energy in lines.

The measured heavier heavy hole resonance in Figure 5-8 reveals a slight jump in magnetic field at 17 Tesla with an energy around 6 meV. We can again find the explanation from the Landau fans in Figure 5-10. Below 17 Tesla, both the n=1 and n=2 spin-up state are fully populated (Figure 5-10 (B)), and, as a result, the conventional heavy heavy hole transition from n=1 to n=2 is forbidden. Instead, the observed transition is from a filled n=2 state to an empty n=3 state. Therefore, the discontinuity in resonance is the valence band version of the level occupancy effect observed in $GaAs/Al_xGa_{1-x}As$ [15].

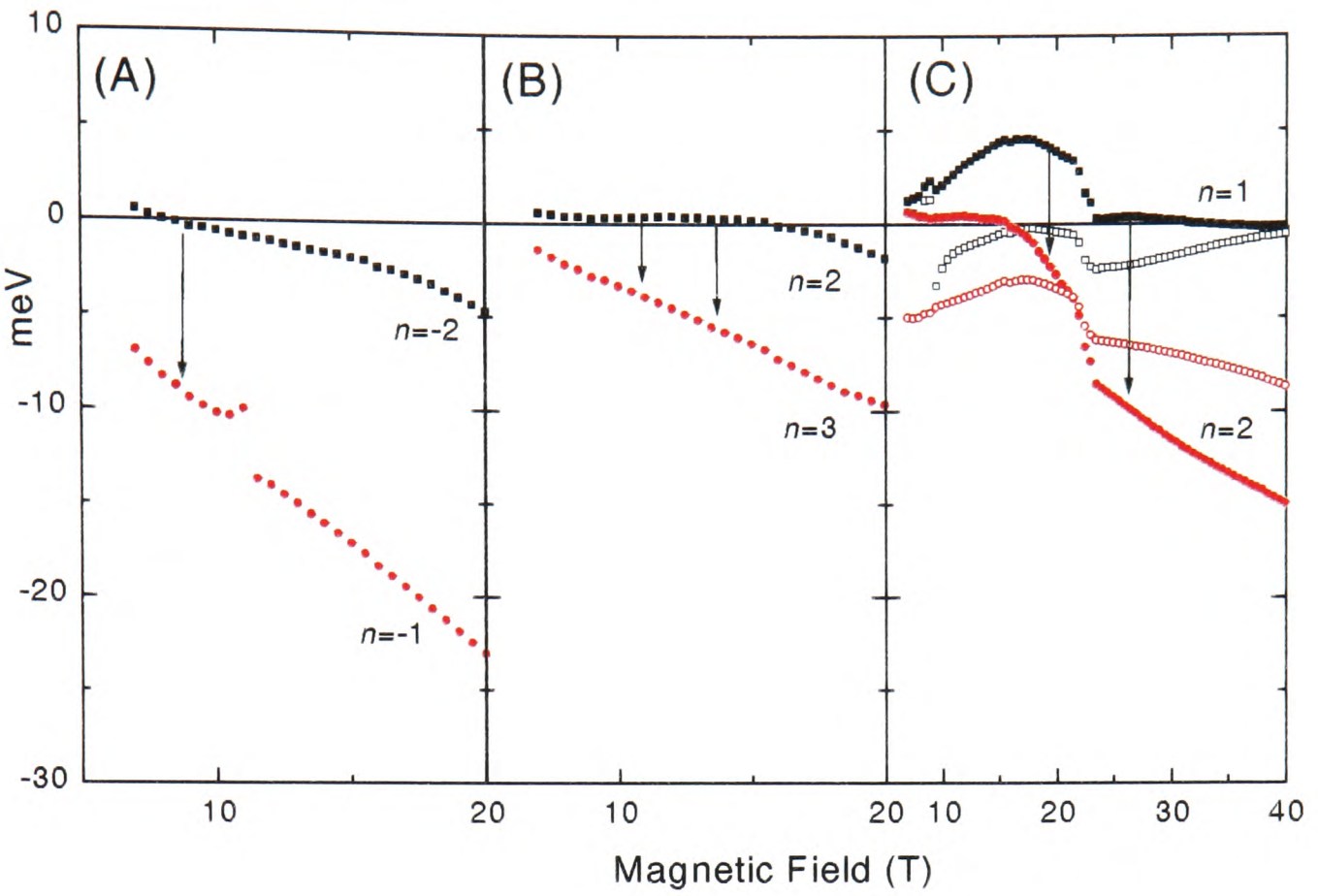

Figure 5-10 Landau fans subtracted by the Fermi energy to outline the possible transitions with initial state in black and final state in red. Arrows indicate the possible resonance between them.

Above 17 Tesla, the only populated hole state is the n=1 spin-up level (Figure 5-10 (C)) and a resonance up to the semimetallic semiconducting transition field (~60 T) should be expected. The fact that we only see a resonance below 25 Tesla must have a deeper explanation than simple level occupancy. To understand this, we dissect the eigenfunction to find out its components following the idea of subband pinning presented earlier in this section. If the Landau level swaps parity with its neighbouring subband, a suppression of the resonance is to be expected.

Figure 5-11 shows the z envelope functions of each Kane state at different magnetic fields for the initial (n=1) and final (n=2) states of cyclotron resonance. The spin-orbit states are omitted due to the relatively small contribution from them. For the heavy and light hole bands, the wavefunctions in the GaSb layer are plotted but the parts in InAs for the electron bands. From the intraband selection rules stated in Chapter 3,

$$\left|\left\langle f\left|\vec{\varepsilon}\cdot\vec{p}\right|i\right\rangle\right| \propto \sum_{m,n}^{\Gamma}\left(\int_{-\infty}^{\infty} e^{i(q_i-q_f)z}\phi_m^{f*}\phi_n^{i}\cdot dz\right)\bullet\left(\sqrt{2\hbar\omega}\left\langle LL_m\middle|LL_n+1\right\rangle\left\langle\Gamma_m\middle|\Gamma_n\right\rangle\right) \qquad (3.24)$$

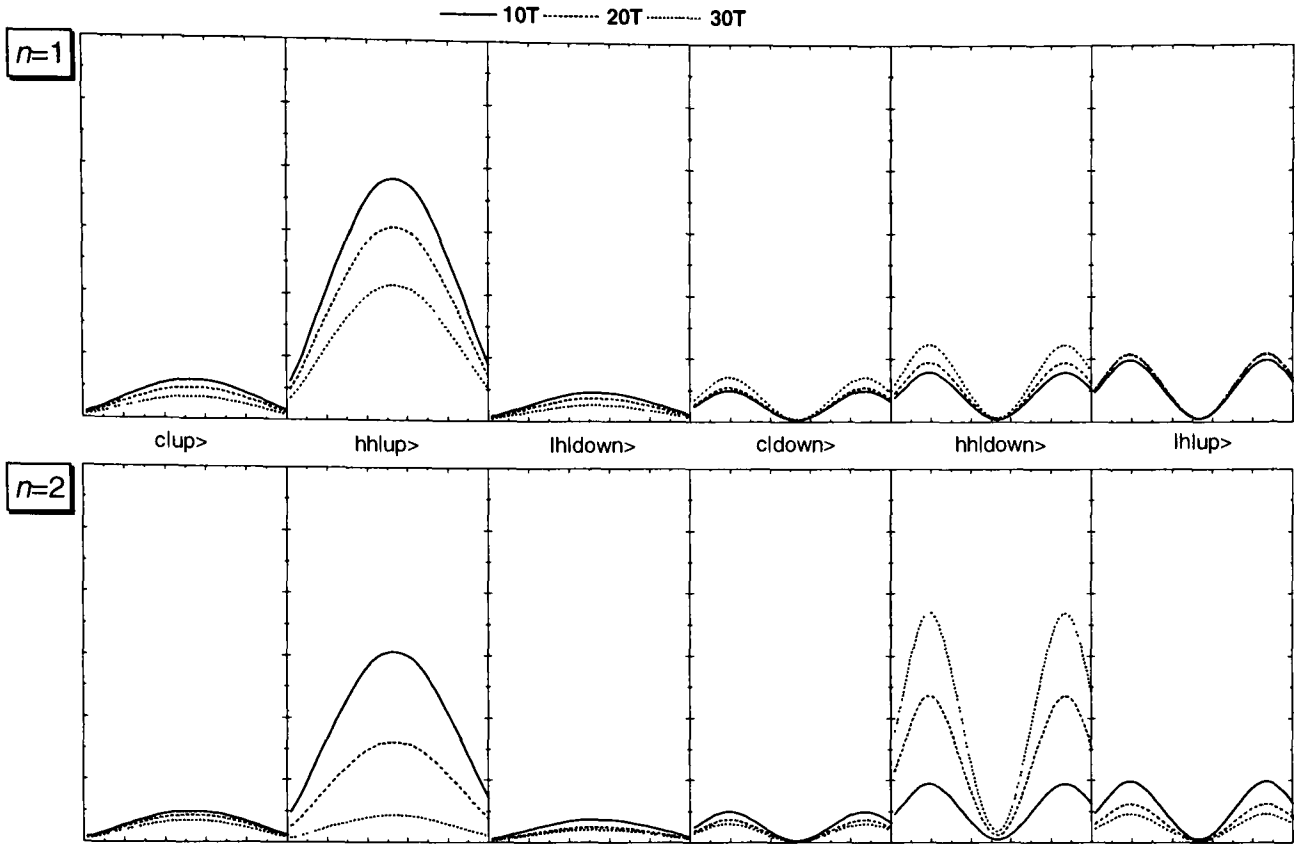

Figure 5-11 The z envelope wavefunctions of each Kane state at different magnetic fields for n=1 or 2.

cyclotron resonance requires the in-plane angular momentum shifting up or down by one quantum within the same basis states. Determining the transition probability is hence reduced to counting the overlap between the envelope wavefunctions of initial and final states.

At 10 Tesla, both the initial and final states show a comparable distribution with the $|hh\uparrow\rangle$ as the main component and consequently the overlap is large giving a clear resonance. When the magnetic field increases to 20 Tesla, the initial state does not change much but the final state turns out to be a 50:50 combination of both spins. By 30 Tesla, the n=2 final state has finished with the process of transforming itself to the spin-down state of HH_1. The wavefunction overlap decreases to only a small proportion of what it is at lower magnetic field and so does the transition rate. Therefore, the subband pinning model described at the beginning of this section suggests suppression of the heavy hole resonance at suitable magnetic fields, which is exactly what we observed in experiments. Figure 5-12 illustrates the evolution of Landau levels responsible for this transition. The

same notation used in Figure 5-7 is employed again to mark the major contributors to the eigenstates.

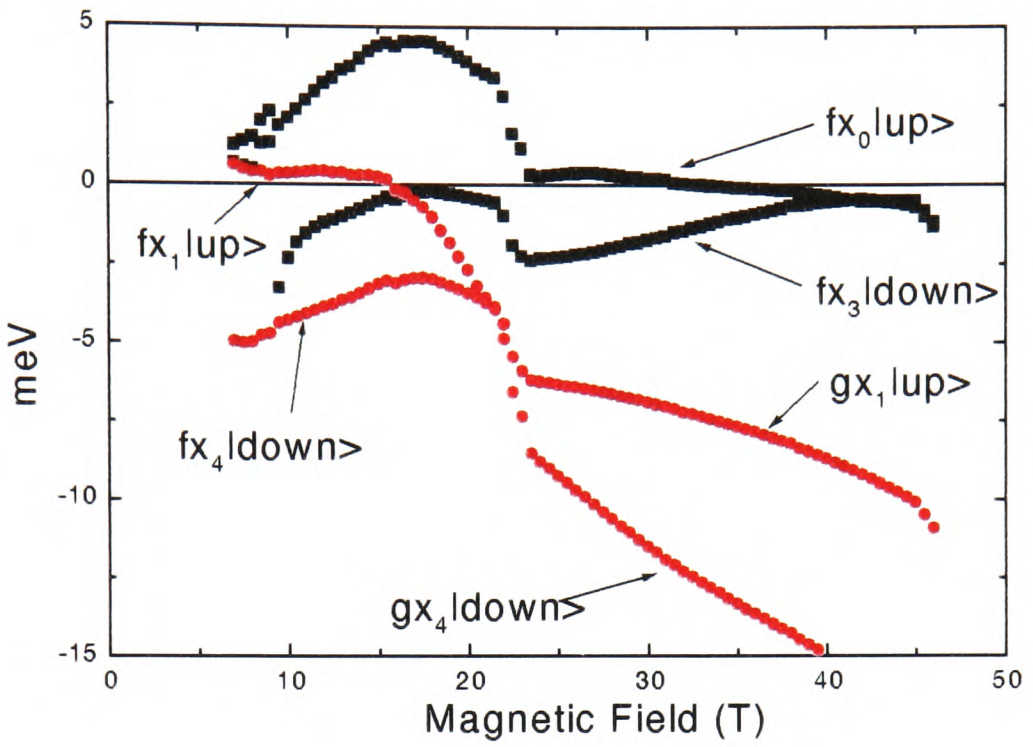

Figure 5-12 The Landau levels responsible for the heavy heavy hole resonance above 17 Tesla with notations used in Figure 5-7 to mark the main contributors towards the eigenfunctions.

As explained earlier, the InAs/GaSb=1 heavy hole subband pinning happens at different fields for different Landau levels. The suppression of transitions is only possible at the field where the final level has transformed itself from HH_0 to HH_1 but the initial level is still in HH_0. When both states have crossed the (HH_0- HH_1) coupling, a strengthening of the resonance again is predicted. We can therefore summarise the pinning effect as followed:

1) At low field, both states are in HH_0 and the cyclotron resonance is possible.
2) At mid field, one state is in HH_1 and the other one in HH_0, which results in a suppression of the resonance.
3) At high field, both states are in HH_1 and the cyclotron resonance revives.

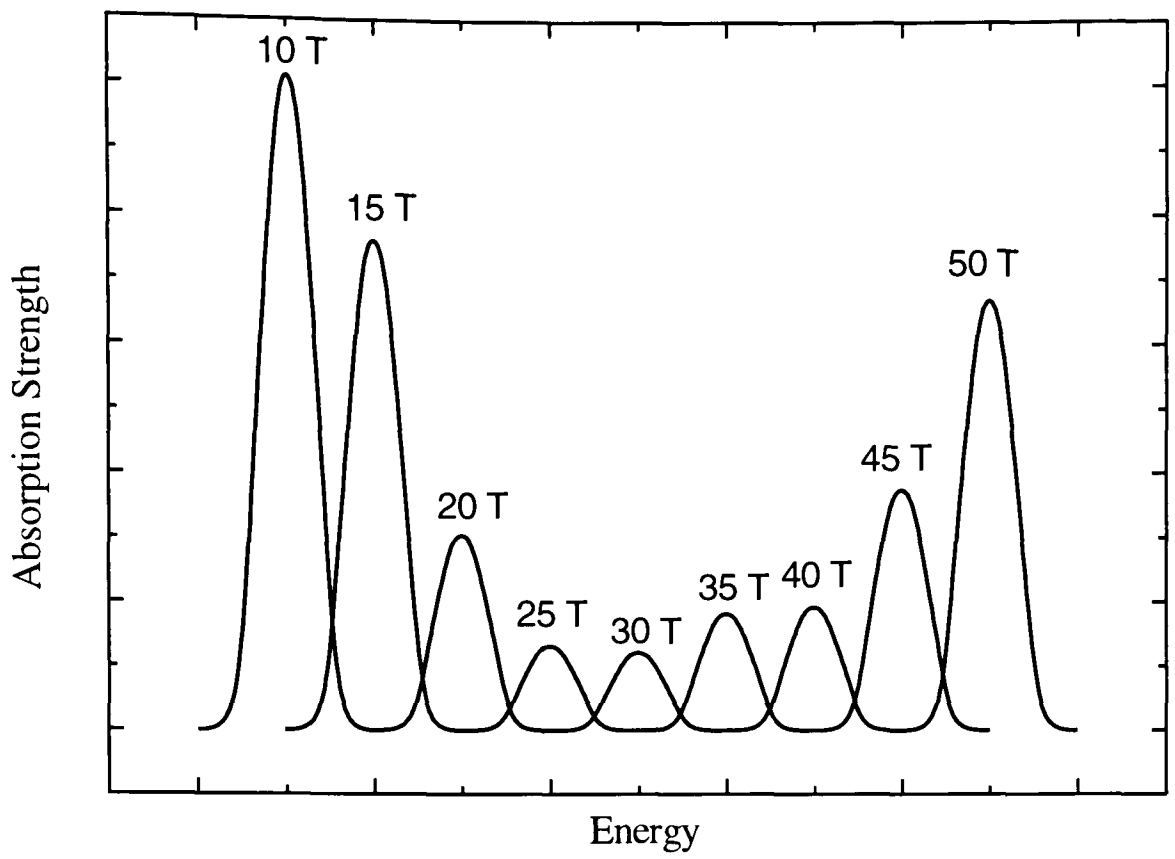

Figure 5-13 The absorption strength of sample 2058 against magnetic field, using the data obtained in Figure 5-11.

Figure 5-13 illustrates the calculated absorption strength based on the same analysis generating Figure 5-11. It shows a severe suppression of absorption between 20 and 45 Tesla. By 50 Tesla, both states have changed their parity and the absorption is allowed again. However, the magnetic field induces the semimetallic-semiconducting transition in this sample is around 65 Tesla as shown in Table 5-2 and, as a result, the resonance will never appear again. Figure 5-14 illustrates both the resonance measured in experiments and transitions extracted from the theoretical calculations explained earlier. The agreement between the two is reasonable.

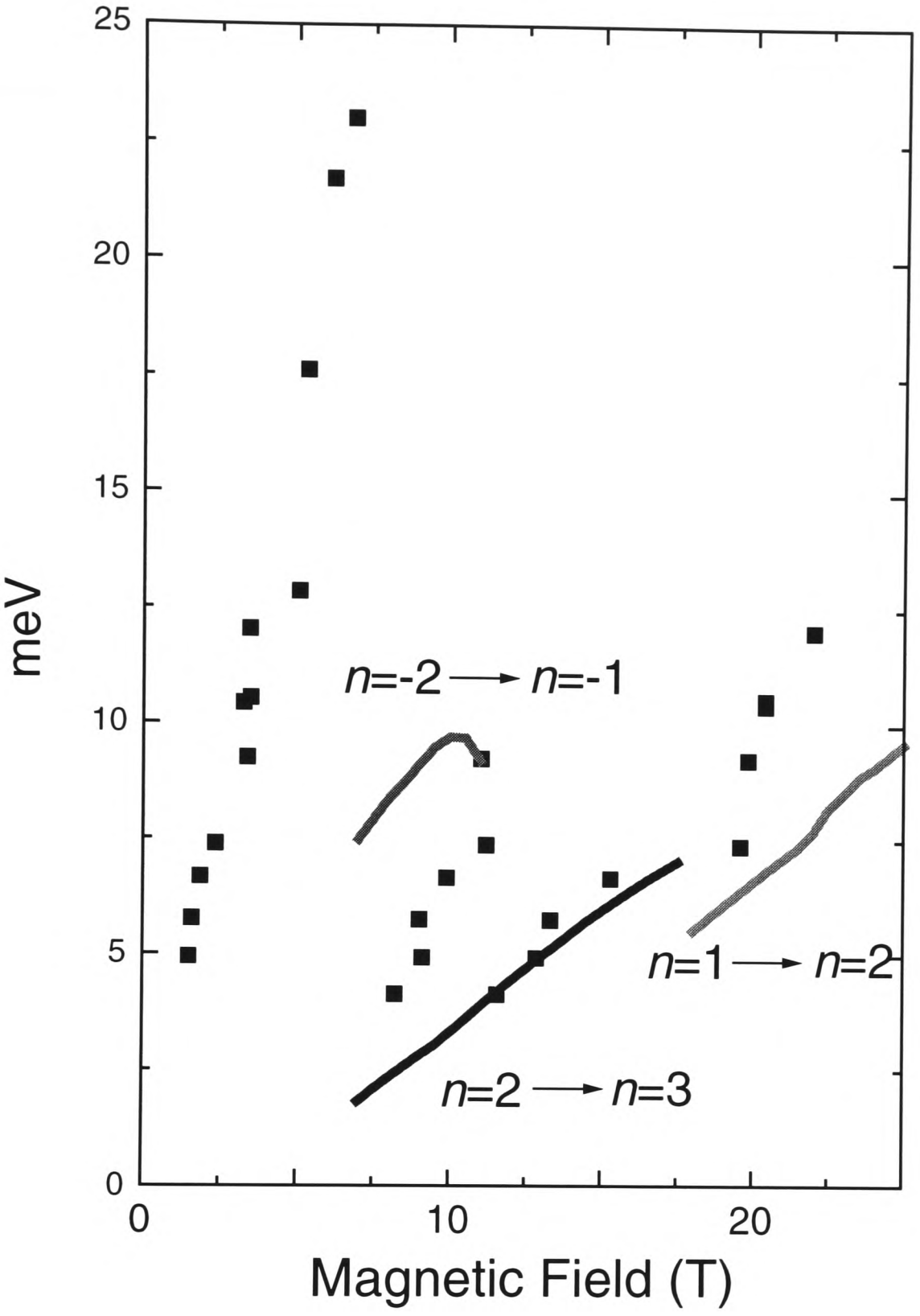

Figure 5-14 The 2058 cyclotron resonance energies together with the transitions predicted by the k.p model.

5.3.2 InAs/GaSb=3

Besides samples 2064 and 2058, which have a similar InAs/GaSb ratio around 1, the remaining three samples in this study (1690, 1691 and 1692) share an InAs/GaSb ratio of 3. The subband pinning in 2058 costs its heavy hole resonance at high magnetic fields. With a ratio of 3, the Landau levels of HH_1 are not inverted in energy at high fields and behaviour unlike 2058 is expected accordingly.

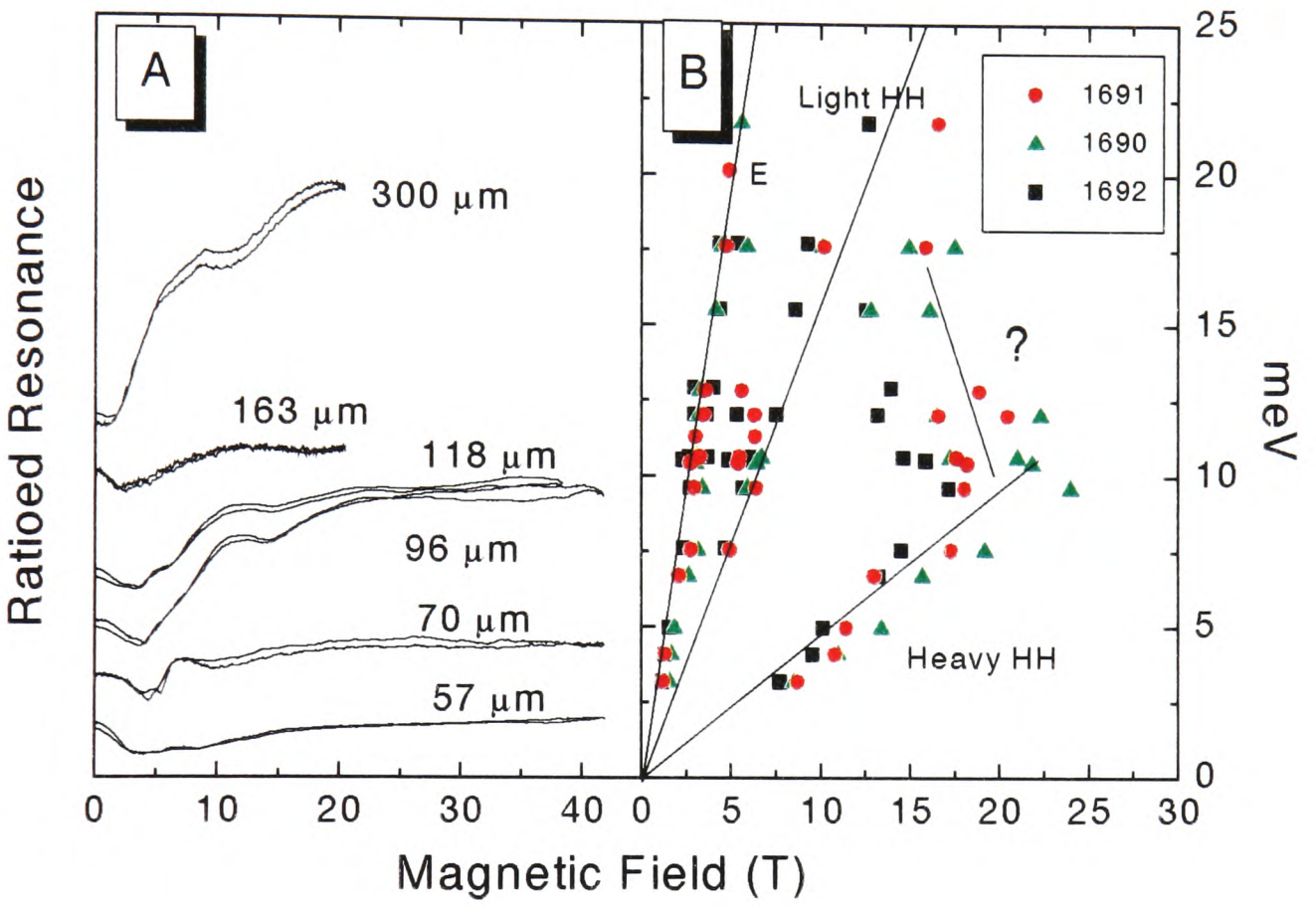

Figure 5-15 (A) The cyclotron resonance traces of a few wavelengths of sample 1692. (B) Resonance energy vs. magnetic field of samples 1690, 1691 and 1692.

Figure 5-15 illustrates the resonance energies of samples 1690, 1691 and 1692 at different magnetic fields with period widths between 340Å and 440Å. Three resonances can be seen which are electron, light heavy hole and heavy heavy hole absorptions. The electron resonance gives an effective mass around $0.03m_0$ with a slight difference between the samples due to the quantum well confinement. The light heavy hole resonance gives a mass of $0.07m_0$ between a resonance energy of 7 meV and 22.8 meV - the shortest wavelength used in this study. The heavy heavy hole resonance is observed between 2 and 10 meV with a mass of $0.22m_0$. Another group of resonances, which is non-existent in 2058,

is seen in all three samples in addition to the major three. Starting from 10 meV, the resonance field moves down with increasing energy. Both this new feature and the heavy heavy hole resonance are very sensitive to the layer width, which shows a near 30% variation between the samples.

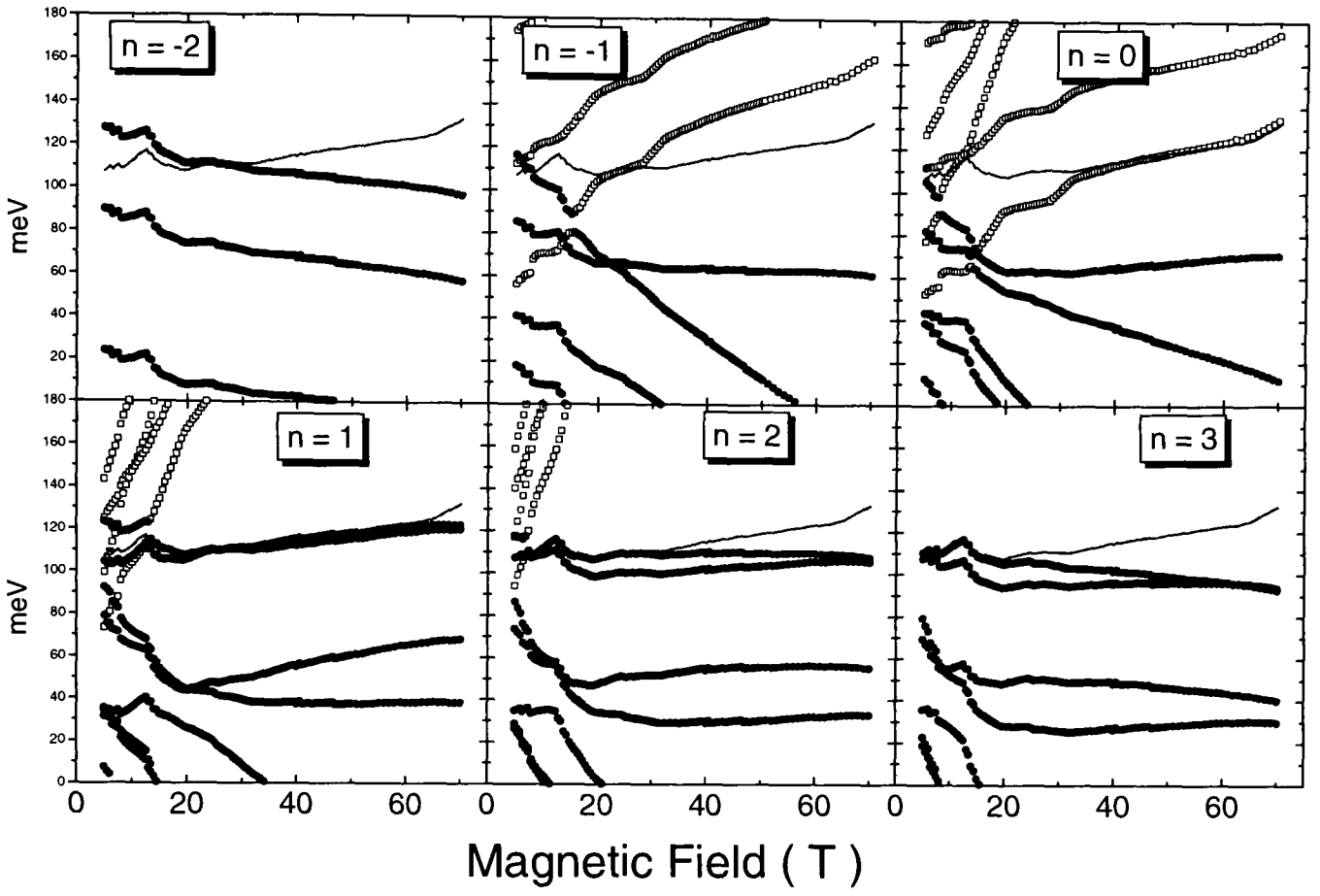

Figure 5-16 Landau fans of sample 1692 are illustrated according to their level indices. Electron and hole states are shown in open and solid scatters, respectively, with the Fermi energy in lines.

Figure 5-16 illustrates the calculated Landau levels of sample 1692 which has the shortest period of all three. In contrast to 2058, the Landau levels move to lower energy with higher index in both HH_0 and HH_1 subbands - a classical act of samples with InAs/GaSb=3. At high fields (>40 T), the HH_1 levels are bending towards HH_0. This is due to the strong coupling with the light hole band nearby - only 40 meV away at zero field - but not the pinning effect between the heavy hole subbands observed in samples with InAs/GaSb=1.

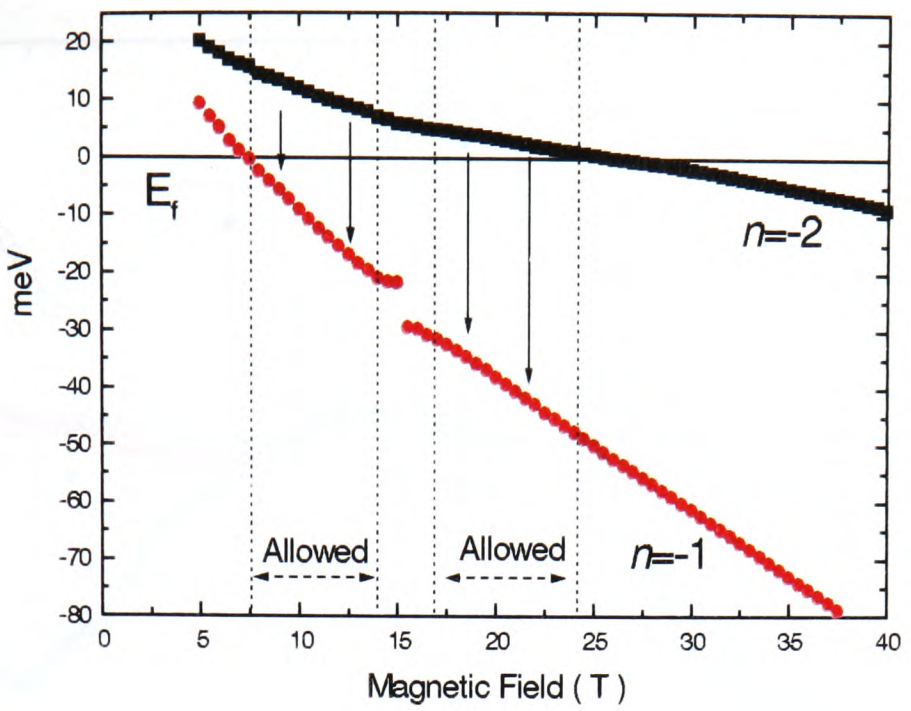

Figure 5-17 The spin down ground state which gives the light heavy hole resonance is plotted relative to Fermi energy together with its final state.

The levels responsible for the light heavy hole transition are plotted relative to the Fermi energy in Figure 5-17. The n=-2 initial state is populated until 25 Tesla, and the final state is empty above 7 Tesla. This agrees well with the experiment where the light heavy hole resonance only appears from 7 Tesla. The discontinuity in energy at 15 Tesla is a result of anticrossing with the conduction band, which predicts a suppression of resonance around that field.

Figure 5-18 illustrates the Landau fans of the particular indices responsible for the heavy heavy hole and, possibly, the new resonance. To deduce the possible resonance more easily, open and solid points are used to label the respective spin-up and spin-down states of the Landau levels. An optical transition can only happen between states with the same spin as required by the selection rules.

Figure 5-18 (B) outlines two possible transitions from both spins of n=2 levels to empty n=3 levels. The spin-down transition starts from 7 Tesla up to 15 Tesla with a maximum energy splitting of 12 meV. The spin-up transition has a shorter life, which goes only up to 12 Tesla with a much smaller splitting around 4 meV. Comparing these two transitions with the experimental results presented in Figure 5-15, the heavy heavy

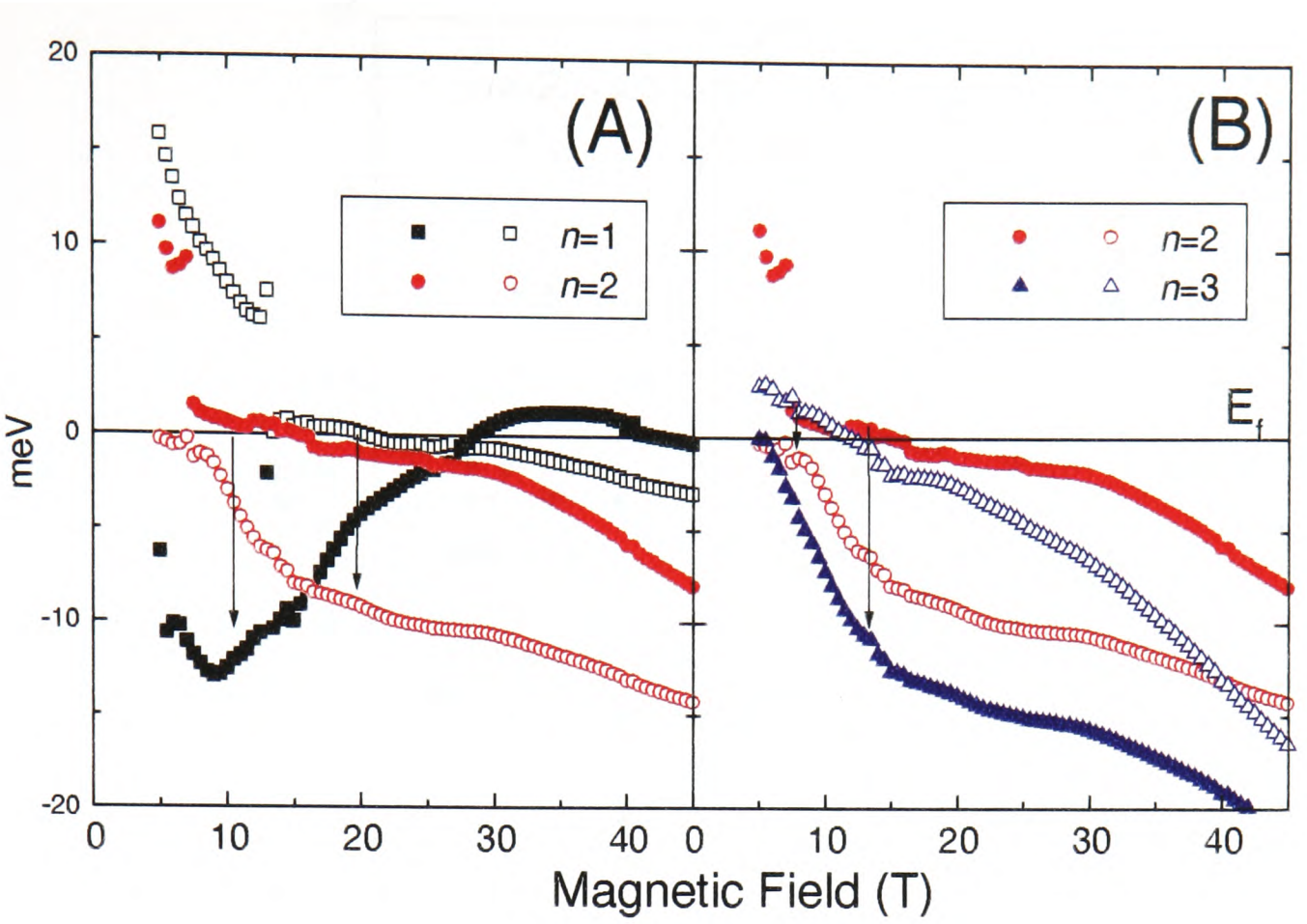

Figure 5-18 Landau fans relative to Fermi energy with different colours for different index. Arrows indicate the possible resonance between them. Solid and open points mark spin-down and spin-up states, respectively.

hole resonance is very likely contributed by the spin-down transition from n=2 to n=3. With an effective mass of 0.2 m_0 and a cut-off field of 15 Tesla, this particular transition agrees very well with the measurements. Figure 5-18 (A) illustrates another two Landau levels which are able to produce a resonance between them. Two arrows indicate the possible optical transitions from filled states to empty states. The left arrow which marks the transition from the spin-down n=2 state to the n=1 state is particularly eye-catching. The energy splitting at 10 Tesla is around 14 meV and decreases with magnetic field to 10 meV at 15 Tesla, where the n=1 state is depopulated. The new resonance is therefore described nicely by this transition! The right arrow marks another possible resonance between the spin-up states. It is, however, not detectable due to the fact that the energy splitting between the initial (n=1) and final (n=2) states does not change much with fields. As the experimental setup uses fixed energy and swept field, a magnetic field independent feature can not be observed.

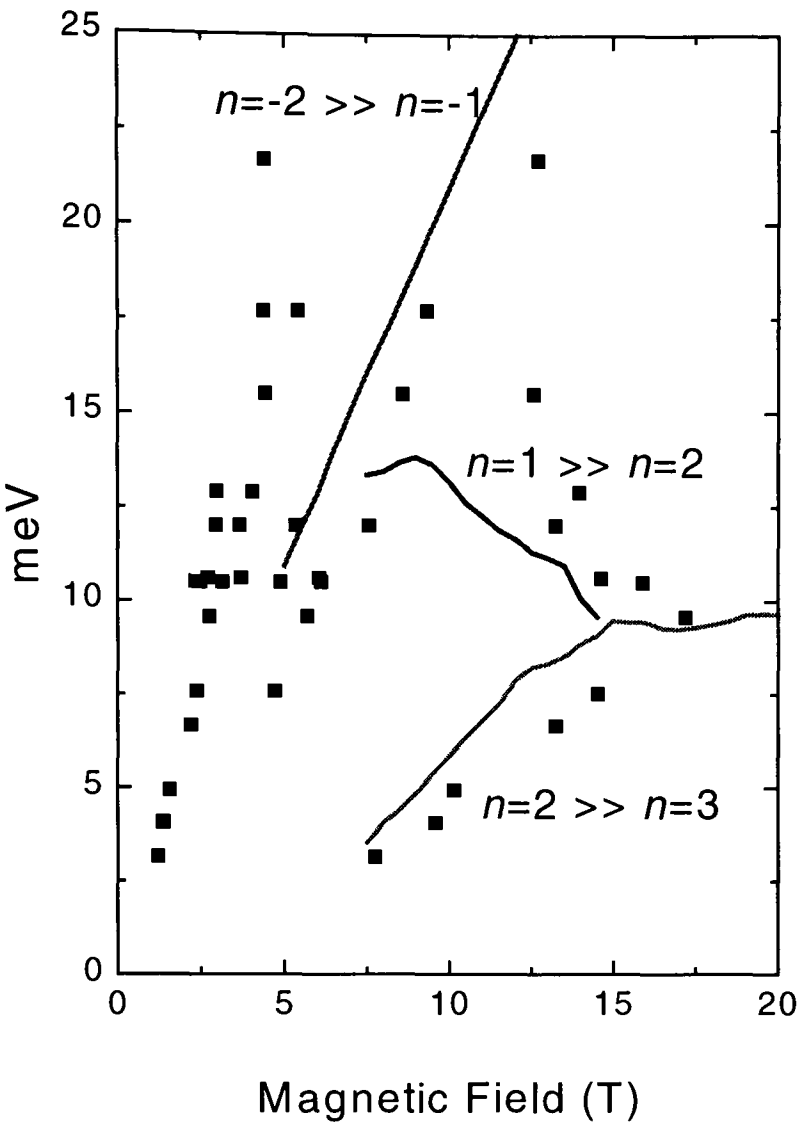

Figure 5-19 The 1692 cyclotron resonance energies together with the transitions predicted by the *k.p* model.

The cyclotron resonance energies of sample 1692 together with its calculated transitions are plotted in Figure 5-19. The theoretical calculation generally agrees with the experiments quantitatively. Moreover, the inverse new resonance between 8 Tesla and 15 Tesla behaves exactly as we expected. In addition to the 1692 modelling, more ***k.p*** calculations have been done to model the two samples with wider periods - 1690 and 1691. Their general behaviours are similar to the 1692 calculation but with different energies. We therefore conclude their experimental results can be understood using the same ideas explained above.

5.4 Conclusion

A series of semimetallic GaSb/InAs superlattices have been studied by cyclotron resonance up to 45 Tesla. The magnetic-field-induced transition between the semimetallic

and semiconducting regimes is observed. A detailed ***k.p*** calculation agrees well with the transition fields measured in experiments.

The hole resonance is extremely complicated due to the strong light hole band coupling in the system. It is found by theoretical ***k.p*** calculations that the valence band structures depend on the layer width ratio between InAs and GaSb almost entirely. With InAs/GaSb=1, the lowest two subbands (HH_0 and HH_1) couple strongly with each other, which can leads to anticrossings of Landau levels between them. A detailed model predicts a suppression of hole resonance at high fields, which is confirmed by experiments. For samples with InAs/GaSb ratio of 3, a new resonance that shifts to lower energy with increasing magnetic field is observed. It is suggested this resonance is contributed by a rather unusual transition from an n=2 state to an n=1 state. Owing to the complex valence band structure in InAs/GaSb, it is advisable to do complete modelling for every sample in order to understand the origin of each individual hole resonance although a certain relation between the band structure and layer thickness ratio has already been established.

References

[1] L. Esaki and L. L. Chang, *J. Magn. Mat.* **11,** 208 (1979).

[2] L. L. Chang, N. Kawai, G. A. Sai-Halasz, R. Ludeke and L. Esaki, *Appl. Phys. Lett.* **35**, 939 (1980).

[3] M. S. Daly, K. S. H. Dalton, M. Lakrimi, N. J. Mason, R. J. Nicholas, M. van der Burgt, P. J. Walker, D. K. Maude and J. C. Portal, *Phys. Rev. B* **53,** R10524 (1996).

[4] J.-P. Cheng, J. Kono, B. D. McCombe, I. Lo, W. C. Mitchel and C. E. Stutz, *Phys. Rev. Lett.* **74,** 450 (1995).

[5] P. Voisin, Y. Guldner, J. P. Vieren, M. Voos, C. Benoit, N. J. Kawai, L. L. Chang and L. Esaki, *J. Phys. Soc. Japan* **49**, Suppl. A 1005 (1980).

[6] N. J. Mason, *Atomic Layer Epitaxy*, edited by T. Suntola and M. Simpson, Blakie (1990).

[7] G. M. Summers, *D. Phil. Thesis,* Oxford (1993).

[8] C. Kittel, *Introduction to Solid State Physics*, 6th edition, John Wiley & Sons, New York (1989).

[9] D. J. Barnes, R. J. Nicholas, R. J. Warberton, N. J. Mason , P. J. Walker and N. Miura, *Phys. Rev. B* **49,** 10474 (1994).

[10] N. J. Kawai, L. L. Chang, G. A. Sai-Halasz, C. A. Chang and L. Esaki, *Appl. Phys. Lett.* **36**, 369 (1992).

[11] T.A. Vaughan, *D. Phil. Thesis,* Oxford (1995).

[12] D. M. Symons, *D. Phil. Thesis,* Oxford (1994).

[13] S. L. Wong, *D. Phil. Thesis,* Oxford (1993).

[14] H. L. Stormer, Z. Schlesinger, A. Chang, D. C. Tsui, A. C. Gossard and W. Wiegmann, *Phys. Rev. Lett.* **51,** 126 (1983).

[15] U. Ekenberg and M. Altarelli, *Phys. Rev. B* **32,** 3712 (1985).

6. Far Infrared Modulated Photoluminescence Study of $GaAs/Al_xGa_{1-x}As$ Heterostructures

6.1 Introduction

The integer and fractional quantum hall effects (IQHE & FQHE) have been the focus of numerous researches since the 1980's [1,2]. The experimental investigations started from magneto-transport measurements in two dimensional systems with only electrons [3] and moved to GaSb/InAs systems with both electrons and holes [4]. The nature of magneto-transport results depends on the interplay between two interacting effects, the disorder potential and electron-electron interactions [5]. Recently, there has been intense interest in the photoluminescence properties of the two-dimensional electron systems (2DES) as a function of the occupancy of Landau levels [6-8] since the spectra of radiative recombination between the 2DES and photo-excited holes are sensitive probes of correlation in the electron ground states [9].

In this chapter, photoluminescence measurements on a series of GaAs/$Al_xGa_{1-x}As$ heterostructures with different electron concentrations at steady magnetic field of up to 11 Tesla have been done. The filling factor (ν) and 2DES density dependent spectra are commented upon. In addition, far infrared radiation is applied to give a further perturbation to this highly correlated system.

6.1.1 Excitonic Effect

The single particle model has been used so far concerning cyclotron resonance experiments. Photo-excitation on intrinsic samples creates pairs of electrons and holes which leads to a Coulombic interaction between them. This produces a spatial correlation which we refer to as the excitonic effect [10]. Using a hydrogen model in three dimensions, we can easily get an expression for the binding energies of excitation states

$$E_n^{3D} = -\frac{\mu e^4}{32\hbar^2\pi^2\varepsilon^2}\frac{1}{n^2} \tag{6.1}$$

where μ is the reduced mass of electron-hole pairs - excitons, and n corresponds to the hydrogenic series of the exciton. The corresponding Bohr radius is

$$a^{3D} = \frac{\varepsilon\hbar^2}{\mu e^2} \tag{6.2}$$

which is the radius of 1s binding. The bulk binding energy - E_1 - for GaAs is 4.2 meV with an exciton radius around 130 Å. A similar analysis for two-dimensional exciton states generates an equivalent set of eigenvalues,

$$E_n^{2D} = -\frac{\mu e^4}{32\hbar^2\pi^2\varepsilon^2}\frac{1}{(n+\frac{1}{2})^2} \tag{6.3}$$

By restricting the excitonic degrees of freedom, the two-dimensional binding energy is increased by a factor of four from the three-dimensional binding energy. Similarly, the two-dimensional 1s exciton radius is half the three-dimensional case.

In an applied magnetic field, each individual electronic state evolves into a series of Landau levels as shown previously. When excitonic interactions are included, however, the eigenenergy of the system becomes considerably more complex, particularly when effects of quantum confinement and valence band states are taken into account. This subject has been the focus of many theoretical studies. There is, however, no exactly soluble theoretical model which can be applied to arbitrary exciton states in arbitrary magnetic field [11]. Qualitatively, we can describe the system by applying two confinements – the magnetic field and the Coulomb interaction between the electron and hole pair. At low fields, the free carrier cyclotron energy is smaller than the exciton binding energy and the cyclotron radius is larger than the exciton radius. The applied field

is hence considered as a perturbation of an otherwise Coulomb force dominated system. At high magnetic fields, the situation is exactly the other way round. As shown in Figure 6-1, the combined magneto-exciton states are parabolic at low field and turn into Landau levels with increasing field.

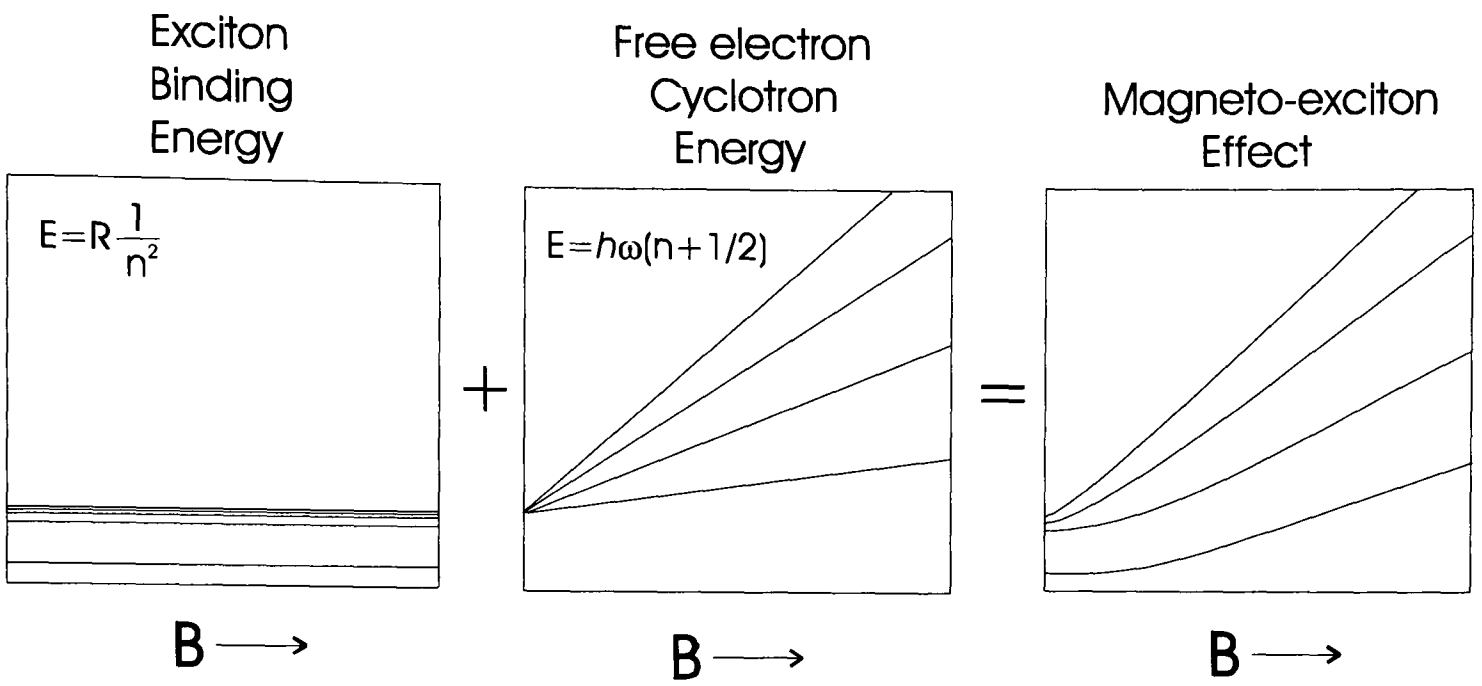

Figure 6-1 Illustrated diagram of the magneto-exciton effect.

Since the above model is a direct extrapolation of the hydrogen atomic model, it only applies to system consisting of only one electron and hole pair. In a system with high carrier density, it is obvious that the carrier sea would screen the Coulomb interaction and prevent an electron from binding with a hole.

6.1.2 Samples

Samples measured in this study are a series of ultra-high-mobility GaAs/$Al_xGa_{1-x}As$ heterojunctions grown by MBE at Philips Research Laboratory by C. T. Foxon and J. J. Harris. The Al fraction x was kept at 33±1%, keeping the barrier height constant about 330 meV. Figure 6-2 shows the growth profile of these samples.

The GaAs substrates are followed by a 50Å period GaAs/$Al_xGa_{1-x}As$ superlattice to trap any residual impurities, principally carbon. 5100 Å of GaAs is grown on top of the superlattice followed by an $Al_xGa_{1-x}As$ spacer layer. Then a lightly doped region of $Al_xGa_{1-x}As$ spread over 2000 Å is grown on top of the spacer layer. The low doping level helps reduce the remote impurity scattering in the sample. Due to the spatial separation

between the 2DES and the dopants, an ultra high mobility can be achieved of up to $4.6x10^6$ $cm^2V^{-1}s^{-1}$ at 4K. Experiments show that the 2DES carrier density is dependent on the thickness of the spacer layers. Spacer layers of 3200 Å and upwards produce insulating samples, however, photo-luminescence can still be measured. Table 6-1 summarizes the properties of all the samples employed in this study.

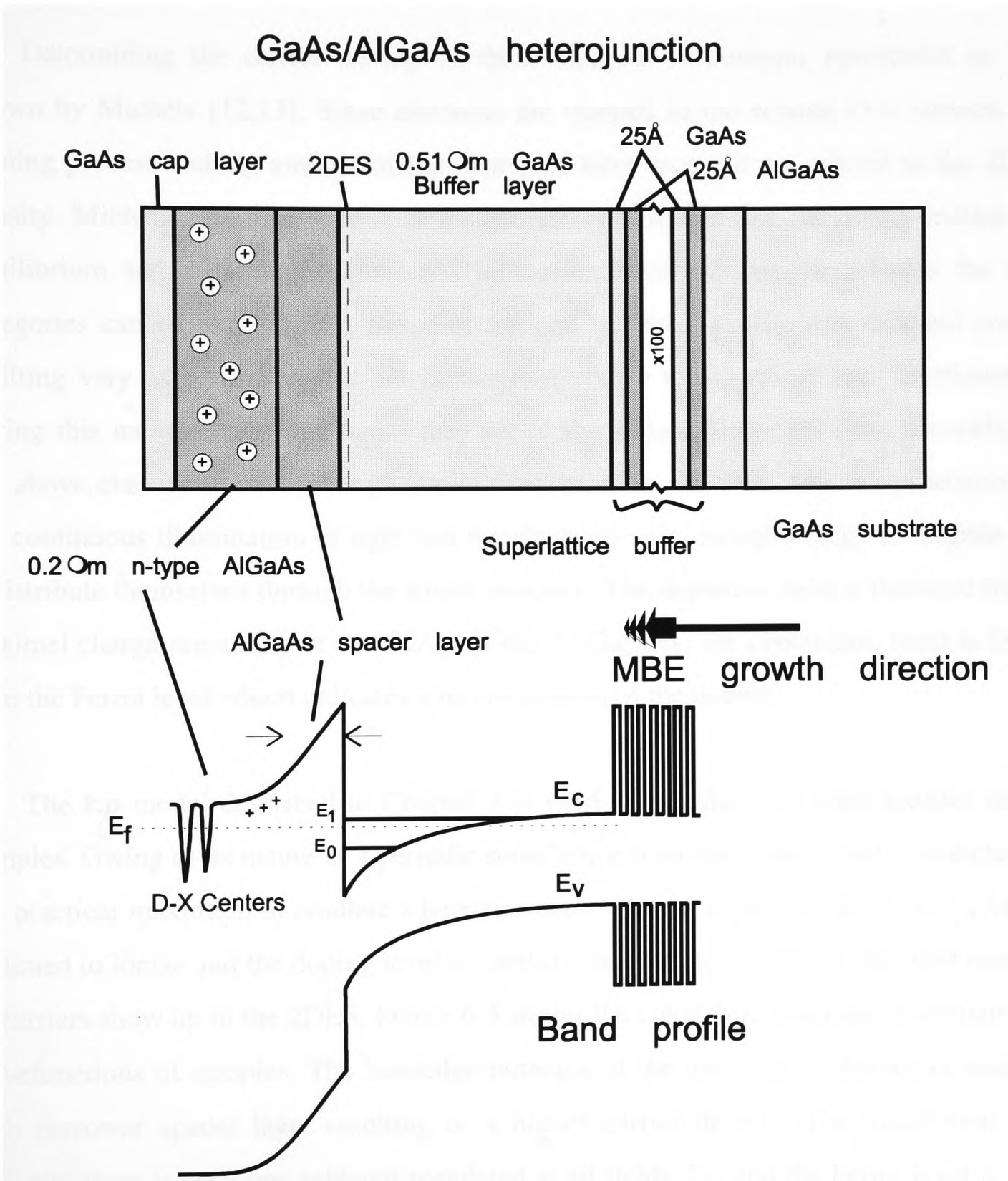

Figure 6-2 Growth profile and resulting band profile of the high mobility GaAs/AlGaAs heterojunctions used in this study.

Table 6-1 List of samples investigated in this study.

Sample number	G650	G640	G646
Spacer Layer (Å)	400	1200	2400
Carrier density (cm^{-2})	$2.26x10^{11}$	$1.17x10^{11}$	$7.0x10^{10}$

Determining the carrier density of these samples is however non-trivial as was shown by Michels [12,13]. Since electrons are trapped in the remote D-X centers, the cooling process and the amount of light samples have received are critical to the 2DES density. Michels classifies it in four categories: non-illuminated, saturated, metastable equilibrium and dynamic equilibrium. The carrier density difference between the four categories can be as high as a factor of ten and the band profile and subband energy splitting vary as well. Samples are illuminated with a low level of laser continuously during this measurement and hence they are in the metastable equilibrium according to the above classification. In this particular configuration, the D-X centers are ionized by the continuous illumination of light and the electrons gain enough energy to migrate and redistribute themselves through the whole structure. The depletion field is flattened by the minimal charge remaining in the GaAs. In the $Al_xGa_{1-x}As$, the conduction band is lower than the Fermi level which indicates a full ionization of the donors.

The ***k.p*** model described in Chapter 3 is used to calculate the band profiles of the samples. Owing to its nature as a periodic superlattice treatment, the period is stretched to the practical maximum to emulate a heterojunction. All the donors in the $Al_xGa_{1-x}As$ are assumed to ionize and the doping level is carefully selected to make sure the right number of carriers show up in the 2DES. Figure 6-3 shows the calculated bandedge potentials and wavefunctions of samples. The bandedge potential at the interface is sharper in samples with narrower spacer layer resulting in a higher carrier density. The calculation also indicates there is only one subband populated at all fields, E_0, and the Fermi level is very close to the E_1 subband at zero field. Our results are in good agreement with those obtained by Michels [13], which involve solving a Poisson equation. One major concern about the validity of my calculations is the application of magnetic field. Since Landau levels cross the Fermi energy with increasing field, one might expect certain number of electrons transferring back and forth between the 2DES and the doping layer. A wider

$Al_xGa_{1-x}As$ layer with suitable doping level, nevertheless, is shown to keep the carriers in check.

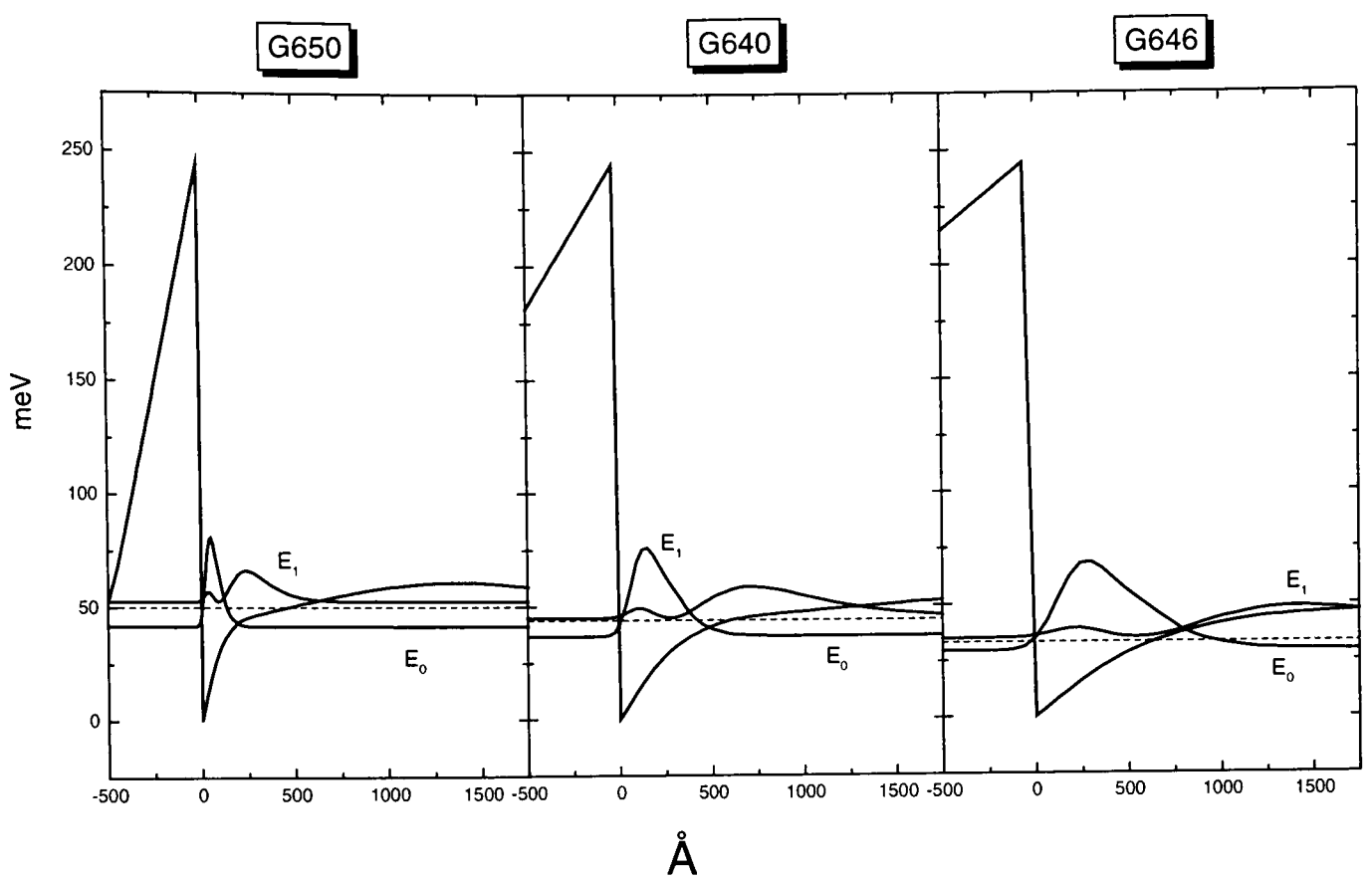

Figure 6-3 Calculated bandedge potential and electron wavefunctions of samples at zero magnetic field using the *k.p* superlattice model described in Chapter 3. The Fermi energies are illustrated in dash lines.

6.2 Experimental Setup

Samples were measured by photoluminescence using the ^{3}He system described in Chapter 2. The system, capable of 330 mK, is sitting inside an old Oxford Instrument superconducting magnet which can give a field up to 14.5 T with the Lambda plate pumped. Nevertheless, the high consumption of liquid Helium while running the ^{3}He fridge prevented me from pumping the Lambda plate at the same time. The maximum magnetic field used in this study is therefore the 4.2 K limitation - 11 T. A calibrated ruthenium oxide resistor is mounted at 2mm away from the sample on the mount to monitor the temperature during the measurement.

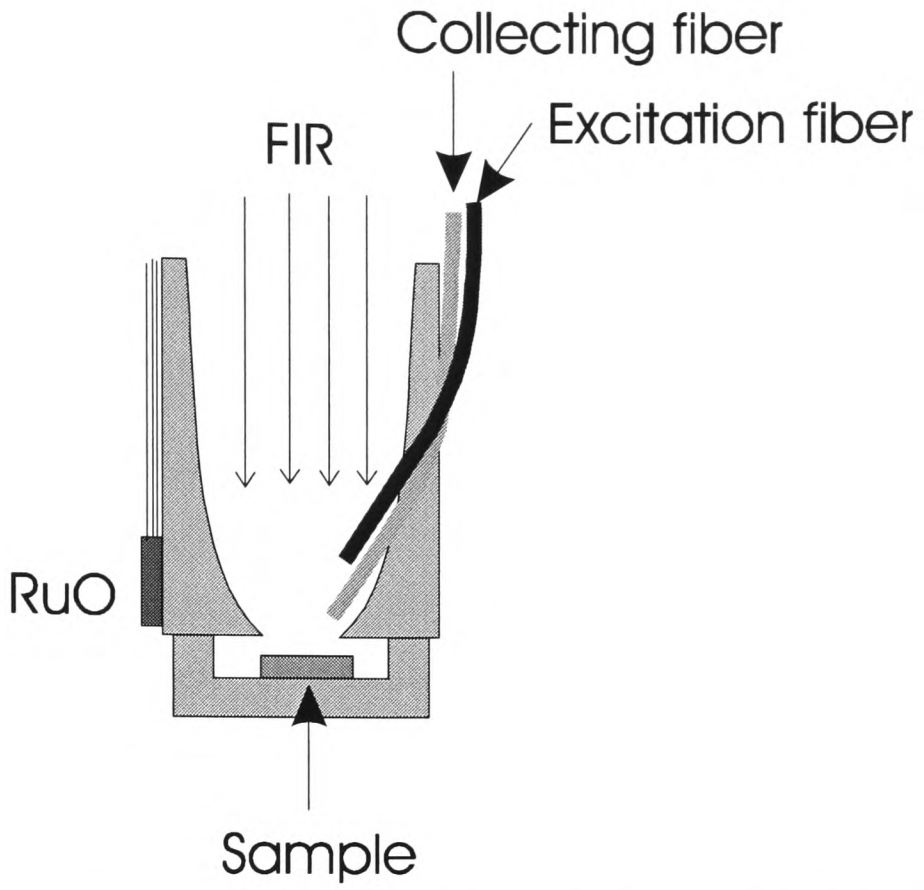

Figure 6-4 A schematic diagram of the FIR light cone and fibers assembly.

The insert has been modified to apply far infrared and visible light at the same time. A hole was drilled at the side of the focusing light cone to let two 600 μm fibers through. The collecting fiber is a 2mm above the sample holder at an angle to eliminate the strong laser beam reflected from the sample surface. The end of excitation fiber is around 2mm further back to give a uniform illumination on the sample. A diode laser, capable of 5mW, provides the excitation beam with a wavelength around 690 nm. It is de-focused to reduce the beam intensity and prevent the possible variation due to mechanical vibration. A neutral density filter is always planted before the fiber end to attenuate the power further. In a measurement, the intensity of the laser light reaching the samples is approximately 10 $\mu W/cm^2$ with an estimate of 90% loss in coupling to the fiber.

The luminescence signal from the collecting fiber is then fed into a one-meter spectrometer. The spectrometer is connected with a nitrogen cooled Si CCD camera (EG&G model 1530c) with a shutter to control the exposure time. Owing to the low illumination employed in this experiment, the exposure time is relatively long, around 60 seconds. Data acquisition is automated using a homemade computer program which sweeps the magnet and takes the spectra in sequence.

6.3 Overview of Photoluminescence Behavior

Figure 6-5 shows a waterfall plot of the conventional photoluminescence spectra, in this case, for G650. These are measured at 340 mK, the base temperature of our system, with a very weak laser beam continuously shining on the sample. At zero field, a single strong peak can be seen at 1514 meV with certain shoulder. This feature moves towards high energy with increasing magnetic field. At around ν=2 (~4.5 Tesla)(ν: filling factor), the luminescence begins getting weaker and is indiscernible by the time the field reaches 5 Tesla. In the mean time, a new luminescence appears 5 meV lower and gets stronger. At ν=1 (~9 Tesla), this low energy peak suddenly plunges down to zero and a new peak appears at the extrapolated position of the high energy ν=2+ features. After a rather brief luminescence intensity transfer with a half width of only 0.3 Tesla, the main peak moves back to lower energy. We categorize the ν=2+ and ν=1 peaks as E_1 feature, as a result of the bulk excitonic recombination from the higher subbands, and the ν=2- and ν=1- peaks as the E_0 feature which comes from the radiative recombination from the E_0 subband. The contour plots of samples measured are shown from Figure 6-6 to Figure 6-8 in an order of their 2DES carrier densities.

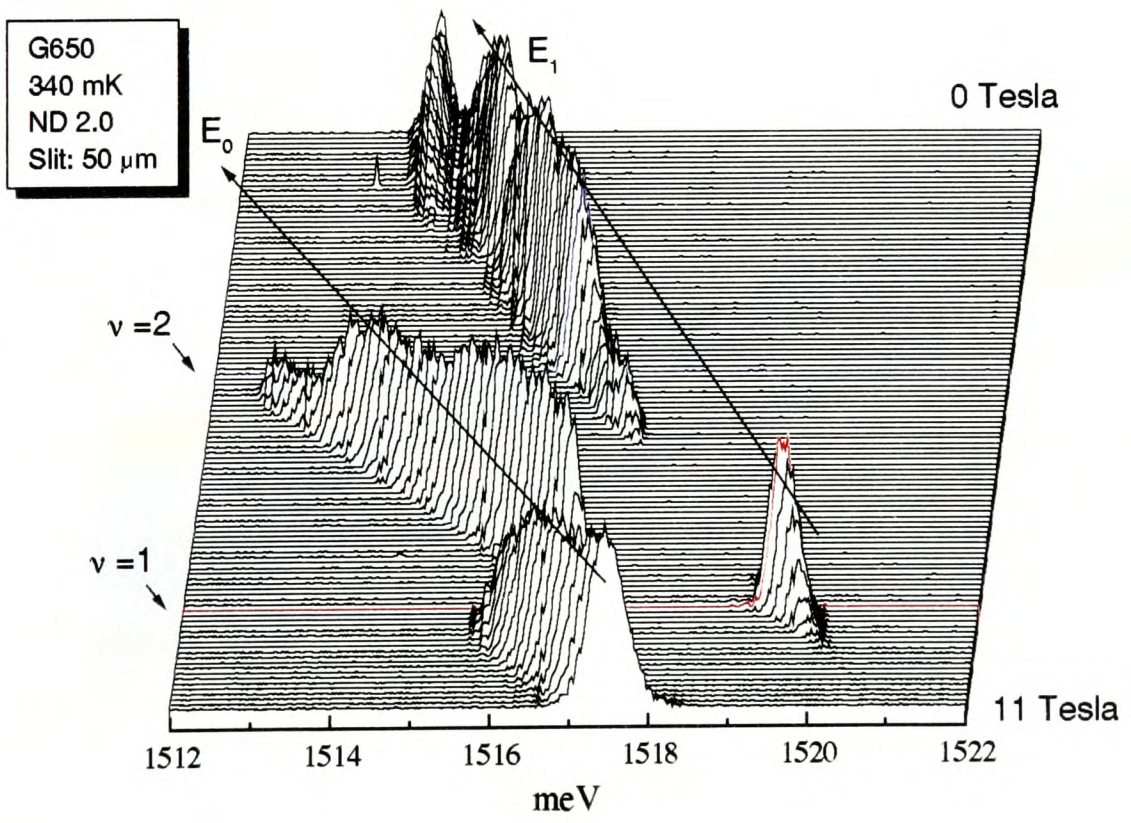

Figure 6-5 Waterfall plot of the photoluminescence of sample G650, the measuring conditions are quoted in the bracket in the top left corner.

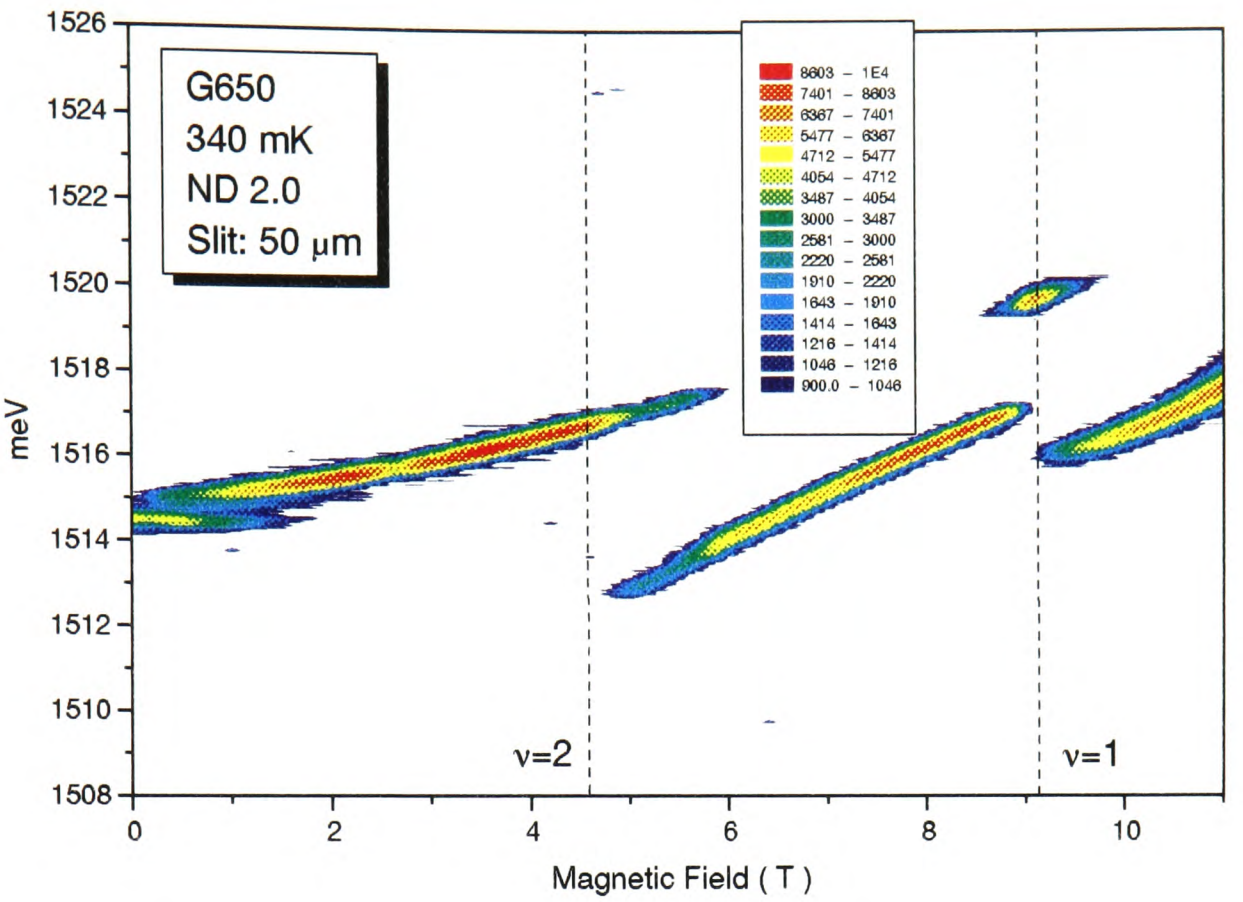

Figure 6-6 The logarithmic contour plot of the photoluminescence intensity of sample G650.

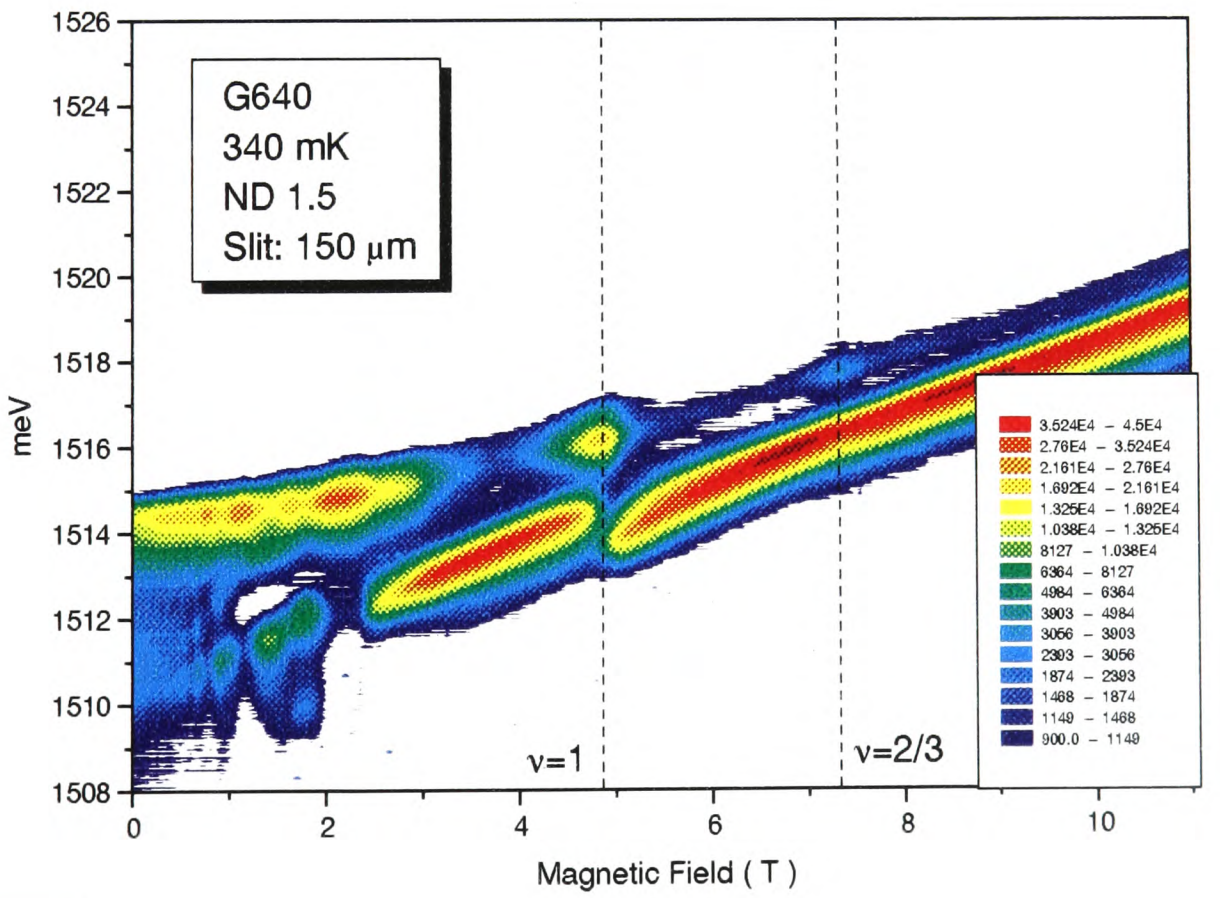

Figure 6-7 The logarithmic contour plot of photoluminescence intensity of sample G640.

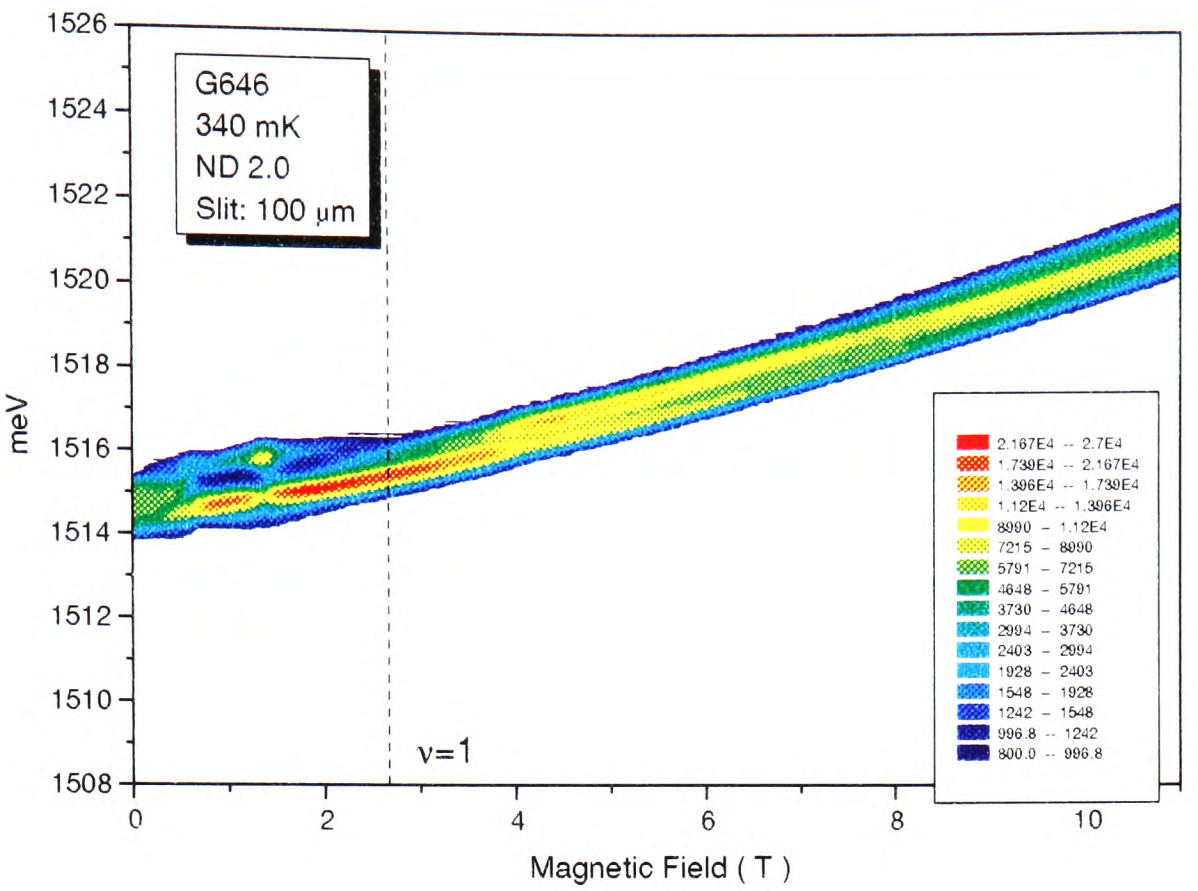

Figure 6-8 The logarithmic contour plot of the photoluminescence intensity of sample G646.

The spectral features of two high carrier density samples (G650 and G640) scale with filling factor, and can be summed up as follows

1) At ν=2+, the E_1 luminescence dominates the spectra which is parabolic with increasing magnetic field.
2) At ν=2-, the spectra are generally E_0 which move up in energy linearly with field.
3) A brief luminescence transfer to E_1 can be seen around ν=1 and an energy gap between the E_0 ν=1- and ν=1+ luminescence is observed as well.

Turberfield [6] interprets the luminescence transfer between E_0 and E_1 as the screening effect. In a partly filled Landau level, electrons can scatter between states and hence increase the wavefunction overlap with the holes but not within a completely filled level. The domination of E_0 features at ν=2- can be interpreted as a result of the scattering within the compressible states while the ν=1 luminescence transfer is the consequence of incompressible states. At ν=2+, the bottom two Landau levels of the E_0 subband are completely filled and one can only find half-filled states at higher Landau levels (Figure

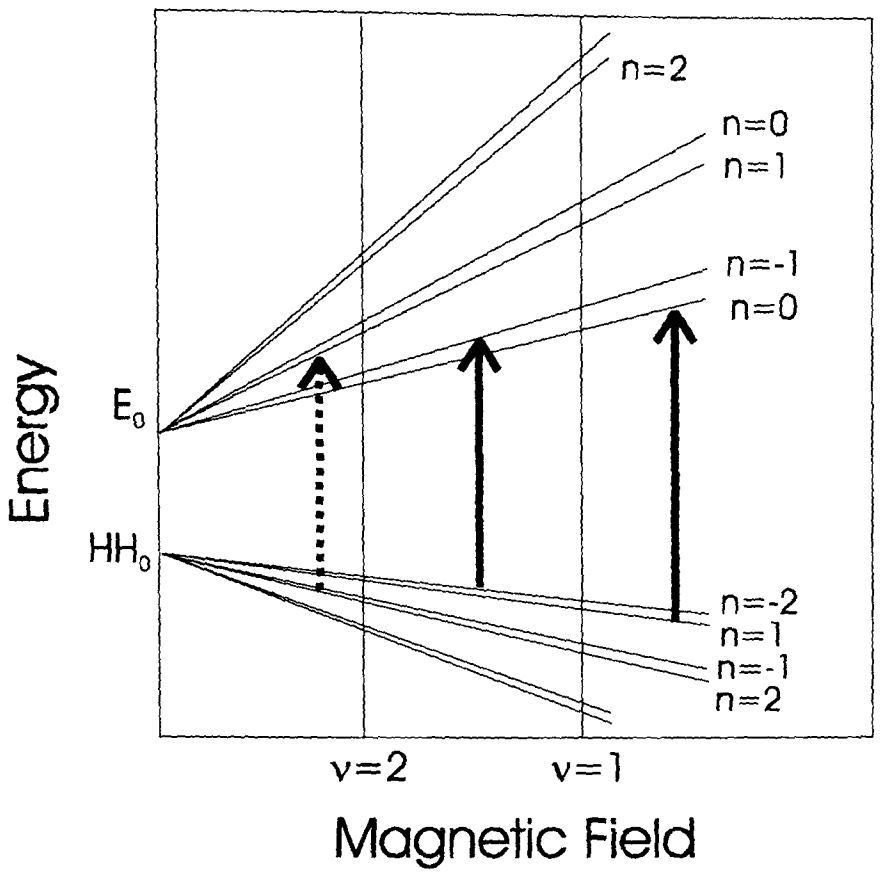

Figure 6-9 Schematic illustration of the possible interband transition at different filling factors.

6-9). These compressible states, though capable of screening, contribute no luminescence. This is because the fast intrasubband relaxation process settles most of the photo-excited holes to the lowest Landau level [14,15]. Since the exciton recombination requires the electron and hole to have the same in-plane angular momentum, it is impossible for electrons from higher Landau levels to generate luminescence. This explains why E_1 luminescence is the main feature at $\nu=2+$.

The discontinuity at $\nu=1$ has been attracting interest recently [6,7]. We understand this red shift in terms of the mechanism of Cooper and Chklovskii [16], which suggests different recombination mechanisms for $\nu=1+$ and $\nu=1-$. For $2>\nu>1$, the luminescence comes from the conventional excitonic recombination of a free exciton consisting of a spin down electron (n=-1) with a valence band hole under the perturbation from a completely filled Landau level (n=0). At $\nu=1-$, the radiative recombination is between a "free hole" and the entire 2DES. The energy shift at $\nu=1$ is therefore the difference in the energies of a spin wave consisting of a widely spaced electron-hole pair and of the conventional exciton binding energy. Recently, Osborne shows that the recombination remains always excitonic for sufficiently small electron-hole separation [17]. This is due to the fact that the ground state energy is determined by both the spin wave energy and exciton binding energy which is a function of the electron-hole separation. The

photoluminescence spectrum of G646, the lowest carrier density sample, agrees with the theory. The calculated bandedge potential shown in Figure 6-3 is rather flat, which suggests a large overlap between the electron and hole wavefunctions.

6.4 Infrared Modulation of the Luminescence

We now discuss the influence of far infrared absorption on the photoluminescence spectrum. The perturbation can either cause classic heating effects on the luminescence - say, line broadening - or induce resonance, or both. No matter which of these two effects happen, the infrared power level is expected to play a major role in the modulation strength. Without a power meter built close to the sample, the only reference for the infrared intensity is the temperature measured by the RuO resistance. This, of course, can only roughly ensure that a similar infrared power is reaching the samples between different spectral scans.

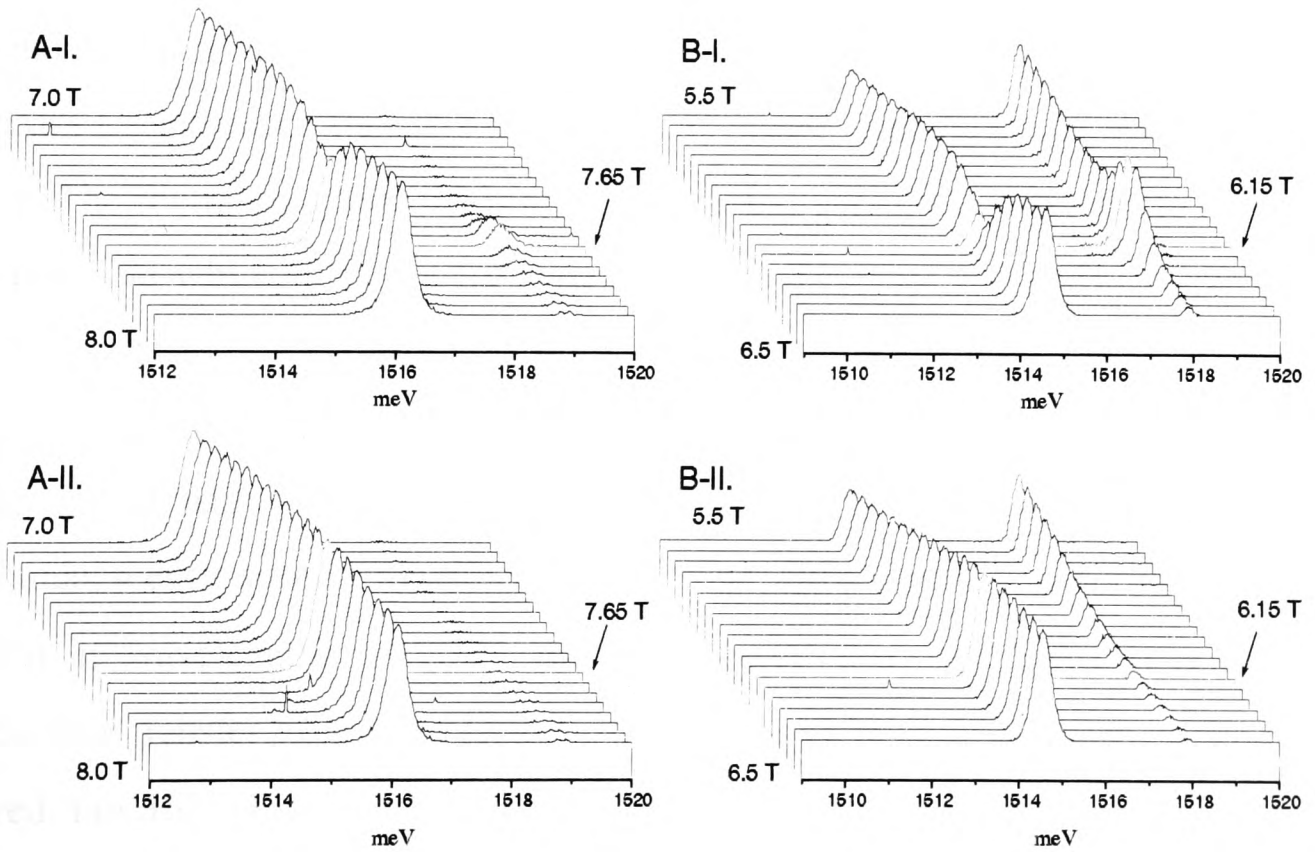

Figure 6-10 Photoluminescence spectra of Sample G650 with and without the infrared modulation in a certain field range. A-I and A-II correspond to the spectra with and without the presence of 96.52 μm (ν=1.21)**, respectively, and B-I and B-II to 118.88 μm** (ν=1.49)**.**

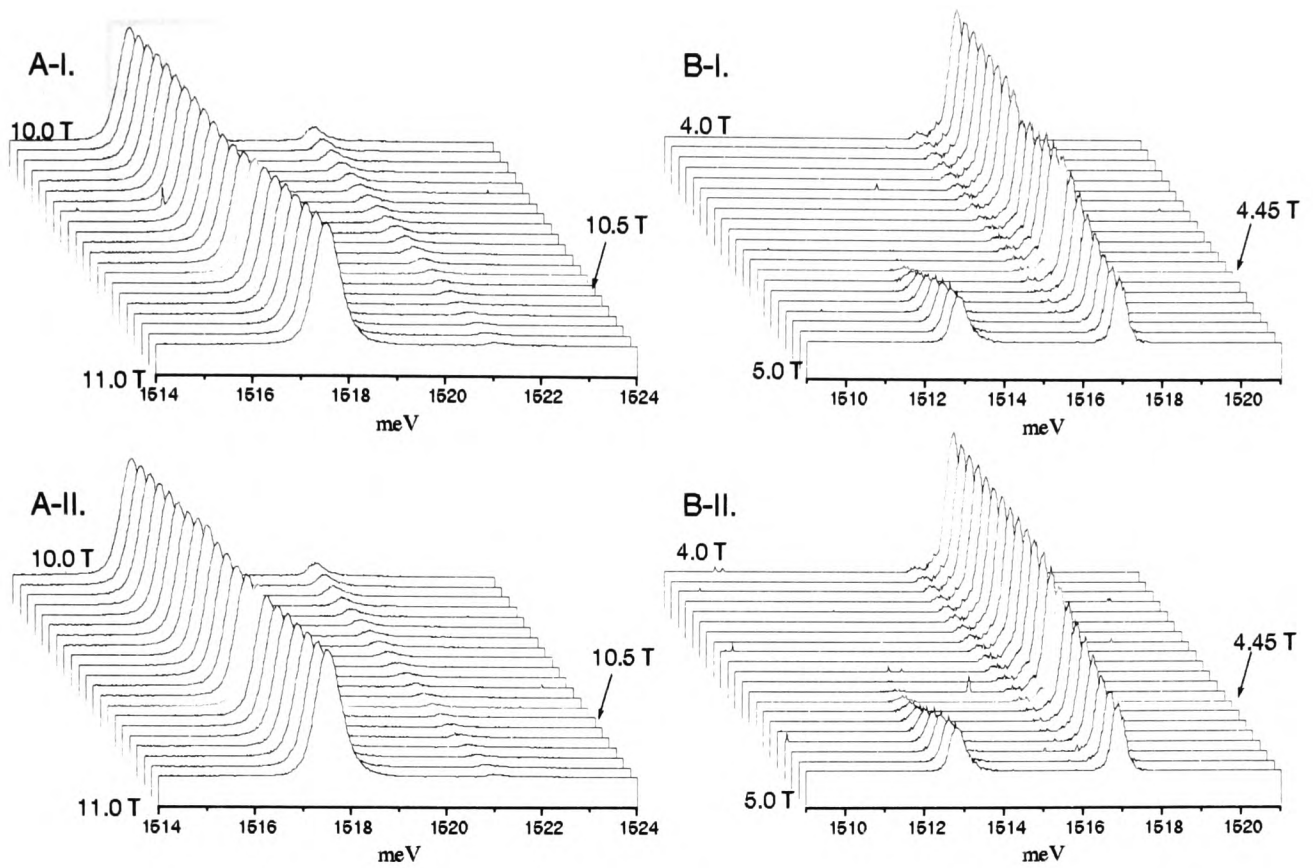

Figure 6-11 Photoluminescence spectra of Sample G650 with and without the infrared modulation in a certain field range. A-I and A-II correspond to the spectra with and without the presence of 70.51 μm (ν=0.88), respectively, and B-I and B-II to 163.03 μm (ν=2.1).

Figure 6-10 shows two series of photoluminescence spectra measured in sample G650 with and without the infrared radiation of wavelength 96.52 μm and 118.88 μm. Significant luminescence transfers from E_0 to E_1 can be seen under the influence of the far infrared. The central magnetic fields of these transfers actually correspond to the cyclotron resonance field which rules out the possibility that these are just global infrared heating. The effective mass deduced from the resonances is around 0.068 m_0, agreeing with ODCR (Optically Detected Cyclotron Resonance) experiments [13]. The resonance is very sharp in field with a halfwidth around 0.15 Tesla. Figure 6-11 shows another two sets of photoluminescence spectra measured in the same sample with and without the infrared radiation at wavelengths of 70.51 μm and 163.03 μm. For 70.51 μm, there is no luminescence transfer from E_0 to E_1 and only very weak modulation on E_0 luminescence is observed. For 163.03 μm, where the E_1 luminescence dominates at its resonance field, the E_1 feature is slightly suppressed by the infrared beam without any extra feature appearing at the high energy side. Figure 6-12 summarizes the far infrared modulated photoluminescence of G650 in contour plots.

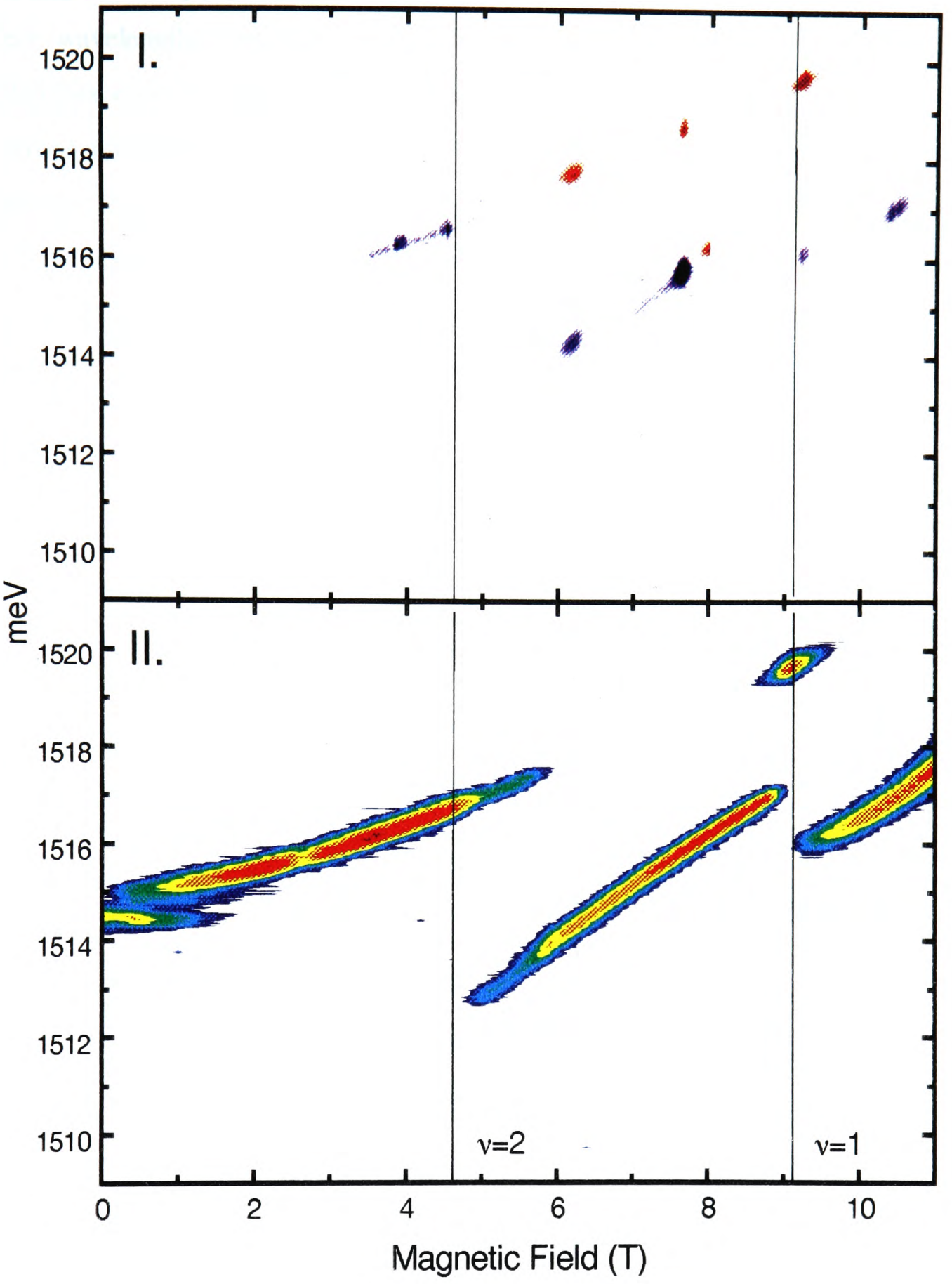

Figure 6-12 Logarithmic contour plots of the PL intensity of sample G650, (I) the intensity change by applied infrared radiation, red and blue represent enhancement and suppression respectively. (II) the photoluminescence intensity without infrared modulation.

In Figure 6-12 (I), the suppression is presented in blue and enhancement in red at six different wavelengths (resonance fields). From the figure, the far infrared modulated photoluminescence is rather obviously dependent on the filling factor. Between ν=1 and ν=2, strong luminescence transfers from E_0 to E_1 are seen at three different wavelengths. Outside this field range, there are only weak suppressions of the major features, which exist in the absence of infrared. To further affirm the dependence on filling factors, we then investigated sample G640 using the same set of infrared lines. Figure 6-13 illustrates the spectra of sample G640 and G650 under the modulation of 118.88 μm. With roughly the same intensity illuminating the samples, the modulations produced by the infrared are different both qualitatively and quantitatively. There is no luminescence transfer from E_0 to E_1 in G640 and the resonance is much weaker. It is indeed very much like the 70.51 μm spectrum of G650 whose filling factor is less than 1. Further investigation with other wavelengths confirms that the systematic dependence is based almost entirely on filling factors rather than anything else.

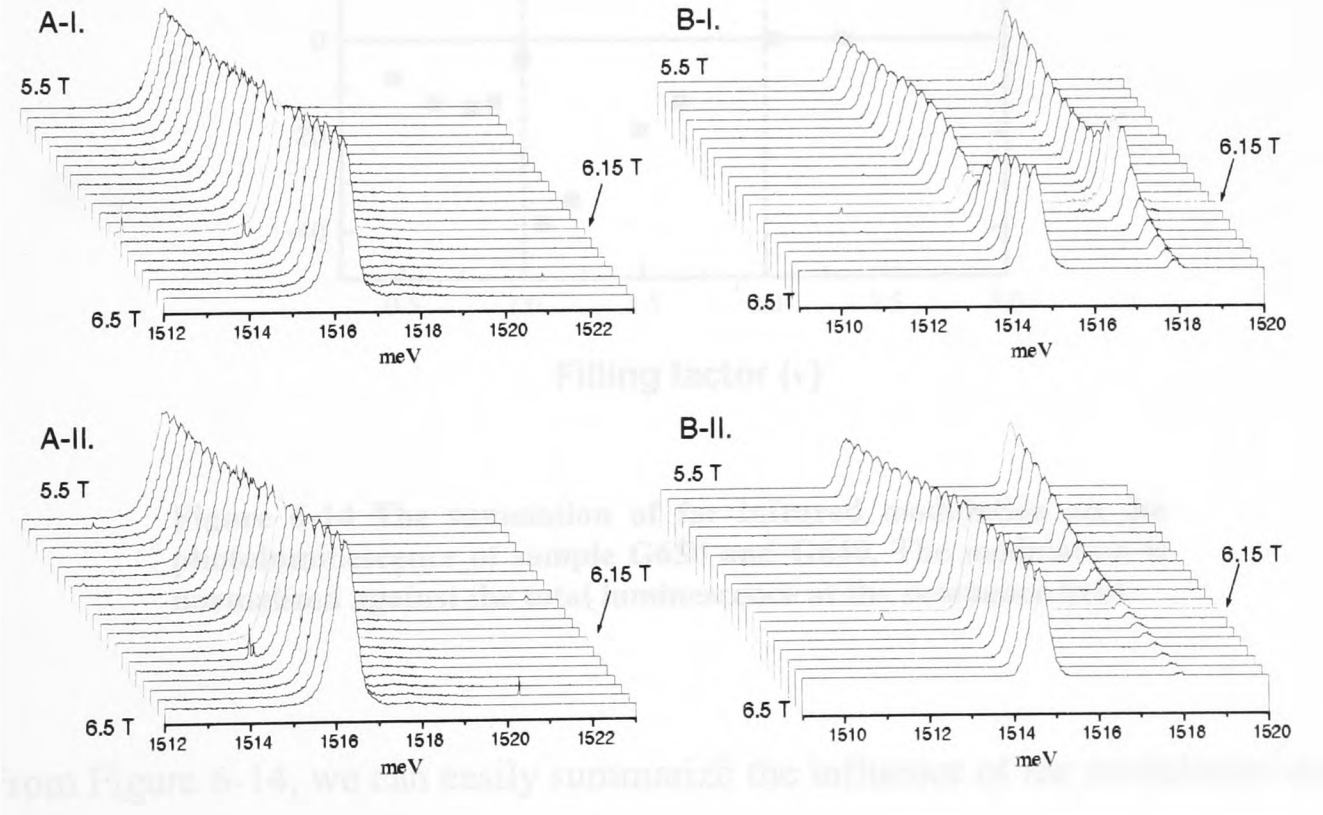

Figure 6-13 A-I and A-II correspond to the photoluminescence spectra of Sample G640 with and without the presence of 118.88 μm (ν=0.78), respectively, and B-I and B-II are those of sample G650, the same spectra presented in Figure 6-10 (B).

A summary of far infrared modulation of the luminescence of samples G650 and G640 is shown in Figure 6-14. Since the experiments are sometimes done using different CCD exposure time and the luminescence is highly dependent on both sample and magnetic field, normalized suppression or enhancement ($\frac{\Delta E_i}{E_1 + E_2}$) is presented to give a more systematic picture of the modulation.

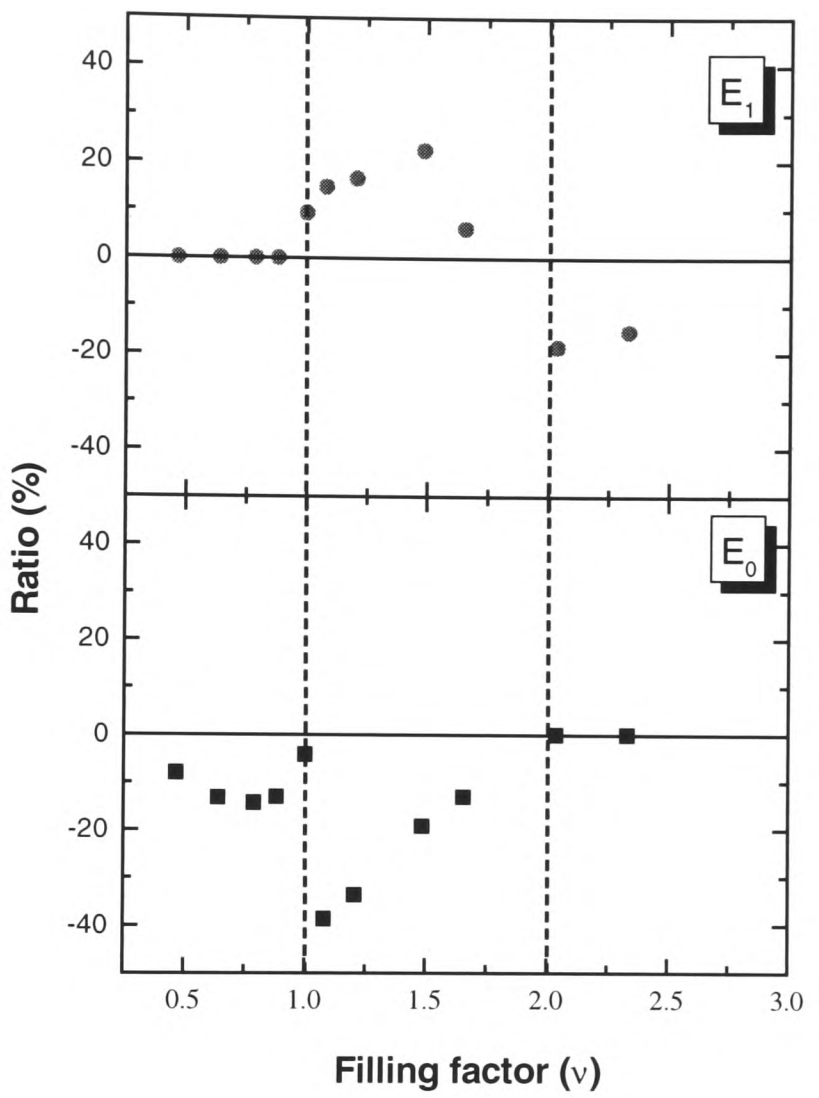

Figure 6-14 The summation of far infrared modulation on the photoluminescence of sample G650 and G640. The modulation is normalized against the total luminescence at the resonance field.

From Figure 6-14, we can easily summarize the influence of the modulation made by the infrared on the photoluminescence of sample G650 and G640 according to filling factor.

1) At ν=1-, the free hole recombination feature is suppressed by applying infrared but no enhancement of the bulk exciton (E_1) feature can be observed.
2) At ν=2+, the E_1 feature is suppressed.

3) In between (2>ν>1), both a suppression of the E_0 excitonic feature and an enhancement of the E_1 feature are clearly observed.

Under the cyclotron resonance excitation, the electrons will redistribute themselves in different Landau levels and three things should be expected from the redistribution. First, the excited electrons in higher Landau levels may recombine with holes and produce luminescence with higher energy than E_0, reflecting the reduced mass of excitons. Second, these electrons may promote E_1 luminescence by relaxing to the E_1 subband and forming excitons. Third, the lattice can be heated by absorbing the infrared directly or scattering with the hot electrons and hence generate phonons to promote the non-radiative recombination and, eventually, reduce the number of holes capable of radiative recombination. Direct emission from higher Landau levels will not happen due to the short electron lifetime in higher levels. The second case is very much dependent on the relaxation process and finally the infrared heating is likely to be a function of absolute power but not individual wavelengths.

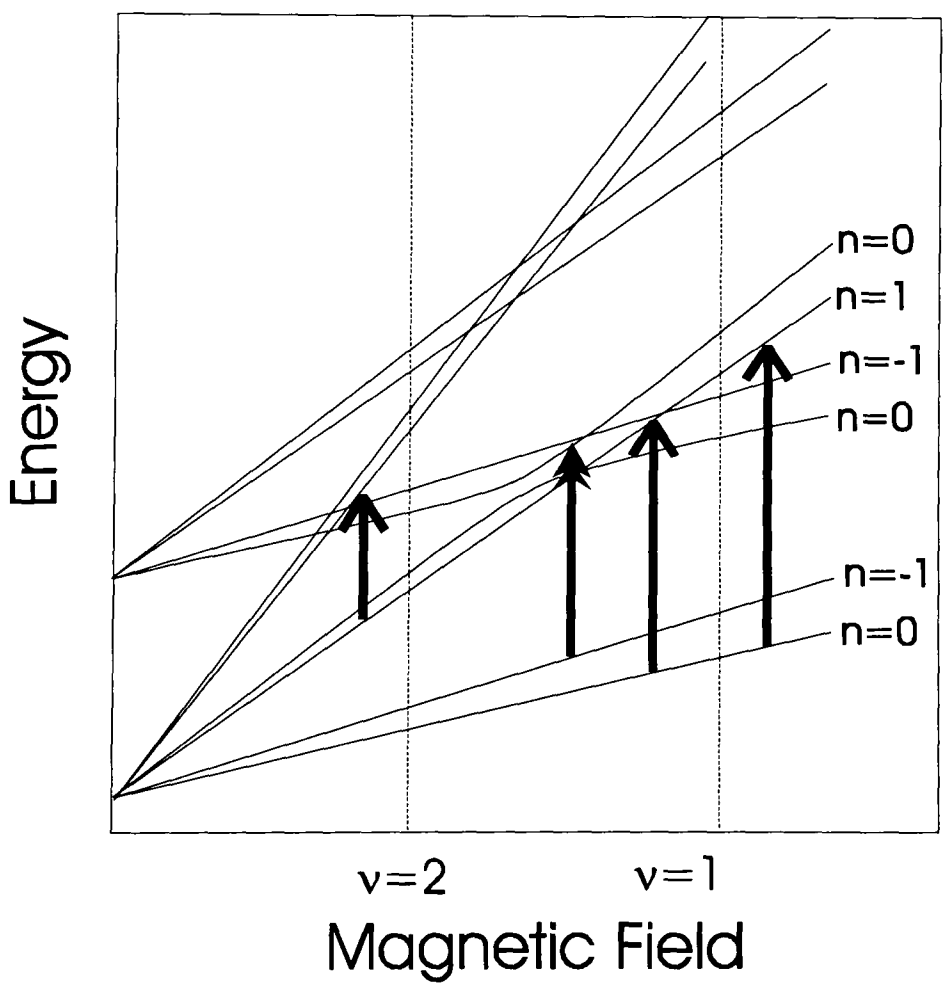

Figure 6-15 A schematic diagram to illustrate the possible cyclotron resonance transitions. n stands for Landau level index.

Figure 6-15 illustrates the possible cyclotron resonance transitions against the filling factors. At ν=1-, the only possible transition is from n=0 to n=1. The relaxation from the n=1 state to either n=0 or n=-1 of E_1 is an intersubband process involving both losing angular momentum and parity flipping, which is slower than the intrasubband relaxation back to the ground state of E_0 [15]. No enhancement of E_1 is therefore expected and so we expect a weak suppression of E_0 luminescence due to the lower E_0 ground level population giving holes a better chance to recombine non-radiatively. For filling factors between 2 and 1 (2>ν>1), two cyclotron transitions are possible – one from a completely filled n=0 level and one from a partly filled n=-1 level. Since the spin-down n=0 upper state in E_0 has the same parity as the spin-up n=0 ground state in E_1 as discussed in Section 3.6.1, it is sensible to count part of the excited electrons as being in the E_1 subband. The signature of this band mixing, of course, is the anti-crossing between the Landau fans as shown in Figure 6-15. With a fixed number of holes waiting for recombination, it is the ratio between the E_1 and E_0 recombination probability that matters, which is a function of both wavefunction overlap and carrier density. A ***k.p*** calculation of G650 at 118.88 μm with a subband separation (E_1–E_0) of 15 meV gives a band mixing around 0.5%. In other words, 0.5% of the electrons in the spin-down n=0 upper state in E_0 can be counted as E_1 electrons. A small proportion it may be, it can still make a significant contribution to the E_1 luminescence due to the larger wavefunction overlap with holes than that of E_0. At ν=2+, the cyclotron transitions are similar to those between ν=1 and ν=2 only with higher Landau level indices. The infrared pumping at the E_0 subband does not contribute much to the E_1 population because the intersubband relaxation is slow without coupling between the states just as happened at ν=1-. The main contributors to luminescence in this regime are electrons photo-excited by the visible laser but not in the 2DES. These electrons are pumped to higher Landau levels of the E_1 subband when in resonance with the infrared photons. In other words, there are fewer electrons resting in the ground state of the E_1 subband and a suppression of luminescence is expected accordingly.

Besides G650 and G640, sample G646 was studied with far infrared modulation as well. The photoluminescence spectrum of this particular sample is always excitonic due to the small electron-hole separation as explained in Section 6.3. The intensity decrease

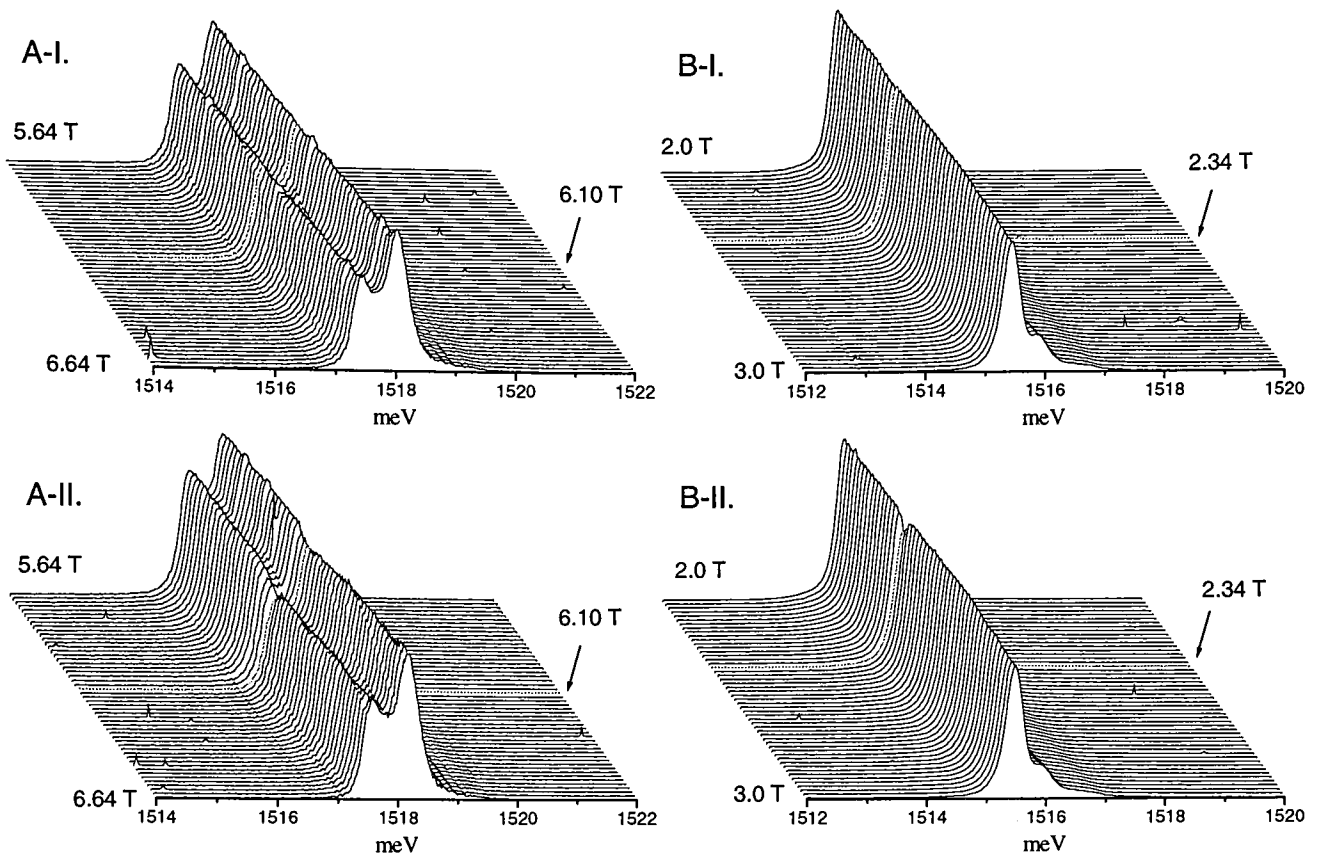

Figure 6-16 Photoluminescence spectra of Sample G646 with and without the infrared modulation in a certain field range. A-I and A-II correspond to the spectra without and with the presence of 118.88 μm (ν=0.44), respectively, and B-I and B-II to 300 μm (ν=1.14).

induced by infrared beam is barely distinguishable (<5%) at all different filling factors. This is similar to what happens to G650 and G640 at ν=2+ - fewer electrons in the ground state under continuous infrared illumination. Figure 6-16 illustrates two of these spectra - one at ν=1.14 and the other one at ν=0.44, all showing rather weak modulation.

6.5 Infrared and Red Laser Power Effects

6.5.1 Effects of Infrared Power on the Strength of Modulation

The relation between infrared power and modulation was studied in sample G650 at resonance with a particular wavelength 118.88 μm. This wavelength is the strongest line available from our far infrared laser with a maximum output power around 10 mW. After the attenuation by optical windows and light pipes, a reasonable 10% (~1mW) can be expected to reach the sample. To carry out the power dependent experiment, a single sheet of standard grade paper is used to provide the attenuation needed. From the long experience with this line, we know by heart that one single sheet blocks 2/3 of the beam. The relative power level is therefore obtained by counting the number of sheets blocking the input end of the light pipe.

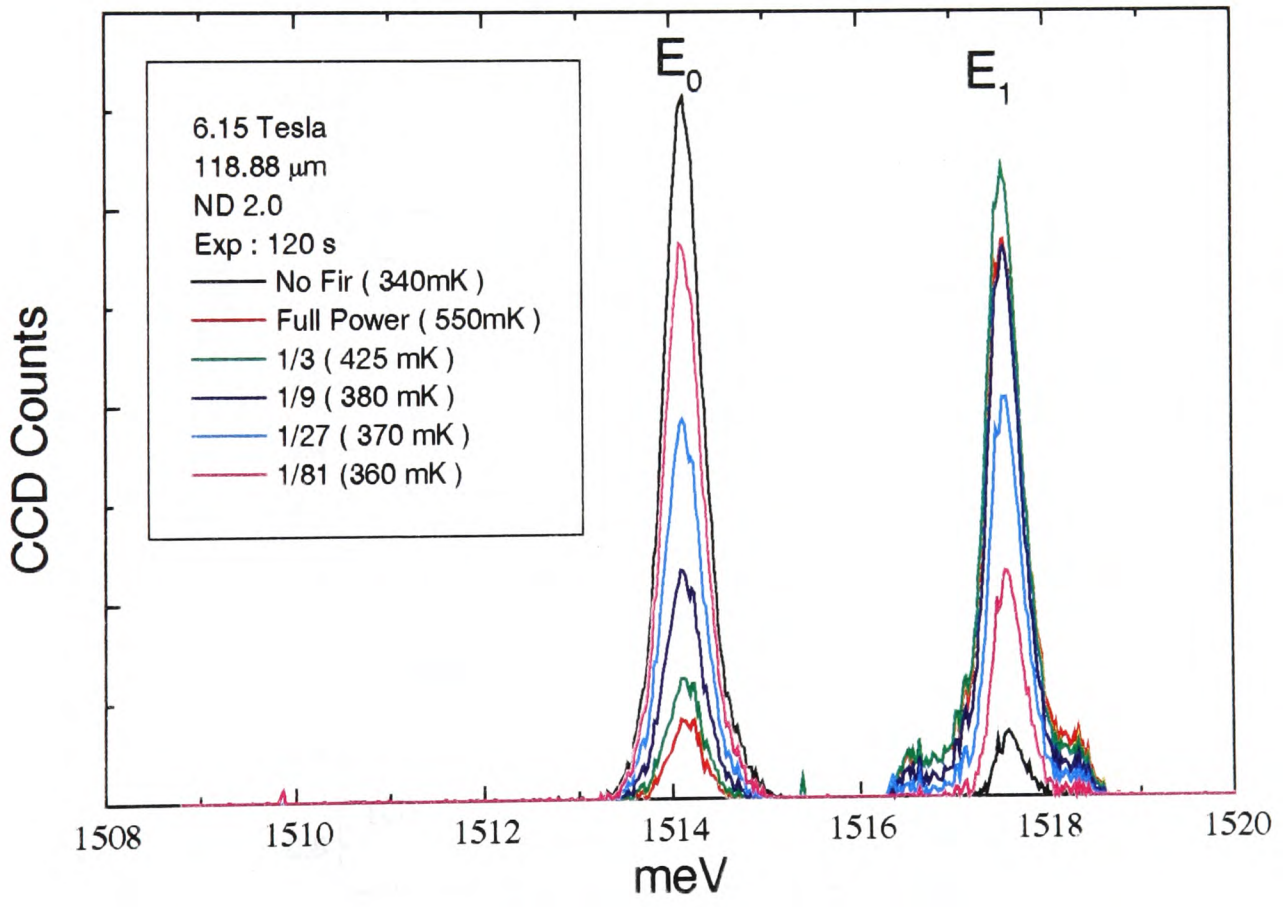

Figure 6-17 The spectra of sample G650 at the 118.88 mm resonance field under different level of infrared illumination.

Figure 6-17 illustrates the spectra at the resonance field (6.15 T) under different levels of infrared illumination. With the full power from the infrared laser, the sample temperature rises up to 580mK and the luminescence transfer from E_0 to E_1 is phenomenal, leaving very little signal from E_0. The modulation then reduces down when less power is used. To understand the behaviour quantitatively, the modulation has been normalized against the total luminescence without far infrared, as shown in Figure 6-18 (A). The suppression or enhancement is very non-linear with the infrared power. The modulation reaches its plateau with more than 25% of the full power. At this point the E_1 luminescence is five times stronger than the E_0 luminescence. Figure 6-18 (B) shows the proportions between E_0 and E_1 luminescence intensities against power levels, which also confirms the 25% limitation. Since the number of holes is determined by the photo-

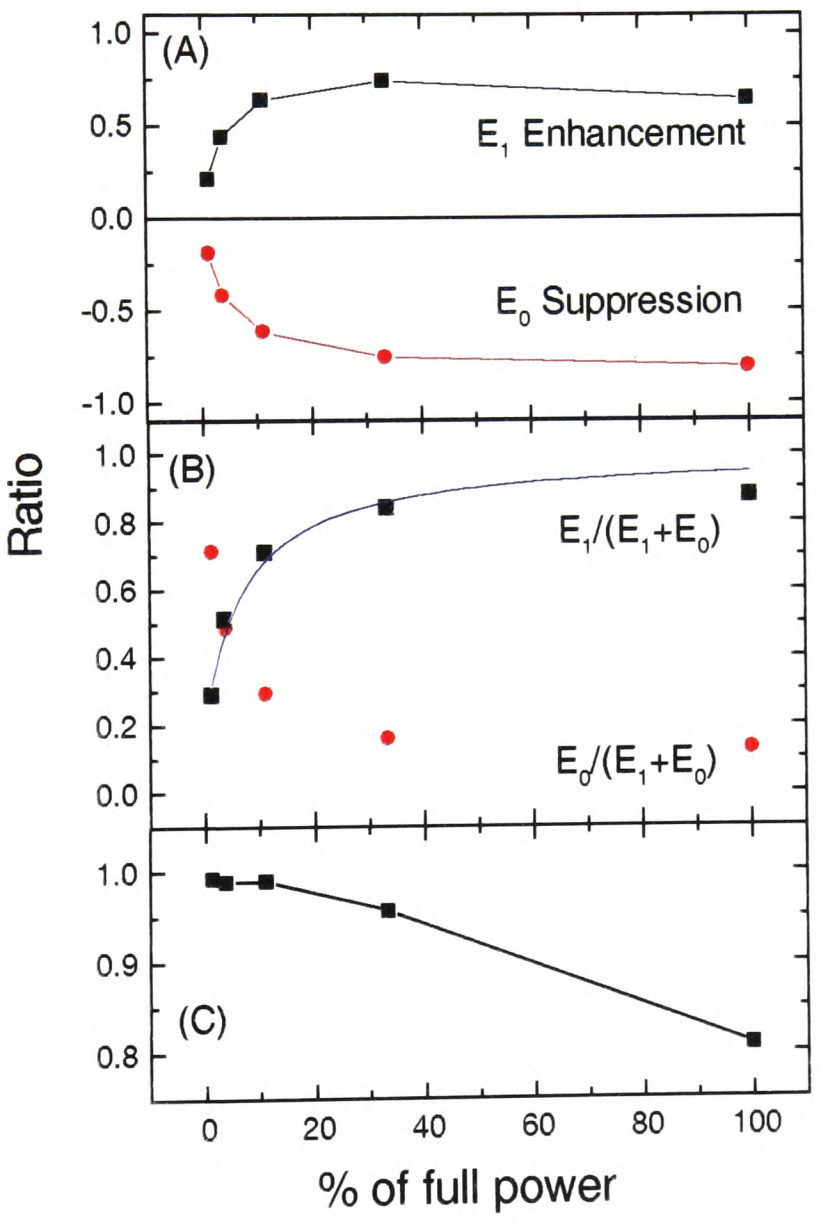

Figure 6-18 The modulation on photoluminescence done by the far infrared. (A) ratio of E_1 and E_0 modulation against the total luminescence without infrared, (B) the proportions of luminescence coming from E_1 and E_0 against the laser intensity and (C) the total intensity changes.

excitation process almost independent of the cyclotron resonance, the E_1/E_0 ratio turns out to be a competition between the two recombination processes. The recombination strength can be represented as

Recombination strength $\propto$ (transition probability) x (population)

The $\frac{E_1}{E_0+E_1}$ ratio is therefore

$$\frac{E_1}{E_0+E_1}=\frac{1}{1+\frac{n_0}{(n_1+n_{HL}X)}\frac{T_0}{T_1}} \tag{6.4}$$

where n_0 and T_0 represent E_0 carrier density and transition probability. n_1 and T_1 are the E_1 carrier density without infrared pumping and the transition probability. n_{HL} is the carrier density of the higher Landau level under cyclotron excitation in the E_0 subband and factor X is defined as the proportion of n_{HL} being credited as in the E_1 subband due to the coupling effect explained in the previous section. With the full power of the infrared laser illuminating on an area of $4mm^2$, n_{HL} is about $3x10^9$ cm^{-2} assuming the lifetime is around 1 ns [18] and 50% of the photons are absorbed. If n_{HL} is linear with the infrared power, which is a sensible assumption, we can then fit the experimental data with Eq. (6.4). Figure 6-18 (B) shows the curve which fits best with the $E_1/(E_0+E_1)$ trace, giving $\frac{XT_1}{T_0}$ around $1.7x10^3$. The efficiency of E_1 recombination is more extraordinary compared to its E_0 counterpart, considering that X can be rather small.

The total photoluminescence levels (E_1+E_0) should ideally be constant due to the fact that the number of holes generated by red laser does not change with the intensity of far infrared. Nevertheless, the infrared beam produces phonons which promote the non-radiative recombination and consequently cuts down the effective number of holes liable for the radiative recombination. Figure 6-18 (C) illustrates the total luminescence against beam intensity which shows a gentle decline dropping down to 80% at the full power of laser.

6.5.2 Red Laser Intensity and Temperature Effect

As stated in Section 6.2, the 2DES density is sensitive to the cooling process and the way samples are illuminated. We study further the effect of laser intensity on the luminescence spectrum. As we increase the intensity of visible laser excitation, two effects are expected. First, more electrons are injected into the conduction band by photo-excitation in the GaAs. The E_1 carrier density is thus increasing proportionally but not the E_0 carrier density. This is because the main contributors to the 2DES in E_0 subband are dopants in the $Al_xGa_{1-x}As$ layer. They are ionized in the metastable regime with little dependence on the illumination level. Second, more holes are injected into the valence band and an increase in total luminescence is consequently expected.

Figure 6-19 shows the spectra of sample G650 at ν~1.5 under different experimental conditions. With a neutral density 2.5 filter at the end of fiber reducing the illumination level down to a few $\mu W/cm^2$, the spectra taken at base temperature (300mK) and 385mK are identical with a single luminescence from E_0 but nothing from E_1. While the

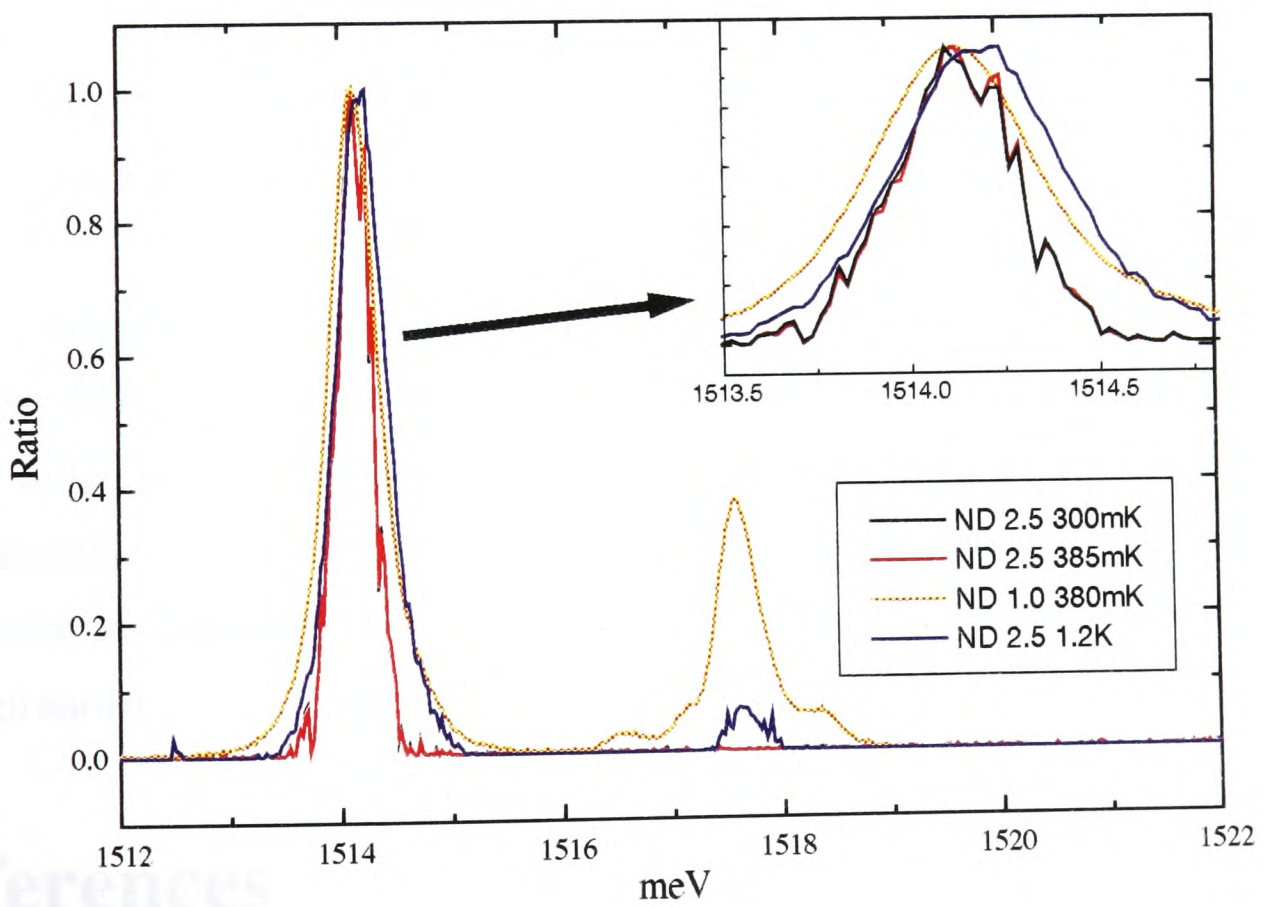

Figure 6-19 The spectra of sample G650 at 6.2 Tesla (ν~1.5) under different measuring conditions. These spectra are normalized against the peak E_0 luminescence and ND stands for neutral density filter.

temperature increases to 1.2 K, the E_0 feature has a longer tail on the high energy side which is a classical heating effect. Besides the E_0 feature, a weak E_1 feature can be seen with only 5% the strength of the E_0 luminescence. We then change the neutral density filter from 2.5 to 1.0, which means 30 times more power on the sample. The temperature rises from 300mK to 380mK and the E_1 luminescence is much more pronounced reaching nearly half the size of the E_0 luminescence. Following the statement made above, this implies that the population in E_1 subband is now 30 times more than before but the 2DES population does not increase very much. The recombination probability is hence on the side of E_1 luminescence if the wavefunction overlaps do not vary significantly along with the illumination power.

6.6 Conclusion

We have studied a series of ultra high mobility GaAs/$Al_xGa_{1-x}As$ heterojunctions using photoluminescence at the ^3He base temperature. A filling factor dependent luminescence transfer between subbands is observed in the high 2DES density samples, which is due to the potential screening from electrons in a half filled Landau levels. At $\nu=1$, there is an energy shift in the E_0 luminescence larger than expected from systems without electron-electron correlation. A new model considering both the excitonic and spin wave energies gives a nice description of the spectra.

The photoluminescence spectra modulated by far infrared radiation are highly dependent on both the filling factors and the carrier densities of samples. It is proposed that the different relaxation processes for electrons after cyclotron resonance excitation are responsible. A detailed investigation on both far infrared and red laser power dependence has been done which is consistent with the photoluminescence mechanism proposed earlier.

References

[1] K. von Klitzing, G. Dorda and M. Pepper, *Phys. Rev. Lett.* **45,** 494 (1980).

[2] D. C. Tsui, R. A. Stormer and A. C. Gossard, *Phys. Rev. Lett.* **48,** 1559 (1982).

[3] For reviews, see K. von Klitzing, *Rev. Mod. Phys.* **58**, 519 (1986) and B. I. Halperin, *Scientific American* **254(4)**, 40 (1986).

[4] M. S. Daly, K. S. H. Dalton, M. Lakrimi, N. J. Mason, R. J. Nicholas, M. van der Burgt, P. J. Walker, D. K. Maude and J. C. Portal, *Phys. Rev. B* **53,** R10524 (1996).

[5] R. E. Prange and S. M. Girvin, *The Quantum Hall Effect*, Springer-Verlag, New York (1987).

[6] A. J. Turberfield, S. R. Haynes, P. A. Wright, R. A. Ford, R. G. Clark, J. F. Ryan, J. J. Harris and C. T. Foxon, *Phys. Rev. Lett.* **65,** 637 (1990).

[7] A. J. Turberfield, R. A. Ford, I. N. Harris, J. F. Ryan, C. T. Foxon and J. J. Harris, *Phys. Rev. B* **47,** 4794 (1993).

[8] E. H. Aifer, B. B. Goldberg and D. A. Broido, *Phys. Rev. Lett.* **76,** 680 (1996).

[9] D. Heiman, B. B. Goldberg, A. Pinczuk, C. W. Tu, A. C. Gossard and J. H. English, *Phys. Rev. Lett.* **61,** 605 (1988).

[10] *Excitons in Confined Systems*, edited by R. del Sole, A. D. Andrea and A. Lapiccirella, Springer-Verlag, Berlin (1988).

[11] G. Duggan, *Phys. Rev. B* **37,** 2759 (1988).

[12] J.G. Michels, R. J. Nicholas, G. M. Summers, D. M. Symons, C. T. Foxon and J. J. Harris, *Phys. Rev. B* **52,** 2688 (1995).

[13] J.G. Michels, *D. Phil. Thesis,* Oxford (1994).

[14] G. Bastards, *Wave Mechanics Applied to Semiconductor Heterostructures*, Halsted Press, John Wiley & Sons, New York (1988).

[15] R. Ferreira and G. Bastard, *Phys. Rev. B* **40,** 1074 (1989).

[16] N. R. Cooper and D. B. Chklovskii, *Phys. Rev. B* **55,** 2436 (1997).

[17] J. L. Osbourne, A. J. Shields, M. Y. Simmons, N. R. Cooper, D. A. Ritchie and M. Pepper, *Preprint.*

[18] I. Maran, W. Seidenbusch, E. Gornik, G. Weimann and M. Shayegan, *Semicond. Sci. Technol.* **9**, 700 (1994).

7. Infrared Induced Intersubband Transition in GaAs/ $Al_xGa_{1-x}As$ Coupled Quantum Wells

7.1 Introduction

Intersubband absorption within semiconductor heterostructures has received substantial attention over the past few years. Previous works have been upon intersubband transitions within both *n*- and *p*- doped systems [1] in the wavelength range between 8 and 15 μm. These quantum well infrared detectors offer an alternative technology to narrow gap materials such as $Hg_xCd_{1-x}Te$ by using the interband properties of mature material systems such as $GaAs/Al_xGa_{1-x}As$. The advantages compared with $Hg_xCd_{1-x}Te$ detectors include the mature GaAs growth and processing technologies, which lead to high uniformity, excellent reproducibility and thus larger area, low cost staring arrays. In addition, the ability to control the band structure accurately, and hence spectral response, allows monolithically integrated multi-spectral infrared detectors as well as the potential for monolithic integration with high-speed GaAs based electronics. Recently, there has been an increasing interest in longer wavelength detectors (>20 μm) due to the promising future of far infrared technology.

Basic physics research has recently yielded many interesting results within this relatively small photon energy range. Internal excitonic transitions have been observed

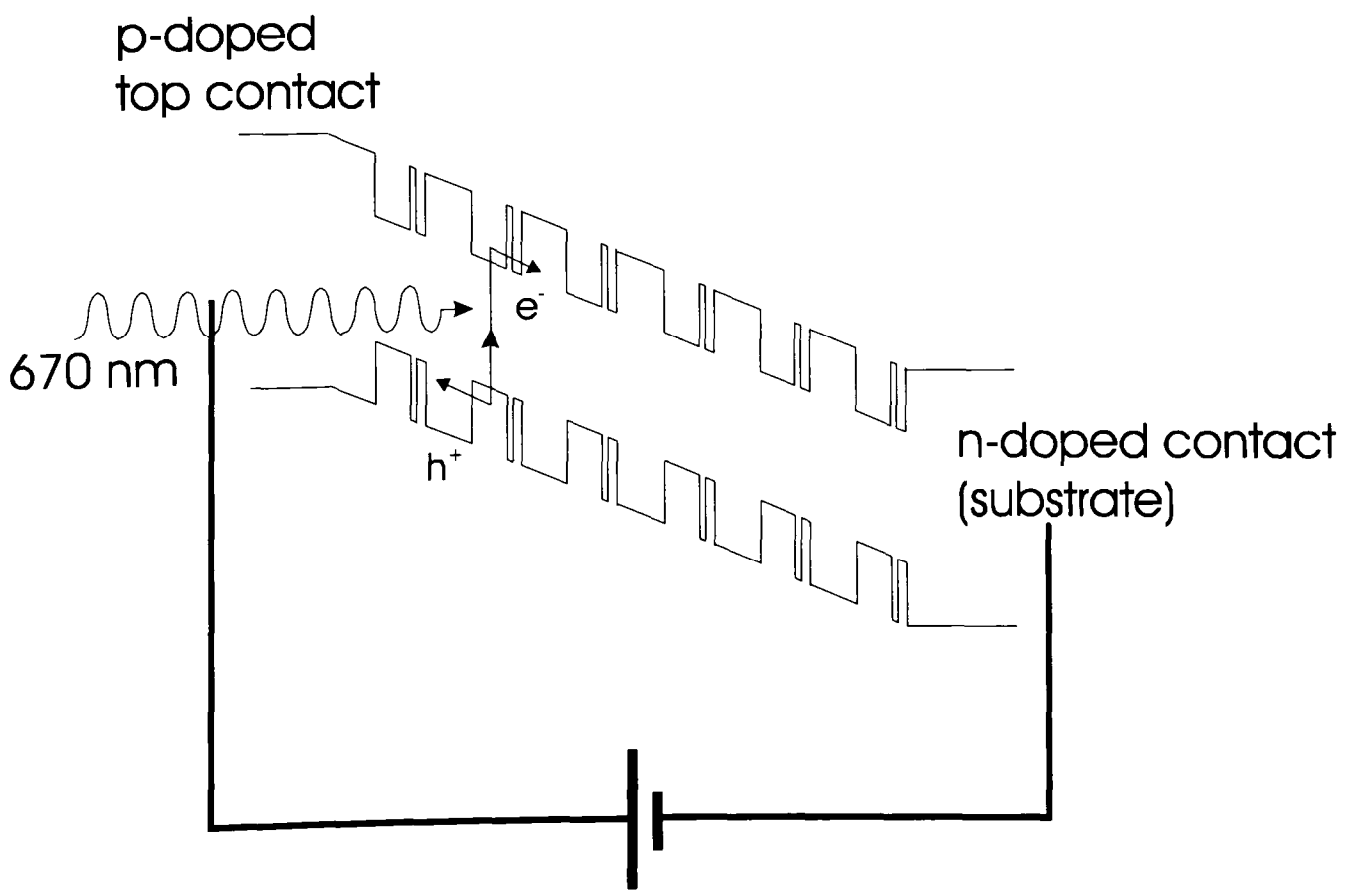

Figure 7-1 Schematic diagram of an intrinsic tunnelling device.

and novel high frequency transport studies have also been undertaken where the cross-over from the classical rectification to quantum effects may be observed. As shown in Figure 7-1, the structure usually consists of multiple quantum wells sandwiched between oppositely doped capping layer and substrate to put electric contacts on. An electric field is applied to the device by biasing it and carriers will tunnel through the structures if they do not recombine optically. If the device is intrinsic, photoexcitation is necessary for generating carriers in the structure. At fixed illumination level and bias, the photocurrent is expected to be constant. If the quantum wells are engineered to facilitate certain intersubband processes, modulations of photocurrent are expected by applying radiation with suitable energy, in this case - far infrared. Within this chapter an investigation into the effect of intersubband absorption on the inter-well tunnelling between coupled quantum wells is presented.

7.1.1 Samples

The sample (G953) investigated in this study was grown at Philips Research Laboratory by molecular beam epitaxy (MBE). The structure is a high-quality *p-i-n* photodiode with quantum wells grown into the intrinsic region. Table 7-1 lists the growth details for sample G953, which consists of 25 coupled quantum well (CQW) pairs grown into the intrinsic region of the diode. The coupled quantum well pair is repeated within the intrinsic region to increase the optical signal. The *p-i-n* diode structure of the sample permits a linear electric field to be applied to the intrinsic region. Any band bending at the interfaces between the doped and intrinsic region is taken up in the buffer layers which sandwich the region. This ensures the quantum wells experience a uniform electric field, which is vital in this study due to the fact that band profile governs the tunnelling process alone.

The photodiode is then fabricated from the wafer into mesa structures at the EPSRC III/V facility in Sheffield. The mesas are processed to have an annular contact. These contacts are formed by metal evaporation. Titanium is deposited first, followed by a gold layer. The resulting contact is approximately 1 μm thick. The two-metal composite contact is used to improve the adhesion of metal to semiconductor. A window is left in the middle of the top contact to facilitate optical access to the active region. The mesa

Table 7-1 Wafer growth details for sample G953.

Thickness (Å)	Al (%)	Ga (%)	Doping (cm^{-3})	Repeats	Notes
1000		100	$2x10^{18}$ (p)		Capping layer
7500	33	67	$1.33x10^{18}$ (p)		
593.6	33	67			Buffer layer
152.6	33	67		25	Thick barrier
158.3		100			Wide well
17.0	33	67			Thin barrier
59.0		100			Narrow well
746.2	33	67			Buffer layer
11.3	100		$4x10^{18}$ (n)	103	Superlattice
11.3		100	$2x10^{18}$ (n)		
10000	67	33	$1.33x10^{18}$ (n)		
1500		100	$4x10^{18}$ (n)		
200		100	$2x10^{18}$ (n)		
		100	n+		Substrate

size in this experiment is 400 μm in diameter and gold gratings are laid down upon the surface to promote the intraband coupling as will be described later. The processed devices are packaged in a standard TO-5 header and gold bond wires are used to connect the sample to the header pins.

Figure 7-2 shows the conduction band profile and calculated wavefunctions of sample G953 using the ***k.p*** model presented in Chapter 3. The energy levels are marked as WW0 (0^{th} subband of the wide well), NW1 (1^{st} subband of the narrow well) and so on. The WW+NW and WW-NW stands for the symmetrical and anti-symmetrical superposition of the wide and narrow subband, respectively. For a barrier as narrow as 17 Å, one might think the structure should be solved as a whole instead of distinguishing between narrow and wide wells and this is exactly what we did. As I shall show later, however, the "narrow well" subband levels shift separately from the "wide well" levels and induce different "coupling" between in varying electric fields. These notations are therefore rather convenient and sensible albeit inaccurate.

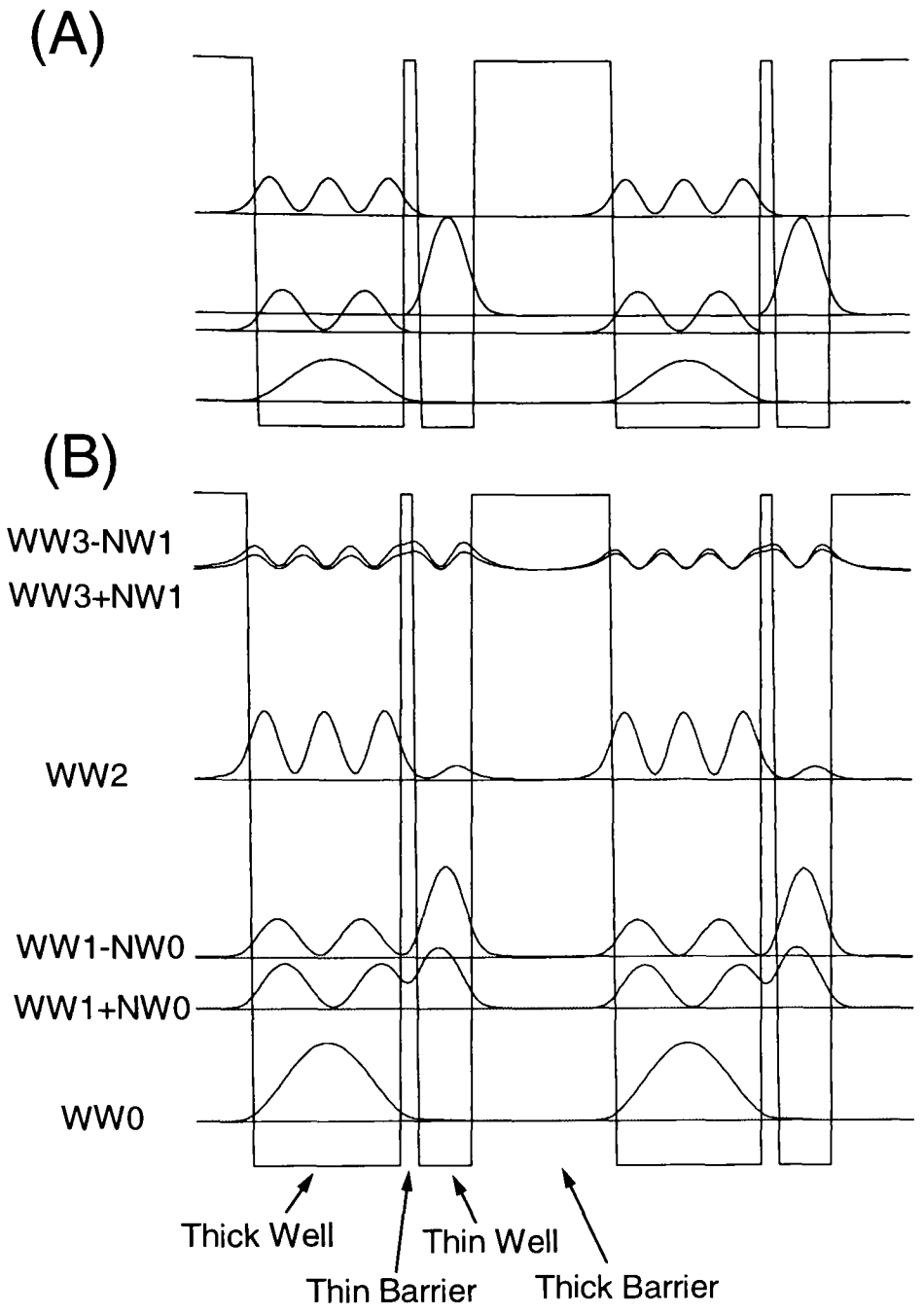

Figure 7-2 Calculated band structures of sample G953, (A) without and (B) with coupling between the wells.

Figure 7-3 illustrates the conduction band profiles under different electric fields. At the lowest electric field illustrated ($2x10^4$ V/cm), the NW0 state decouples with the WW1 state giving an energy splitting between the bottom two states around 22 meV. The ground state, which contributes most to the tunnelling process, is WW0. As the field increases to $4x10^4$ V/cm, NW0 and WW0 couple strongly and the energy splitting reduces to 12 meV. With even higher electric field applied ($6x10^4$ V/cm), NW0 and WW0 move away from each other and the ground state turns out to be NW0. It is natural that pumping electrons from WW0 to NW0 or vice versa using infrared beams with suitable energy may modulate the photocurrent. The resonance energy dependence on bias makes the structure a possible tuneable infrared detector. A summary of the anti-crossing between the two lowest energy states can be found in Figure 7-3. It may be

worth mentioning that the electric fields from theoretical calculations do not transform to the actual biases applied directly due to the complexity of the sample structure. Experimental data are used to fit the bias with its corresponding field in this study.

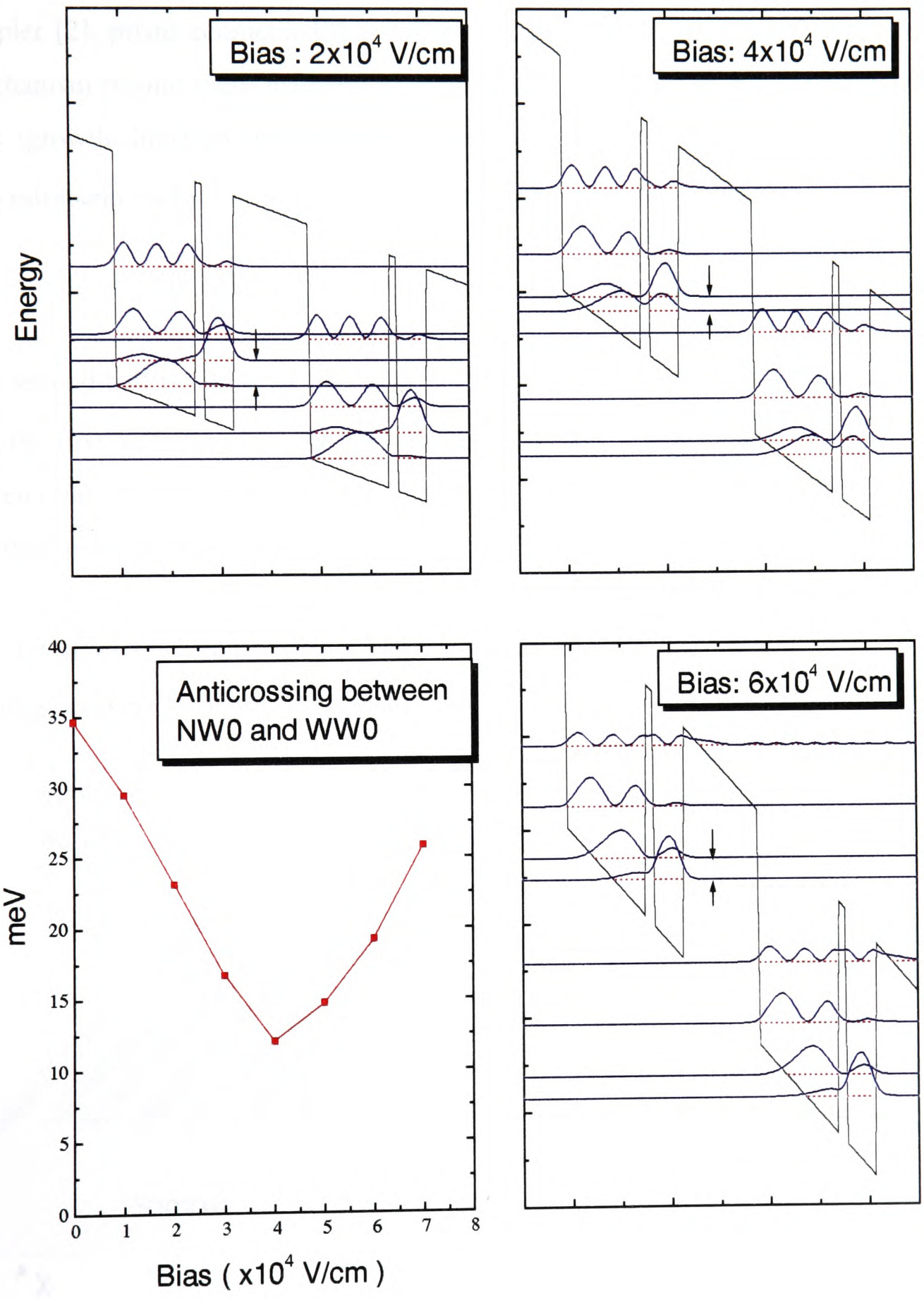

Figure 7-3 Conduction band profiles of G953 under different bias. Also shows the anticrossing between the bottom two subbands.

7.1.2 Grating Coupler

In order to modulate the tunnelling process by pumping carriers from the lowest subband, far infrared radiation is applied. Nevertheless, as shown in Eq. (3.23), the intraband process is actually forbidden in zero magnetic field. To activate the intersubband transition, various techniques have been used including the waveguide coupler [2], prism geometry [3] and Brewster angle orientation [4]. The actual working mechanism behind these different approaches is to produce an electric field along the z-axis (growth direction) which introduces a new term into the interaction Hamiltonian. The intraband transition matrix element $\langle f|\vec{\varepsilon}\cdot\vec{p}|i\rangle$ can thus be written as

$$\left|\langle f|\vec{\varepsilon}\cdot\vec{p}|i\rangle\right| \propto \sum_{m,n}^{\Gamma}\left(\int_{-\infty}^{\infty}\phi_m^{f^*} p_z \phi_n^i \cdot dz\right)\bullet\left(\int \chi_m^{f^*}\chi_n^i \cdot dxdy\langle\Gamma_m|\Gamma_n\rangle\right) \tag{7.1}$$

The second half is non-zero only if $\chi_m^f = \chi_n^i$, ensuring in-plane momentum conservation, and the first half represents the wavefunction overlap between the final state and the first differential of the initial state. This new allowed transition is therefore between neighbouring subbands with the same in-plane momentum.

Of all the methods which attempt to introduce extra electric fields into the structure, grating couplers have advantages over the rest in many ways. The major benefits include the feasibility of using normal incidence and a higher coupling efficiency [5,6]. To demonstrate that, an extra electric field can be generated simply by applying metal strips to the samples, we first consider a plane electromagnetic (EM) wave incident normally on a grating consisting of infinitely thin and conducting strips on the surface of a semiconductor as shown in Figure 7-4. The z-component of the

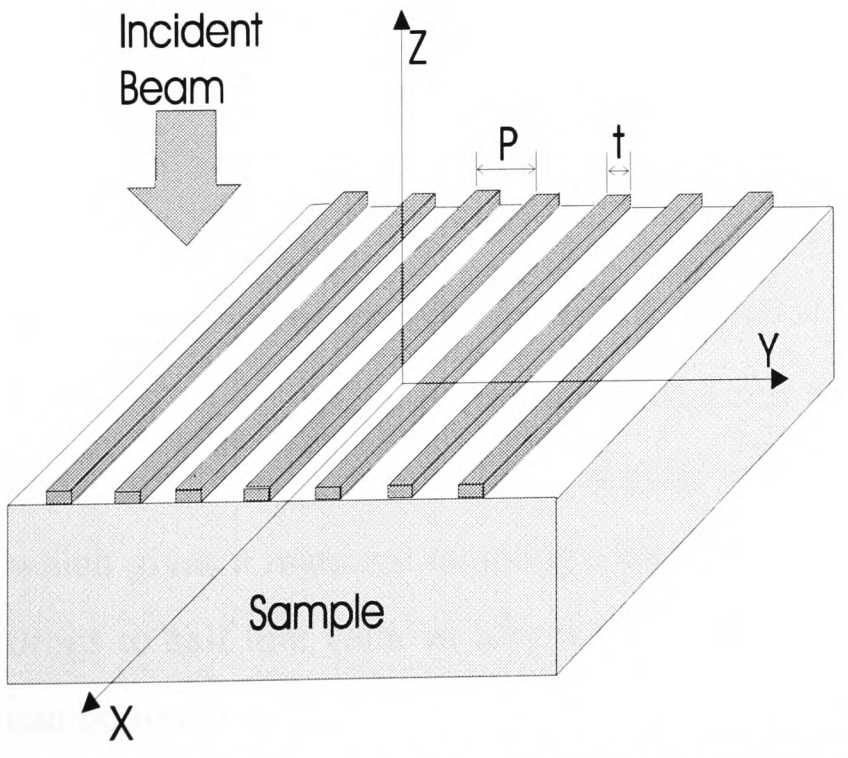

Figure 7-4 Metallic grating structure. p is the period and t is the width of the metal strip.

electric field E_z can be derived from the Maxwell equation

$$\nabla \times \vec{H} = \vec{j} + \varepsilon \frac{\partial \vec{E}}{\partial t} \tag{7.2}$$

hence

$$E_z = \frac{c}{i\omega n}\left(\frac{\partial H_y}{\partial x} - \frac{\partial H_x}{\partial y}\right)$$

where ω is the frequency of the EM wave and n is the index of refraction of the semiconductor in the wavelength range of interest. For the coordinate chosen, $\vec{H}$ is a function of y and z only since any shift along x is just a matter of reference frame. Therefore, the x-polarised wave (E_x, H_y) does not contribute to E_z. The incident wave with component (E_y, H_x) is given by

$$E_y = E_{y0}e^{-ikz}, H_x = H_{x0}e^{-ikz} \tag{7.3}$$

where the time dependence $e^{i\omega t}$ has been omitted for simplicity. The total field after diffraction by the grating can be written

$$H_x = H_{x0}e^{-ikz} + \sum_{j=-\infty}^{\infty} R_j e^{ik(y\sin\phi_j + z\cos\phi_j)}, z > 0 \tag{7.4}$$

$$H_x = -\sum_{j=-\infty}^{\infty} T_j e^{ik'(y\sin\phi'_j - z\cos\phi'_j)}, z < 0$$

where R_j and T_j are the reflection and transmission coefficients of the jth order, respectively. ϕ_j and ϕ'_j are the diffraction angles inside and outside the materials. Meeting the boundary condition, the z-component of the electric field in the semiconductor can be written as

$$E_z = -\sum_{j=-\infty}^{\infty} T_j \left(\frac{j\lambda}{np}\right) e^{ik'(y\sin\phi_j - z\cos\phi_j)} \tag{7.5}$$

p is the period of the gratings and λ is the wavelength of the incident beam. According to Eq. (7.5), an optimised grating period can be evaluated. The grating applied to G953 consists of closely-spaced lines of gold with a width of 10 μm and a period of 20 μm, which gives a maximal coupling efficiency at a wavelength of 66 μm and the efficiency drops to half that value at longer wavelengths. A good review of the coupling efficiency can be found in Ref. [7].

7.2 Photocurrent Study

The inter-well carrier tunnelling process is investigated by photocurrent measurements in varying electric field. Since the quantum wells of G953 are intrinsic, a constant carrier injection is necessary, and in this case, it is done by a 670 nm diode laser. The particular wavelength lies between the bandgap of GaAs wells and $Al_xGa_{1-x}As$ barriers. Thus at low temperature, where the thermally assisted escape from the wells is negligible, the measured photocurrent is primarily a function of the inter-well tunnelling.

7.2.1 Experimental Setup

Figure 7-5 shows a schematic diagram of the experimental arrangement for the photocurrent study. The samples are mounted on a 3D transition stage placed at the end of the insert. This allows accurate positioning of the device at the centre of both the visible and far infrared laser beams. The visible wavelength light from the suitably attenuated 670 nm laser is delivered co-linearly with the infrared laser beam, similar to the arrangement shown in Figure 6-4. To make sure the same amount of visible light is

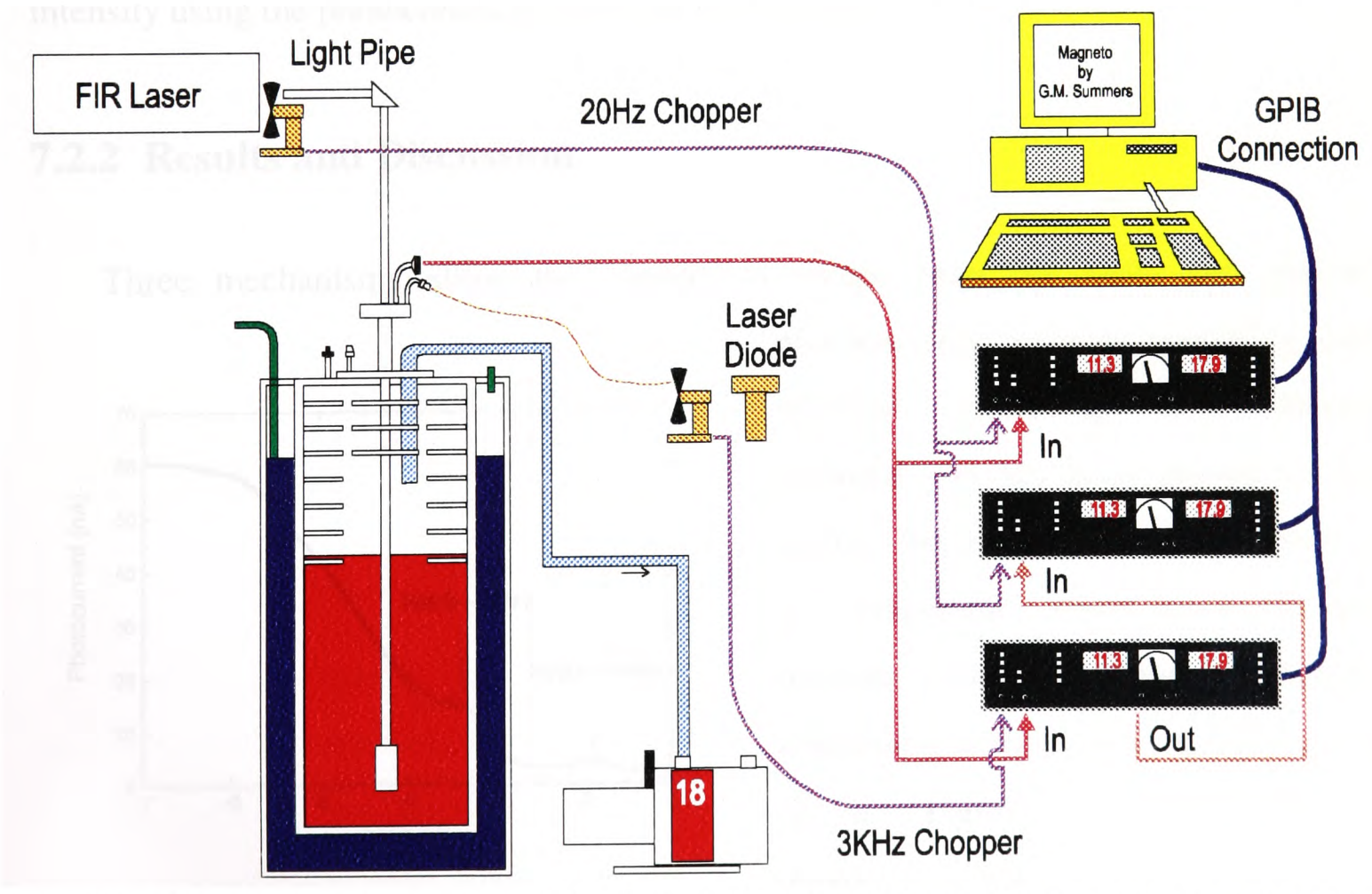

Figure 7-5 Experimental arrangement for the far infrared modulated photocurrent measurements.

reaching the sample consistently, the laser diode is carefully defocused while monitoring the photocurrent. A Keithley 236 measuring unit is used as the voltage source to offer the electric field cross the coupled quantum wells. In contrast to previous studies [8], the sample is immersed in the Helium bath instead of using Helium gas as a heat exchange medium. The Ge photodetector used to do cyclotron resonance experiments in pulsed magnetic field is mounted close to the sample to monitor the far infrared intensity.

The detection scheme is very similar to that of the ODCR. The visible excitation beam is chopped at 3 kHz and the far infrared laser is chopped at 20 Hz. The experiment requires at least two lock-in amplifiers as the resulting photocurrent signal possesses two frequency components, one due to the excitation of the visible light and the other due to the modulation of the infrared beam. The photocurrent is detected using a current pre-amplifier with the reference signal from the mechanical chopper wheel. The pre-filter of the photocurrent lock-in amplifier is set to be flat, so that the modulation of photocurrent can be measured by a second lock-in amplifier which is connected to the output of the first with the reference signal from the infrared chopper. The first lock-in, therefore, gives the photocurrent and the second lock-in outputs the modulation due to the infrared illumination. A third lock-in amplifier is usually employed to monitor the infrared intensity using the photoconductivity of the Ge detector.

7.2.2 Results and Discussion

Three mechanisms allow the carriers to escape from the wells and generate photocurrents: resonant tunnelling, non-resonant tunnelling and thermal emission. As has been proven by Fox [9,10], thermal emission is minute at low temperature, which leaves the non-resonant tunnelling being the principal contributor with resonant features on top of it. Figure 7-6 illustrates the photocurrent trace of G953 at 2 K. With

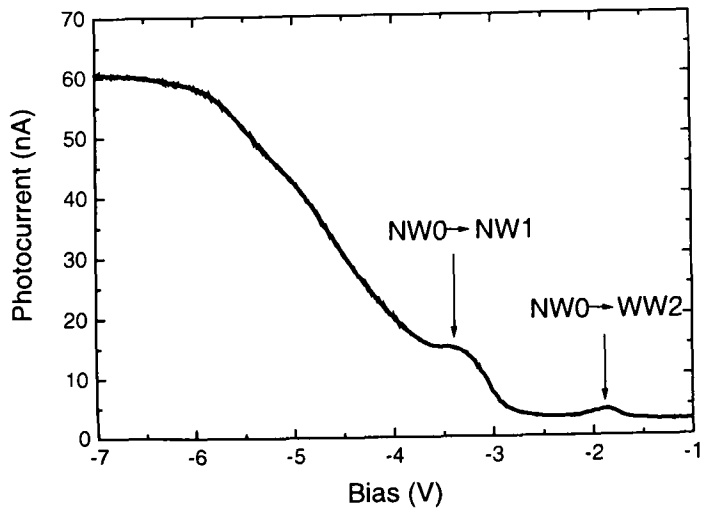

Figure 7-6 The photocurrent trace of G953 at 2K.

low inverse bias (<-2 V), the non-resonant tunnelling is very weak due to the high effective barriers. As the bias increases, the tunnelling efficiency takes off and reaches the plateau above -6 V, where all the photo-injected carriers are swept out of sample. The resonant tunnelling peaks at -1.8 V and -3 V correspond to the electron tunnelling from NW0 through the thick barrier to WW2 and NW1, respectively. A connection between the calculated band profile in Figure 7-3 and photocurrent trace can thus be established, which also yields the valuable subband anticrossing vs. bias relation.

In contrast to the previous study [11,12] where the measurements were done at 4 K cooled via ^{4}He gas, the sample was in direct contact with 2 K ^{4}He liquid this time. The far infrared effects were very complex in the earlier experiments. The modulation was highly dependent on the infrared power. Besides, the signal changed at different infrared chopping speed - a signature of slow processes due to lattice heating [13]. By immersing the sample in liquid, we are able to get rid of these effects which obscured the intersubband process in the past. Figure 7-7 shows the photocurrent traces done under different conditions. The 4 K trace shows two clear peaks corresponding to resonant tunnelling and is positive at all fields. The 2 K trace is generally negative at high bias (> -3.5V) with the same two resonant peaks at low fields.

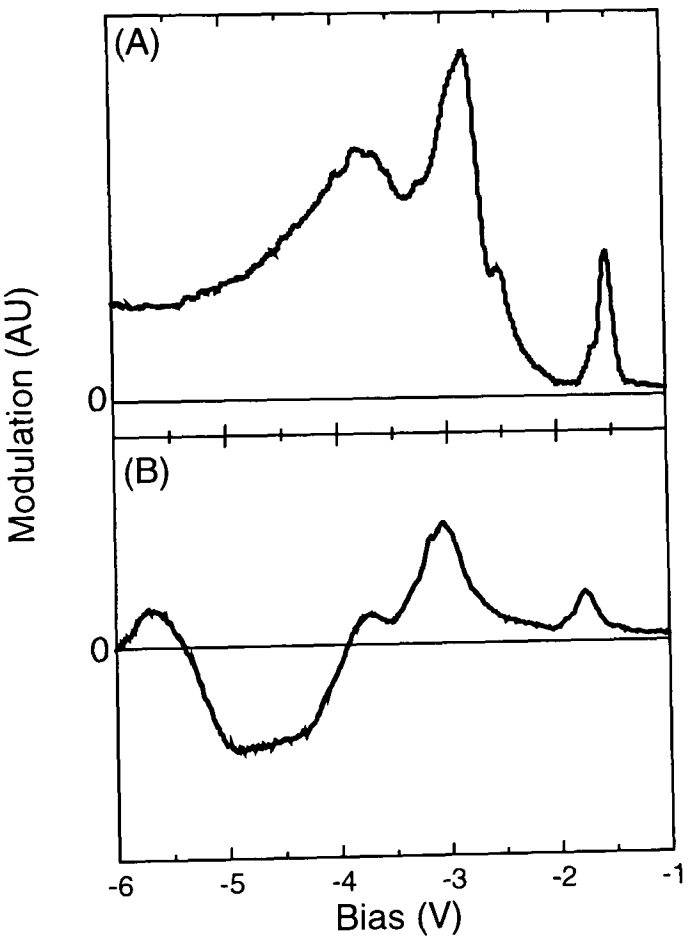

Figure 7-7 The far infrared modulation by 57 mm at (A) 4 K with jacket and (B) 2 K in liquid.

The far infrared induced effects can generally be put into two categories: intersubband and intrasubband. The former may be either resonant or non-resonant and the latter includes the lattice heating effect. The intrasubband process always promotes the inter-well tunnelling (positive signal) by scattering electrons higher up in the subbands. On the contrary, the effect is very much determined by electric fields for the

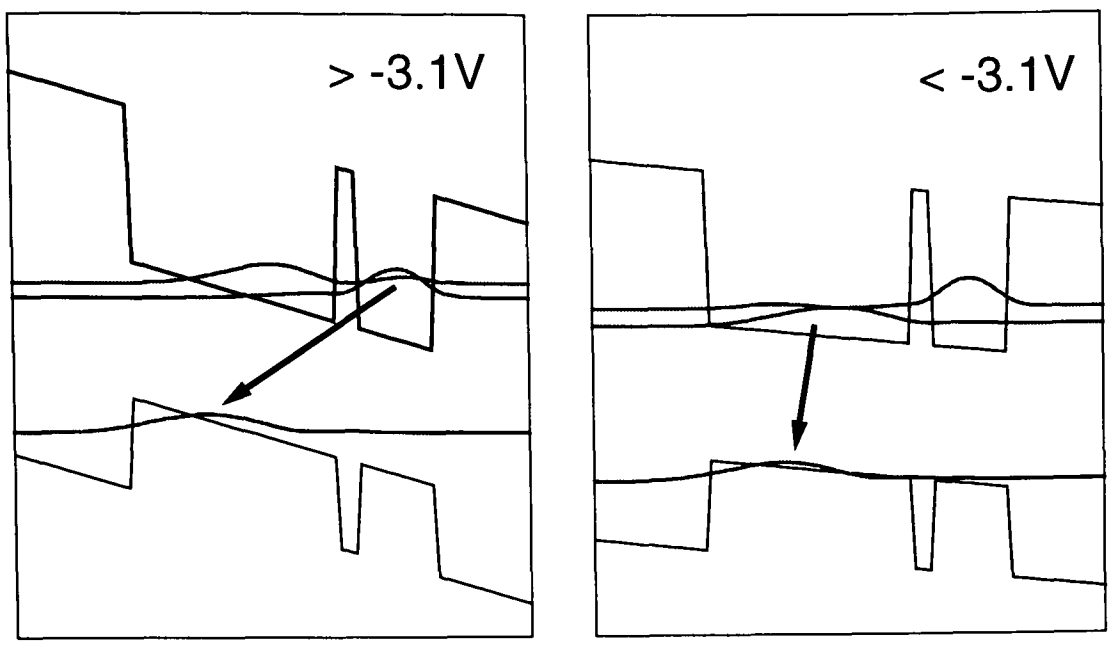

Figure 7-8 Band profiles in the indirect (left) and direct (right) recombination regimes. The arrow indicates the lowest energy recombination channel.

intersubband process. As shown in Figure 7-8, the ground state moves from WW0 to NW0 with an inverse bias higher than -3.1 V. Therefore, the intersubband process will promote inter-well tunnelling by pumping electrons from wide wells to narrow wells at low fields but suppress tunnelling at high fields by pumping in the reverse direction. Another description is based on the radiative recombination processes. At high fields, the infrared moves electrons to WW0 which has larger overlap with the hole wavefunctions and thus enhances the recombination and suppresses the photocurrent. Table 7-2 summarises the effect of far infrared illumination.

Table 7-2 The summation of effects by infared modulation at different biases. PC for photocurrent and PL for photoluminescence.

		Bias>-3.1 V (NW0<WW0)	Bias<-3.1 V (NW0>WW0)
PC	Intrasubband	Enhanced	Enhanced
	Intersubband	Suppressed	Enhanced
PL	Intrasubband	Suppressed	Suppressed
	Intersubband	Enhanced	Suppressed

The 4 K data shown in Figure 7-7 are the superposition of these two effects but dominated by intrasubband process. Direct contact with the liquid can remove the bolometric effect completely and increase the lifetime of other intrasubband processes, and, as a result, makes the intersubband effect more pronounced. This explains the opposite response at high fields. Features at -1.8 V and -3 V are probably the result of non-resonant intersubband process by exciting electrons from WW0 to NW0.

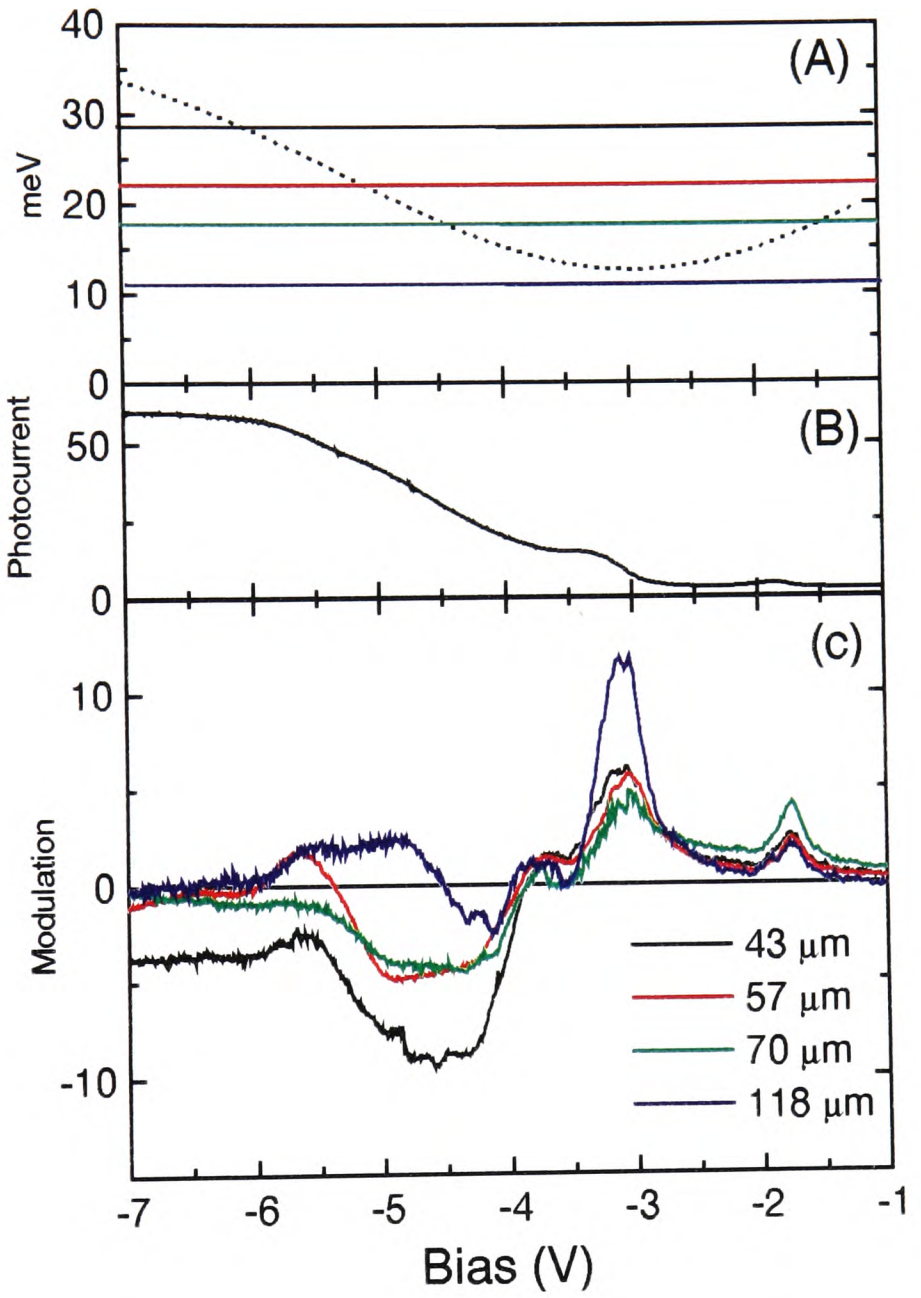

Figure 7-9 (A) The energy of the NW0-WW0 intersubband transition against calibrated bias with far infrared photon energies marked. (B) The photocurrent characteristic as shown in Figure 7-6. (C) The change in photocurrent when radiation is incident for four different wavelengths.

Figure 7-9 shows the modulation by infrared for four different wavelengths. The traces agree well with the intersubband effect introduced earlier but are still influenced by the intrasubband process. At a bias higher than -3.5 V (higher than the anticrossing point), the modulation of photocurrent is generally negative due to the non-resonant intersubband

process but strongly dependent on the infrared wavelength. This is understood as a result of the valence band resonance [13]. At such high bias, the Stark effect [9] in the valence band can produce a subband splitting as big as the infrared energy, and, consequently, ground state holes are able to absorb the infrared and jump to excited states. These excited holes are too heavy for inter-well tunnelling but can still affect photocurrents by perturbing the recombination process. It is therefore not easy to identify the potential conduction band resonances in this regime.

At lower bias, the non-resonant intersubband features at resonant tunnelling positions (-1.8 V and -3 V) look quite similar for all infrared wavelengths. After careful observation of the normalised traces in Figure 7-9 (C), however, one can find certain differences between them. The peak at -3 V is most strongly enhanced by 118.88 μm while the peak at -1.8 V is most strongly enhanced by 70.51 μm. Figure 7-9 (A) shows the anti-crossing splitting between the ground and the first excited states (NW0 and WW0). At -2.9 V, the subband splitting is about 11 meV, close to the photon energy of 118.88 μm radiation (10.8 meV). The further enhancement at -3 V for this particular wavelength can thus be credited as the intersubband resonance. For 70.51 μm (17.6 meV), the corresponding resonance field is -1.6 V which results in the enhancement at -1.8 V in experiments. This is because -1.6 V is well within the low tunnelling efficiency regime and, consequently, any modulation of photocurrent is very unlikely to be seen. The observable feature of this resonance, therefore, turns out to be the tail effect in the resonant tunnelling peak (-1.8 V).

7.3 Photoluminescence Study

Photoluminescence experiments have been carried out with and without the modulation by far infrared beams. They are intended to investigate the optical properties of the sample and compare them with the characteristics obtained from the photocurrent measurements.

7.3.1 Experimental Setup

The setup to conduct the far infrared modulated photoluminescence is very similar to the one presented in Section 7.2.1 without the lock-in amplifiers. Signals are collected with the CCD camera used in the previous study of Chapter 6 but a 1/4 meter light path spectrometer is employed to give a wider cover in wavelengths. Since the size of the mesa is very small, one may expect the photoluminescence comes from both the device and the materials surrounding it if the fibre end is too far away from the mesa, which will make the experiment impossible. In order to get the fibre end as close to the mesa as possible, only one 400 μm fibre is used to both deliver the illumination and collect the luminescence. At the spectrometer end, two convex lenses are positioned parallel to each other. They are carefully arranged to make sure the two focal points of the lens set sit on either the fibre end or the input slit of the spectrometer. A small mirror mounted on two crossed fishing lines, hangs between the lenses. The red laser beam is reflected from the mirror and focuses on the fibre end to offer the excitation needed. The emerging luminescence is then collected by the first lens and travels parallel to its light path before reaching the second lens which focuses it again at the spectrometer slit. The mirror and the support lines inevitably block part of the signal. However, the first lens spreads the luminescence on to a bigger area and hence cut down the loss. The same idea is used in reflective telescopes.

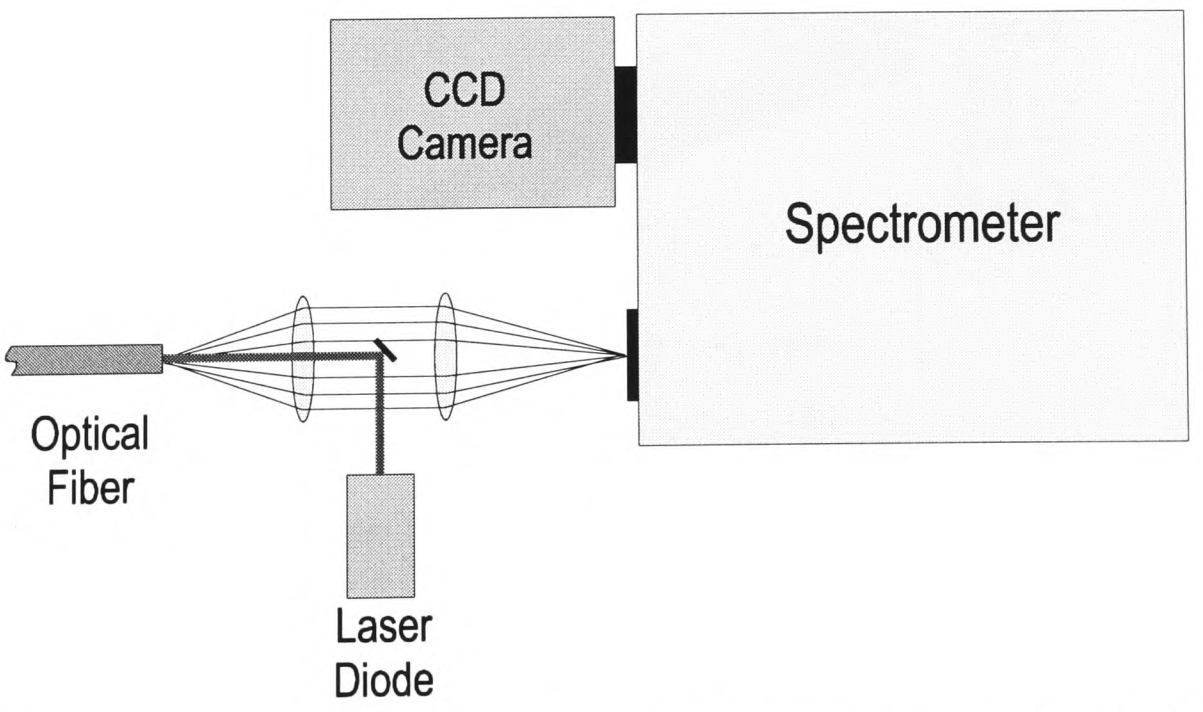

Figure 7-10 Experimental arrangement for the far infrared modulated photoluminescence measurements

Figure 7-11 shows the 4 K photoluminescence spectra of sample G953 as a function of applied bias. The waterfall plot at upper half gives a clear picture of the spectra and the bias dependent behaviour is better illustrated in the contour plot below. The main luminescence peak is observed to shift to longer wavelength as the field across the diode is increased. This is due to the decreasing energy difference between lowest electron and hole levels. The field independent luminescence at 1535 meV is not from the mesa but the area surrounding it. As explained previously, it is inevitable but has been reduced to the lowest possible level.

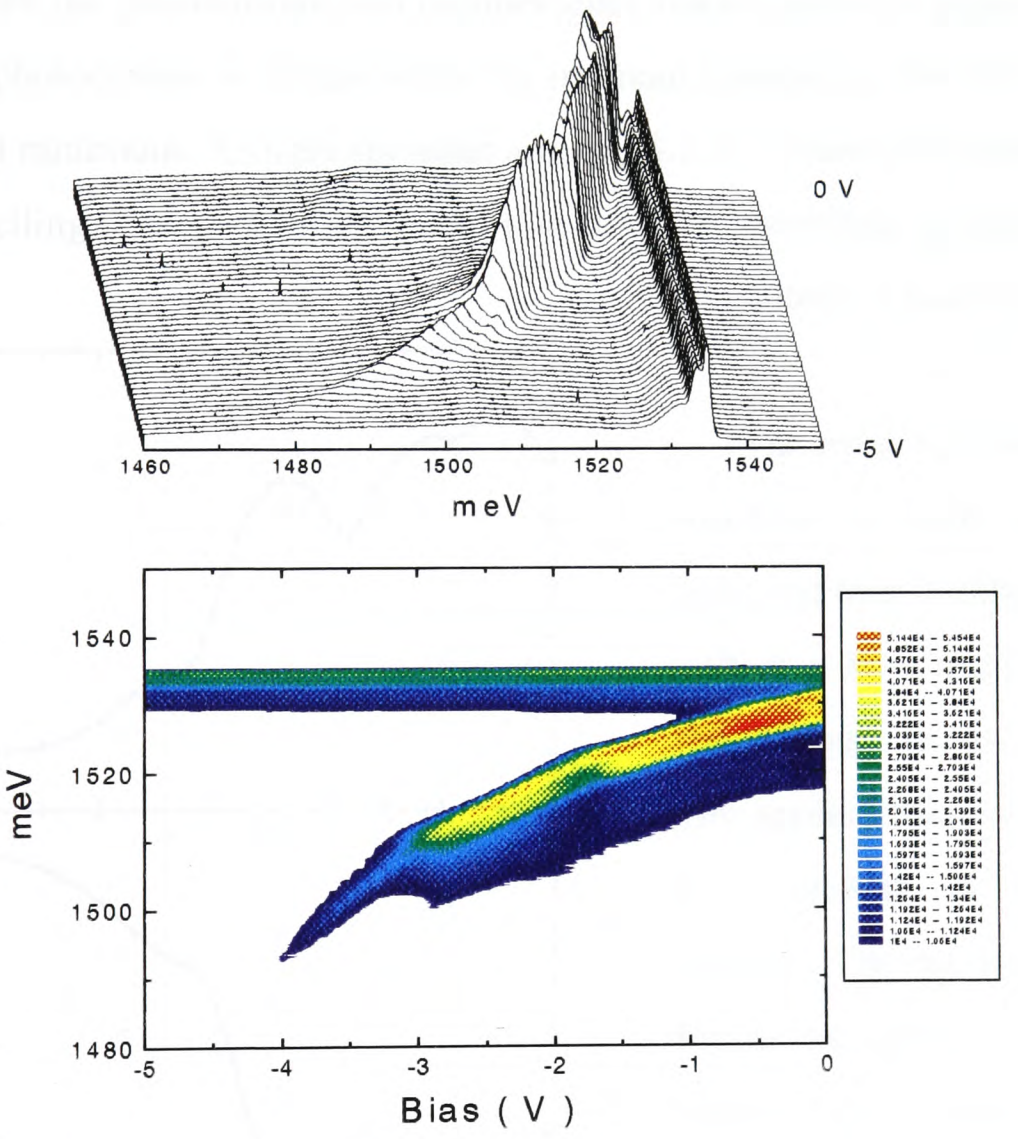

Figure 7-11 The upper half shows the waterfall plot of photoluminescence spectra under different biases with the corresponding contour plot showing in the lower half. The fringe on the contour plot is nothing physical but computational due to the spacing between spectra (only 51 spectra horizontally).

At low field, the luminescence is complex with multiple peaks, which is due to the lifting of valence band degeneracy by strains introduced by the metal gratings applied. The main peak shifts slowly with increasing electric field and a slight reduction in intensity can be seen at -1.8 V. At around -3.1 V, the luminescence decreases in magnitude dramatically and increases its shift in energy until it completely disappears. To understand the relation between luminescence intensity and electric fields, signals are integrated at each field and plotted along with the photocurrent trace in Figure 7-12. Presuming the non-radiative recombination process does not change much with electric fields, the injected carriers can either tunnel through the barriers to generate photocurrents or recombine with holes to give luminescence. The idea is confirmed by the mirror relation between the photocurrent and luminescence traces shown in Figure 7-12. At -1.8 V, where the photocurrent is enhanced by the resonant tunnelling, the total luminescence reaches a local minimum. A slight shoulder around -3.5 V outlines the position of another resonant tunnelling. The high efficiency of non-resonant tunnelling at higher field marks the decline of luminescence.

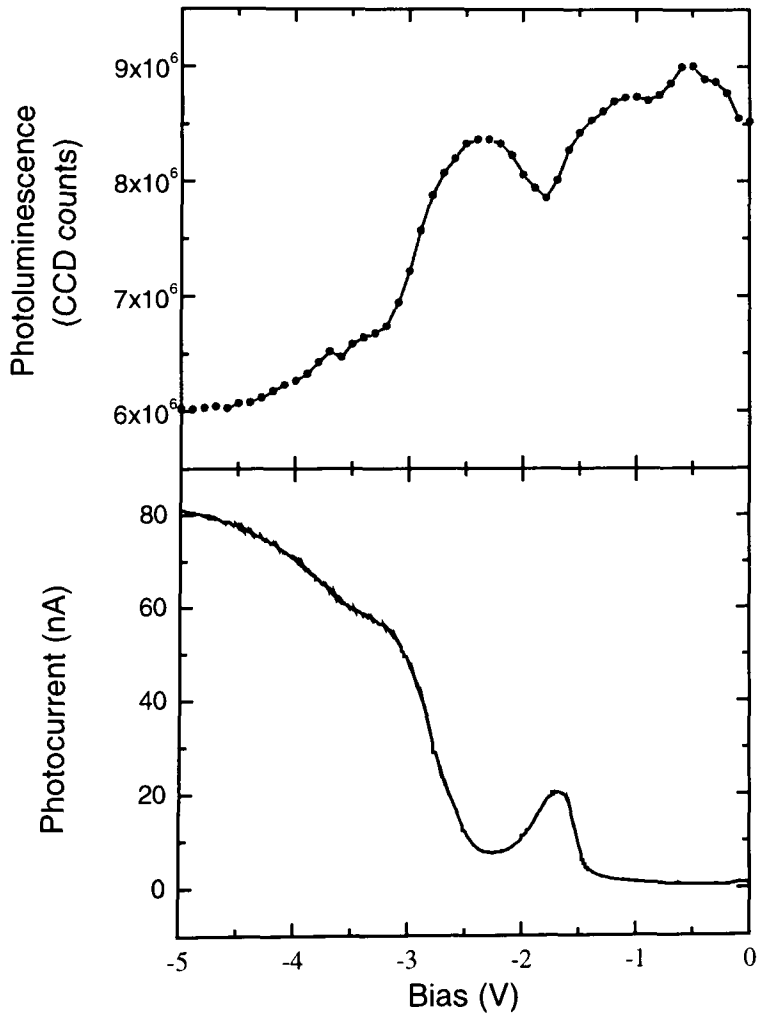

Figure 7-12 Photocurrent trace and photoluminescence magnitude of G953 plotted against bias at 4 K.

The main luminescence peak is observed to shift slowly at low field, and then exhibit a much larger shift at a bias higher than -3.1 V. The change in exciton shift rate with applied bias can be understood as a change in the nature of excitons. The energy shift is mainly due to the quantum confined Stark effect of the ground electron level. At low field (<-3.1 V), the ground state is WW0 and changes to NW0 at high field. As the confinement energy for narrow wells is stronger than for wide wells, the Stark shift

is enhanced in the narrow wells, which explains the sudden change in shift gradient. At the same time, the excitonic recombination transforms from direct to indirect as shown in Figure 7-8. This offers an alternative view of the sample characteristics. Under low applied fields, the photoluminescence efficiency of the sample is high and the photocurrent signal is small. This is because the large overlap between the electron and hole wavefunctions leads to fast recombination and the thick barriers reduce the non-resonant tunnelling efficiency. As the field is increased, the effective barrier height decreases and the tunnelling probability hence increases, which means a decline of photoluminescence. The luminescence is further reduced when the excitonic recombination turns to be indirect under a reverse bias higher than -3.1 V.

Figure 7-13 shows the modulation of the photoluminescence caused by 118.88 μm. This effect is so weak that no modulation can be seen unless we use the full laser power of each lines. It has been shown in a previous study [11] that the carrier heating in this sample can obscure the possible intersubband resonance. It is therefore not surprising we do not see infrared dependent modulation. The overall behaviour is a suppression of the luminescence at all electric fields, which agrees very much with the intrasubband heating picture introduced in the previous section. With the infrared illuminating the sample, the electrons are heated either through intrasubband absorption or lattice scattering. The non-resonant tunnelling is promoted thanks to these hot carriers, which means a reduction in radiative recombination. At high field, the modulation is apparently more efficient than that at low field considering the absolute luminescence intensity without infrared. This is due to the relative low effective barrier in this regime. At low field, a slight differential type of signal is observed. This is understood as an effect combining the suppression with a shift to longer wavelength, evidence for a change in lattice temperature.

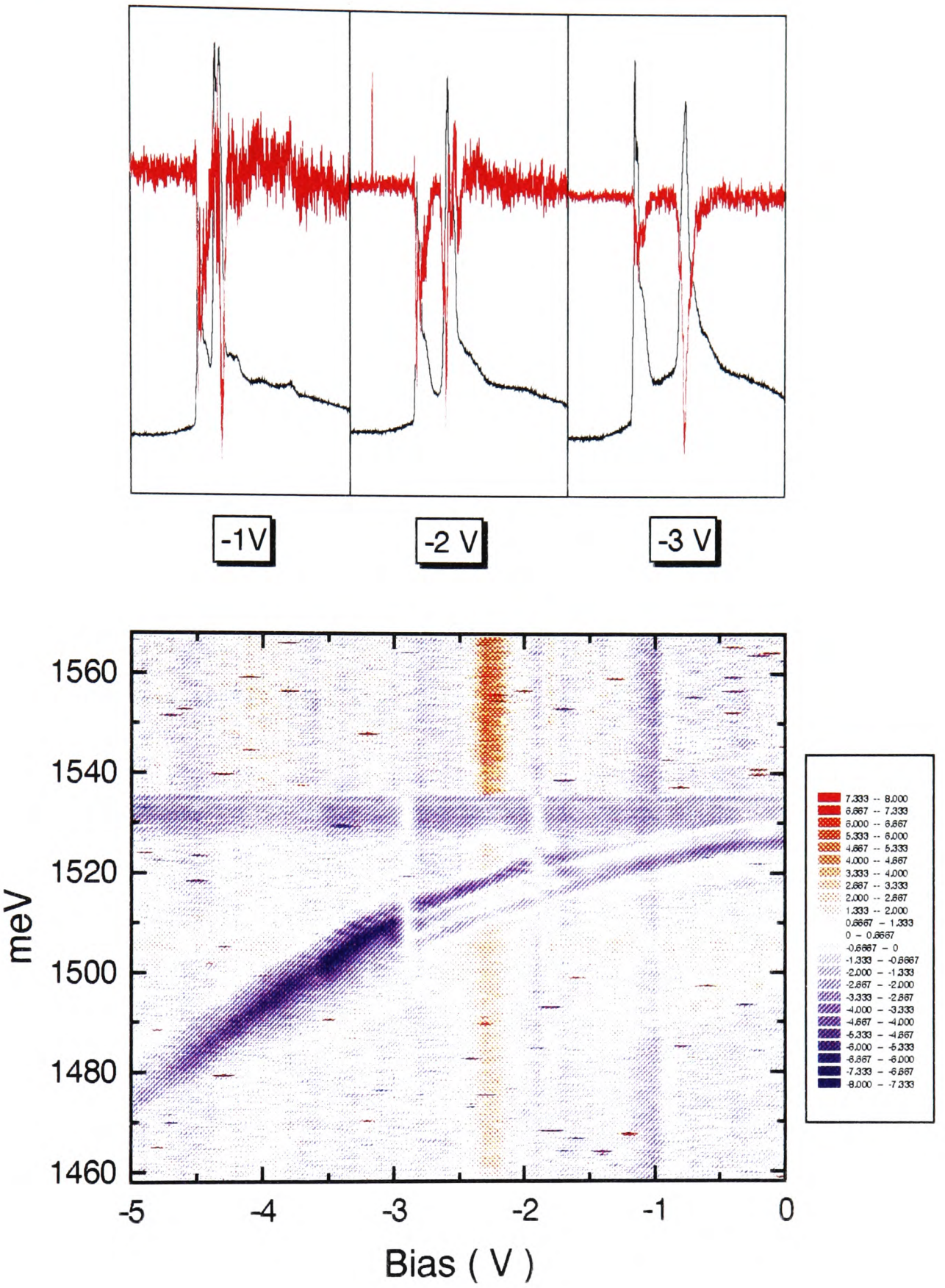

Figure 7-13 The effect of far infrared on photoluminescence done by 118.88 μm. The upper half shows the luminescence in black and modulation in red at three particular biases with the lower half illustrating the whole modulation in contour plot.

7.4 Conclusion

The effect of far infrared radiation on carriers in a GaAs/$Al_xGa_{1-x}As$ coupled quantum well photodiode has been investigated. The absolute change in photocurrent is affected by intrasubband carrier heating severely. Only by immersing the sample in liquid Helium can we promote the intersubband process otherwise dwarfed by the heating. When the far infrared photons are resonant with the intersubband transition between the anticrossing electronic subbands of the coupled quantum well, we observe an enhancement of the photocurrent in the device. This, however, can only be observed at low bias. At high inverse bias, the valence band resonance kicks in which obscures the conduction band resonance. The low bias regime, due to its low quantum efficiency nature, can only show resonances close to the two resonant tunnelling peaks. The limited operating bias and low temperature requirement convince us that the device studied is inefficient as an electronic detector.

The photoluminescence spectra measured at 4 K agree well with the intrasubband heating picture, which shows suppression at all fields regardless of the infrared photon energy. The modulation efficiency at high field is quite astonishing given the fact that the luminescence is weak compared to low field. This is possibly due to the low effective barrier, and, as a result, the intrasubband processes promote the inter-well tunnelling immensely.

References

[1] For a review of quantum well infrared photodevices, B. F. Levine, *J. Appl. Phys.* **74**, R1 (1993).

[2] B. F. Levine, R. J. Malik, J. Walker, K. K. Choi, C. G. Bethea, D. A. Kleinman and J. M. Vanderberg, *Appl. Phys. Lett.* **50**, 273 (1987).

[3] B. D. McCombe, R. T. Holm and D. E. Schafer, *Solid State Comm.* **32**, 603 (1979).

[4] M. Nakayama, H. Duwahara, H. Kato and K. Kubota, *Appl. Phys. Lett.* **51**, 1741 (1987).

[5] K. W. Goossen and S. A. Lyon, *Appl. Phys. Lett.* **47**, 1257 (1985).

[6] Lian Zheng, W. L. Schaich and A. H. MacDonald, *Phys. Rev. B* **41**, 8493 (1990).

[7] W. J. Li and B. D. McCombe, *J. Appl. Phys.* **71**, 1038 (1992).

[8] A. M. Tomlinson, C. C. Chang, R. J. Stone, C. T. Foxon, R. J. Nicholas and A. M. Fox, *Phys. Stat. Sol (b)* **204**, 166 (1997).

[9] R. G. Ispasoiu, A. M. Fox, C. T. Foxon, J. E. Cunningham and W. Y. Jan, *Semicond. Sci. Technol.* **9**, 545 (1994).

[10] A. M. Fox, R. G. Ispasoiu, C. T. Foxon, J. E. Cunningham and W. Y. Jan, *Appl. Phys. Lett.* **63**, 2917 (1993).

[11] R. J. Stone, J. G. Michels, S. L. Wong, C. T. Foxon, R. J. Nicholas and A. M. Fox, *Appl. Phys. Lett.* **69**, 3569 (1996).

[12] R. J. Stone, *D.Phil thesis*, Oxford (1997).

[13] A. M. Tomlinson, C. C. Chang, R. J. Nicholas and A. M. Fox, *Proceedings of 24th International Conference on the Physics of Semiconductors*, World Scientific, Singapore (1998).

Appendix I The 8-band zero field bulk k.p Hamiltonian for the [001] orientation.

$c\uparrow,\lvert 1/2,+1/2\rangle$	$hh\uparrow,\lvert 3/2,+3/2\rangle$	$lh\downarrow,\lvert 3/2,-1/2\rangle$	$so\downarrow,\lvert 1/2,-1/2\rangle$	$c\downarrow,\lvert 1/2,-1/2\rangle$	$hh\downarrow,\lvert 3/2,-3/2\rangle$	$lh\uparrow,\lvert 3/2,+1/2\rangle$	$so\uparrow,\lvert 1/2,+1/2\rangle$
$(F+1/2)k^2$ $+E_G$							
$\sqrt{1/2}Pk_-$	$-1/2(\gamma_1-2\gamma_2)k_z^2$ $-1/2(\gamma_1+\gamma_2)k_+k_-$						
$-\sqrt{1/6}Pk_+$	$\sqrt{3/4}(\mu k_-^2+\overline{\gamma}k_+^2)$	$-1/2(\gamma_1+2\gamma_2)k_z^2$ $-1/2(\gamma_1-\gamma_2)k_+k_-$					
$\sqrt{1/3}Pk_+$	$-\sqrt{3/2}(\mu k_-^2+\overline{\gamma}k_+^2)$	$-\sqrt{2}\gamma_2k_z^2$ $-\sqrt{1/2}\gamma_2k_+k_-$	$-\Delta-1/2\gamma_1k^2$				
0	0	$-\sqrt{2/3}Pk_z$	$-\sqrt{1/3}Pk_z$	$(F+1/2)k^2$ $+E_G$			
0	0	$-\gamma_3\sqrt{6(n+2)B}k_z$	$-\gamma_3\sqrt{3(n+2)B}k_z$	$-\sqrt{1/2}Pk_+$	$-1/2(\gamma_1-2\gamma_2)k_z^2$ $-1/2(\gamma_1+\gamma_2)k_+k_-$		
$-\sqrt{2/3}Pk_z$	$\sqrt{3}\gamma_3k_+k_z$	0	$\sqrt{9/2}\gamma_3k_+k_z$	$\sqrt{1/6}Pk_-$	$\sqrt{3/4}(\overline{\gamma}k_-^2+\mu k_+^2)$	$-1/2(\gamma_1+2\gamma_2)k_z^2$ $-1/2(\gamma_1-\gamma_2)k_+k_-$	
$\sqrt{1/3}Pk_z$	$-\sqrt{3/2}\gamma_3k_+k_z$	$\sqrt{9/2}\gamma_3k_-k_z$	0	$\sqrt{1/3}Pk_-$	$\sqrt{3/2}(\overline{\gamma}k_-^2+\mu k_+^2)$	$\sqrt{2}\gamma_2k_z^2$ $-\sqrt{1/2}\gamma_2k_-k_+$	$-\Delta-1/2\gamma_1k^2$

Appendix II. The 8-band magnetic field bulk k.p Hamiltonian for the [001] orientation.

n	n-1	$n+1$	$n+1$	$n+1$	$n+2$	n	n
$c,\left\|\frac{1}{2},+\frac{1}{2}\right\rangle$	$hh,\left\|\frac{3}{2},+\frac{3}{2}\right\rangle$	$lh,\left\|\frac{3}{2},-\frac{1}{2}\right\rangle$	$so,\left\|\frac{1}{2},-\frac{1}{2}\right\rangle$	$c,\left\|\frac{1}{2},-\frac{1}{2}\right\rangle$	$hh,\left\|\frac{3}{2},-\frac{3}{2}\right\rangle$	$lh,\left\|\frac{3}{2},+\frac{1}{2}\right\rangle$	$so,\left\|\frac{1}{2},+\frac{1}{2}\right\rangle$

$$
\begin{array}{cccccccc}
2(F+\frac{1}{2})(n+\frac{1}{2})B & & & & & & & \\
+\frac{1}{2}B+E_G & & & & & & & \\
P\sqrt{nB} & -(\gamma_1+\gamma_2)(n-\frac{1}{2})B & & & & & & \\
 & -\frac{3}{2}\kappa B & & & & & & \\
-P\sqrt{\frac{1}{3}(n+1)B} & \bar{\gamma}B\sqrt{3n(n+1)} & -(\gamma_1-\gamma_2)(n+\frac{3}{2})B & & & & & \\
 & & +\frac{1}{2}\kappa B & & & & & \\
P\sqrt{\frac{2}{3}(n+1)B} & -\bar{\gamma}B\sqrt{6n(n+1)} & \sqrt{2}\gamma_2 B(n+\frac{3}{2}) & -\Delta-\gamma_1(n+\frac{3}{2})B & & & & \\
 & & -\sqrt{\frac{1}{2}}B(\kappa+1) & +(\kappa+\frac{1}{2})B & & & & \\
0 & 0 & 0 & 0 & 2(F+\frac{1}{2})(n+\frac{3}{2})B & & & \\
 & & & & -\frac{1}{2}B+E_G & & & \\
0 & 0 & 0 & 0 & -P\sqrt{(n+2)B} & -(\gamma_1+\gamma_2)(n+\frac{5}{2})B & & \\
 & & & & & +\frac{3}{2}\kappa B & & \\
0 & 0 & 0 & 0 & P\sqrt{\frac{1}{3}(n+1)B} & \bar{\gamma}B\sqrt{3(n+1)(n+2)} & -(\gamma_1-\gamma_2)(n+\frac{1}{2})B & \\
 & & & & & & -\frac{1}{2}\kappa B & \\
0 & 0 & 0 & 0 & P\sqrt{\frac{2}{3}(n+1)B} & \bar{\gamma}B\sqrt{6(n+1)(n+2)} & -\sqrt{2}\gamma_2 B(n+\frac{1}{2}) & -\Delta-\gamma_1(n+\frac{1}{2})B \\
 & & & & & & -\sqrt{\frac{1}{2}}B(\kappa+1) & -(\kappa+\frac{1}{2})B
\end{array}
$$

H_0

$$
\begin{array}{cccccccc}
0 & & & & & & & \\
0 & 0 & & & & & & \\
0 & 0 & 0 & & & & & \\
0 & 0 & 0 & 0 & & & & \\
0 & 0 & -\sqrt{\frac{2}{3}}P & -\sqrt{\frac{1}{3}}P & 0 & & & \\
0 & 0 & -\gamma_3\sqrt{6(n+2)B} & -\gamma_3\sqrt{3(n+2)B} & 0 & 0 & & \\
-\sqrt{\frac{2}{3}}P & \gamma_3\sqrt{6nB} & 0 & 3\gamma_3\sqrt{(n+1)B} & 0 & 0 & 0 & \\
\sqrt{\frac{1}{3}}P & -\gamma_3\sqrt{3nB} & 3\gamma_3\sqrt{(n+1)B} & 0 & 0 & 0 & 0 & 0
\end{array}
$$

$H_1 * k_Z$

n $c,\left\vert \frac{1}{2},+\frac{1}{2}\right\rangle$	n-1 $hh,\left\vert \frac{3}{2},+\frac{3}{2}\right\rangle$	$n+1$ $lh,\left\vert \frac{3}{2},-\frac{1}{2}\right\rangle$	$n+1$ $so,\left\vert \frac{1}{2},-\frac{1}{2}\right\rangle$	$n+1$ $c,\left\vert \frac{1}{2},-\frac{1}{2}\right\rangle$	$n+2$ $hh,\left\vert \frac{3}{2},-\frac{3}{2}\right\rangle$	n $lh,\left\vert \frac{3}{2},+\frac{1}{2}\right\rangle$	n $so,\left\vert \frac{1}{2},+\frac{1}{2}\right\rangle$
$F+\frac{1}{2}$							
0	$-\frac{1}{2}(\gamma_1-2\gamma_2)$						
0	0	$-\frac{1}{2}(\gamma_1+2\gamma_2)$					
0	0	$-\sqrt{2}\gamma_2$	$-\frac{1}{2}\gamma_1$				
0	0	0	0	$F+\frac{1}{2}$			
0	0	0	0	0	$-\frac{1}{2}(\gamma_1-2\gamma_2)$		
0	0	0	0	0	0	$-\frac{1}{2}(\gamma_1+2\gamma_2)$	
0	0	0	0	0	0	$\sqrt{2}\gamma_2$	$-\frac{1}{2}\gamma_1$

$H_2 * k_Z^2$

Parameter	InAs	GaSb	GaAs
Lattice Constant (Å)	6.0584	6.0954	5.6533
Bandgap E_G (meV)	418	810	1518
Spin-Orbit Splitting Δ (meV)	380	775	340
F	-0.25	-0.17	-0.09
γ_1	1.97	2.58	1.21
γ_2	-0.48	-0.58	-0.72
γ_3	0.44	0.65	0.08
$\bar{\gamma}$	-0.02	0.035	-0.32
μ	-0.46	-0.615	-0.4
κ	1.17	1.43	-1.62
$E_p = 2P^2$ (eV)	22.2	22.4	28.0
Dielectric Constant	15.15	15.69	12.53

[001] magnetic field ***k.p*** matrix and material parameters used in the calculations.